HARMONIZATION OF WFI DATA FROM THE CBERS-4, CBERS-4A AND AMAZONIA-1 SATELLITES FOR AGRICULTURAL APPLICATIONS

Lucas Volochen Oldoni

Doctorate Thesis of the Graduate Course in Remote Sensing, guided by Drs. Ieda Del'Arco Sanches, and Michelle Cristina Araujo Piccoli, approved in August 18, 2022.

URL of the original document:
<http://urlib.net/8JMKD3MGP3W34T/47M46US>

INPE

São José dos Campos

2022

HARMONIZATION OF WFI DATA FROM THE CBERS-4, CBERS-4A AND AMAZONIA-1 SATELLITES FOR AGRICULTURAL APPLICATIONS

Lucas Volochen Oldoni

Doctorate Thesis of the Graduate Course in Remote Sensing, guided by Drs. Ieda Del'Arco Sanches, and Michelle Cristina Araujo Piccoli, approved in August 18, 2022.

INPE

São José dos Campos

2022

INSTITUTO NACIONAL DE PESQUISAS ESPACIAIS
Secretaria de Pós-Graduação - SEPGR

DEFESA FINAL DE TESE DE LUCAS VOLOCHEN OLDONI
REG 142956/2018, BANCA Nº 204/2022

No dia 18 de agosto de 2022, por teleconferência, o(a) aluno(a) mencionado(a) acima defendeu seu trabalho final (apresentação oral seguida de arguição) perante uma Banca Examinadora, cujos membros estão listados abaixo. O(A) aluno(a) foi APROVADO(A) pela Banca Examinadora, por unanimidade, em cumprimento ao requisito exigido para obtenção do Título de Doutor em Sensoriamento Remoto. O trabalho precisa da incorporação das correções sugeridas pela Banca Examinadora e revisão final pelo(s) orientador(es).

Novo Título: "Harmonization of WFI data from the CBERS-4, CBERS-4A and Amazonia-1 satellites for agricultural applications"

Membros da banca:

Dr. Lenio Soares Galvao – Presidente – INPE
Dra. Ieda Del'Arco Sanches – Orientadora – INPE
Dra. Michelle Cristina Araujo Piccoli – Orientadora – Université catholique de Louvain - UCLouvain
Dr. Vitor Souza Martins – Membro Externo – Mississippi State University
Dr. João Francisco Gonçalves Antunes – Membro Externo – EMBRAPA

Documento assinado eletronicamente por **Vitor Souza martins (E)**, **Usuário Externo**, em 15/09/2022, às 10:28 (horário oficial de Brasília), com fundamento no § 3º do art. 4º do Decreto nº 10.543, de 13 de novembro de 2020.

Documento assinado eletronicamente por **João francisco gonçalves antunes (E)**, **Usuário Externo**, em 16/09/2022, às 10:56 (horário oficial de Brasília), com fundamento no § 3º do art. 4º do Decreto nº 10.543, de 13 de novembro de 2020.

Documento assinado eletronicamente por **Michelle Cristina Araujo piCcoli (E)**, **Usuário Externo**, em 16/09/2022, às 12:15 (horário oficial de Brasília), com fundamento no § 3º do art. 4º do Decreto nº 10.543, de 13 de novembro de 2020.

Documento assinado eletronicamente por **Ieda Del Arco Sanches**, **Pesquisadora**, em 16/09/2022, às 16:55 (horário oficial de Brasília), com fundamento no § 3º do art. 4º do Decreto nº 10.543, de 13 de novembro de 2020.

Documento assinado eletronicamente por **Lênio Soares Galvão**, **Pesquisador**, em 19/09/2022, às 08:44 (horário oficial de Brasília), com fundamento no § 3º do art. 4º do Decreto nº 10.543, de 13 de novembro de 2020.

A autenticidade deste documento pode ser conferida no site https://sei.mcti.gov.br/verifica.html, informando o código verificador **10426946** e o código CRC **80C4F261**.

Referência: Processo nº 01340.005697/2022-31

SEI nº 10426946

Science can never solve one problem without raising ten more problems.

George Bernard Shaw

To my parents,

Ana and Olivino,

ACKNOWLEDGMENTS

To all my friends at INPE, for the friendship, laughing, ideas, talks, and adventures. In special, to all my colleges from 2018, friends of room 04/SERE II and ASA, the AgriRS team, and to Victor, Denis, Bruno, Hilton, Naty, Bernardo, Mikha, Andeise, Gustavo, and Eloisa.

And thanks to many other friends and colleagues that would be impossible to mention here.

ABSTRACT

Brazil faces the challenge of conciliating food production with natural vegetation preservation, and the government has been investing in earth observation satellites to assist in this task. In this context, images from the Wide-Field Imager (WFI) sensor onboard the China-Brazil Earth Resources Satellite (CBERS-4), CBERS-4A, and Amazonia-1 have been used in remote sensing applications in Brazil. Combining the data from the WFI sensors onboard the three satellites will allow 1-to-3-day revisit frequency. However, the integration of three sensors of different platforms requires several considerations to derive a consistent time series of surface reflectance or derived product (e.g., vegetation indices). Thus, the main objective of this research is to integrate WFI data from CBERS-4, CBERS-4A, and Amazonia-1 into a harmonized time series for agricultural monitoring. There are five main topics in this research: (i) cloud masking evaluation, (ii) geometric accuracy assessment, (iii) bi-directional effects normalization, (iv), inter-satellite cross-sensor comparison, and (v) usage of time series in an agricultural application. Initially we analyzed two cloud mask algorithms to apply to the WFI data. This is an essential product for time series analysis. The Automatic Time-Series Analysis (ATSA) proved to be more balanced between omission and inclusion errors than the CMASK, despite the need for a time series to be applied. In a second study, we evaluated the geometric accuracy of the WFI data in three cases: band-to-band, multitemporal, and compared to Sentinel-2/MSI data. Large displacements were observed against the MSI data, reaching 1.45 pixels (93m) for CBERS-4/WFI and Amazonia-1/WFI, and 2.5 pixels (138 m) for CBERS-4A/WFI. Thus, a framework for automatically correcting these displacements was implemented. After the co-registration procedures, the geometric accuracy of the images was improved, reaching an average root mean square error (RMSE) of spatial shifts on a tile basis less than 0.29±0.05 pixels. In the third study, we quantified the existing angular effects in the WFI data and compared six approaches to normalizing these effects. All six approaches were able to reduce directional effects, while only those using full Bidirectional Reflectance Distribution Function (BRDF) normalization were able to reduce angular effects due to illumination effects. In the fourth study, inter-satellite WFI cross-comparison was performed and transformation function between satellites were derived. The BRDF normalization and co-registration reduced the differences between the WFI data from three satellites in most cases. The WFI data from CBERS-4 and CBERS-4A were more similar to each other compared to Amazonia-1 WFI data, the formation of two distinct clusters in the blue and NIR bands. Despite that, statistical transformation functions were derived and surface reflectance of one sensor was converted to the other. In the last study, we combined our previous findings in a case study to map corn frost-damaged areas in western Paraná state by extracting phenological metrics from WFI-based Normalized Difference Vegetation Index (NDVI) time series using all three satellites. These phenological metrics allowed us to separate areas affected by two frost events from areas that had already been harvested or were in senescence or not affected. This application proves the potential of combining the WFI data from the three satellites for agricultural monitoring.

HARMONIZAÇÃO DE DADOS WFI DOS SATELITES CBERS-4, CBERS-4A E AMAZONIA-1 PARA APLICAÇÕES AGRÍCOLAS

RESUMO

O Brasil enfrenta o desafio de conciliar a produção de alimentos com a preservação da vegetação nativa, e o governo vem investindo em satélites de observação da Terra para auxiliar nessa tarefa. Nesse contexto, imagens do sensor *Wide-Field Imager* (WFI) a bordo do *China-Brazil Earth Resources Satellite* (CBERS-4), CBERS-4A e Amazonia-1 têm sido utilizados em aplicações de sensoriamento remoto no Brasil. A combinação dos dados dos sensores WFI a bordo dos três satélites permitirá uma frequência de revisita de 1 a 3 dias. No entanto, vários fatores relacionados ao sensor, à aquisição de dados e ao alvo precisam ser considerados para que os dados de diferentes sensores possam ser combinados em uma única série temporal consistente, ou seja, em que a refletância da superfície ou produto derivado (por exemplo, índices de vegetação) possa ser comparado ao longo do tempo e suas variações se devem apenas à mudança do alvo/cultura agrícola e não a outros fatores. Assim, o principal objetivo desta pesquisa é integrar os dados WFI do CBERS-4, CBERS-4A e Amazônia-1 em uma única série temporal mais consistente para monitoramento agrícola. A pesquisa foi dividida em cinco partes: (i) avaliação de máscaras de nuvens, (ii) avaliação da acurácia geométrica, (iii) normalização de efeitos bidirecionais, (iv), comparação cruzada dos sensores entre satélites e (v) uso de séries temporais em uma aplicação agrícola. Inicialmente analisamos dois algoritmos de máscara de nuvem para aplicar aos dados WFI. Este é um produto essencial para a análise de séries temporais. O *Automatic Time-Series Analysis* (ATSA) mostrou-se mais equilibrado entre erros de omissão e inclusão do que o CMASK, apesar da necessidade da utilização de uma série temporal. Em um segundo estudo, avaliamos a acurácia geométrica dos dados WFI em três casos: banda a banda, multitemporal e usando os dados do Sentinel-2/MSI como referência. Grandes deslocamentos foram observados em relação aos dados MSI, chegando a 1,45 pixels (93m) para o CBERS-4/WFI e Amazônia-1/WFI, e 2,5 pixels (138 m) para o CBERS-4A/WFI. Assim, foi implementado um esquema para correção automática desses deslocamentos. Após os procedimentos de corregistro, a acurácia geométrica das imagens foi melhorada, atingindo um erro quadrático médio (RMSE) médio de deslocamentos espaciais usando os tiles como referência inferior a 0,29±0,05. Em seguida, quantificamos os efeitos angulares existentes nos dados WFI e comparamos seis abordagens para normalizar esses efeitos. Todas as seis abordagens foram capazes de reduzir os efeitos direcionais, enquanto apenas aquelas que usaram a normalização *Bidirectional Reflectance Distribution Function* (BRDF) completa foram capazes de reduzir os efeitos angulares em função dos ângulos de

iluminação. Em nosso quarto estudo, a comparação cruzada WFI entre satélites foi realizada e funções de transformação entre satélites foram derivadas. O corregistro e a normalização BRDF reduziram as diferenças entre os dados WFI dos diferentes satélites na maioria dos casos. Os dados WFI do CBERS-4 e CBERS-4A foram mais semelhantes entre si. Quando comparados com os dados do Amazonia-1/WFI, houve a formação de dois clusters distintos nas bandas azul e NIR. Apesar disso, foram derivadas funções de transformação estatística que permitem a conversão da refletância da superfície de um sensor para o equivalente ao outro. Por fim, em nosso quinto estudo, combinamos nossas descobertas anteriores em um estudo de caso para mapear áreas agrícolas afetadas por geadas no oeste do estado do Paraná extraindo métricas fenológicas da série temporal de Índice de Vegetação por Diferença Normalizada (NDVI) do sensor WFI dos três satélites. Essas métricas fenológicas permitiram separar áreas afetadas por dois eventos de geada de áreas que já haviam sido colhidas, ou estavam em senescência, ou que não foram afetadas. Essa pesquisa comprova o potencial de combinar os dados WFI dos três satélites para monitoramento agrícola.

Palavras-chave: Wide-Field Imager, BRDF, corregistro, comparação cruzada, monitoramento agrícola, série temporal.

LIST OF FIGURES

LIST OF TABLES

LIST OF ACRONYMS AND ABBREVIATIONS

AEA	Albers Equal Area
ARD	Analysis-Ready Data
AROSICS	Automatic and Robust Open-Source Image Co-Registration Software
ATSA	Automatic Time-Series Analysis
BRDF	Bidirectional Reflectance Distribution Function
CBERS	China-Brazil Earth Resources Satellite
CCD	High Resolution Charge-coupled devices Camera
CONAB	National Supply Company
CPs	Control Points
DETER	Real-Time Deforestation Detection System
EO	Earth observation
EROS	Earth Resources Observation and Science
ESA	European Space Agency
ETM+	Enhanced Thematic Mapper
EVI	Enhanced Vegetation Index
FOV	Field of View
GRI	Global Reference Image
HOT	Haze Optimized Transformation
HRC	High Resolution Panchromatic Imaging Camera
IBGE	Brazilian Institute of Geography and Statistics
INPE	Brazilian National Institute for Space Research
IRMSS	Infrared Multispectral Scanner
IRS	Infrared System
LP DAAC	Land Processes Distributed Active Archive Center
LULC	Land Use and Land Cover
LUM	Look-Up Map
MAE	Mean Absolute Error
MGRS	Military Grid Reference System

MODIS	Moderate Resolution Imaging Spectroradiometer
MSI	Multi-Spectral Instrument
MUX	Multispectral Camera
NBAR	Nadir BRDF-Adjusted Reflectance
NDVI	Normalized Difference Vegetation Index
NIR	Near Infrared
OA	Overall Accuracy
ODR	Orthogonal Distance Regression
OLI	Operational Land Imager
OLS	Ordinary least-squares
PA	Producer's Accuracy
PAN	Panchromatic and Multispectral Camera
RAA	Relative Azimuthal Angle
RANSAC	Random Sampling Consensus
RBF	Radial Basis Function
RF	Random Forest
RMSE	Root Mean Square Error
RS	Remote Sensing
RTLS	RossThick-LiSparse-Reciprocal
SAM	Spectral Angle Mapper
SBAF	Spectral Band Adjustment Factor
SITS	Satellite Image Time Series
STD	Standard Deviation
SWIR	Short Wave InfraRed
SZA	Solar Zenith Angle
TM	Thematic Mapper
TPS	Thin-Plate Splines
UA	User's Accuracy
UTM	Universal Transverse Mercator
VI	Vegetation Index
VNIR	Visible and Near-Infrared
VZA	View Zenith Angle

CONTENTS

1 INTRODUCTION

Global food production needs to meet the increased projected demands of population growth, dietary changes, and increasing bioenergy use to ensure food security (KEARNEY, 2010; PELLETIER; TYEDMERS, 2010; TILMAN et al., 2011). Brazil is one of the world's largest producers and exporters of agricultural commodities (FAOSTAT, 2022), with a great potential of increasing crop production (DIAS et al., 2016), in order to supply this growing global demand. However, in recent years, part of the growth of the cultivated area has taken place on native vegetation (ZALLES et al., 2019; POTAPOV et al., 2021). Therefore, Brazil has the challenge of increasing crop production and preserving the natural vegetation from being converted into cropland (SOTERRONI et al., 2019; PICOLI et al., 2020a).

In this scenario, there is an increasing need to monitor Brazilian crop production and supply chain as well as your areas of natural vegetation (ZU ERMGASSEN et al., 2020; CHAVES et al., 2021a). The monitoring of agricultural activity becomes an essential task, generating valuable information for all those involved in the sector and for the formulation of public policies. Due to the large territorial extension of Brazil and the high dynamics of agricultural activity, remote sensing (RS) is the most viable data source for large area crop monitoring (ATZBERGER, 2013; BÉGUÉ et al., 2018). Satellite-based RS data provide information over large areas in short periods allowing to subsidize the implementation of public policies related to food security, reducing deforestation, climate change, and agriculture dynamics (ATZBERGER, 2013; DIAS et al., 2016; BÉGUÉ et al.,

2018; WHITCRAFT et al., 2019; SALES; STROBL; ELLIOTT, 2022). These data can be used to classify crop types, estimate phenological stages, estimate yield, among others (FRITZ et al., 2019).

Nevertheless, the application of optical remote sensing data in tropical regions can be challenging due to constant cloud cover during the growing season of crops (WHITCRAFT et al., 2015b; PRUDENTE et al., 2020). According to Whitcraft et al. (2015a), data are required at least every eight days to monitor agricultural activity. Due to cloud cover, in some regions, a revisit frequency of 2 days or more is required to maximize the opportunities of cloud-free observations through optical orbital SR. In addition, for agricultural monitoring to cover all sizes of fields, sensor data with a medium spatial resolution (10-100 m) is essential (WHITCRAFT et al., 2015b). Combining several Earth observation (EO) satellites is one way to overcome this limitation and achieve the necessary revisit frequency for proper monitoring (WHITCRAFT et al., 2015b; WULDER et al., 2015).

In this context, China-Brazil Earth Resources Satellite (CBERS) Program has been providing multi-temporal data for assessing and monitoring natural resources in Brazil (FONSECA et al., 2014). Currently, two CBERS satellites are in operation, the CBERS-4 and CBERS-4A and both have the Wide-Field Imager (WFI) camera in the payload module. The WFI is a multispectral camera acquires Visible and Near-Infrared (VNIR) bands, with a spatial resolution of 55-64m at nadir and a 5-day temporal resolution at the Equator. The CBERS-4/WFI imagery have been used for agricultural and environmental monitoring (PICOLI et al.,

2020b; CHAVES et al., 2021b), and they are the primary data source for the Real-Time Deforestation Detection System (DETER), which generates data to support Brazil's actions in protecting Amazon rainforest against deforestation (INPE, 2019). In addition, another WFI sensor with characteristics similar to the CBERS-4 and -4A is onboard of Amazonia-1, the first EO satellite completely designed, integrated, tested, and operated by Brazil (INPE, 2021a). Combining data from the WFI sensors from the three platforms (CBERS-4, CBERS-4A, and Amazonia-1) will allow a near-daily revisit with a medium spatial resolution and will benefit agricultural and environmental monitoring (FONSECA et al., 2014; PICOLI et al., 2020b; CHAVES et al., 2021b). Particularly, WFI constellation is highlighted to overcome cloud cover limitations over the main harvest seasons across Brazilian producers' regions (WHITCRAFT et al., 2015b; PRUDENTE et al., 2020) and meet the required temporal resolutions indicated by Whitcraft et al. (2015a) for crop monitoring.

However, to integrate data from different sensors into the same time series, it is necessary to reduce possible spectral, geometric, spatial, calibration, and angular differences (CLAVERIE et al., 2018). Fritz et al. (2019) indicate that a better understanding of discrepancies between spectral data and vegetation indices from different sources is still one of the gaps in agricultural monitoring programs. This research topic has recently gained more attention, with remaining challenges (WULDER et al., 2015; MANSARAY et al., 2019).

Despite the great potential for agricultural monitoring in integrating the data acquired by the WFI sensors onboard the CBERS-4, CBERS-4A, and Amazonia-

1 in a single time series, this has not yet been documented in the literature. The hypothesis of this work is that the WFI data from CBERS-4, CBERS-4A and Amazonia-1 can be integrated into a single consistent and seamless time series for agricultural applications. This research investigates possible sources of differences between WFI data acquired on three satellites to improve the data quality and generate a more consistent time series.

1.1 Objectives

The main objective of this research is to integrate WFI data from CBERS-4, CBERS-4A, and Amazonia-1 into a single and more consistent time series for agricultural monitoring. The specific objectives are:

1.1.1 Specific objectives

- Perform accuracy assessment of cloud mask and cloud shadow mask detection algorithms for WFI data;

- Propose a framework for automatic sub-pixel registration of WFI images from CBERS-4, CBERS-4A, and AMAZONIA-1;

- Evaluate six approaches for angular normalization of WFI images;

- Derive transformation functions to convert the reflectance of one sensor to the equivalent of what would be obtained by the other sensor based on inter-satellite cross-comparison of WFI data from CBERS-4, CBERS-4A, and Amazonia-1;

- Integration of WFI data from CBERS-4, CBERS-4A, and Amazonia-1 in a single time series for mapping frost-damaged corn areas.

2 THEORETICAL BACKGROUND

This chapter describes a theoretical background about agriculture and its monitoring (2.1), the Brazilian remote sensing program (2.2), and integration of remote sensing data from optical sensors (2.3). The idea is to provide an overview of the context and the state-of-art that was further explored in the next chapters.

2.1 Agriculture and its monitoring

Due to the economic importance and to ensure food security, agricultural monitoring is essential. This information is important to everyone involved in the production chain, from the government, industries, cooperatives, and producers, to avoid excess or lack of products, assist in planning and avoid losses. In this sense, accurate information on the spatial and temporal distribution of land use for agriculture, crop yield and production, is a starting point for the development of public policies aimed at making production more sustainable (DIAS et al., 2016).

Brazil uses subjective data sources (interviews with people, agencies and entities related to agriculture, e.g., farmers, companies, cooperatives, supplier banks) in the official estimates of agricultural production carried out by the Brazilian Institute of Geography and Statistics (IBGE) and by the National Supply Company (CONAB). Although highly useful, these surveys do not allow the quantification of errors and the spatial representation of the estimates (FORMAGGIO et al., 2003; SANTOS et al., 2014; SCHULTZ, 2016).

In this context, the SR can significantly contribute by providing accurate and timely information on the agricultural sector, being probably the best way to obtain unbiased information on large areas (ATZBERGER, 2013). Among the information about agriculture that can be inferred by SR are mapping of agricultural areas, agricultural calendar (start, end and length of the crop growing cycle), agricultural intensity maps (number of crop growing cycles per year), crop types maps, yield and production estimate (FRITZ et al., 2019). However, agricultural monitoring through SR is still challenging. This is especially true in tropical regions, such as Brazil, where the favorable climate allows multiple crops per year and different cropping systems (e.g., no-till, minimal cultivation, irrigation, crop rotation and early varieties, integrated crop–livestock system) (FORMAGGIO; SANCHES, 2017). In addition, there is great diversity in the phenological cycle of crops and in the agricultural calendar.

Annual crops are highly dynamic in time, with a significant change in the amount of biomass occurring within a week (DUVEILLER et al., 2013). For an adequate monitoring of annual agricultural crops, it is necessary to use orbital images with a weekly interval, or even smaller, during the entire phenological cycle (WHITCRAFT et al., 2015c; WHITCRAFT et al., 2015d). The temporal resolution is related to the type of monitoring performed. For example, agricultural calendar (WHITCRAFT et al., 2015d) and yield (GAO et al., 2018) estimates require a higher temporal resolution than necessary for mapping cropland.

Orbital sensors acquire images from the same place on the earth's surface regularly, enabling the images obtained by them to be calibrated, allowing the

comparison of measurements at different times. Thus, each pixel location (x, y) in consecutive times, t_1, ..., t_m, constitutes a Satellite Image Time Series (SITS) (PICOLI et al., 2018). Agricultural monitoring is often performed using Vegetation Index (VI) SITS (ATZBERGER, 2013). VIs are mathematical combinations of spectral reflectance at different wavelengths, mainly in the visible and near-infrared (VNIR) regions and can be related to biophysical characteristics of vegetation (VIÑA et al., 2011). IVs such as the Normalized Difference Vegetation Index (NDVI) (ROUSE et al., 1974a) and the Enhanced Vegetation Index (EVI) (HUETE et al., 2002), can be used as an indicator of the temporal evolution of green biomass throughout the growing cycle of crops (Figure 2.1), showing low values at the beginning, gradually increasing until the maximum biomass and decreasing with the end of the growing cycle (ESQUERDO; ZULLO JÚNIOR; ANTUNES, 2011).

Figure 2.1 – Example of an average NDVI time series from a municipality and the respective phenological phases.
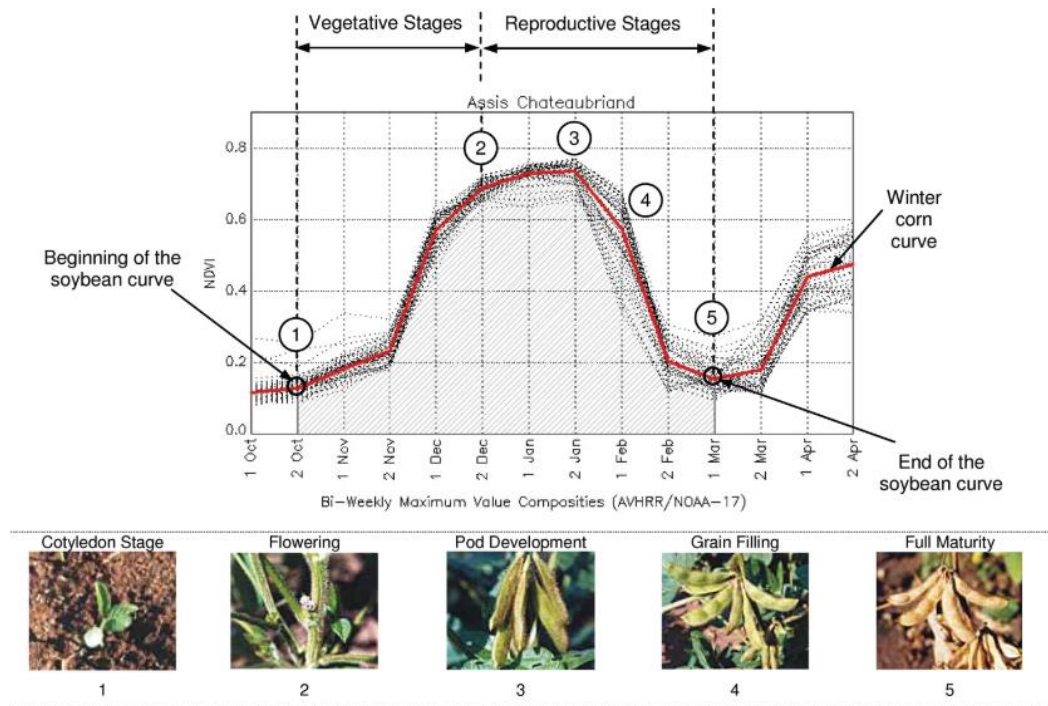
Source: Esquerdo, Zullo Júnior and Antunes (2011).

Several agricultural monitoring methodologies require dense SITS (high temporal frequency). The MODIS sensor, onboard Terra and Aqua satellites, can provide this type of data with high temporal resolution, and it has been the main sensor employed in agricultural monitoring, mainly due to its daily acquisitions, the 16-day compositions of IVs (EVI and/or NDVI), and the moderate spatial resolution (250 m) (ATZBERGER, 2013; BÉGUÉ et al., 2018). MODIS SITS applications include monitoring phenological development stage and crop progress (GAO et al., 2017), agricultural calendars (WHITCRAFT, 2015d), agricultural expansion (ADAMI et al., 2012), mapping of agricultural areas (WALDNER; CANTO; DEFOURNY, 2015), distinguish and map crop species (ZHONG et al., 2016; CHEN et al., 2018), estimate yield (AZZARI; JAIN; LOBELL, 2017; GAO et al.,

8

2018), in addition to identifying the dynamics and cycles of annual crops (Figure 2.2). However, in some regions that have greater spatial heterogeneity, with fragmented, irregular and smaller fields, the 250 m spatial resolution of the MODIS sensor can be a limiting factor, both for mapping (YAN; ROY, 2014; FRITZ et al., 2015; ZHONG et al., 2016a), and for estimating yield (GAO et al., 2018).

Figure 2.2 – Example of an area with three annual growing cycles of agricultural crops identified with MODIS NDVI SITS.

Source: Esquerdo et al. (2020).

Optical sensors, such as MODIS, are dependent on clear sky conditions to acquire useful images. Persistent cloud cover combined with low revisit frequency can prevent the observation of crucial stages of crop growing by optical sensors (especially crops of annual cycle) (GRIFFITHS et al., 2019). This can be a limiting factor, especially in tropical regions (SANO et al., 2007; SUGAWARA; RUDORFF; ADAMI, 2008; WHITCRAFT et al., 2015b; EBERHARDT et al., 2016; PRUDENTE et al., 2020). Eberhardt et al. (2016) observed a maximum average probability of occurrence of cloud-free observations of 30% for the months of December and January in the states of Paraná and São Paulo, a period in which crops are experiencing intense vegetative growth in almost the entire country (WHITCRAFT et al., 2015d). According to Whitcraft (2015a), in much of Brazil during the month of January, to obtain a cloud-free image every 8 days with 70%

9

probability, a revisit of 1-2 days is necessary. To obtain the same result with 95% probability, the frequency of observations must be greater than one day.

Thus, no medium spatial resolution optical sensor alone with free data can provide the frequency of acquisitions necessary for adequate agricultural monitoring in Brazil (WHITCRAFT et al., 2015b). This is the main reason why the monitoring of crop development conditions and productivity estimation with medium spatial resolution (10-100m) has not yet reached a large scale around the world. This is one of the gaps in agricultural monitoring systems, so that they can cover all fields sizes (FRITZ et al., 2019). Therefore, the integration of images from multiple sensors to generate dense and consistent SITS becomes an essential task for agricultural monitoring. This, considering that in a consistent time series the surface reflectance or derived product (e.g., IVs) can be compared over time and its variations are due only to the change in the target/crop and not due to other factors.

2.2 Brazilian remote sensing program

The incorporation of Brazil into a long-term remote sensing program has begun with the establishment of the China Brazil Earth Resources Satellite (CBERS) program (PINTO et al., 2016a). The CBERS program has been developed under a cooperation agreement between Brazil and China for making and operating remote sensing satellites providing multi-spectral data for monitoring and studying the natural resources and anthropogenic phenomena (EPIPHANIO, 2009, 2011a; FONSECA et al., 2014). CBERS-1, the first satellite developed, was launched on 14 October 1999 by the Chinese Long March 4B launcher from the

Taiyuan Satellite Launch Center in China (PONZONI; ZULLO; LAMPARELLI, 2008). CBERS-1 remained functional until August 2003 (PINTO et al., 2016a). The second satellite (CBERS-2) was launched successfully from the same launch center on 21 October 2003 and carried an identical payload as CBERS-1: Wide Field Imager (WFI), High Resolution Charge-coupled devices Camera (CCD), and the Infrared Multispectral Scanner (IRMSS) (PONZONI; ZULLO; LAMPARELLI, 2008). The CCD camera had visible, near infrared (NIR) and panchromatic bands, with 20 m spatial resolution and a 26-day revisit. IRMSS sensor had the same revisit period as the CCD camera, with panchromatic, SWIR, and TIR bands, at spatial resolution of 80 and 160 m. Finally, the WFI had red and NIR bands with spatial resolution of 260 m and a revisit time of 3-5 days. The third satellite of the program, CBERS-2B, was launched in 2007 and operated until June 2010 (PINTO et al., 2016a), and had characteristics very similar to its predecessors, with the difference that the IRMSS sensor was replaced by the High Resolution Panchromatic Imaging Camera (HRC), with a single panchromatic band of 2.7 m of spatial resolution (EPIPHANIO, 2009). In 2004, the Brazilian National Institute for Space Research (INPE) began providing free and open access to CBERS data acquired directly by its ground receiving station or recorded on board the satellite which caused an exponential increase in the number of RS data users in Brazil (FONSECA et al., 2014).

CBERS-3 and CBERS-4 were developed as part of the second generation of the Chinese-Brazilian cooperation effort, with improved payload characteristics (EPIPHANIO, 2009). CBERS-3 was launched on 9 December 2013, also by a Long-March 4B rocket from the Taiyuan base in China, however, the satellite was

lost due to failure on the launcher's third stage (PINTO et al., 2016a). The fifth satellite of the CBERS Program, CBERS-4, was successfully launched from the Taiyuan Satellite Launch Center on 7 December 2014 (PINTO et al., 2016a), and provides free daily remote sensing images of the Brazilian territory and other regions of the Earth (CHAVES et al., 2021b), i.e., South America, Africa, and China. CBERS-4 carries four cameras in the payload module: Panchromatic and Multispectral Camera (PAN); Multispectral Camera (MUX); Infrared System (IRS); Wide-Field Imager (WFI) (EPIPHANIO, 2011a). The PAN camera has 3 visible bands up to 10 m and a panchromatic band up to 5 m, with a temporal resolution of 52 days. The MUX camera has visible and NIR (VNIR) bands with a spatial resolution of 20 m and a 26-day revisit time. The IRS camera has a revisit period equal to MUX, and panchromatic, SWIR and TIR bands, with a spatial resolution of 40 m (80 m for the TIR) (EPIPHANIO, 2009, 2011a). The WFI sensor had improvements over the first generation of CBERS satellites, with 4 multispectral bands in the VNIR, spatial resolution of 64 m at the nadir, while maintaining the revisit time capacity of 5 days at the equator (PINTO et al., 2016a).

On 20 December 2019, CBERS-4A, the sixth satellite of the CBERS Program, was launched from the Taiyuan Satellite Launch by the Chinese Long March 4B launcher (INPE, 2021b). CBERS-4A has three cameras: Wide Scan Multispectral and Panchromatic Camera (WPM), MUX and WFI. The WPM camera has 4 multispectral bands in the VNIR and a panchromatic band. The multispectral bands have a spatial resolution of 8 m and the PAN of 2 m, with a revisit time of 31 days. The MUX and WFI sensors have the same sensor characteristics as

presented in the CBERS-4, only with a change in spatial resolution from 20 m to 16 m in the MUX camera and from 64 m to 55 m in the WFI sensor (INPE, 2021b). On February 28, 2021, Brazil launched the Amazonia-1, the first EO satellite completely designed, integrated, tested, and operated by the country (INPE, 2021a). The Amazonia-1 satellite also carries a WFI sensor in its payload module, with similar spectral, temporal, and spatial characteristics to the WFI onboard of CBERS-4 satellite.

Among the sensors onboard Brazilian EO satellites, the WFI sensor has better characteristics to monitor dynamic activities due to its high temporal resolution. The CBERS-4/WFI imageries have been used for agricultural and environmental monitoring (PICOLI et al., 2020b; CHAVES et al., 2021b), and they are the primary data source for the Real-Time Deforestation Detection System (DETER), which produces daily alerts on changes in forest cover in the Brazilian Legal Amazon, to support surveillance work and control from authorities of deforestation by identifying clear-cutting and forest degradation (DINIZ et al., 2015; INPE, 2019). By combining the data from the three satellites it is possible to obtain a one-to-two-day revisit time with medium spatial resolution (Figure 2.3). This will improve the capacity to detect deforestation in the Amazon rainforest (INPE, 2019) and other biomes. In addition, the WFI data combination will allow more detailed information about agricultural production like crop type mapping, crop phenological growing assessment, yield estimation, and crop sowing and harvest progress (Figure 2.3b). Nevertheless, combining data from different satellite sensors, even with similar characteristics, involves challenges that will be discussed in the next section.

Figure 2.3 – Example of combining WFI data from CBERS-4 (C4), CBERS-4A (C4A) and Amazonia-1 (AM1) satellites over an area with predominance of agriculture in Primavera do Leste, Mato Grosso, Brazil (a), with the detailing of second crop corn harvest progress in central pivot areas (Lat, Lon: -15.370559, -54.437669) (b).
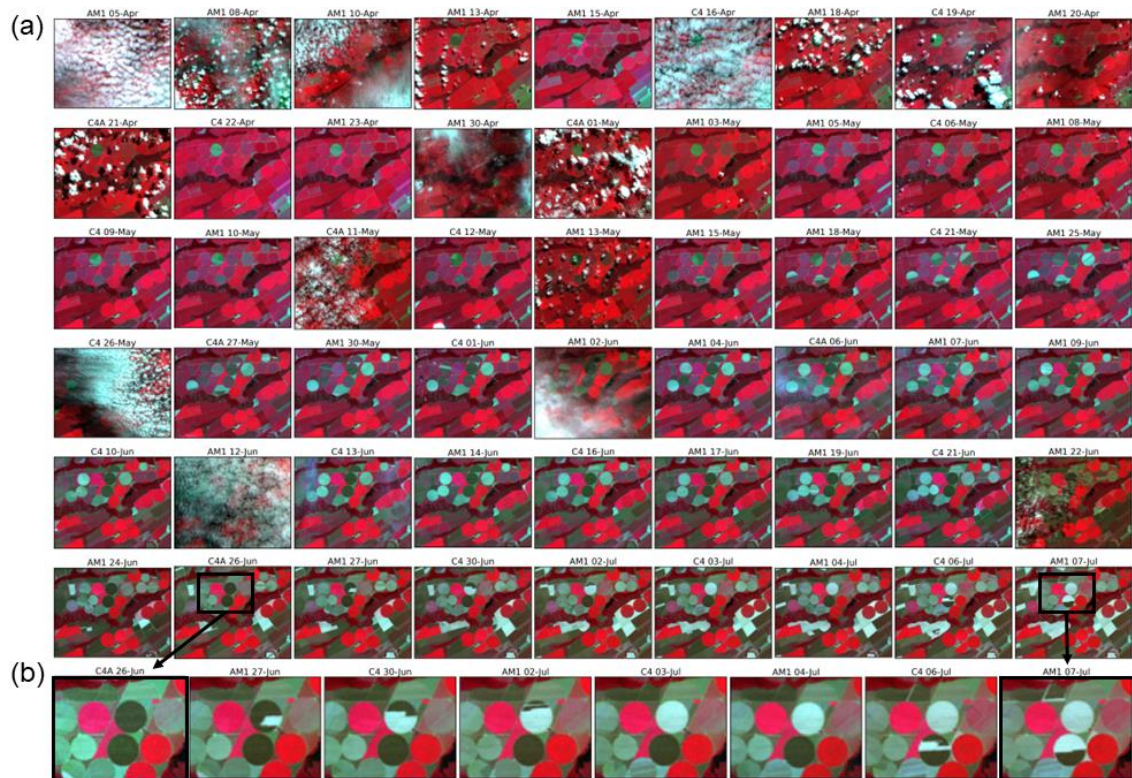
2.3 Integration of remote sensing data from optical orbital sensors

The acquisition of useful optical images with medium spatial resolution over large areas is limited by the frequency of temporal observation, latitude, sensor-specific acquisition conditions and period, as well as atmospheric contamination, including cloud, shadow, fog and smoke (WULDER et al., 2015). The combined use of data generated by different orbital sensors enables the development of virtual constellations with high temporal resolution and medium spatial resolution (WULDER et al., 2008; GOWARD et al., 2012). The main objective of a virtual

constellation is to increase the temporal revisit frequency of medium spatial resolution sensors.

However, the combination of different sensors involves challenges related to orbital, spatial, number, width, and position of spectral bands (MANDANICI; BITELLI, 2016), and also related to target characteristics (FLOOD, 2017). Thus, in order to be able to combine the surface reflectance between different sensors and over time, procedures for data harmonization are needed (GOWARD et al., 2012; WULDER et al., 2015). This enables data from different sensors to be combined into the same consistent and seamless time series (CLAVERIE et al., 2018). The main factors that generate differences between the surface reflectance obtained from different sensors are geometric and radiometric calibration, atmospheric correction, difference in spectral response function and observation geometry (FLOOD, 2017; CLAVERIE et al., 2018; HELDER et al., 2018; MARTINS et al., 2018; ZHANG, et al., 2018). These factors will be discussed in the next sections.

2.3.1 Geometric accuracy

A prerequisite for quantitative remote sensing applications is the accuracy and consistency of geolocation, especially for multi-temporal image analysis, so that images acquired from different sensors and dates can be compared directly (GAO; MASEK; WOLFE, 2009). The comprehensive analysis of geometric accuracy of the data from orbital sensors provides important guidance for improving geolocation accuracy and data application (JING et al., 2021). Although satellite data is usually registered accurately, displacements of up to a

15

few pixels are common in these data sources (YAN et al., 2016; SCHEFFLER et al., 2017; SKAKUN et al., 2017a). In these cases, it may be necessary to co-register the data from the different sensors before they can be integrated into the same consistent time series (CLAVERIE et al., 2018).

2.3.2 Atmospheric correction

Surface reflectance products are important for quantitative RS applications, being essential for combining data from different sensors in order to generate a consistent time series (HELDER et al., 2018). The use of different atmospheric correction algorithms can increase the differences between the surface reflectance of the sensors, as each model has different associated uncertainties depending on atmospheric correction inputs and how the atmospheric parameters are calculated (MARTINS et al., 2017; HELDER et al., 2018). Thus, the use of different algorithms should be carefully analyzed (MARTINS et al., 2017), and the ideal would be to use the same atmospheric correction model (MARTINS et al., 2017; CLAVERIE et al., 2018).

2.3.3 Spectral adjustment

Although sensors generally have similar bands in certain regions of the electromagnetic spectrum, there may be differences in the relative spectral response function between them. The importance of differences arising from relative spectral response function depends on the application and approach adopted to perform the time series analysis (MANDANICI; BITELLI, 2016). Methods based on physical quantities recovered by RS reflectance or empirical approaches based on multispectral indices are more affected by relative spectral

response function differences (VAN DER WERFF; VAN DER MEER, 2016). Thus, for proper interoperability of data from different sensors, it is desirable to perform spectral adjustment (HELDER et al., 2018). Two approaches are usually used to convert the reflectance of a sensor into the equivalent of the other sensor: using the Spectral Band Adjustment Factor (SBAF) (CHANDER et al., 2010; PINTO et al., 2016b; CLAVERIE et al., 2018; MARTINS et al., 2018); and through empirical comparison (ROY et al., 2016a; ZHANG et al., 2018). The SBAF is target specific and requires a hyperspectral data source to be calculated (HELDER et al., 2018), thus, allowing the reflectance of one sensor to be converted to a reflectance equivalent to that of the other. In the empirical approach, the real data are compared, and statistical transformation functions are derived to allow the conversion of data from one sensor into the equivalent of the other.

2.3.4 Angular normalization

Most surfaces are not isotropic, and angular effects may occur due to the variation of the viewing and illumination angles (observation geometry) (BRÉON; VERMOTE, 2012). This can generate significant variation in surface reflectance, even in the absence of change in vegetation condition/type or ground cover (GAO et al., 2014). Therefore, it may be necessary to normalize these effects for data integration (HELDER et al., 2018), so that in the analysis of the time series, the changes that occur are due to the crop canopy condition instead of artefacts of sun-target-sensor geometry (GAO et al., 2014). Expressing the pixel reflectance as a function of that geometry provides the Bidirectional Reflectance Distribution

Function (BRDF) (BRÉON; VERMOTE, 2012; FLOOD et al., 2013). BRDF effects are accentuated in sensors with a large Field of View (FOV) such as MODIS (SCHAAF et al., 2002). However, previous studies have shown this effect in narrow FOV sensors (FLOOD et al., 2013; GAO et al., 2014; ROY et al., 2016b, 2017; FRANCH et al., 2019), and proposed the angular normalization for data integration (FLOOD, 2017; CLAVERIE et al., 2018; ZHANG et al., 2018). According to Claverie et al. (2018), it is desirable to normalize the data to a nadir view zenith angle (VZA) and constant solar zenith angle (SZA), which is known as Nadir BRDF-Adjusted Reflectance (NBAR).

2.3.5 Cloud and cloud shadow mask

Although cloud masks and cloud shadows are not essential for the integration of data from different sensors, most time series applications of optical RS images require a cloud mask and cloud shadow with good accuracy (CLAVERIE et al., 2018). Omission of clouds can lead to errors that propagate to high-level products, while commission errors can lead to a reduced number of valid observations and, therefore, decrease the cloud-free observations (SKAKUN et al., 2022). Currently, there are a large number of methodologies to generate cloud and cloud shadow mask (FOGA et al., 2017; ZHU; HELMER, 2018; SKAKUN et al., 2022), which can be used for different sensors depending on their characteristics. Sensors with fewer spectral bands have greater limitations in the cloud mask and cloud shadow mask algorithms that are supported (ZHU; HELMER, 2018). Furthermore, it is important to evaluate and compare the cloud mask and cloud shadow algorithms available to sensors in different situations to

provide guidance in the application of optical RS data (FOGA et al., 2017; SKAKUN et al., 2022).

3 MATERIAL AND METHODS

In this chapter, we present a general description of the material and methods used in this research. First, we describe the thesis organization and show a general flowchart (3.1). Lastly, we describe the RS data (3.2) used in the analyses.

3.1 Thesis organization

This thesis is structured into a brief contextualization and theoretical background, general methods, five articles (Figure 3.1), overall discussion, contributions, and conclusions. Initially, we described the data used in the following chapters. In the first paper, we presented an accuracy assessment and comparison between two cloud masks algorithms for the WFI data. In the second paper, we evaluated the geometric accuracy of WFI images and presented a framework for sub-pixel automatic registration. In the third paper, we evaluated the angular effects on WFI images and compared six normalization approaches. In the fourth paper, we performed inter-satellite cross-comparison of WFI data and transformation functions are derived to convert the reflectance of one sensor to the equivalent of what would be obtained by the other sensor. In the fifth paper, we applied the developed algorithms to integrate the WFI data from the satellites in a single time series to map the corn frost-damaged areas in Paraná, as a study case in application to agricultural monitoring. Lastly, we discussed the main research findings and highlighted the main contributions and conclusions.

Figure 3.1 – Flowchart of this research.
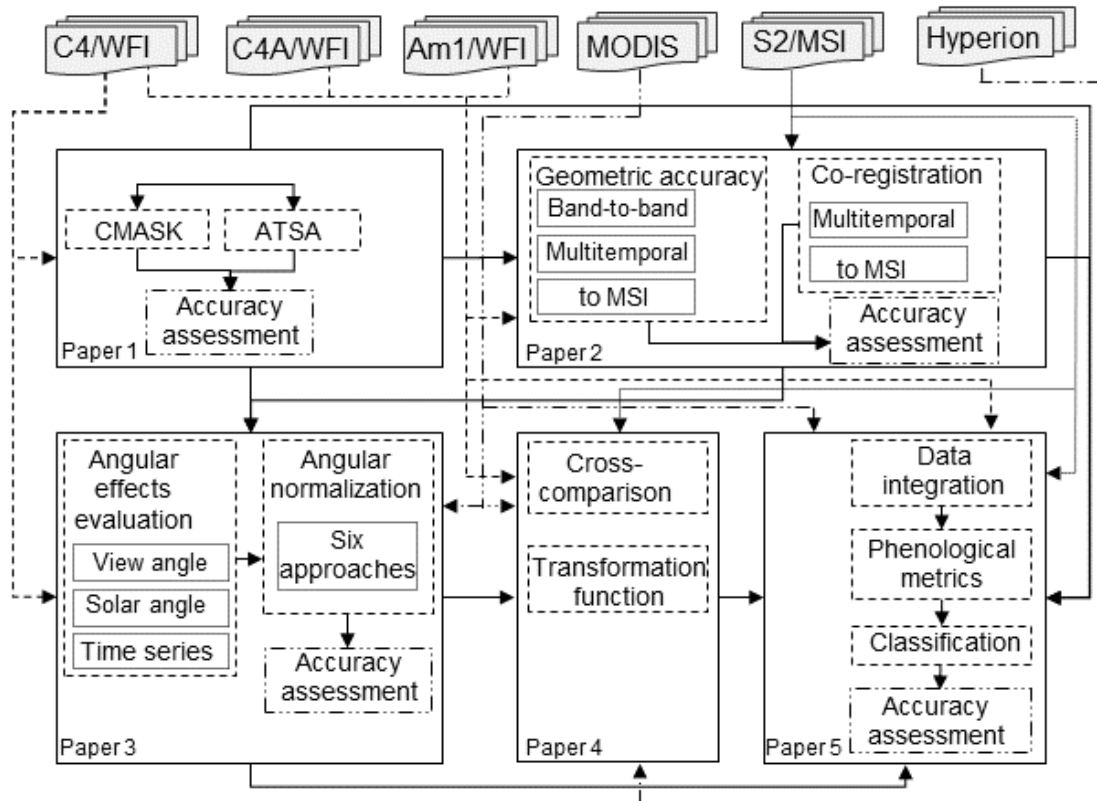
3.2 Remote sensing data

3.2.1 WFI sensor

The WFI sensors onboard CBERS-4, CBERS-4A, and Amazonia-1 satellites are a pushbroom imaging spectrometer acquiring data at four similar spectral bands, three at visible wavelengths (Blue, Green, and Red) and one at near-infrared (NIR). WFI has a large FOV of ±28.63⁰. The temporal resolution for each sensor is five days at the Equator. Because of the altitude difference between the satellites, the CBERS-4A images have a spatial resolution of 55 m, while those by CBERS-4 and Amazonia-1 have 64 m. The characteristics of the WFI sensors are summarized in Table 3.1.

Table 3.1 – Summary of the characteristics of WFI sensors onboard CBERS-4, CBERS-4A, and Amazonia-1.

Characteristic	CBERS-4/WFI	CBERS-4A/WFI	Amazonia-1/WFI
Technique	Pushbroom	Pushbroom	Pushbroom
Altitude	778 km	628.6 km	752 km
Spectral Bands	Blue: 0.45-0.52 µm Green: 0.52-0.59 µm Red: 0.63-0.69 µm NIR: 0.77-0.89 µm	Blue: 0.45-0.52 µm Green: 0.52-0.59 µm Red: 0.63-0.69 µm NIR: 0.77-0.89 µm	Blue: 0.45-0.52 µm Green: 0.52-0.59 µm Red: 0.63-0.69 µm NIR: 0.77-0.89 µm
Spatial Resolution	64 m	55 m	64 m
Swath width	866 km	684 km	850 km
FOV	±28.63º	±28.63º	±28.63º
Temporal Resolution	5 days	5 days	5 days
Radiometric Resolution	10 bits	10 bits	10 bits

Source: Epiphanio (2011b); Pinto et al. (2016a); INPE (2021a;b) and Moutinho (2021).

3.2.2 MSI sensor

Sentinel-2A and Sentinel-2B satellites were launched in 2015 and 2017, respectively, within the European Copernicus program (DRUSCH et al., 2012). These two satellites have the Multi-Spectral Instrument (MSI) onboard, an optical pushbroom sensor that acquires images of the Earth's surface in 13 spectral bands from visible and NIR to Short Wave InfraRed (SWIR) region at 10 m, 20 m, and 60 m spatial resolution (GASCON et al., 2014).

3.2.3 MODIS sensor

The MODIS sensors onboard the Terra and Aqua platforms provide at least two observations per day, making it possible to obtain a set of observations at different angular configurations in a short period of time. The MODIS sensor images are distributed in several products with different processing levels. MCD43A products provide information on MODIS BRDF/albedo. The weighting parameters for isotropic, volumetric, and geometric kernels (LUCHT; SCHAAF; STRAHLER, 2000) are retrieved as the best fit to the BRDF model from the accumulation of bidirectional observations obtained from both platforms over a 16-day period (SCHAAF et al., 2002) (for the Collection V006 MODIS BRDF/Albedo product) and stored in the MCD43A1 product. MODIS BRDF/albedo algorithm uses different strategies to retrieve the BRDF depending on the number and distribution, and quality of observations within this period (SCHAAF et al., 2002). The BRDF/Albedo band quality associated with the retrieve information of the BRDF parameters is stored in a similar product, the MCD43A2. The MCD43A4 BRDF-Adjusted Reflectance (NBAR) product uses the BRDF parameters to normalize reflectance values to nadir view given the mean SZA of the 16-day period, minimizing the effects of the anisotropic scattering and the view angle, resulting in a more stable and consistent product (LUCHT; ROUJEAN, 2000; SCHAAF et al., 2002). MCD43A product data are computed daily for MODIS spectral bands 1–7 in the Collection 6 and temporally weighted for the ninth day of the 16-day recovery period. The MCD43A images are distributed in sinusoidal projection at 500 m of spatial resolution, covering an area of approximately 10° x 10°.

4 ACCURACY ASSESSMENT OF CLOUD MASK DETECTION ALGORITHMS FOR CBERS-4/WFI IMAGERY[1]

Our first paper presented the accuracy assessment and comparison of two cloud mask algorithms for CBERS-4/WFI data. The results support the understanding of strengths and weaknesses of the algorithms in order to guide the use of cloud masks necessary for the further analyses proposed in this thesis (presented in the next chapters).

4.1 Introduction

Optical satellite imagery are widely used to map land use and land cover (LULC), monitor crops and ecosystems, and estimate land surface parameters, enabling a better understanding of the Earth system's functioning and how it has changed over time (COHEN; GOWARD, 2004; HANSEN; LOVELAND, 2012; WULDER et al., 2015, 2018; GÓMEZ; WHITE; WULDER, 2016; ZHU; HELMER, 2018; ENNOURI; KALLEL; ALBANO, 2019). Nonetheless, in optical remote sensing images, clouds and their corresponding shadows are inevitable and limit the potential of the imagery for ground information extraction (LI et al., 2019b). Estimates show that the global mean cloud cover over land surfaces is greater than 55% (ROSSOW; SCHIFFER, 1999; KING et al., 2013). In tropical regions, this value can be even higher, as in the Amazon region, where the frequency of

---

[1] Most part of this chapter was published in the OLDONI, L. V.; SANCHES, I. D.; PICOLI, M. C. A. ACCURACY ASSESSMENT OF CLOUD MASK DETECTION ALGORITHMS FOR CBERS-4 WFI IMAGERY. ISPRS Annals of the Photogrammetry, Remote Sensing and Spatial Information Sciences, v. V-3–2022, n. June, p. 61–67, 17 maio 2022.

cloud cover is higher than 80% in the wet season (PRUDENTE et al., 2020). Many applications need remote sensing data periodically, as is the case of LULC change and agricultural monitoring, and cloud contamination of optical imagery presents a major limitation (HANSEN; LOVELAND, 2012; WHITCRAFT et al., 2015b).

Thus, accurately extracting clouds and cloud shadows from cloud-contaminated images can help reduce the negative influences that cloud coverage brings to the automated application of the imagery (LI et al., 2017b), especially in dense time series focused on agricultural monitoring (BENDINI et al., 2019). Furthermore, due to the large amount of data required for multi-temporal and large-scale studies, it is important to acquire cloudless images automatically (SUN et al., 2017). Therefore, masking clouds and cloud shadows is often the first and most necessary step of image pre-processing in optical remote sensing applications (BRAATEN; COHEN; YANG, 2015; ZHU; HELMER, 2018; BAETENS; DESJARDINS; HAGOLLE, 2019).

Automatic and accurate detection of clouds and cloud shadows is challenging (ZHU; WOODCOCK, 2012, 2014; LI et al., 2017b; ZHU; HELMER, 2018). Different clouds with different spectral signatures (BIAN et al., 2016) can be easily confused with some cloud-free bright objects on the land surface (ZHU; HELMER, 2018). Furthermore, the spectral signature of thin clouds can be similar to the signature of the land surfaces underneath, as the observed reflectance contain a mixture of cloud and land signals, making them more difficult to identify (ZHU; WOODCOCK, 2014; BAETENS; DESJARDINS; HAGOLLE, 2019). Cloud

shadows are another challenge as they are easily confused with dark land surfaces due to the spectral similarity between them (ZHU; WOODCOCK, 2012; ZHU; HELMER, 2018).

Despite the challenges mentioned above, various methods have been successfully developed to detect clouds and cloud shadows. The methods for masking cloud and cloud shadows can be divided into two categories according to the single or multi-temporal images that the algorithms use (LI et al., 2017b). Most single-image methods screen clouds in individual images using predefined or adaptive thresholds (ZHU; HELMER, 2018). Single images methods require fewer input data than multi-temporal methods, and they are more popular (LI et al., 2017b). In multi-temporal methods, the temporal information in the images acquired at different times is used to detect clouds and shadows (ZHU; HELMER, 2018). The idea of these algorithms is that clouds and cloud shadows will cause sudden changes to the reflectance, and by comparing the image analysed with a reference without clouds, the clouds and cloud shadows will be easily detected (ZHU; WOODCOCK, 2014). Multi-temporal methods usually achieve a higher cloud detection accuracy by requiring more scenes over a short period (LI et al., 2017b). But this may cause problems for applications like change detection because LULC change will also result in sudden changes in satellite observations (ZHU; WOODCOCK, 2014).

Most of the methods for detecting clouds and cloud shadows were designed for images of a specific sensor. Fmask, for example, was originally designed for cloud screen and cloud shadows in Thematic Mapper (TM) and Enhanced

Thematic Mapper (ETM+) sensors on board Landsat satellites (ZHU; WOODCOCK, 2012). Later, this algorithm was improved to be used on Landsat-8/OLI (Operational Land Imager) and Sentinel-2/MSI images (ZHU; WANG; WOODCOCK, 2015; QIU; ZHU; HE, 2019). Other algorithms are image processors, which generate the cloud mask as part of the converting radiance process at the top of the atmosphere to surface reflectance (SANCHEZ et al., 2020). This is the case of the Sen2Cor algorithm (LOUIS et al., 2016), developed for Sentinel-2 MSI images. However, these algorithms use specific bands that many other sensors do not have (e.g., cirrus, SWIR, thermal) (ZHU; HELMER, 2018).

The WFI sensor has only four spectral bands (i.e., Blue, Green, Red, and NIR). Due to the limited number of spectral bands, detecting clouds and cloud shadows in WFI images is even more challenging, and few algorithms have been developed for such characteristics. For example, the Fmask needs SWIR and thermal spectral bands in older versions and at least SWIR and cirrus bands in newer versions (ZHU; WOODCOCK, 2012; ZHU; WANG; WOODCOCK, 2015). These bands are not present in the WFI sensor, which makes the Fmask unfeasible to be applied to the images of this sensor. The Automatic Time-Series Analysis (ATSA) (ZHU; HELMER, 2018) is suitable for sensors such as the WFI since it needs a minimum number of bands and fewer predefined parameters. This algorithm can be applied for areas with persistent clouds.

The reliability of the cloud mask is also a key element that determines the noise present in the reflectance time series (BAETENS; DESJARDINS; HAGOLLE,

2019). In practice, performance assessment is done by selecting representative images and assessing how well each algorithm performs in each image (SANCHEZ et al., 2020). Several studies have compared the accuracy of different cloud and cloud shadow detection algorithms. For exemple, Foga et al. (2017) assessed the accuracy of multiple cloud masking algorithms to determine the best globally applicable algorithm to be used in future Landsat quality assurance data products. Sanchez et al. (2020) compared four cloud detection methods (Fmask 4, MAJA, Sen2Cor 2.8, and s2cloudless) for Sentinel-2/MSI images in the Amazon region. Their results showed that FMask 4 has the best overall accuracy on images of the Amazon region.

Although the remote sensing community is making extensive use of CBERS-4/WFI data and the importance of cloud and cloud shadow masks for optical analysis of satellite imagery is well known, no cloud and cloud shadow masks assessment has been documented yet in the literature for this sensor. Thus, the objective of this work is to compare two cloud detection algorithms for CBERS-4/WFI images: the CMASK and the ATSA. The CMASK was previously used to generate WFI data cubes (FERREIRA et al., 2020), and the ATSA was initially tested with Landsat-8/OLI, Landsat-4/MSS, and Sentinel-2/MSI images (ZHU; HELMER, 2018).

4.2 Material and methods

4.2.1 Study sites

We selected four Military Grid Reference System (MGRS) tiles (Figure 4.1) with different characteristics of LULC and cloud cover incidence. Since ATSA

algorithm needs a time series, we decided to use subsets delimited by the MGRS

tiles then we cropped every WFI image that intersected with these tiles.

Figure 4.1 – Location of the four MGRS tiles (red hatched) used as study sites and the WFI tiles (unfilled polygons).

Map data © OpenStreetMap contributors
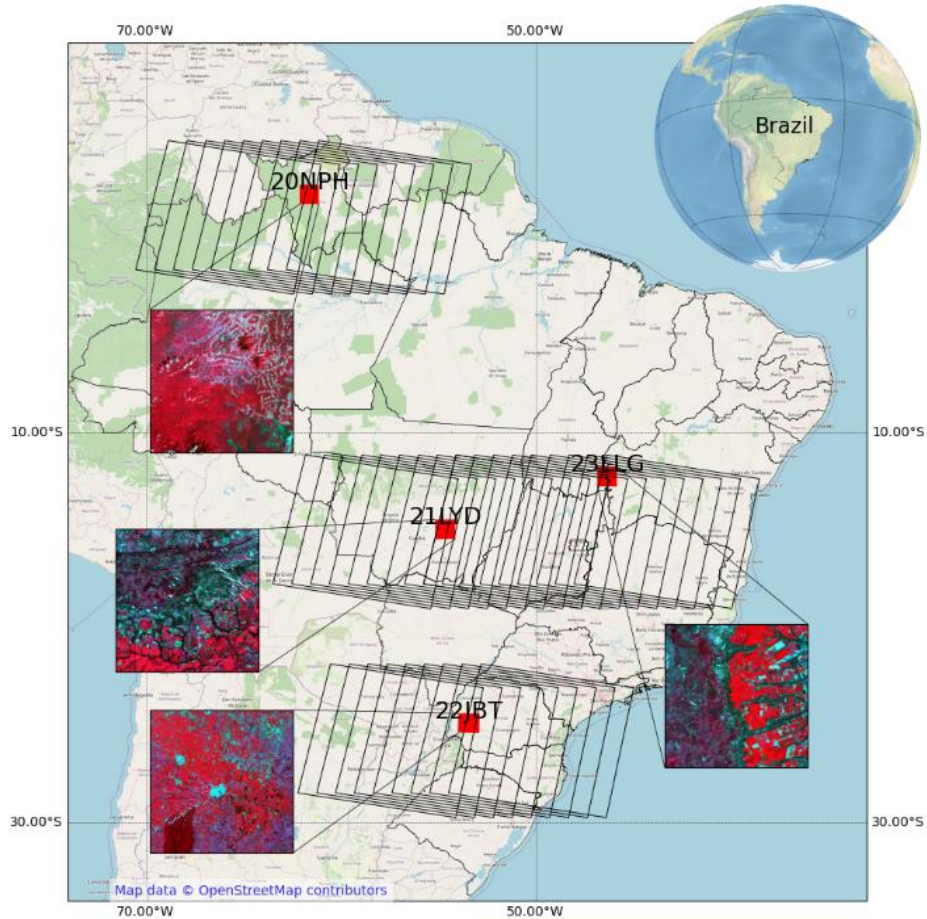
The 20NPH tile is in the Amazon biome. The predominant LULC in this region is

forest formation and pasture (SOUZA et al., 2020). This tile has a high incidence

of clouds all year round (PRUDENTE et al., 2020), making difficult to acquire

cloud-free images. Tiles 21LYD and 23LLG are in the Cerrado biome. The

predominant LULC in these tiles are intensive agriculture, pasture, grassland,

and savanna formation (SOUZA et al., 2020). In these two tiles, there are well

defined dry and rainy seasons. Thus, during December and February, the rainy season, there is a high incidence of clouds. However, during the dry season (from June to August), clouds have low incidence (PRUDENTE et al., 2020). Tile 22JBT is located in the Atlantic Forest biome (SOUZA et al., 2020), a region with a predominance of annual agriculture. In this tile, there is a high incidence of clouds between December and January and a medium incidence in the rest of the year (EBERHARDT et al., 2016; PRUDENTE et al., 2020).

4.2.2 WFI data

For our study, we obtained all available WFI images Level-4 intersecting the four MGRS tiles from January 1, 2020, to June 30, 2020, from the National Institute for Space Research (INPE) catalog website (http://www.dgi.inpe.br/catalogo/). The WFI Level 4 images provided by the INPE are geometrically corrected with ground control points and ortho-rectified (INPE, 2021c). The surface reflectance images were generated by MS3 software (SILVA; ANDRADE, 2013). We acquired 54, 68, 62, and 62 images for the tiles 20NPH, 21LYD, 22JBT, and 23LLG, respectively.

4.2.3 Cloud mask and cloud shadow detection algorithms

4.2.3.1 CMASK

The MS3 software was used to generate the CMASK (SILVA et al., 2016) in this work. CMASK classifies the image as clear or cloudy. CMASK is also used by the Brazil Data Cube project to generate ARD (analysis-ready data) data cubes for Brazil (FERREIRA et al., 2020). In CMASK, the reflectance of spectral bands is used to compute the NDVI, Whiteness Index (WI) and Haze Optimized

30

Transformation (HOT). The cloud detection is based on applying three filters from thresholds on these three indices. More details about CMASK can be found at Silva et al. (2016).

4.2.3.2 Automatic Time-Series Analysis (ATSA)

The ATSA was designed to identify clouds and cloud shadows in multitemporal optical images, being more suitable for areas with persistent clouds, and can be used for sensors with a limited number of spectral bands (ZHU; HELMER, 2018). The algorithm has five main steps: (i) calculate cloud and shadow indices to highlight cloud and cloud shadow information; (ii) obtain an initial cloud mask by unsupervised classifier; (iii) refine the initial cloud mask by analyzing the time series of a cloud index; (iv) predict the potential shadow mask using geometric relationships; and (v) refine the potential shadow mask by analyzing time series of a shadow index (ZHU; HELMER, 2018).

The ATSA algorithm needs a water mask. We selected images with less than 5% clouds in the metadata to create the water mask. Afterward, we collected samples by visual interpretation of these images. We applied the supervised classifier Spectral Angle Mapper (SAM) over the stack of these selected images (Souza et al., 2013). We extracted the mask of water/no water, along with the elevation and azimuth solar angles information from the metadata, and we used it as input to the ATSA algorithm.

Some parameters need to be configured in the ATSA algorithm. First, the longest and shortest distance between the shadow and its corresponding cloud must be selected. These values were empirically set to 1 and 40 pixels (64 m and 2560

m, respectively) after inspection of the images, as recommended by Zhu and Helmer (2018). ATSA uses these values to estimate shadow zones. Two other parameters, A and B, are the thresholds used by ATSA to identify cloud and shadow, respectively. We evaluated different combinations of A and B. We considered values of A equal to 0.5, 1.0, and 1.5, and B equal to 1.0 and 3.0. As the original algorithm was tested with Landsat data, and the WFI data has a lower spatial resolution (64 m), we changed the filter to remove isolated pixels from 4 to 2 inside the 3-by-3 neighborhood, for both cloud and cloud shadow.

4.2.4 Accuracy assessment

We assessed the cloud mask accuracy for CMASK and ATSA, and the accuracy of the cloud shadow mask for ATSA on a tile basis. For this, we randomly chose four images in each tile, and for each image, we randomly selected 100 sample points. These points were tagged by a remote sensing expert through image visual interpretation, following previous work (SANCHEZ et al., 2020). Thus, each tile had a total of 400 points for accuracy assessment. The photo interpreter labeled each sample as "*Cloud*", "*Cloud shadow*", or "*Clear*", based on images in a true-colour composite (red, green, and blue) and a false-colour composite (NIR, red, and green). Furthermore, the interpreter was unaware of the classes of the validation sample points in the cloud mask.

We generated an error matrix from the random sampling points. Thus the overall accuracy (OA), user's accuracy (UA), and producer's accuracy (PA) (FOODY, 2002) were derived from the error matrices. OA indicates the proportion of correctly classified pixels, and it's calculated by dividing the total number of

correctly classified pixels by the sample size. The PA indicates the probability of a reference pixel is correctly classified, and it's calculated by dividing the total number of correct pixels in a class by the total number of pixels of that class. The UA is calculated by dividing the total number of correct pixels in a class by the total number of pixels classified in that class, it indicates the probability that a pixel classified on the map actually represents that category (CONGALTON, 1991).

While the ATSA classifies images into three classes (*Clear*, *Cloud*, and *Cloud shadow*), the CMASK classifies them into two classes (*Clear* and *Cloud*). Therefore, we initially evaluated the accuracy of the ATSA considering the three classes and different combinations of parameters A and B (as described in Section 4.2.3.2). Afterward, to compare ATSA with CMASK, we consider only two classes for the two algorithms: *Clear* and *Not clear*. Thus, the *Cloud* and *Cloud shadows* classes have been grouped into the *Not clear* class for ATSA.

4.3 Results and discussion

In our experiments, when we considered the three classes (*Clear*, *Cloud*, and *Cloud shadows*), for all analysed tiles except 23LLG, the parameter A equal to 0.5 had the higher OA (Figure 4.2). For tile 23LLG, the highest value of OA was obtained with A equal to 1.0, while the lowest value was obtained with A equal to 0.5. Considering parameter B, except for tile 22JBT, the highest OA was reached with a parameter value equal to 3.0.

Figure 4.2 – Overall accuracy for different A and B parameters combinations in ATSA algorithms considering three classes: *Cloud, Cloud shadow*, and *Clear*.
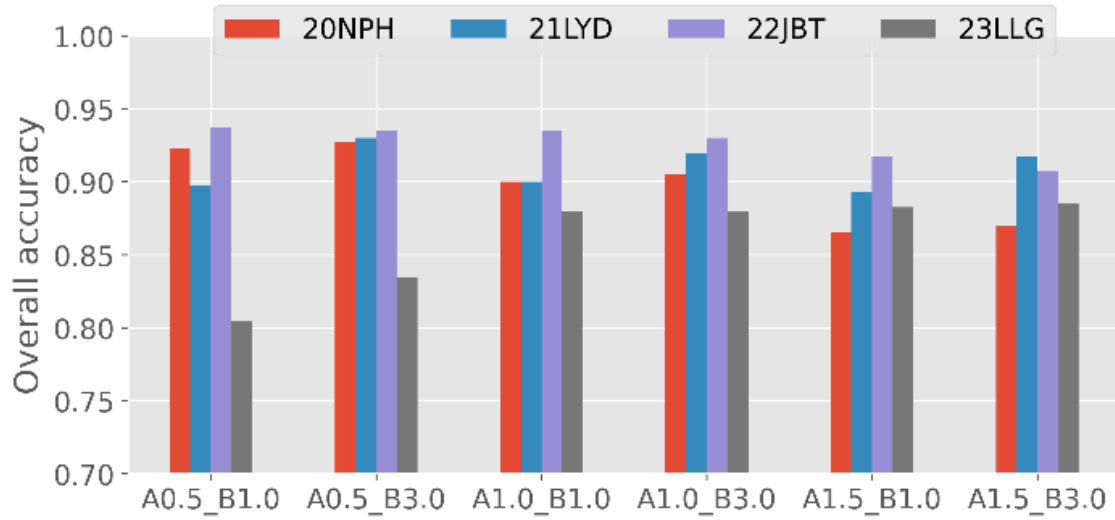
When we consider only two classes (Figure 4.3), *Clear* and *Not Clear*, the OA is generally greater than in the case of three classes (Figure 4.2). However, the OA patterns for parameters A and B are similar. Low values of A result in high OA, except for tile 23LLG. Meanwhile, low values of B result in smaller OA, except for tile 22JBT.

Figure 4.3 – Overall accuracy for CMASK and different combinations of A and B parameters in ATSA algorithms considering two classes: *Clear* and *No clear*.
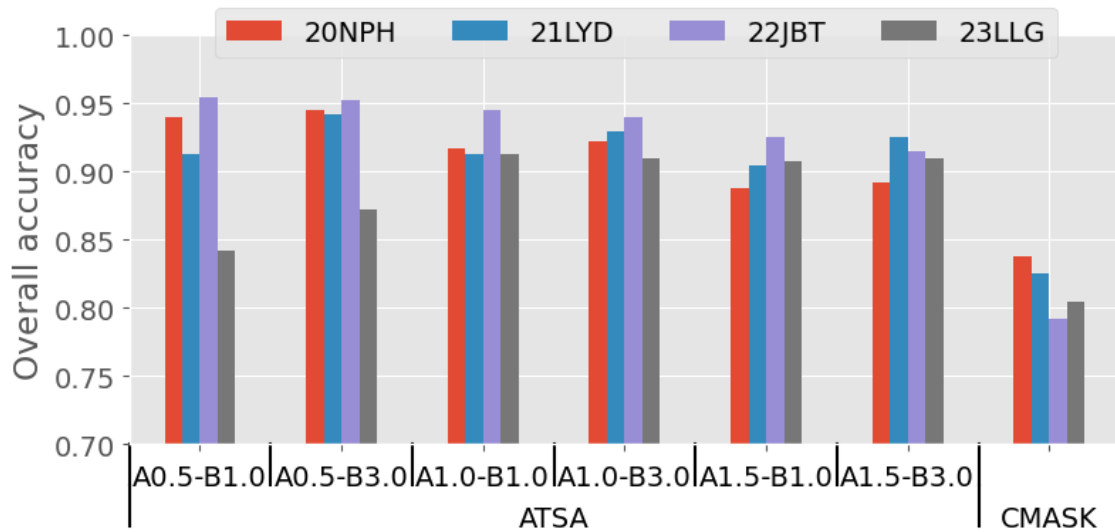
Comparing OA between ATSA and CMASK, any combination of the A and B parameters in ATSA results in higher OA than CMASK. The lowest value of OA was 0.91 in the 23LLG tile, considering the combination of A equal to 1.0 and B equal to 3.0 in ATSA. In comparison, the highest value of OA for CMASK was on the 20NPH tile, with the OA equal to 0.84.

For the case of the three classes, increasing the parameter A values in ATSA, there is an increase of UA for the *Cloud* class and a decrease for the *Clear* class (Figure 4.4). Conversely, increasing the parameter A value reduces the PA for the *Cloud* class and increases it for the *Clear* class. By reducing the parameter A value, more pixels are detected as clouds, reducing the omission error of the *Cloud* class. However, this also increases the number of clear pixels misclassified as clouds, increasing the commission error of the *Cloud* class. In most cases, the

UA and PA for ATSA were higher for the *Cloud* class than for the *Cloud shadow* class. A similar result was found by Zhu and Helmer (2018).

Figure 4.4 – User's accuracy (UA) and Producer's accuracy (PA) for different combinations of A and B parameters value in ATSA algorithm considering three classes: *Cloud, Cloud shadow*, and *Clear*.
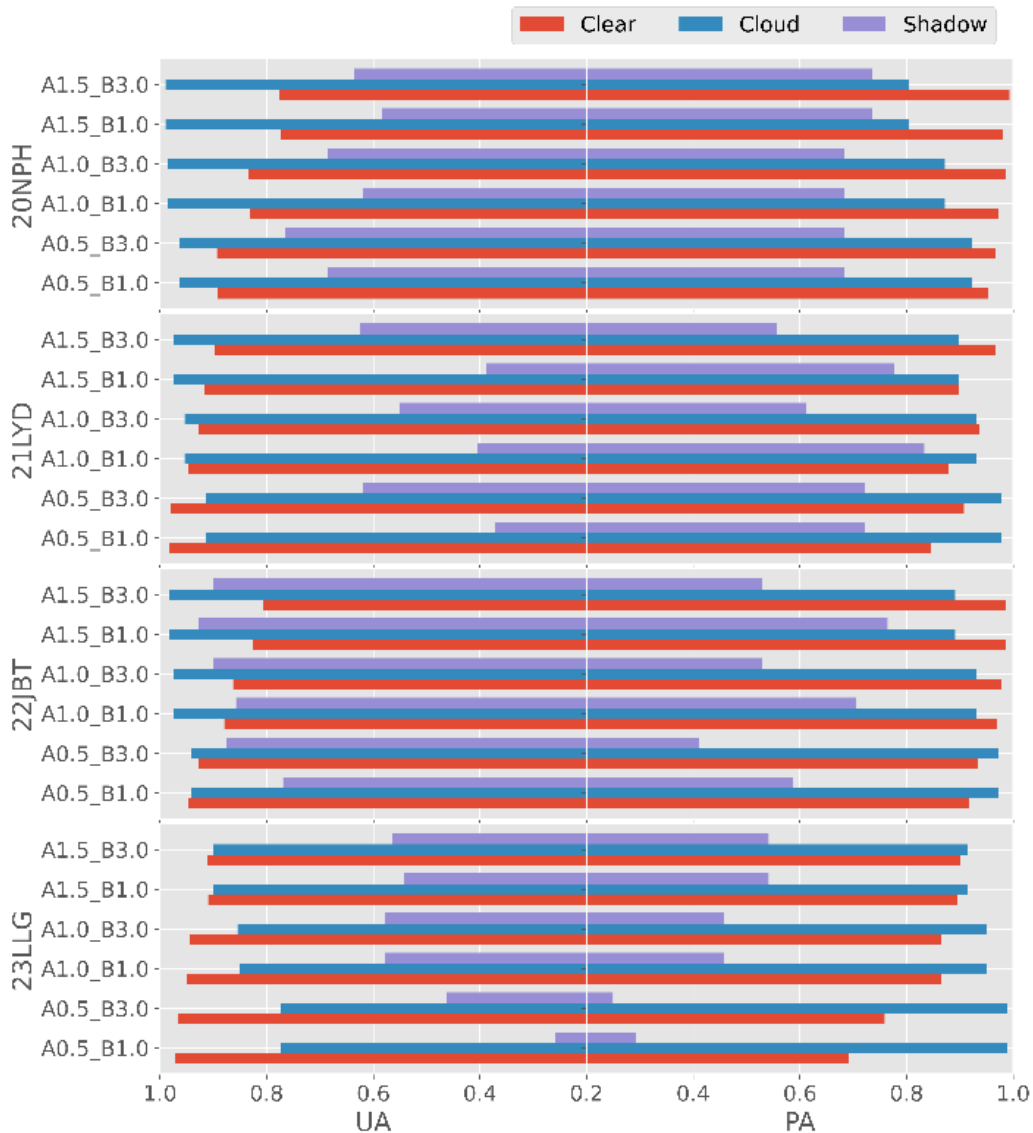
For the *Cloud shadow* class, in tiles 21LYD and 22JBT, the PA was higher with parameter B equal to 1.0. There was practically no difference in PA for the other tiles when parameter B was equal to 1.0 or 3.0. For most tiles and the parameter

A values, the UA was higher when parameter B was equal to 3.0. The confusion of the *Cloud shadows* class occurred when it was classified as *Cloud*, mainly on the edges of clouds, and the *Clear* class was misclassified as *Cloud shadow*. One of the possible reasons of confusion in the *Cloud shadow* class can be the replacement of the SWIR band by the NIR band. In the case of the tests performed by Zhu and Helmer (2018), they used SWIR in the shadow index. However, as WFI does not have a SWIR band, we needed to replace it with the NIR band, as Zhu and Helmer (2018) suggested.

In the ATSA algorithm, when the *Cloud* and *Cloud shadow* classes are combined in the *No clear* class, and the parameter A value is increased, there is an increase in the UA and a reduction in the PA for the *No clear* class (Figure 4.5). On the other hand, there is a reduction in UA and an increase in PA for the *Clear* class when the parameter A value is increased. Increasing the B parameter value results in an increase in UA, for the *No clear* class, and in PA, for the *Clear* class, in most cases.

CMASK presented UA close to 1.0 for the *No clear* class and PA close to 1.0 for the *Clear* class. However, it presented an omission error between 25% and 36% for the *No clear* class, and commission errors between 29% and 39% for this class. Almost all pixels classified in the *No clear* class are clouds. However, the CMASK fails to classify many cloud pixels in the *No clear* class and misclassify them in the *Clear* class. CMASK also doesn't classify cloud shadows, which increases the omissions in the *No clear* class.

Figure 4.5 – User's accuracy (UA) and Producer's accuracy (PA) for CMASK and different combinations of A and B parameters values in ATSA algorithm considering two classes: *Clear* and *No clear*.
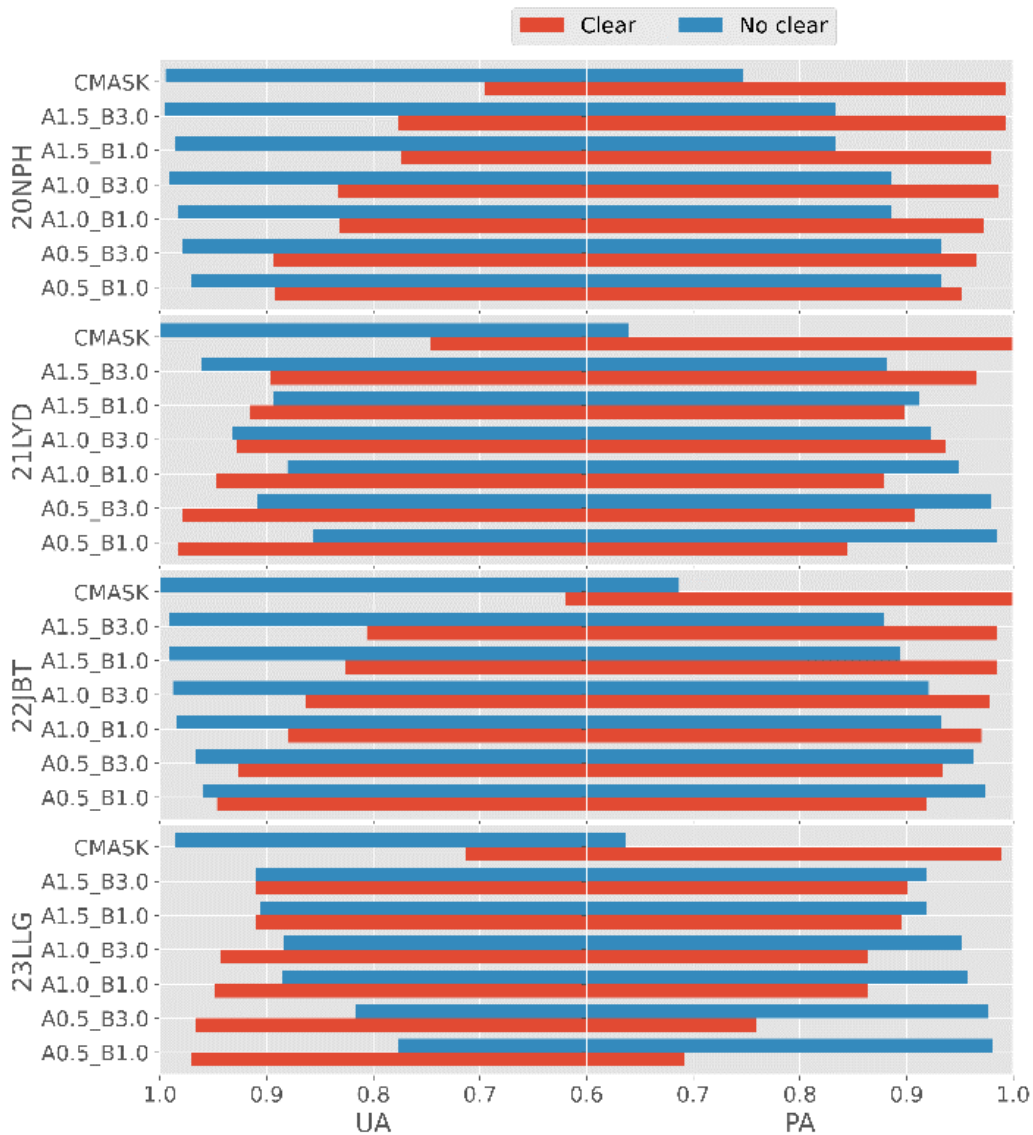
As shown in Figure 4.6a, CMASK fails to classify many clouds' edges as *Cloud* and does not detect smaller clouds. CMAKS also does not identify semi-transparent clouds (Figure 4.6b), in addition to not identifying cloud shadows. This explains the large number of omission errors in the *No clear* class (Figure 4.5).

Figure 4.6 – Detail of cloud masks and cloud shadow generated by ATSA (with parameter A equal to 0.5, 1.0, and 1.5, and B equal to 3.0) and by CMASK over images false-colour composite (RGB: NIR-red-green) for the subset of the image of the day 05-Jun-2020 in tile 21LYD (a) and day 28-May-2020 for the subset of tile 23LLG (b).
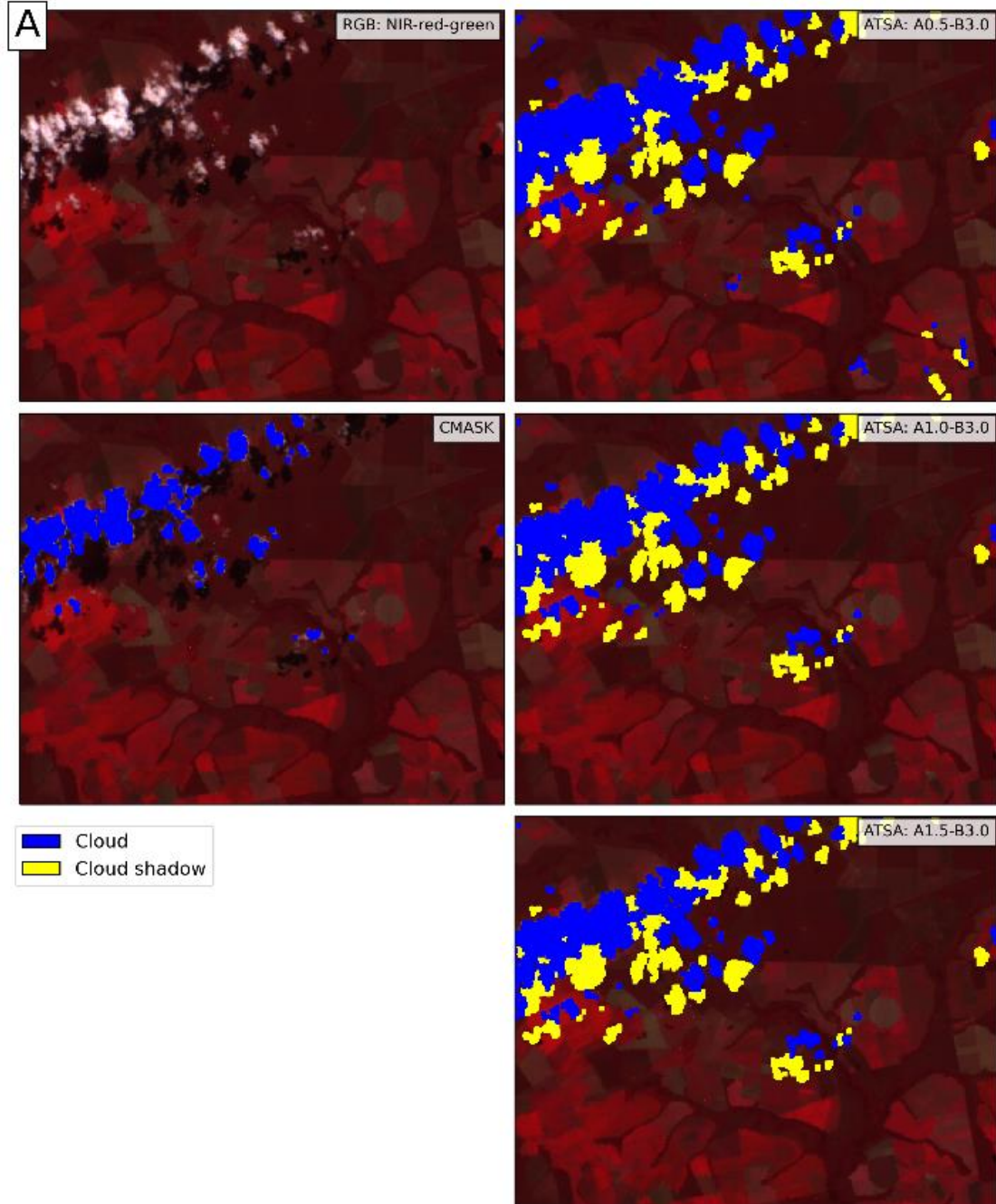
Figure 4.6 – Conclusion.
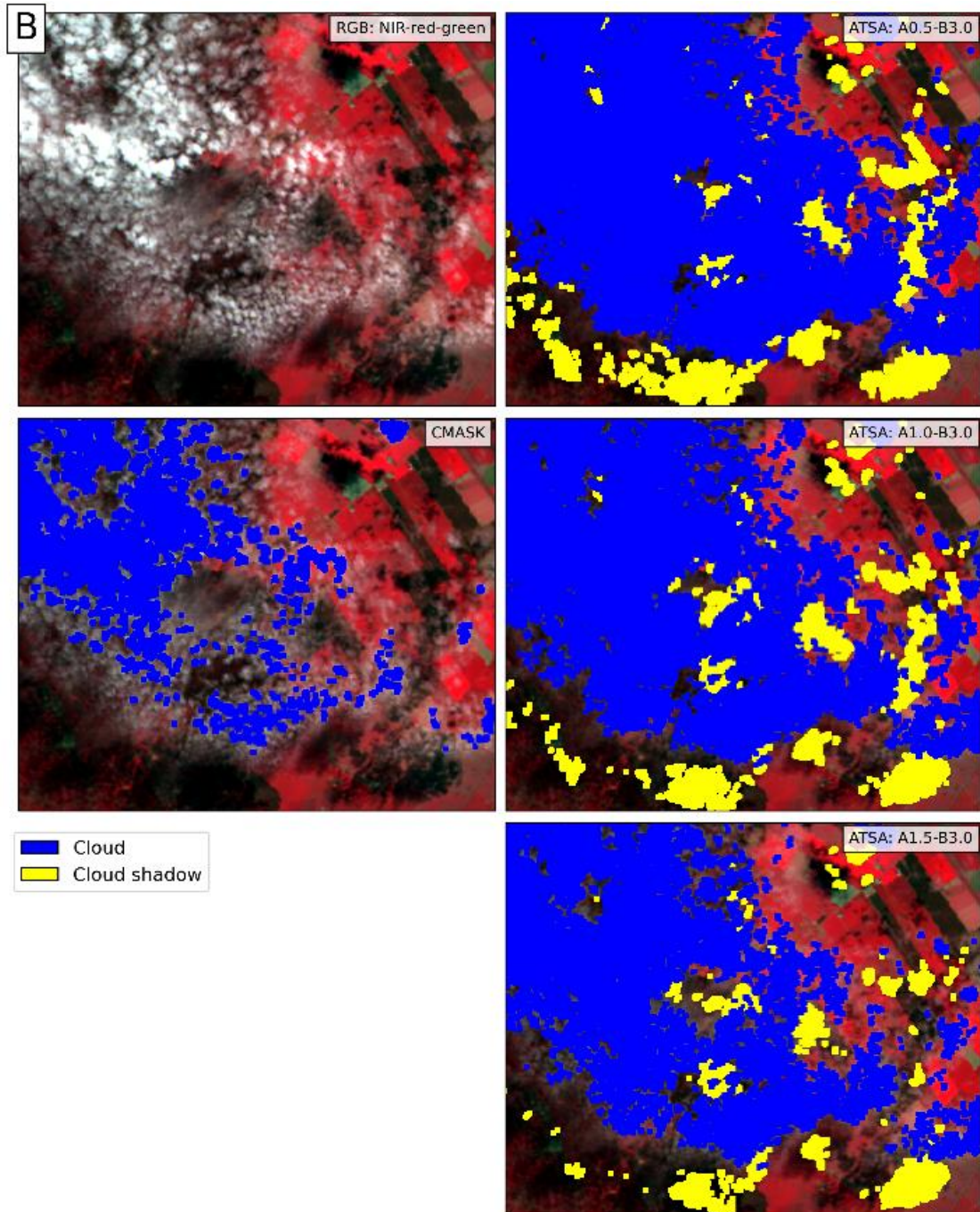
The ATSA algorithm can better detect the edges of clouds and small clouds and are able to detect shadows (Figure 4.6). However, when parameter A was equal to 0.5, it presented cloud and cloud shadows commission errors (see the

southeast part of Figure 4.6). As ATSA calculates the potential shadow zones using sun-cloud geometry, commission errors in cloud identification can lead to commission errors in cloud shadow identification, as in this case. ATSA can detect semi-transparent clouds better than CMASK (Figure 4.6). However, when parameter A is equal to 1.5, some edges of semi-transparent clouds are not detected either.

In our analysis, the ATSA parameters A and B strongly influenced omission and commission errors (Figure 4.4, Figure 4.5 e Figure 4.6). Therefore, the proper choice of these parameters is important. The performance of cloud detection algorithms may depend on the region's characteristics where it is being used. However, studies targeting specific regions can guide these algorithms (SANCHEZ et al., 2020). In our study, parameters A equal to 1.0 and B equal to 3.0 presented a better balance between omission and commission errors. However, for the regions where we conducted our analyses, and for the case of applications sensitive to noise induced by clouds, it may be better to choose parameters A equal to 0.5 and B equal to 3.0.

4.4 Conclusions

In this study, we assessed the accuracy of two cloud mask algorithms for the CBERS-4/WFI data. The CMASK and the ATSA were selected because they are suitable for WFI's number of spectral bands (total of four). For ATSA, we also evaluated the accuracy with different A and B parameters settings. The ATSA showed overall accuracy (OA) superior to CMASK. Considering the parameters A equal to 1.0 and B equal to 3.0, in all tiles, the ATSA OA was higher than 0.91,

while for the CMASK, the OA did not exceed 0.84. The CMASK had omission errors for the *Clear* class and commission errors for the *No clear* class close to zero. However, there were several omission errors (25% to 36%) for the *No clear* class, failing to classify cloud in this class and misclassifying them in the *Clear* class. ATSA algorithm was successful in balancing omission and commission errors using the parameters A equal to 0.5 and 1.0 and B equal to 3.0. Despite the need of image time series, the ATSA proved suitable for screening cloud and cloud shadows in CBERS-4/WFI imagery. Applying the ATSA algorithm in these images can enhance the robustness of the methods used for several applications such as agricultural and environmental monitoring and deforestation detection. We believe that the results are also valid for WFI data from CBERS-4A and Amazonia-1 due to the similarity between the sensors.

5 GEOMETRIC ACCURACY ASSESSMENT AND A FRAMEWORK FOR AUTOMATIC SUB-PIXEL REGISTRATION OF WFI IMAGES FROM CBERS-4, CBERS-4A, AND AMAZONIA-1 SATELLITES OVER BRAZIL[2]

This chapter presents the geometric accuracy assessment of images from CBERS-4, CBERS-4A, and AMAZONIA-1 satellites over Brazil and describes a framework for automatic sub-pixel registration of these data to improve their geometric accuracy. Due to the findings of this part of the research, the automatic registration introduced in this chapter was used in the following analyses (presented in the following chapters).

5.1 Introduction

A prerequisite to applying satellite imagery is the consistency of geolocation accuracy (HELDER et al., 2018; DONG et al., 2019; JING et al., 2021). This is essential to produce analysis-ready data (ARD) that combines satellite images from different dates or sensors, which are often organized as multidimensional data cubes (GAO; MASEK; WOLFE, 2009; FERREIRA et al., 2020). Although remote sensing data are usually available as georeferenced datasets, slight displacements among images of different dates or sensors often exist (YAN et al., 2016, 2018; SCHEFFLER et al., 2017; SKAKUN et al., 2017a). These displacements can be caused by multiple factors, such as instrument sensing geometry, surface relief, and perturbations in sensor's motion relative to the surface (WOLFE et al., 2002; STOREY; CHOATE; LEE, 2014). This

---

[2] A paper based on this chapter is currently under review at the Remote Sensing Applications: Society and Environment.

misregistration can influence the results of remote sensing data analysis, including the accuracy of land use and land cover classification (GU; CONGALTON; PAN, 2015; GÓMEZ; WHITE; WULDER, 2016; GU; CONGALTON, 2020), change detection (DAI, 1998; BROWN; FOODY; ATKINSON, 2007), spatiotemporal data fusion (TANG; WANG, 2019), Earth surface motion measurements (STUMPF; MICHÉA; MALET, 2018), and time series analysis (HUANG et al., 2009).

The geometric accuracy quantification provides important guidance to improving geolocation accuracy and data application (JING et al., 2021). Each remote sensing instrument has its own registration accuracy specification, geometry, processing, and reference image characteristics. As a result, many studies have been conducted to determine the geometric quality of images from different orbital sensors, such as the Moderate Resolution Imaging Spectroradiometer (MODIS) (WOLFE et al., 2002; WOLFE; NISHIHAMA, 2009), FengYun-3C Microwave Radiation Imager Data (TANG et al., 2016), Geostationary Ocean Color Imager (JEONG; HAN; PARK, 2020), Himawari-8/Advanced Himawari Imager (YAMAMOTO et al., 2020), Suomi National Polar-orbiting Partnership/Advanced Technology Microwave Sounder (ZHOU; YANG; ANDERSON, 2019), FengYun- 3D/MEdium Resolution Spectral Imager II (JING et al., 2021), *PRecursore IperSpettrale della Missione Applicativa* (COGLIATI et al., 2021), Sentinel-2/MSI (SKAKUN et al., 2017b; YAN et al., 2018), and Landsat-8/OLI (STOREY; CHOATE; LEE, 2014). Although the remote sensing community widely uses the WFI data, their geometrical accuracy has not yet undergone assessment.

44

Control Points (CPs) are frequently used to determine the geometric quality of satellite data, representing correspondence between the sensed images and an image used as a reference (EASTMAN; LE MOIGNE; NETANYAHU, 2007). The CPs can quantify the displacements between the sensed and the reference images and quantify the geometric quality of the sensed image (WOLFE et al., 2002; SCHEFFLER et al., 2017; SKAKUN et al., 2017b, 2017a; STUMPF; MICHÉA; MALET, 2018; COGLIATI et al., 2021; JING et al., 2021). Usually, there are two types of methods to derive CPs automatically (FONSECA; MANJUNATH, 1996; ZITOVÁ; FLUSSER, 2003): (1) feature-based methods and (2) area-based methods. The former extracts salient structures in the image, and the latter uses cross-correlation information in the spatial or frequency domain as a similarity indicator (FONSECA; MANJUNATH, 1996; ZITOVÁ; FLUSSER, 2003). The abilities of these methods to characterize the geometric errors are limited and dependent on different factors (WU; NAEGELI; WUNDERLE, 2019; JING et al., 2021).

When the displacements in the sensed image are larger than the user's needs, it may be necessary to align it with the reference image, to reduce the impacts on the application of the images (FONSECA; MANJUNATH, 1996; ZITOVÁ; FLUSSER, 2003; EASTMAN; LE MOIGNE; NETANYAHU, 2007; PAUL; PATI, 2021a). The image registration process uses the CPs to determine a spatial transformation between the reference and the sensed images constructed through a mapping function (FONSECA; MANJUNATH, 1996). This transformation function maps points from the reference image to points in the sensed image (SKAKUN et al., 2017a). The function choice depends on the type

of geometric distortions present in the sensed image (FONSECA; MANJUNATH, 1996). While simpler displacements can be modelled with polynomial functions, non-linear shifts may need more complex functions (SKAKUN et al., 2017a).

Although new co-registration methods have recently been developed, such as those using deep learning (VAKALOPOULOU et al., 2019; LEE; SIM; OH, 2021), they are more computationally complex and time consuming (PAUL; PATI, 2021b), and simpler methods have proved to be appropriate for registering some sensor data (YAN et al., 2016; SKAKUN et al., 2017a). Despite these approaches having been applied to data from other sensors, such as Landsat-8/OLI and Sentinel-2/MSI, they have not yet been evaluated for WFI sensors that have greater complexity, with two optics, a FOV, and more complex orbits imaging the same point on the earth's surface from multiple overpasses.

As mentioned above, WFI data is an important resource for agricultural and environmental monitoring in Brazil. However, its geometric quality has not yet been documented, which may cause uncertainties to application potential. So, in this work, we present the first evaluation of the geometric accuracy of the images acquired by the WFI sensor onboard CBERS-4, CBERS-4A, and Amazonia-1 satellites. This chapter has two main objectives: (i) to assess the geometric accuracy of WFI images in different spectral channels, from multitemporal data and comparing with Sentinel-2/MSI data, and (ii) to propose a framework for automatic registration of WFI data with sub-pixel registration accuracy, using open-source software to find consistent CPs and evaluating multiple mapping functions capable of handling linear and non-linear displacements. This

framework can assist the CBERS and Amazonia-1 technical team in providing consistent and robust WFI data, and it will guide the users to improve the geometric quality of the images.

5.2 Study site

We selected four tiles from the Military Grid Reference System (MGRS) as the basis for our analysis (Figure 5.1), covering different latitudes of Brazil. These places are in locations with different latitudes, longitudes, slope, biomes, land use and land cover, and cloud cover characteristics. The 20NQG tile is located in the Brazilian state of Roraima, in the Amazon biome, where the predominant land covers are forest and grassland (SOUZA et al., 2020). In Roraima, there is high cloud cover frequency throughout the year (PRUDENTE et al., 2020), reducing the probability of cloud-free image acquisition.

Figure 5.1 – Study sites location. The MGRS tiles (20NQG, 21LYD, 22JBT, and 23LLG) are shown in red hatched. The WFI tiles from Amazonia-1, CBERS-4, and CBERS-4A are shown in red, green, and blue, respectively. The images shown on tiles 20NQG (Amazonia-1 21-Apr-2021 path/row: 035/019), 21LYD (Amazonia-1 15-Apr-2021 path/row: 037/017), 22JBT (CBERS-4A 19- Feb-2021 path/row: 224/108 and 116), and 23LLG (CBERS-4 23-Jan-2021 path/row: 157/11) are false color compositions (NIR-red-green).
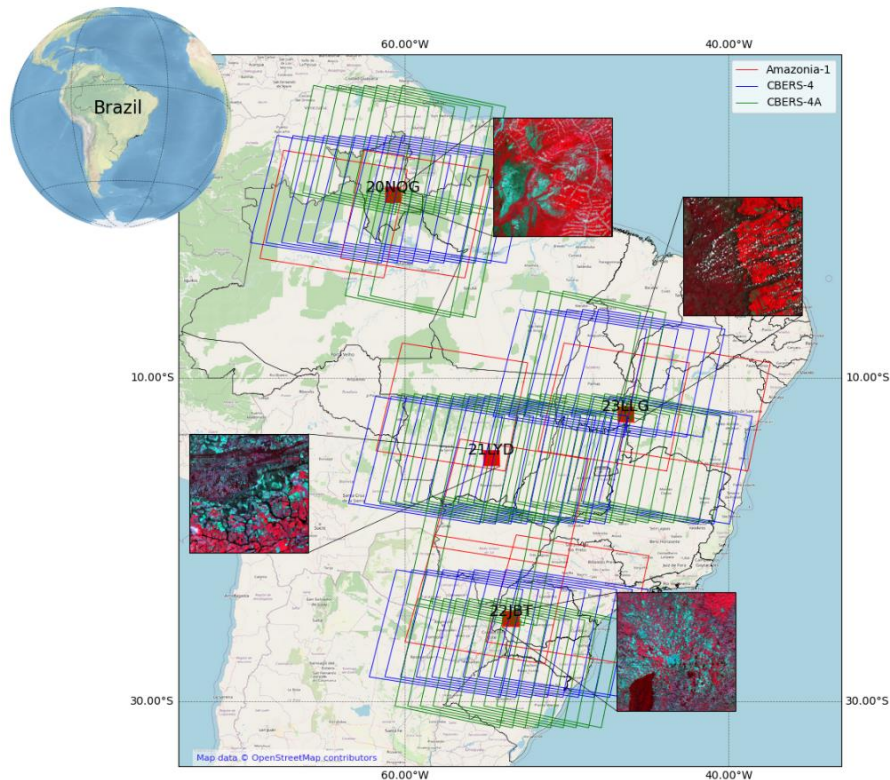
Tiles 21LYD is in Mato Grosso state, and 23LLG is between Tocantins (half west) and Bahia (half east) states. Both tiles are located in the Cerrado biome, Brazil. These two regions have a high frequency of cloud cover between December and February and a low frequency between June and August (PRUDENTE et al., 2020). Large-scale intensive agriculture is predominant in the southern part of the tile 21LYD, with usually two crop seasons per year, where changes are rapid due to seasonal crop development. In the northern part of this tile, there is a predominance of pasture and natural vegetation, mainly savannas (SOUZA et

al., 2020). The portion of the tile 23LLG located in Bahia has a predominance of annual agriculture. In contrast, the portion located in the Tocantins has a predominance of pasture, grassland, and savanna formation (SOUZA et al., 2020). There is still a difference in altitude between the part in the Tocantins and the part in Bahia, with the first one having ~400 m of altitude and the second ~800 m of altitude, and a high slope between then.

Tile 22JBT is in Paraná state, in Brazil's Atlantic Forest biome. In this tile, the predominance is annual agriculture with two crop seasons per year (SOUZA et al., 2020). But the fields are smaller than those present in Mato Grosso or Bahia (IBGE, 2017). There is a high frequency of cloud cover from December to February and an average frequency for the rest of the year (PRUDENTE et al., 2020).

5.3 Remote sensing data acquisition

5.3.1 Wide-Field Imager – WFI

We acquired all the WFI images Level 4 with less than 50% cloud cover between January 1st and June 31st, 2021, that intersected the study area (Figure 5.1) acquired by CBERS-4, CBERS-4A, and Amazonia-1, from INPE website (http://www.dgi.inpe.br/catalogo/ and http://www2.dgi.inpe.br/catalogo/explore). The WFI Level 4 images provided by the INPE are geometrically corrected with ground control points and ortho-rectified (INPE, 2021c). We used the surface reflectance product, derived by the MS3 software (SILVA; ANDRADE, 2013). The product is delivered in the Universal Transverse Mercator (UTM) projection with

the World Geodetic System 1984 (WGS84) datum. The number of images downloaded per tile is presented in Table 5.1.

Table 5.1 – Number of images used in the analyses.

MGRS tile	CBERS-4/WFI	CBERS-4A/WFI	Amazonia-1/WFI
20NQG	8	12	4
21LYD	37	27	31
22JBT	31	31	27
23LLG	36	45	30
Total	112	115	92

5.3.2 Sentinel-2/MSI

We used Sentinel-2/MSI Level-2A (L2A) product as reference in our analysis. This product is radiometrically and geometrically corrected with ortho-rectification, and atmospherically corrected to surface reflectance (ESA, 2015). The MSI L2A from Baseline v03.00 onwards uses Global Reference Image (GRI) (DECHOZ et al., 2015) in its processing chain (ESA, 2021). GRI is a set of orthorectified Sentinel-2/MSI cloud-free images used as a ground control reference to improve geolocation accuracy to meet the requirements of multi-temporal registration of 0.3 pixels for 10 m bands (GAUDEL et al., 2017). The MSI L2A images are provided in UTM projection with WGS84 datum using the U.S. MGRS as a reference to the tiling grid.

We downloaded one Sentinel-2/MSI L2A cloud-free image for each MGRS tile described in Section 5.2. The images are from 02-19-2021, 06-17-2021, 05-25-2021, and 05-24-2021 for the tiles 20NQG, 21LYD, 22JBT, and 23LLG, respectively. The image for tile 23LLG was acquired by the Sentinel-2A, and the others by the Sentinel-2B. The images are from the Processing Baseline v03.00,

except the image from tile 20NQG, which is from v02.14 because no cloud-free image from this tile was found in v03.00. In the period of the selected images, the geometric refinement product (which uses the GRI) was not yet available for Brazil, even at Baseline V03.00 (ESA, 2021). Thus, the Sentinel-2/MSI images used as reference have 0.4 pixels at 10 m mean multi-temporal misregistration (YAN et al., 2018). Therefore, our analysis is relative to Sentinel-2/MSI than an assessment of the WFI absolute geolocation. Although concerning the WFI resolution, this Sentinel-2/MSI misregistration is small, equivalent to 0.063 pixels of the CBERS-4/WFI and Amazonia-1/WFI images and 0.07 pixels of the CBERS-4A/WFI images, and we assume that Sentinel-2/MSI is an appropriate reference with minor uncertainties introduced by its own misregistration issues.

5.4   Methodology and framework

We propose a framework for automatic sub-pixel registration of WFI data onboard CBERS-4, CBERS-4A, and Amazonia-1 satellites. This framework contains three main steps (Figure 5.2), acquisition of input data (satellite images), geometric accuracy assessment (generation of control points and spatial registration evaluation), and co-registration steps (sub-pixel registration to correct the displacements). These steps are described in the following sections.

Figure 5.2 – Methodological framework for geometric accuracy assessment and registration.
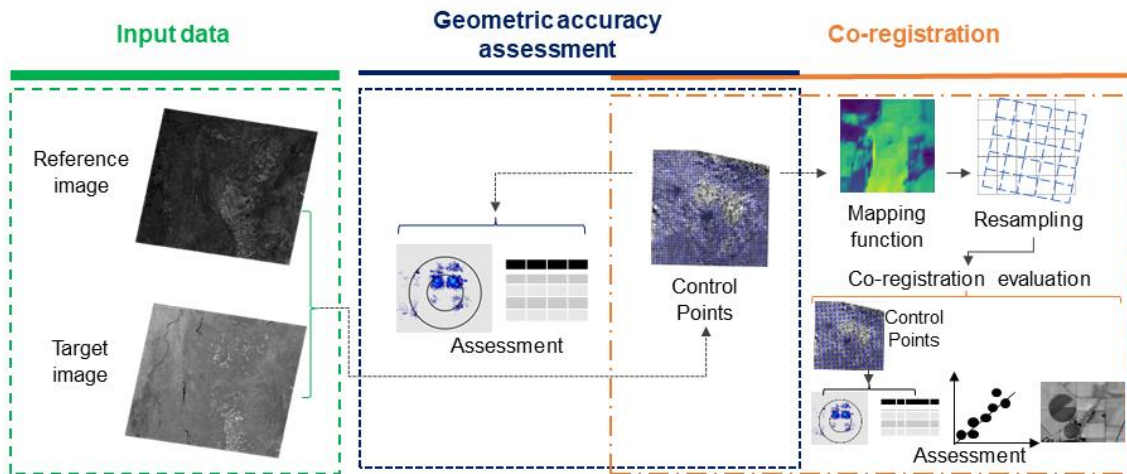
5.4.1 Generation of control points

The general procedure for image-to-image registration automatically generates CPs between a reference image and a sensed (or target) image (SKAKUN et al., 2017a). These CPs can quantify the displacements between the reference and the target images. Building a spatial transformation that aligns the reference image and the target image using CPs and warping the target image with geometric transformation is necessary to correct the displacements (SKAKUN et al., 2017a).

The CPs were generated using the Python implementation of the Automatic and Robust Open-Source Image Co-Registration Software (AROSICS) (SCHEFFLER et al., 2017). In the local registration approach, AROSICS applies phase correlation to a regular grid in a moving-window way. Phase correlation produces good results due to a distinct sharp peak in the cross-power spectrum indicating the registration points (FOROOSH; ZERUBIA; BERTHOD, 2002;

SCHEFFLER et al., 2017; SKAKUN et al., 2017a), even when there are substantial ground cover changes between different images (ROGASS et al., 2013; KRAVCHENKO; LAVRENYUK; KUSSUL, 2014). As phase correlation can only be used for two input images with the same pixel dimensions and spatial extension, AROSICS performs a pixel grid equalization if the images have different characteristics (SCHEFFLER et al., 2017). After the subset images of each matching window are transformed into the frequency domain and are phase-correlated to generate their cross-power spectrum, they are transformed back into the spatial domain. The sharp peak of the cross-power spectrum in the spatial domain is used first to quantify image integer shifts. Subsequently, AROSICS temporarily moves the subset of the target image according to the calculated integer shifts. Both subset images (reference and integer corrected target) are again transformed into the frequency domain allowing for sub-pixel shifts estimation (SCHEFFLER et al., 2017). AROSICS also implements complementary validation techniques that allow filtering unreliable CPs, including a reliability measure (SCHEFFLER et al., 2017), a Mean Structural Similarity Index (WANG et al., 2004), and the Random Sampling Consensus (RANSAC) (FISCHLER; BOLLES, 1981). More details of the AROSICS are found in Scheffler et al. (2017).

5.4.2 Geometric accuracy assessment

To evaluate the WFI images geometric accuracy, we calculated the root mean square error (RMSE) (Equation (5.1) from the displacements of the CPs identified by AROSICS.

$$\Delta x = x_r - x_t$$

$$\Delta y = y_r - y_t$$

$$RMSE = \sqrt{\frac{1}{N}\sum_{n=1}^{N}((\Delta x)^2 + (\Delta y)^2)}$$

(5.1)

where N is the number of CPs after filtering, and Δx and Δy are the displacements in x and y directions, x_t and y_t are the locations in target images, x_r and y_r are the locations in reference images. Furthermore, we used scatter plots between the shifts in x and y directions for a qualitative analysis of spatial displacements.

The WFI image geometric accuracy assessment was divided into three parts. The first one evaluates the spatial registration between different WFI spectral bands (Section 5.4.2.1), the second evaluates the multitemporal registration for applications in time series analysis (Section 5.4.2.2), and the third analyses the WFI registration related to Sentinel-2/MSI data. We selected Sentinel-2/MSI data because it has an accurate registration (ESA, 2021) considering the spatial resolution of the WFI images (Section 5.4.2.3).

5.4.2.1 Inter-channel spatial registration evaluation

Inter-channel spatial registration accuracy refers to the registration accuracy between two spectral bands (band-to-band geometric performance)

(BARAZZETTI; CUCA; PREVITALI, 2016). The displacement between bands in pushbroom sensors can occur due to slight geometric misalignments between neighboring detectors and to micro-vibrations of the sensor during its overpass in space (SCHEFFLER et al., 2017). We evaluated the WFI blue, green, and red bands using the NIR band as reference. NIR band provides a wide dynamic range of values for multiple land cover types and is less sensitive to atmospheric effects (SKAKUN et al., 2017a). NIR band has been widely used for registration evaluation and registration from multitemporal and multi-sensor data (YAN et al., 2016; SKAKUN et al., 2017a; CLAVERIE et al., 2018). However, to use the NIR as a reference for these cases, the other bands must be properly registered with the NIR band. AROSICS did not identify clouds as outliers for the band-to-band case in our initial assessments. Then, we only evaluated the images with less than 2% cloud cover from our initial dataset, leaving out 10, 18, and 18 images from CBERS-4, CBERS-4A, and Amazonia-1, respectively. We used a grid resolution of 200 pixels and a window size of 200 × 200 pixels, and the full image for the Inter-channel case. The grid resolution will define the distance between CPs, and the window size will define the dimension of the matching window.

5.4.2.2 *Multi-temporal WFI geometric accuracy evaluation*

To assess the multitemporal registration accuracy of the WFI data for each image selected in each tile (target image), we considered the previous WFI image as the reference image. The multitemporal analyses were performed considering the NIR band in the reference and target image. The WFI sensor can acquires images from the same area of the Earth's surface from many overpasses, making it difficult to analyse the entire image. Our analysis was performed considering

only the MGRS tile. All the images that intersected each of the MGRS tiles were clipped to the tile's size.

In many cases, WFI images overlapping the same MGRS tile covering the same geographic region might have different UTM assigned zones. AROSICS cannot work directly with different UTM zones, so we first warped the reference image to Albers Equal Area (AEA) projection and then to the same UTM zone as the target image, using a cubic resampling algorithm. For this case, we used a grid resolution and a window size of 20 pixels and 400 × 400 pixels, respectively. The grid resolution defines the distance between CPs. Small values in grid resolution enable model more complicated distortions (SCHEFFLER et al., 2017). The window size represents the size of the subset used to apply phase correlation.

5.4.2.3 Registration accuracy between WFI and Sentinel-2/MSI

As mentioned before, Sentinel-2/MSI misregistration is small in comparison with the spatial resolution of WFI data, so using Sentinel-2/MSI images as a reference is suitable for evaluating misregistration from WFI images as well as performing registration. Furthermore, other works also used MSI images as references for registration (CLAVERIE et al., 2018). As described in Section 5.4.2.1, when the WFI (target) image has a different UTM zone than the Sentinel-2/MSI used as a reference image, we warped the reference image first to AEA projection and later to the same UTM zone as the target image using cubic resampling algorithm. We selected the 10 m MSI NIR (B08; 0.832 µm) band as a reference. We used a grid resolution and a window size of 50 pixels and 400 × 400 pixels, respectively. An

example of CPs identified by AROSICS between a CBERS-4A/WFI image and a

Sentinel-2/MSI image used as reference is shown in Figure 5.3.

Figure 5.3 – Shift vector of the CPs identified by AROSICS between the NIR band of
CBERS-4A/WFI image (acquired on 26-Jun-2021, path/row: 211/148) and
Sentinel-2/MSI image (acquired on 25-May-2021, tile 22JBT) used as
reference. The length of the displacement vector is given by the colorbar,
and in the map it was multiplied by a factor of 40.
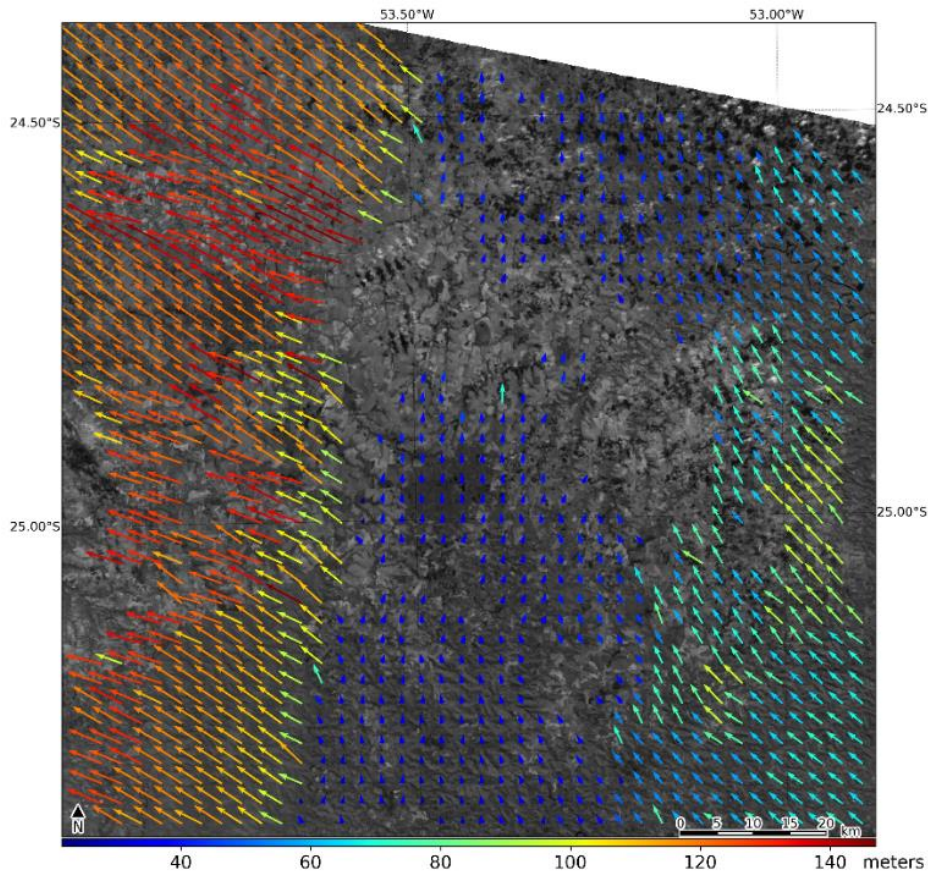
5.4.3 Sub-pixel registration to correct the displacements

Co-register was performed in the cases presented in Sections 5.4.2.2 and

5.4.2.3. To correct the misregistration in the target image it is necessary to build

a transformation function (*f;* Equation (5.2) to find correspondence between

points in the target image (x_t, y_t) and points in the reference image (x_r, y_r) (FONSECA; MANJUNATH, 1996; SKAKUN et al., 2017a).

$$(x_t, y_t) = f(x_r, y_r) \tag{5.2}$$

The function *f* was created using the CPs identified by AROSICS. The RANSAC filter was not applied to filter the CPs used in the misregistration correction. In some cases, in tests performed (not showed), it eliminated the CPs from some parts of the images, reducing the quality of the co-register. Other authors have also found this aggressive removal of CPs using RANSAC (STUMPF; MICHÉA; MALET, 2018).

In the case of multitemporal WFI registration, a 3rd-degree polynomial was used as a transformation function. For the case of registration between WFI and MSI images, three polynomial models and one Random Forest (RF) regression model were compared to create the transformation function (they are detailed in Sections 5.4.3.1 and 5.4.3.2).

After the transform function was created, the target image was warped using a cubic resampling technique. A transformation from UTM to AEA has also been added to the processing chain. This allows all images to have the same spatial reference system without additional resampling, avoiding undesired geometric and spectral image quality degradation. The coordinate transformation was performed using the *pyproj* package (SNOW et al., 2021), and the resampling was performed using the *scipy* package (VIRTANEN et al., 2020).

After performing the registration, AROSICS was used again to find CPs between the reference image and the registered image to assess the co-registration's

accuracy. Then, RMSE (Eq(5.1) was recalculated based on these points to quantify the accuracy of the co-registration.

5.4.3.1 Polynomial model

The *f* function was built as a 1st, 2nd, and 3rd-degree polynomial function using the CPs generated by AROSICS. The polynomial function (Eq(5.3) has the form (SCHMIDT; KING; MCVICAR, 2008; SKAKUN et al., 2017a):

$$x_t = P_{x,n}(x_r, y_r) = \sum_{i=0}^{n} \sum_{i+j \leq n} a_{i,j} x_r^i y_r^j$$

(5.3)

$$y_t = P_{y,n}(x_r, y_r) = \sum_{i=0}^{n} \sum_{i+j \leq n} b_{i,j} x_r^i y_r^j$$

where x_t and y_t are the locations in target images, x_r and y_r are the locations in reference images, *n* is the polynomial degree, $a_{i,j}$ and $b_{i,j}$ are the model parameters, *i* and *j* represent the indices for the parameters *a* and *b*, and the exponent for x_r and y_r. The model parameters were fitted using the ordinary least square (OLS) method, which minimizes the residual sum of squares between the observed and the predicted values. The *Scikit-Learn* (PEDREGOSA et al., 2011) python package was used to fit the polynomial models.

5.4.3.2 Random Forest model

The RF is a machine learning algorithm that uses an ensemble of decision trees (BREIMAN, 2001). The bagging (BREIMAN, 1996) and the Classification And Regression Trees (CART- Breiman et al. 1984)-split criterion scheme are combined in RF (BIAU; SCORNET, 2016b). The algorithm grows many decision trees, and the final prediction value corresponds to the averaged output of all

individual decision trees for regression problems. Each tree is independently created during the training process using bootstrap samples from the training dataset (REIS et al. 2020). The best cut is selected at each node of each tree by optimizing the CART-split criterion, based on quality measure of a split (BIAU; SCORNET, 2016b). RF regression provides high accuracy and robustness with fast, flexible, robust, and accurate predictive capabilities (REIS et al. 2020). RF can account for local non-linear distortions (SKAKUN et al., 2017a).

The RF regression implemented in *Scikit-Learn* (PEDREGOSA et al., 2011) was used to build a transformation function using a 2nd order polynomial pre-processing (SKAKUN et al., 2017a). In this case, x_r, y_r, x_r^2, y_r^2, $x_r y_r$ were input features to the RF model, trained to predict points in the sensed image. The number of trees was set to 1000, and the maximum depth of the tree was set to 50. The Mean Absolute Error (MAE) was selected as a measure of the quality of a split in the RF algorithm.

5.5 Results and discussion

We present and discuss our results in three parts: first, the evaluation of the inter-channel spatial registration (Section 5.5.1); second, the assessment of the multi-temporal WFI geometric accuracy (Section 5.5.2); and for last, the registration accuracy between WFI and Sentinel-2/MSI images (Section 5.5.3).

5.5.1 Inter-channel spatial registration evaluation

In the inter-channel case, the spatial registration of the blue, green, and red bands in relation to NIR band was evaluated. Note that most alignment errors detected from CPs obtained by AROSICS have less than 0.5 pixels (Figure 5.4). While the

shifts in the three bands of CBERS-4/WFI and Amazonia-1/WFI are similar in the
x and y directions, the CBERS-4A/WFI has greater shifts in the y direction than
in the x direction.

Figure 5.4 – Distribution of misregistration shifts between blue, green, and red bands to
NIR band for CBERS-4/WFI, CBERS-4A/WFI, and Amazonia-1/WFI from
CPs identified by AROSICS. The largest and smallest circles have a 1.0
pixel and 0.5 pixel radius, respectively, at 64 m for CBERS-4/WFI and
Amazonia-1/WFI, and 55 m for CBERS-4/WFI. The colorbar represents
the number of CPs.
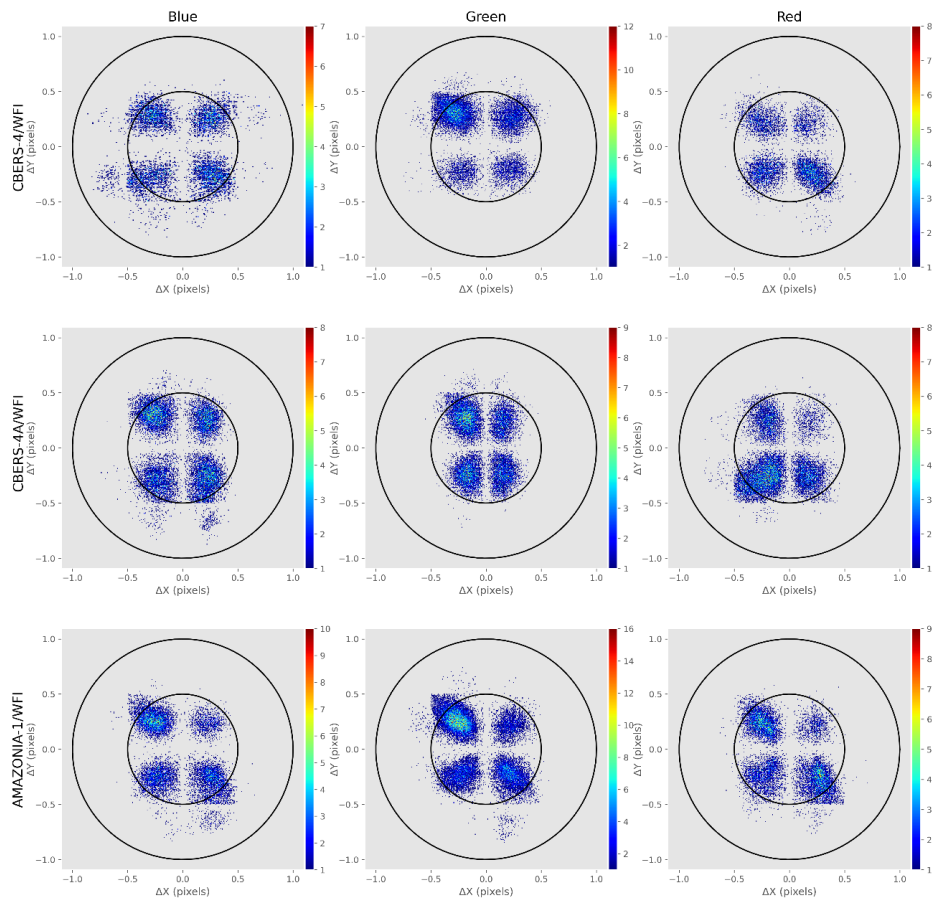
The greater RMSE average of the alignment errors was 0.44±0.03 pixel in the
CBERS-4/WFI blue band (Table 5.2). It can be seen in the scatter plot (Figure
5.4) that for this band, there is a larger number of CPs with shifts greater than 0.5
pixels. The same happened for the green band, but the dispersion was smaller in

this case. The highest RMSE average of the misregistration between bands was observed for the blue band relative to the NIR for the three satellites. The smaller RMSE average was observed for the green band, except for CBERS-4/WFI, where the smaller RMSE average was observed for the red band, with 0.36±0.02 pixels (Table 5.2).

Table 5.2 – Mean (standard deviation) RMSE of the spatial shifts detected between blue, green, and red bands to NIR band for CBERS-4/WFI, CBERS-4A/WFI, and Amazonia-1/WFI from CPs identified by AROSICS.

	Blue band	Green band	Red band
CBERS-4/WFI	0.4384 (0.0960)	0.4042 (0.0915)	0.3562 (0.0595)
CBERS-4A/WFI	0.3957 (0.1015)	0.3305 (0.0915)	0.3709 (0.0661)
Amazonia-1/WFI	0.4115 (0.1320)	0.3747 (0.1504)	0.3961 (0.1212)

Scheffler et al. (2017) detected alignment errors up to 0.33 pixels at 20 m spatial resolution between band 7 (0.783 µm) and band 8A (0.865 µm) of Sentinel-2/MSI. Patterns in the form of block-like error clusters and wave-like patterns were found. According to the authors, they are due to slight geometric misalignments between neighbouring Sentinel-2/MSI detectors and micro-vibrations of the sensor during its overpass in space. Although WFI is also a pushbroom sensor with several arrays of detectors as MSI, we did not find patterns in the misalignment between WFI bands that could explain these displacements. Rather, shifts with random directions were found. As no large shifts between bands were found, a correction of the detected displacement was not performed in the inter-channel case, considering that additional resampling induces an alteration in the pixel value (SCHEFFLER et al., 2017). Furthermore, the WFI cloud mask omits many clouds, and AROSICS does not detect some CPs over clouds as erroneous in the band-

to-band case, probably because the same cloud is imaged in the reference band and the target band. Unreliable CPs can also negatively impact cross-band registration (EASTMAN; LE MOIGNE; NETANYAHU, 2007).

5.5.2 Multi-temporal WFI geometric accuracy evaluation

Evaluating the multi-temporal geometric accuracy of WFI images aims to assess the suitability of using the data directly in time series analyses. The misregistration patterns of CBERS-4/WFI (Figure 5.5a) and CBERS-4A/WFI (Figure 5.5b) are similar for different MGRS tiles. Tiles 21LYD and 23LLG have the largest shifts, predominately in the *y*-direction. These two tiles are at close latitudes and have large altitude transitions with ~900 m on one part of the tile and ~350 m on the other. This can be one of the causes of these misregistration. The predominance of shifts in Amazonia-1/WFI is in the *x*-direction (Figure 5.5c).

The RMSE average of the WFI multi-temporal misregistration was higher for the CBERS-4A, reaching 0.87±0.34 pixels in the 23LLG tile (Table 5.3). In CBERS-4 and CBERS-4A, the higher RMSE average was identified in the 21LYD tiles. In the case of Amazonia-1, the 23LLG tile presented the smaller RMSE average with 0.45±0.16 pixels. After registration, the higher RMSE average was 0.39±0.06 pixels for the Amazonia-1/WFI (Table 5.3). RMSE average after registration was lower for CBERS-4/WFI on all tiles except for 23LLG. In addition to reducing the RMSE average of the spatial shifts in all cases, there was a great reduction in the standard deviation after the multitemporal registration of WFI data.

Table 5.3 – Mean (standard deviation) RMSE of the spatial shifts detected between multitemporal WFI images for CBERS-4/WFI, CBERS-4A/WFI, and Amazonia-1/WFI from CPs identified by AROSICS before and after registration.

Before co-register	20NQG	21LYD	22JBT	23LLG
CBERS-4/WFI	0.513 (0.267)	0.624 (0.257)	0.487 (0.090)	0.550 (0.168)
CBERS-4A/WFI	0.545 (0.237)	0.797 (0.315)	0.780 (0.271)	0.868 (0.336)
Amazonia-1/WFI	0.508 (0.097)	0.701 (0.260)	0.630 (0.185)	0.450 (0.173)
After co-register				
CBERS-4/WFI	0.257 (0.055)	0.300 (0.035)	0.304 (0.041)	0.318 (0.044)
CBERS-4A/WFI	0.318 (0.135)	0.355 (0.062)	0.336 (0.046)	0.320 (0.057)
Amazonia-1/WFI	0.387 (0.056)	0.310 (0.047)	0.316 (0.0467)	0.305 (0.053)

Figure 5.5 – Distribution of misregistration shifts between multitemporal NIR WFI images for CBERS-4 (a), CBERS-4A (b), and Amazonia-1 (c) before and after registration from CPs identified by AROSICS. The largest and the smallest circles have a 1.0-pixel and 0.5-pixel radius, respectively, at 64 m for CBERS-4/WFI e Amazonia-1/WFI, and 55 m for CBERS-4/WFI. The colorbar represents the number of CPs.
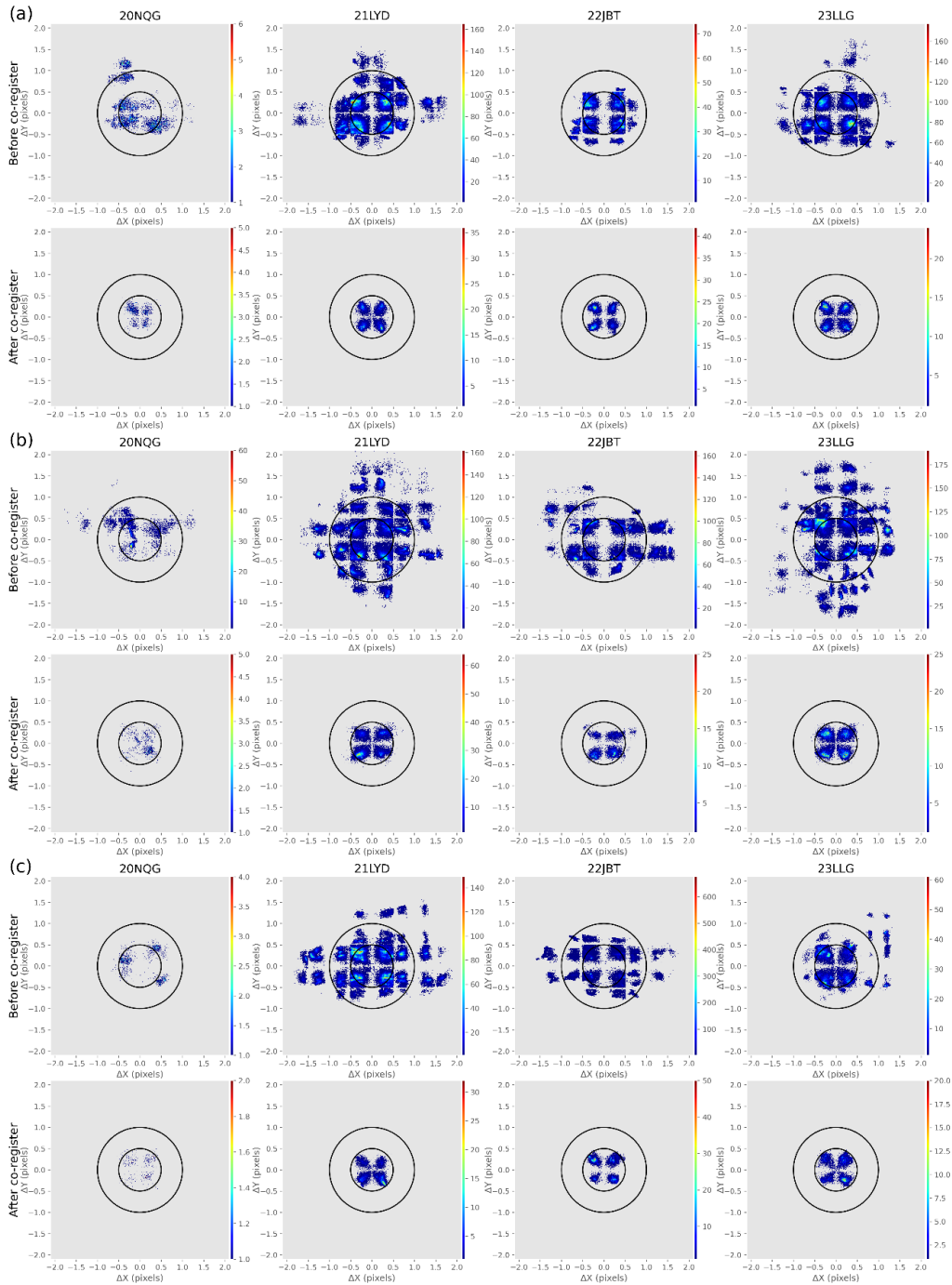
5.5.3 Registration accuracy between WFI and Sentinel-2/MSI

As we found large displacement in the multi-temporal registration case, we did not conduct a registration assessment of multi-sensor WFI imagery (across satellites) because these geometric errors would propagate. Instead, we evaluated the geometric accuracy of WFI data relative to Sentinel-2/MSI data, as MSI data has higher spatial resolution than WFI data, in addition to having known absolute geolocation and multi-temporal registration (ESA, 2021). Furthermore, the MSI data underwent geometric refinement, obtaining absolute geolocation error better than 5.6 m (at 95.45% confidence) and multi-temporal registration better than 4 m (at 95.45% confidence) (ESA, 2021).

Most CPs fell within the 1-pixel shift circle for CBERS-4/WFI (Figure 5.6) and Amazonia-1/WFI (Figure 5.8) data. For CBERS-4A/WFI data, most shifts were greater than 1-pixel (Figure 5.7). There seems to be some sort of systematic misalignment between CBERS-4A/WFI and Sentinel-2/MSI data, with shifts predominating in the southwest direction for all tiles. The displacements found are much higher than the geolocation errors of the MSI images. In addition, the WFI images of the three satellites were evaluated using the same MSI images as a reference and only the CBERS-4A/WFI images showed this pattern. This different spatial pattern of displacements found in CBERS-4A/WFI is not expected, as the WFI data of the three satellites are orthorectified using the same set of CP chips built from Landsat-8/OLI imagery. Causes of sensor misregistration are complex and may be related to inadequate knowledge and/or modelling of the interior and exterior orientation sensor and geometric relief

distortion imposed by digital elevation model inaccuracies (YAN et al., 2016), despite the four tiles having different relief conditions.

Figure 5.6 – Distribution of misregistration shifts in CBERS-4/WFI images before and after registration from CPs identified by AROSICS using Sentinel-2/MSI as reference. The largest and smallest circles have a 1.0 pixel and 0.5-pixel radius, respectively, at 64 m. The colorbar represents the number of CPs.
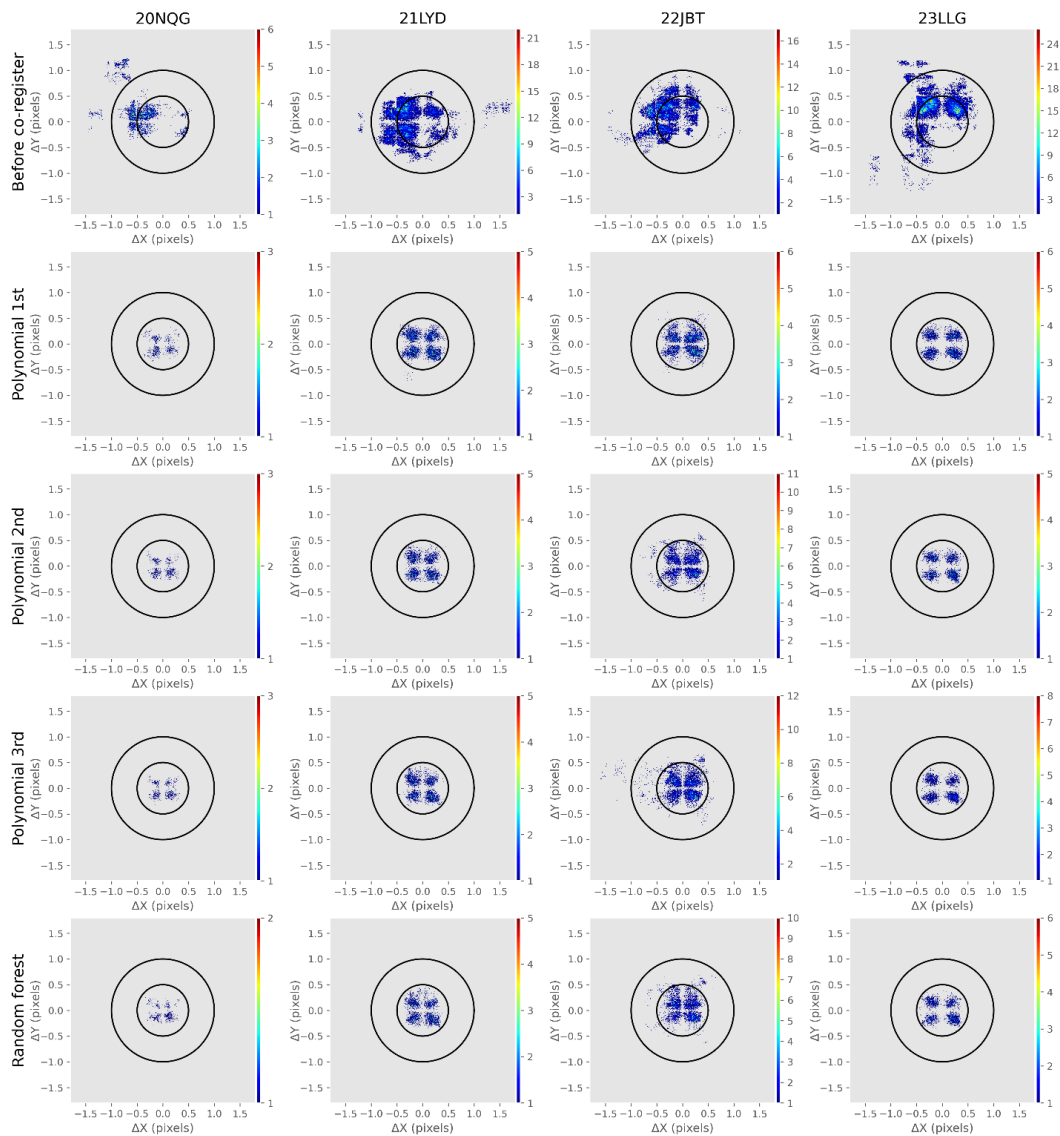
While the biggest shifts reached -1.45 pixels (93 m) in the x-direction for CBERS-4/WFI (Table 5.4) and Amazonia-1/WFI (Table 5.6), in CBERS-4A/WFI, they

reached 2.5 pixels (138 m) (Table 5.5). CBERS-4A/WFI had the highest RMSE average across all tiles, reaching 1.42±0.21 on the 20NQG tile. CBERS-4/MSI had the smaller RMSE average across all tiles, except for the 23LLG tile, where the RMSE average for Amazonia-1 was lower (0.46±0.15). For the data from the three satellites, the RMSE average was higher in the 20NQG tile. This tile is in a region with a high incidence of clouds (PRUDENTE et al., 2020), which can affect the identification of CPs in WFI image and Landsat-8/OLI chips for the orthorectification process and generation of the WFI Level-4 product by the provider. Also, the higher incidence of clouds in the 20NQG tile reduced the number of images available for our analysis compared to the other tiles.

Figure 5.7 – Distribution of misregistration shifts in CBERS-4A/WFI images before and after registration from CPs identified by AROSICS using Sentinel-2/MSI as reference. The largest and smallest circles have a 1.0 pixel and 0.5-pixel radius, respectively, at 55 m. The colorbar represents the number of CPs.
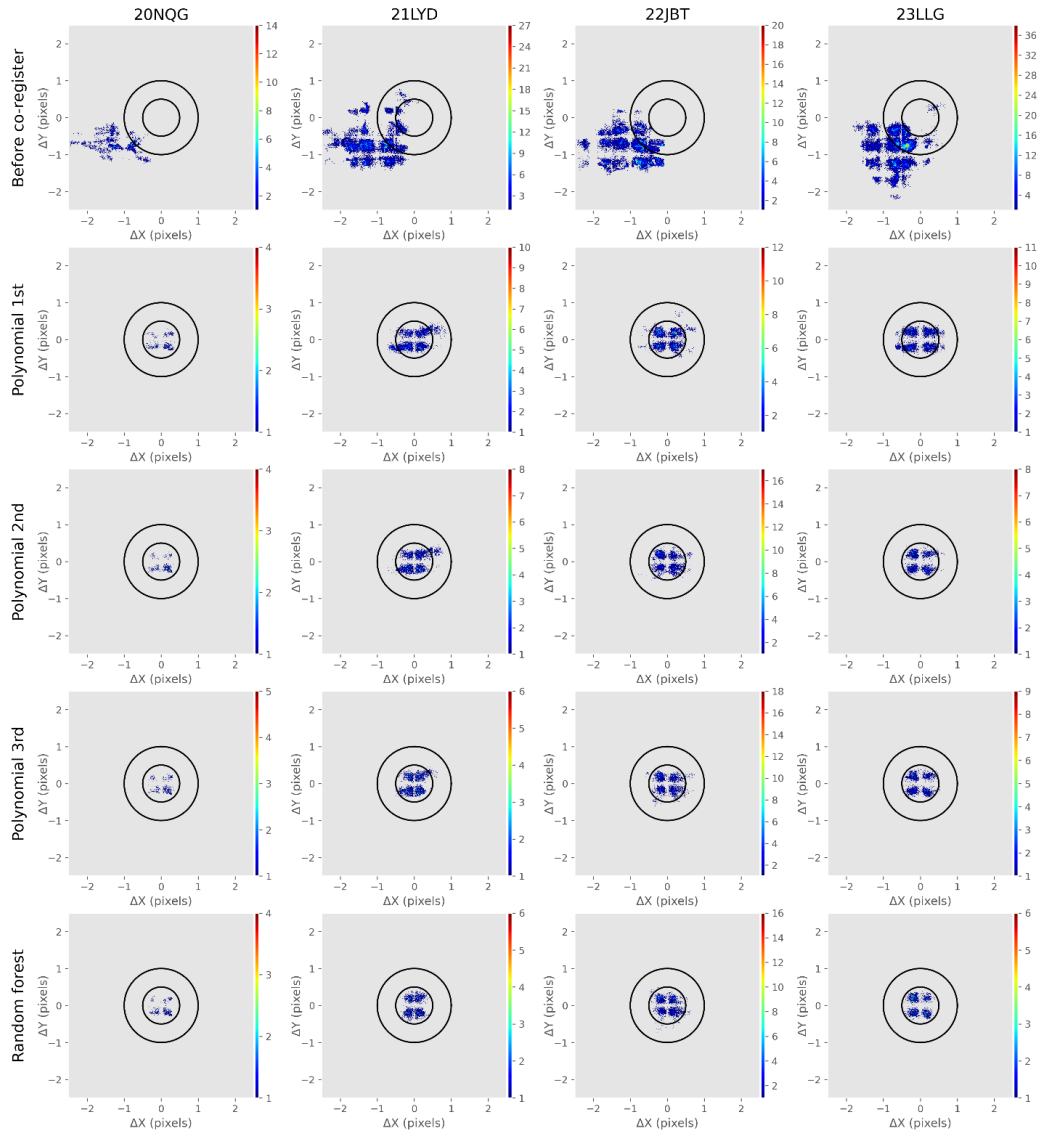
To correct the misregistration, we built different transformation functions from the CPs obtained by AROSICS using the 1st, 2nd, and 3rd order polynomial functions, in addition to the RF regressor. The difference between the results of the four transformation functions from the CPs identified by AROSICS for the

CBERS-4A/WFI image acquired on 26-Jun-2021 (Figure 5.3), using the Sentinel-2/MSI image as a reference is shown in Figure 5.9. In the *x*-direction, the biggest shifts are concentrated on the east and west edges of the image, while the smallest shifts are concentrated in the central part of the image (Figure 5.3). The transformation function using the 3rd-degree function managed to adapt better to these misalignments compared to the lower degree polynomials in this case (Figure 5.9). RF, in turn, was better for handling this non-linear displacement than the polynomial functions.

Figure 5.8 – Distribution of misregistration shifts in Amazonia-1/WFI images before and after registration from CPs identified by AROSICS using Sentinel-2/MSI as reference. The largest and smallest circles have a 1.0 pixel and 0.5-pixel radius, respectively, at 64 m. The colorbar represents the number of CPs.
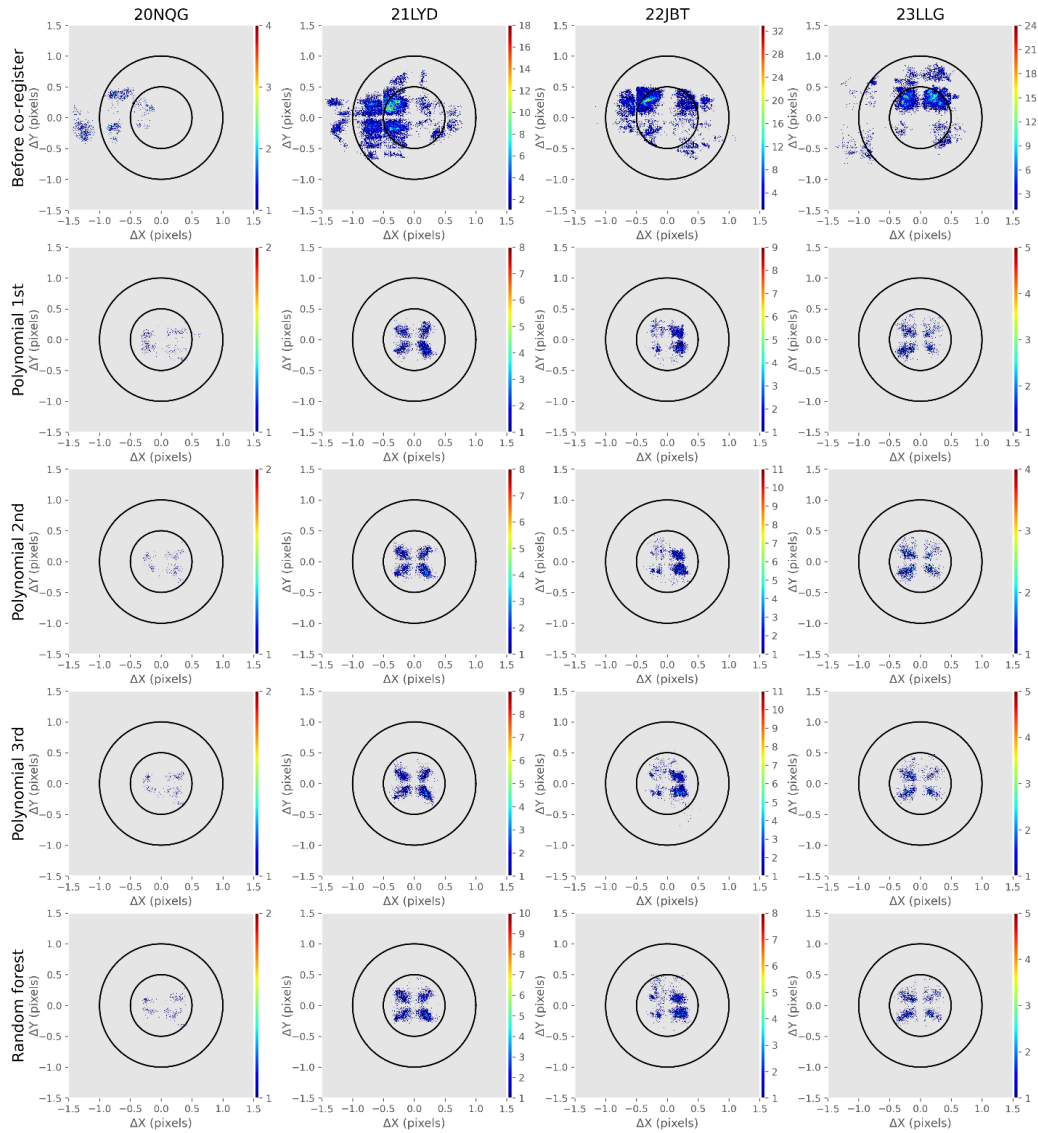
Table 5.4 – Mean and standard deviation (std) of RMSE, and maximum (max) and minimum (min) value shifts in the x and y directions of the CPs identified by AROSICS between CBERS-4/WFI and Sentinel-2/MSI images, before and after the registration.

Co-register	Tile	Δx		Δy		RMSE	
		min	max	min	max	mean	std
Before co-register	20NQG	-1.454	0.557	-0.345	1.224	0.617	0.306
	21LYD	-1.251	1.735	-0.803	0.631	0.486	0.195
	22JBT	-1.452	1.176	-0.621	0.940	0.492	0.142
	23LLG	-1.424	0.689	-1.345	1.192	0.502	0.162
Polynomial 1st	20NQG	-0.414	0.335	-0.352	0.325	0.246	0.074
	21LYD	-0.454	0.462	-0.713	0.464	0.283	0.062
	22JBT	-0.468	0.584	-0.578	0.652	0.289	0.066
	23LLG	-0.454	0.455	-0.410	0.429	0.296	0.049
Polynomial 2nd	20NQG	-0.374	0.392	-0.275	0.340	0.231	0.060
	21LYD	-0.369	0.457	-0.350	0.494	0.264	0.055
	22JBT	-0.828	0.530	-0.769	0.666	0.286	0.072
	23LLG	-0.466	0.421	-0.344	0.387	0.281	0.049
Polynomial 3rd	20NQG	-0.314	0.355	-0.390	0.293	0.232	0.061
	21LYD	-0.447	0.427	-0.349	0.427	0.261	0.055
	22JBT	-1.633	0.604	-0.722	0.651	0.296	0.095
	23LLG	-0.460	0.425	-0.408	0.389	0.282	0.050
Random Forest	20NQG	-0.339	0.319	-0.297	0.248	0.217	0.061
	21LYD	-0.361	0.405	-0.350	0.484	0.260	0.052
	22JBT	-0.761	0.647	-0.635	0.689	0.280	0.069
	23LLG	-0.442	0.420	-0.403	0.382	0.276	0.053

Table 5.5 – Mean and standard deviation (std) of RMSE, and maximum (max) and minimum (min) value shifts in the x and y directions of the CPs identified by AROSICS between CBERS-4A/WFI and Sentinel-2/MSI images, before and after the registration.

Co-register	Tile	Δx		Δy		RMSE	
		min	max	min	max	mean	std
Before co-register	20NQG	-2.516	-0.288	-1.234	-0.135	1.419	0.247
	21LYD	-2.516	0.210	-1.429	0.776	1.406	0.342
	22JBT	-2.482	-0.072	-1.555	0.220	1.361	0.314
	23LLG	-1.825	0.672	-2.196	0.395	1.120	0.372
Polynomial 1st	20NQG	-0.464	0.357	-0.307	0.286	0.287	0.057
	21LYD	-0.803	0.918	-0.474	0.475	0.319	0.104
	22JBT	-0.807	0.781	-0.543	0.780	0.309	0.059
	23LLG	-0.686	0.693	-0.433	0.471	0.339	0.072
Polynomial 2nd	20NQG	-0.392	0.355	-0.316	0.303	0.274	0.049
	21LYD	-0.704	0.779	-0.409	0.463	0.288	0.079
	22JBT	-0.781	0.677	-0.498	0.473	0.285	0.052
	23LLG	-0.520	0.654	-0.416	0.435	0.300	0.049
Polynomial 3rd	20NQG	-0.356	0.351	-0.300	0.264	0.273	0.051
	21LYD	-0.529	0.677	-0.379	0.481	0.282	0.063
	22JBT	-0.589	0.737	-0.604	0.466	0.285	0.055
	23LLG	-0.475	0.533	-0.489	0.431	0.298	0.051
Random Forest	20NQG	-0.351	0.330	-0.295	0.259	0.274	0.051
	21LYD	-0.377	0.473	-0.435	0.481	0.272	0.052
	22JBT	-0.462	0.635	-0.733	0.493	0.275	0.049
	23LLG	0.401	-0.472	-0.449	0.406	0.295	0.047

Table 5.6 – Mean and standard deviation (std) of RMSE, and maximum (max) and minimum (min) value shifts in the x and y directions of the CPs identified by AROSICS between Amazonia-1/WFI and Sentinel-2/MSI images, before and after the registration.

Co-register	Tile	Δx		Δy		RMSE	
		min	max	min	max	mean	std
Before co-register	20NQG	-1.446	-0.104	-0.422	0.495	0.869	0.386
	21LYD	-1.442	0.785	-0.681	0.800	0.558	0.188
	22JBT	-1.164	1.111	-0.691	0.566	0.494	0.097
	23LLG	-1.376	0.739	-0.744	0.890	0.458	0.151
Polynomial 1st	20NQG	-0.342	0.630	-0.334	0.298	0.263	0.066
	21LYD	-0.360	0.374	-0.362	0.338	0.243	0.050
	22JBT	-0.365	0.340	-0.498	0.372	0.246	0.030
	23LLG	-0.470	0.370	-0.395	0.447	0.290	0.060
Polynomial 2nd	20NQG	-0.307	0.406	-0.341	0.313	0.252	0.061
	21LYD	-0.419	0.438	-0.392	0.404	0.244	0.052
	22JBT	-0.389	0.377	-0.425	0.451	0.248	0.037
	23LLG	-0.454	0.413	-0.407	0.440	0.284	0.057
Polynomial 3rd	20NQG	-0.300	0.406	-0.343	0.312	0.260	0.063
	21LYD	-0.405	0.410	-0.357	0.398	0.242	0.049
	22JBT	-0.351	0.525	-0.682	0.539	0.253	0.038
	23LLG	-0.461	0.473	-0.369	0.493	0.277	0.063
Random Forest	20NQG	-0.305	0.420	-0.340	0.282	0.260	0.069
	21LYD	-0.471	0.413	-0.294	0.477	0.250	0.049
	22JBT	-0.337	0.388	-0.404	0.514	0.258	0.045
	23LLG	-0.431	0.404	-0.332	0.473	0.284	0.062

The residues of the registration of the CBERS-4A/WFI image acquired on 26-Jun-2021, using the CPs obtained by AROSICS (Figure 5.3) and the transformation functions built with the 1st, 2nd, and 3rd order polynomials, and the RF regressor (Figure 5.9), and warped with the cubic resampling technique are shown in Figure 5.10. The co-registered image using the 1st degree polynomial as the transformation function had the largest residuals, especially in the central part of the image, where there were smaller shifts before the registration (Figure 5.10). As the degree of the polynomial used in this case increased, the residuals reduced. The RMSE dropped from 1.61 pixels before registration to 0.47, 0.42, and 0.35 pixels after registration, using the

transformation function built from the 1st, 2nd, and 3rd-degree polynomials, respectively. In the case of registration using non-linear RF regression as the transformation function, the residuals were uniformly reduced throughout the image. This case had the greatest RMSE reduction after registration, with an RMSE of 0.25 pixels.

Figure 5.9 – Displacement modelled in x and y by the transformation functions constructed using the polynomial function of 1st, 2nd, and 3rd degrees, and by RF, from CPs identified by AROSICS between a CBERS-4A/WFI image (acquired in 26-Jun-2021, path/row: 211/148) and a Sentinel-2/MSI image (acquired in 25- May-2021, tile 22JBT) used as reference.
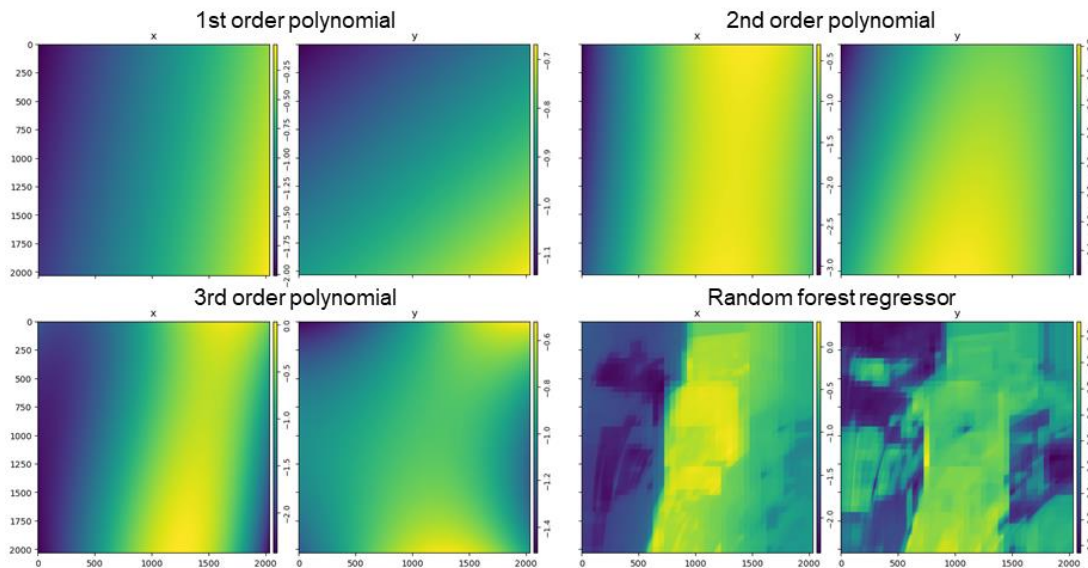
Considering the entire dataset analysed, there was also a considerable reduction in the RMSE average after registration using all transformation functions. The highest RMSE average went from 0.62±0.31, 1.42±0.25, 0.87±0.39 to 0.30±0.05, 0.34±0.07, 0.29±0.06 after registration for CBERS-4/WFI, CBERS-4A/ WFI, and Amazonia-1/WFI, respectively (Figure 5.6-Figure 5.8, Table 5.4-Table 5.6). These registration residues are close to those obtained by previous works that registered Landsat-8/OLI and Sentinel-2/MSI data. Scheffler et al. (2017)

achieved RMSE reduction from 2.31 to 0.3 pixels after co-registration. Yan et al. (2016) obtained RMSE between 0.286 and 0.309 10 m pixels after co-registration using 1st order and 2nd order polynomial transformation function and RMSE larger than 0.5 pixels using translation as transformation function.

Figure 5.10 – Residues from registration using the 1st, 2nd, and 3rd-degree polynomials, and RF, as transformation functions for CBERS-4A/WFI image (acquired in 26-Jun-2021, path/row: 211/148), using Sentinel-2/MSI image (acquired in 25- May-2021, tile 22JBT) as a reference. The length of the displacement vector in the map was multiplied by a factor of 100.
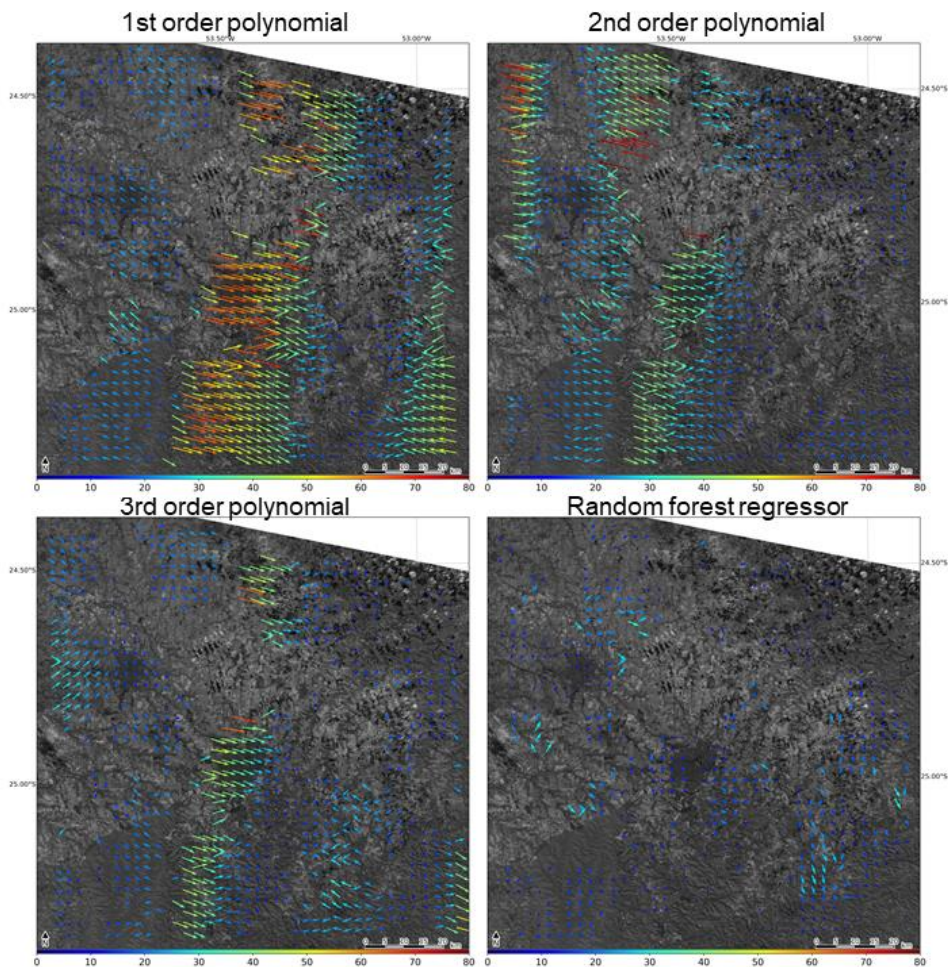
In most tiles, for the three-satellite data, the transform function using the 1st-degree polynomial had an RMSE average greater than the higher degree

76

polynomial functions or the RF regressor. The RMSE average was similar between the 2nd and 3rd-degree polynomials for the three-satellite data. Some tiles had a lower average RMSE average with the 2nd-degree polynomial transform and others with the 3rd-degree polynomial function. For CBERS-4/WFI and CBERS-4A/WFI data, the co-register using the transformation function built with the RF regressor obtained a lower RMSE average than the functions built using polynomial models. For the CBERS-4/WFI data, the RMSE average using the RF regressor ranged from 0.22±0.06 to 0.28±0.07 pixel, while for the CBERS-4A/WFI, it ranged between 0.27±0.05 and 0.29±0.05 pixel. For Amazonia-1/WFI, the RF regressor obtained was surpassed by the 2nd degree polynomial model in all tiles (except for 23LLG), where the RMSE average ranged between 0.24±0.05 and 0.28±0.06 pixel. The RF slightly outperforms the 2nd and 3rd degree polynomial model in most cases (Table 5.4-Table 5.6) but is more complex to implement and more time consuming. Taking this into account, the use of the 2nd degree polynomial proved to be appropriate for registration of the WFI data as it is simpler and had a similar result to the best transformation model. Although, if the user needs more accurate results and is not concerned about time consuming, RF would be advisable.

Yan et al. (2016) found prediction errors of similar magnitude when comparing the 1st order (also referred to as affine transformation) and the 2nd order polynomial transformation functions to register Landsat-8/OLI and Sentinel-2/MSI data. Despite this, according to the authors, the affine transformation proved to be more robust than the 2nd order polynomial transformation function, as it is less sensitive to the number and spatial distribution of CPs. The best result found for

the registration of WFI data using a higher polynomial order function may indicate greater displacement complexity. Only scaling, translation, and rotation, the operations provided by the affine transformation (BROWN, 1992), are insufficient to model the misregistration. Scheffler et al. (2017) attribute directional variations of remaining shifts after the registration of the TerraSAR-X multi-temporal dataset to their assumption that initial misregistration patterns can be modelled by a more or less affine transformation and suggest that a higher-order polynomial transformation model may reduce these effects. The best result obtained by the RF regressor as a transformation function can be attributed to its ability to model non-linear displacements, as presented in Figure 5.9. Skakun, Roger, et al. (2017) also got better results with RF regression as transformation functions. It slightly outperforms the translation, 1st order polynomial, Gaussian Radial Basis Function (RBF), and Thin-Plate Splines (TPS) to register multi-temporal Sentinel-2A/MSI images and Landsat-8/OLI with Sentinel-2A/MSI images.

The non-linear shifts shown in Figure 5.3 follow the flight line direction with a pattern of an along-track striping artifacts. These patterns are similar to those found by Scheffler et al. (2017) when analysing the Sentinel-2A/MSI multi-channel registration and by Stumpf et al. (2018) analysing the Sentinel-2/MSI images multi-temporal register. According to these authors, this type of displacement is caused due to slight geometric misalignments between sensor detector arrays of pushbroom satellites. These types of displacement are addressed implicitly by using transformation functions that can account for local non-linear distortions (e.g., RF regressor, RBF model). Still, for certain applications, it may be necessary to use the information of the detector footprints'

position on the ground to get a more accurate registration (STUMPF; MICHÉA; MALET, 2018).

The result of correcting the misregistration is shown in Figure 5.11. The effects of misregistration on the displacement between the CBERS-4A/WFI image and the Sentinel-2/MSI image and between the CBERS-4A/WFI image and the Amazonia-1/MSI image are observed. The effects of misalignment were mainly noticed on the roads and in the central irrigation pivot (Figure 5.11a and Figure 5.11c). After the registration is performed using the CPs identified by AROSICS to build a transformation function with the RF regressor, it is not possible to observe displacement between CBERS-4A/WFI and Sentinel-2/MSI images (Figure 5.10b), or CBERS-4A/WFI and Amazonia-1/WFI images (Figure 5.10d). The effect of misregistration depends on the landscape spatial heterogeneity and the satellite imagery application. In heterogeneous landscape regions, the effect of registration errors has a greater impact than in homogeneous regions (TANG; WANG, 2019; GU; CONGALTON, 2020). For example, in areas with a predominance of agriculture (Figure 5.11), the misregistration impact is probably much larger than in larger areas with the same land cover, as in the Amazon Forest. However, the near real-time forest monitoring (DINIZ et al., 2015) needs high accuracy in the geolocation because new small deforestation in the borders of older deforestation can be understood as an image displacement and not be reported.

Figure 5.11 – CBERS-4A/WFI (path/row: 211/148) image acquired on June 26th, 2021, on top of a, b, c, and d. Sentinel-2/MSI (tile T22JBT) image acquired on May 25th, 2021, used as a reference at the bottom of a and b. Amazonia-1/WFI (path/row: 035/019) image acquired on June 25th at the bottom of c and d. Images before (a and c) and after (b and d) registration using the RF regressor as transformation function. The CBERS-4A/WFI and Amazonia-1/WFI are co-registered using the Sentinel-2/MSI as reference.
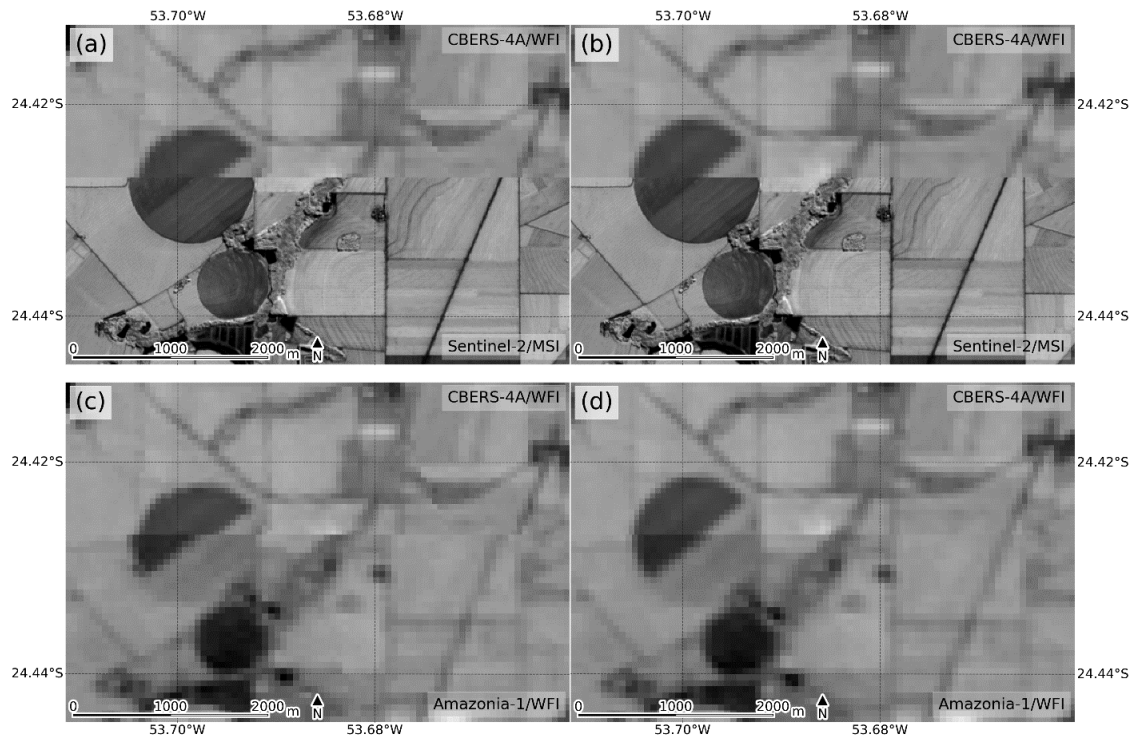
The scatter plot between two CBERS-4A/WFI images acquired four days apart (10-Jun-2021 and 14-Jun-2021) before and after correcting the misregistration is presented in Figure 5.12. The images are from close dates, so it is unlikely that there will be major changes on the land surface. After correcting the misregistration, there is also a greater spectral agreement between the two images, with the correlation coefficient (r) going from 0.90 to 0.95. Furthermore, using our proposed framework there is a reduction in data dispersion (Root Mean Square deviation - RMSD from 0.027 to 0.021), with the regression line getting closer to the identity line. The registration of WFI imagery from CBERS-4,

CBERS-4A, and Amazonia-1 can improve the consistency of these data for time series analysis. Thus, our results show that it is possible to improve the WFI images quality. In this way, in the future, it would be possible to use/incorporate the WFI images in the LULC program.

Figure 5.12 – Scatter plot between CBERS-4A/WFI images from 10-Jun-2021 (path/row: 208/132) and 14-Jun-2021 (path/row: 201/132), before and after co-register. RMSD is the Root Mean Square deviation.
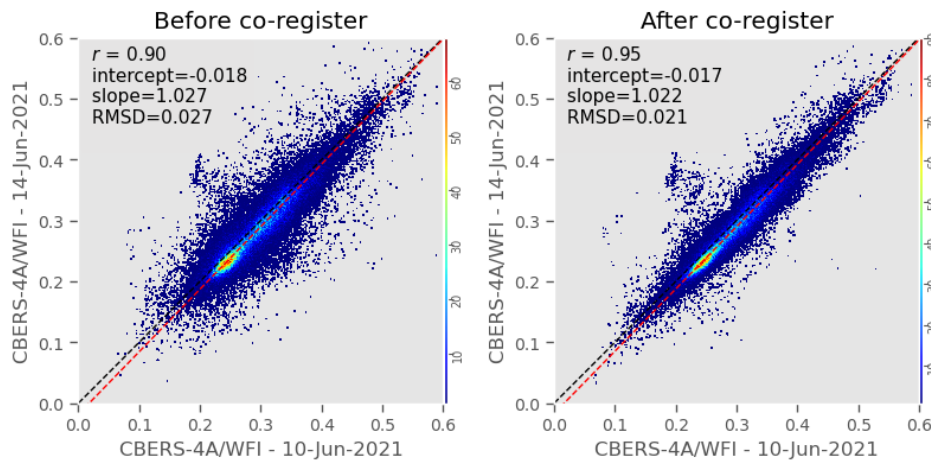
5.6 Conclusion

The geometric accuracy of satellite images is crucial for most remote sensing applications, as misregistration can lead to biased results. This study assessed, for the first time, the geometric accuracy of WFI imagery from CBERS-4, CBERS-4A, and Amazonia-1. For this, CPs were generated using the AROSICS package (SCHEFFLER et al., 2017). The inter-channel registration was assessed by using the NIR band as a reference. The highest RMSE average was in the blue band relative to the NIR band, with 0.44±0.03, 0.39±0.03, and 0.41±0.04 pixel, for CBERS-4/WFI, CBERS-4A/WFI, and Amazonia-1/WFI, respectively. The multi-temporal geometric accuracy of each image (target) was evaluated considering

the previous image as a reference. In this case, on a tile basis, the RMSE average reached 0.87±0.34 pixels for CBERS-4A/WFI in the 23LLG tile; respectively, 0.62±0.26 and 0.70±0.26 pixels for CBERS-4/WFI and Amazonia-1/WFI in the 21LYD tile. This study further analysed the geometric accuracy of WFI data using Sentinel-2/MSI as a reference. The biggest shifts were 1.45 pixels (93m) for CBERS-4/WFI and Amazonia-1/WFI, while for CBERS-4A/WFI was 2.5 pixels (138 m). CBERS-4A/WFI had the highest RMSE average across all tiles, reaching 1.42±0.21 pixels on the 20NQG tile. Based on our results, then multi-temporal image data comparisons (e.g., land cover change) cannot be effectively conducted.

After finding these misregistrations, a framework was proposed to automatically register WFI images, evaluating the 1st, 2nd, and 3rd-degree polynomials, and RF regressor as mapping functions. The RMSE average was similar between the 2nd and 3rd-degree polynomials for the three-satellite data. Some tiles had a lower RMSE average with the 2nd-degree polynomial transform and others with the 3rd-degree polynomial function. For Amazonia-1, using the 2nd-degree polynomial model, the RMSE average ranged between 0.24±0.05 and 0.28±0.06 pixel. For CBERS-4/WFI and CBERS-4A/WFI data, the registration using the transformation function built with the RF regressor was able to better model non-linear displacement and allowed to obtain a lower RMSE average compared to the functions built using polynomial models. In this case, the RMSE average ranged from 0.22±0.06 to 0.28±0.07 pixel and 0.27±0.05 to 0.29±0.05 pixel for CBERS-4/WFI and CBERS-4A/WFI, respectively. Despite this, the RF only slightly outperforms the 2nd and 3rd degree polynomial model in most cases but

is more complex to implement and more time consuming. Taking this into account, the use of the 2nd degree polynomial proved to be appropriate for registration of the WFI data as is simpler and had a similar result to the best transformation model.

Given the displacements found in our analyses, image registration is a required step for further time series analysis of WFI images in several applications that require precise sub-pixel registration, but mainly in those spatially heterogeneous such as agriculture. As a result, the framework proposed in this study allowed the registration of WFI images automatically. In addition, the framework proved to be fundamental for image registration for works that involve multi-temporal analysis of WFI images or when they are combined with other data sources, substantially reducing misregistration and providing more consistent and robust data. The present study is the first to assess the geometric accuracy of the WFI sensor. Brazil had put a lot of effort into developing and launching the three WFI sensors, our study contributes to obtaining improved results and fostering the use of WFI data in the country. The CBERS legacy includes two decades of observations, and we expect the same to happen with the Amazonia satellite, so proposing improvements to the data from the sensors onboard these satellites is fundamental.

6 EVALUATION OF SIX APPROACHES FOR CORRECTING BIDIRECTIONAL EFFECTS ON CBERS-4/WFI IMAGES FROM BRAZIL

6.1 Introduction

Monitoring vegetation and land surface characteristics using images from space-borne sensors depends on the relationship between biophysical quantities in the ground and the spectral radiance measured by sensors on the satellites (FLOOD et al., 2013). However, measurements retrieved by orbital sensors can have significant variation caused by several factors that are not directly related to the land surface. As most surfaces are anisotropic, their directional reflectance is dependent on the sun-target-sensor geometry. Variations in viewing and illumination geometry can cause significant spatial and temporal variation in the retrieved directional reflectance independent of variations in the land surface characteristics (FLOOD, 2013; GAO et al., 2014). These variations can be modeled by the Bidirectional Reflectance Distribution Function (BRDF), that describes the scattering of incident light from one direction in the hemisphere into another direction (SCHAEPMAN-STRUB et al., 2006).

The BRDF effect can be strong in instruments with large FOV such MODIS (PETRI; GALVÃO; LYAPUSTIN, 2019), with approximately 55 degree both sides of nadir. MODIS has a low spatial resolution (between 250 m and 1000 m) but a high revisit rate (twice daily). Considerable effort has been invested to characterize and remove BRDF effects from MODIS images (SCHAAF et al., 2002). The high repeatability of MODIS makes it possible to acquire images with different angular configurations in a short period of time. Thus, based on the

assumption that there are no surface changes in this period, and that the reflectance changes are due to the directional effects, the BRDF is modeled for each band, with parameterization by pixel at each 16-day period. This allows normalization of reflectance to standard angular configurations.

Bidirectional effects have also been identified in medium spatial resolution sensors (HANSEN et al., 2008; ROY et al., 2008, 2016b, 2017; LI et al., 2010; POTAPOV et al., 2012; FLOOD, 2013; FLOOD et al., 2013; GAO et al., 2014), even though they generally have a much lower swath compared to MODIS. Thus, it is desirable to understand and correct these bidirectional effects for many quantitative applications that use data from adjacent paths or from time series with different viewing and solar geometries (GAO et al., 2014; ROY et al., 2016b). However, due to the lower temporal frequency of acquisitions and the low angular sampling, it becomes more difficult to remove the bidirectional effects in data from medium spatial resolution sensors in a per-pixel basis in the same way as it is done with MODIS (FLOOD et al., 2013; CLAVERIE et al., 2015).

For Landsat imagery, which has a narrow swath (7.5º both sides of nadir), Hansen et al. (2008) and Potapov et al. (2012) found a reflectance gradient as a function of the view zenith angle (VZA), with an increase in the reflectance from forward direction to backward direction, allowing normalization to nadir viewing based on a simple linear regression. Other approaches used the BRDF model initially developed for MODIS. Roy et al. (2008) used directly BRDF MODIS parameters from corresponding 500 m MODIS pixels to adjust Landsat imagery. Li et al. (2010) used regional BRDF information averaging the MODIS BRDF

parameters by Landsat scene, and applying the same parameters to the entire scene. Shuai et al. (2011) extracted BRDF parameters for different land cover types based on MODIS pure pixels and used this information to correct directional effects on the corresponding land cover types. Flood et al. (2013), considering that at least a major component of the BRDF can be assumed to be the same across all pixels, derived a single fixed set of BRDF spectral model parameters from the Landsat imagery itself, using images from opposite sides in the overlapping areas between paths. Roy et al. (2016) also used the single fixed set of BRDF spectral model parameters derived from a large amount of globally and temporally distributed MODIS BRDF product pixels to normalize the angular effects in Landsat images. This approach was also evaluated for Sentinel-2/MSI data (ROY et al., 2017), which have a larger FOV than Landsat (with a swath width of approximately 12º both sides of nadir (DRUSCH et al., 2012)).

The BRDF effects are much stronger in data from medium resolution wide swath sensors (GAO et al., 2014) or with off-nadir pointing capability sensors (FLOOD et al., 2013) compared to narrow swath ones. Gao et al. (2014) built an 8-day 1-degree Look-Up Map (LUM) with BRDF parameters per-crop type based on MODIS pure pixels extracted from a detailed crop type map for the United States, accounting for spatial and temporal differences in the BRDF parameters. Then, the BRDF LUM was applied to data from AWiFS, a wide swath sensor (25° both sides of nadir), to correct directional effects. Flood et al. (2013) also used their approach to correct bidirectional effects in SPOT-5 HRG imagery, with a VZA of up to 20° off-nadir. Claverie et al. (2015) evaluated several methods to correct a sample of SPOT-4 data with a maximum VZA of 28°, assuming no variation of

the BRDF shape in space, or deriving the parameters from the MODIS data. Although all methods reduced the bidirectional effects, they showed different results. Van doninck and Tuomisto (2017) also made a similar observation when evaluating various methods to normalize bidirectional effects in Landsat images over the Amazon Forest, noting that the best results were obtained by deriving the BRDF coefficients from the image itself, although all methods were able to reduce the angular effects.

For CBERS-4/WFI data, Pan et al. (2020) modeled the BRDF parameters from measuring angular data by an unmanned aerial vehicle. BRDF parameters were used to increase the accuracy of radiometric calibration of WFI data. They found a difference of up to 10% in the reflectance modeled in off nadir view relative to the nadir view from desert surface. Depending on the surface and spectral band for the VZA range of wide swath medium resolution sensors such as WFI, the reflectance difference between nadir and off nadir view can be greater, reaching 60% (GAO et al., 2014). Thus, as the same surface point is observed from up to nine different paths by the CBERS-4/WFI, BRDF effects can cause inconsistency in the time series. Therefore, it becomes important to understand and normalize the BRDF effects in CBERS-4/WFI images in order to generate more consistent time series. This is also important so that the data from the CBERS-4/WFI can be combined with that generated by the WFI sensors onboard the CBERS-4A and Amazonia-1 in the future, in order to generate a consistent almost daily time series.

In this paper, we assessed the angular effects in CBERS-4/WFI images over various land cover types in a large area over Brazil and evaluated six approaches for normalizing BRDF effects in WFI imagery. These approaches were initially developed for data from other sensors with FOV lower than the WFI. Thus, it becomes important to assess their performance on the WFI as well.

6.2 Data

6.2.1 CBERS-4/WFI

CBERS-4/WFI Level-4 images from 2020, were obtained from the National Institute for Space Research (INPE) catalog website (http://www.dgi.inpe.br/catalogo/). The WFI Level 4 images provided by the INPE are geometrically corrected with ground control points and ortho-rectified (INPE, 2021c). We use the surface reflectance product, processed by the MS3 software (SILVA; ANDRADE, 2013). The product is delivered in the Universal Transverse Mercator (UTM) projection with the World Geodetic System 1984 (WGS84) datum.

6.2.2 MODIS

We downloaded the data from products MCD43A1, MCD43A2 and MCD43A4 (Version 006) for the same date and which covered each of the 461 CBERS-4/WFI images. A total of 1081 images of each product were downloaded from NASA's Land Processes Distributed Active Archive Center (LP DAAC) products located at the USGS Earth Resources Observation and Science (EROS) Center (https://lpdaac.usgs.gov/products). In some cases, more than one MODIS image was needed to cover the CBERS-4/WFI image. We only use the data from

MODIS products referring to the spectral bands of blue (B3), green (B4), red (B1), and NIR (B2), which can be considered equivalent to the respective bands B13 (blue), B14 (green), B15 (red) and B16 (NIR) of the WFI data. Although the bandwidths and spectral response function are not the same.

6.2.3 Land use and land cover data

A land use and land cover map were used to select only vegetation areas. Data from MapBiomas Collection 5 for the year 2019 (most recent data during the processing of the data of this chapter) about Brazil were downloaded. MapBiomas is a multi-disciplinary network that produced land use and land cover maps between 1985 and 2019 for Brazil, based on applied random forest to Landsat archive using Google Earth Engine (SOUZA et al., 2020). MapBiomas data is one of the most comprehensive and detailed land use and land cover maps for the country at 30 m pixel resolution. From the MapBiomas map, we retained only the classes referring to vegetation, i.e., Forest Formation, Savanna Formation, Grassland, Pasture, Forest Plantation, Soybean, Other Temporary Crops, Sugarcane, Perennial Crop, Mosaic of Agriculture and Pasture.

6.3 Methodology

6.3.1 MODIS-CBERS-4/WFI reflectance bias

The gradient introduced by surface anisotropy and VZA variation is approximately linear in narrow swath sensors, i.e., Landsat ($\pm$ 7.5º) (HANSEN et al., 2008; POTAPOV et al., 2012). In the present study we test whether this assumption can be made to reduce BRDF effects in CBERS-4/WFI data, which is a wide swath sensor, with a much larger VZA than Landsat. The linear relationship that

characterizes this gradient can be obtained directly from the relationship between the surface reflectance and the VZA when analyzing the same type of land cover (HANSEN et al., 2008; VAN DONINCK; TUOMISTO, 2017). However, when the scene has different types of land cover, this relationship cannot be obtained directly. So, we follow the approach used by Potapov et al. (2012), using MODIS data as a reference.

The product MCD43A4, MODIS Nadir BRDF-Adjusted Reflectance (NBAR), was selected as a reference because the directional effects were already removed from the surface reflectance. First the CBERS-4/WFI data were resampled to 500 m using average algorithm to match the resolution of the MCD43A4 product. All 500 m pixels that had within some CBERS-4/WFI pixels marked as cloud in the cloud mask were not considered. The mean bias between the MODIS NBAR and the CBERS-4/WFI surface reflectance data was calculated and aggregated at every 1º VZA. The reflectance gradient (α) was estimated for each of the reflective bands as the slope of the linear regression between the surface reflectance bias of MODIS and CBERS-4/WFI (ρ) and the VZA (v) as follows:

$$\rho = \alpha\,v + b \tag{6.1}$$

The intercept (b) represents systematic bias between the NBAR and the surface reflectance of the CBERS-4/WFI, which are constant across the scene, such as difference in atmospheric correction algorithm, bandwidths, and spectral response function. As the objective is just to eliminate the directional effects of the VZA, only the α was considered, while the b was not applied to normalization.

In some scenes clouds may be concentrated on only one side of the image. This may impact the estimation of the reflectance gradient through linear regression, probably due to omission errors in the cloud mask. A Random Sample Consensus (RANSAC) filter was used to detect outliers and eliminate them from the linear regression. This method will be called Approach 1 from now on. The other approaches will be detailed in Sections 6.3.2 and 6.3.3.

6.3.2 BRDF model and BRDF parameters from MODIS

The operational MODIS BRDF algorithm makes use of the semiempirical kernel-driven RossThick-LiSparse Reciprocal BRDF model, that expresses land surface reflectance as the sum of a parameter and two kernels, that represent an isotropic scattering, a volumetric scattering and a geometric-optical surface scattering component (SCHAAF et al., 2002) in the following form (ROUJEAN; LEROY; DESCHAMPS, 1992):

$$R(\theta, \upsilon, \phi, \lambda) = f_{iso}(\lambda) + f_{vol}(\lambda)\, K_{vol}(\theta, \upsilon, \phi) + f_{geo}(\lambda)\, K_{geo}(\theta, \upsilon, \phi) \tag{6.2}$$

where R is the modeled reflectance, K_{vol} and K_{geo} are the kernel functions that describe volumetric and geometric scattering components, and f_{iso}, f_{vol} and f_{geo} are the three model parameters. The K_{vol} is represented for the RossThick kernel (ROUJEAN; LEROY; DESCHAMPS, 1992), and K_{geo} for the reciprocal form of the LiSparse model (WANNER; LI; STRAHLER, 1995), while by definition, the isotropic kernel component is unity. K_{vol} and K_{geo} are dependent of a viewing and illumination geometry, and f_{iso}, f_{vol} and f_{geo} are spectrally dependent. As MODIS can obtain multiple observations with different angular configurations in a short period of time, the model parameters (f_{iso}, f_{vol} and f_{geo}) can be fitted

empirically from the observations themselves, using either a full inversion or the magnitude inversion approach (SCHAAF et al., 2002).

From the backup algorithm in MODIS BRDF algorithm, a magnitude inversion approach (SCHAAF et al., 2002) can be used to adjust the directional surface reflectance at a set of angles A $(\theta_A, \upsilon_A, \phi_A)$ to the value equivalent to what it would have had if it had been observed from a different set of angles B $(\theta_B, \upsilon_B, \phi_B)$ (FLOOD, 2013; GAO et al., 2014), assuming that the modeled reflectance R and a surface reflectance ρ represent the same BRDF shape (FLOOD, 2013; VAN DONINCK; TUOMISTO, 2017):

$$\rho(\theta_B, \upsilon_B, \phi_B) = \frac{R(\theta_B, \upsilon_B, \phi_B)}{R(\theta_A, \upsilon_A, \phi_A)} \rho(\theta_A, \upsilon_A, \phi_A) \ (2) \tag{6.3}$$

With the parameter models obtained every 16 days, this approach has also been used to remove the directional effects in the MODIS images themselves (SCHAAF et al., 2002). As the revisit period for medium spatial resolution sensors is longer, it is difficult to obtain multiple observations with different angular configurations in a short period of time to regularly derive the BRDF model parameters from the image itself. So MODIS derived BRDF parameters have been employed to correct directional effects in medium resolution narrow swath sensor data (i.e., Landsat), from coincident observations (ROY et al., 2008; LI et al., 2010; SHUAI et al., 2011; FLOOD, 2013; VAN DONINCK; TUOMISTO, 2017) or unique set of parameters derived around the world (ROY et al., 2016b, 2017). Here we evaluate the applicability of using MODIS-derived BRDF parameters for correct the angular effects on data from a wide swath medium resolution sensor, the CBERS-4/WFI. We tested four cases considering different ways to assimilate

the MODIS BRDF parameters into the BRDF correction of the CBERS-4/WFI data.

Approach 2. The MODIS BRDF parameter are taken from the pixel MODIS that match with the CBERS-4/WFI pixel (this is the approach used by Roy et al. (2008)). The images from MCD43A1 V6 product corresponding to the same date as the CBERS-4/WFI images were reprojected to 64 m in the AEA projection, using the nearest neighbor algorithm.

Approach 3. A single set of MODIS BRDF parameters averaged for each CBERS-4/WFI image being adjusted (this is the approach used by Li et al. (2010)). Only pixels with highest quality in the quality data (MCD43A2) and over land were used to calculate the average parameters for each scene. Pixels with cloud values in the cloud mask of the CBERS-4/WFI images were also not used.

Approach 4. A set of BRDF MODIS parameters is averaged per class from "pure" homogeneous MODIS pixels (this case was based on the approach used by Shuai et al. (2011)). Initially an unsupervised K-means classification was generated with 10 classes for each CBERS-4/WFI image. Only MODIS pixels that contained more than 70% of a single class at the CBERS-4/WFI resolution were considered as candidate for "pure" pixels and thus used to calculate the average parameters. Furthermore, as in Approach 3, only the pixels with the highest quality in the MCD43A2 data, over land, and which did not contain clouds in the CBERS-4/WFI image were considered. Finally, a set of MODIS BRDF parameters is used for each class and for each image.

Approach 5. Here we evaluate the use of the fixed BRDF coefficients derived by Roy et al. (2016) (Table 6.1). These coefficients were also derived from the MCD43A product which were globally and temporally distributed (>15 billion pixels). These coefficients were initially used to remove the bidirectional effects in Landsat 7/ETM+ data (ROY et al., 2016b) and later also evaluated for Sentinel-2/MSI data (ROY et al., 2017). Both the ETM+ and the MSI are narrow swath sensors (FOV ±7.5º and ±12.5º, respectively). Here we evaluate whether these same coefficients can remove the BRDF effects from the CBERS-4/WFI data, a wide swath sensor (FOV ±28.63°).

Table 6.1 – Fixed BRDF coefficients derived by Roy et al. (2016).

Band	f_{iso}	f_{geo}	f_{vol}
Blue	0.1690	0.0227	0.0574
Green	0.0774	0.0079	0.0372
Red	0.1306	0.0178	0.0580
NIR	0.3093	0.0330	0.1535

Source: Roy et al. (2016).

6.3.3 BRDF parameters derived from CBERS-4/WFI itself

The insufficient number of observations in a short period of time with different angular configurations makes difficult to invert the BRDF parameters of the medium spatial resolution images themselves on a per-pixel basis and regularly in time as is done for MODIS data. However, Flood et al. (2013) has developed a methodology that allows inverting the BRDF parameters from the medium resolution images themselves, making the assumption that at least one major component of the BRDF can be assumed to be common to all pixels. It is similar

to the Roy et al. (2016) methodology, so a single set of BRDF parameters can be used to normalize all images.

Approach 6: We use the Flood et al. (2013) approach to derive the BRDF parameters, with the simplification done by Van doninck and Tuomisto (2017), which ignores topography and diffuse illumination. Because of the global BRDF assumption, the parameters are estimated for the reflectance ratio of Equation (6.3). To obtain a single solution for the parameters it is necessary to cancel the f_{iso} parameter, in the form $f'_{vol} = f_{vol}/f_{iso}$ and $f'_{geo} = f_{geo}/f_{iso}$ (FLOOD et al., 2013). Then minimizing the cost function C a single set of estimates of f'_{vol} and f'_{geo} can be obtained (FLOOD et al., 2013; VAN DONINCK; TUOMISTO, 2017):

$$C = \frac{1}{N} \sum_{i=1}^{N} \left| \rho(A,\lambda) - \rho(B,\lambda) \frac{1 + f'_{vol}(\lambda) \, K_{vol}(A) + f'_{geo}(\lambda) \, K_{geo}(A)}{1 + f'_{vol}(\lambda) \, K_{vol}(B) + f'_{geo}(\lambda) \, K_{geo}(B)} \right| \qquad (6.4)$$

where N is the number of observed pixel pairs used. These pairs of pixels were obtained in the areas of overlap between acquisitions of adjacent path so that each observation is in the opposite view directions, as suggested by Flood et al. (2013) and which will be further detailed in Section 6.3.4. We used the Nelder-Mead simplex algorithm available in Scipy to perform the minimization of the C function and obtain of f'_{vol} and f'_{geo} for each waveband separately.

6.3.4 Accuracy assessment of the methods for angular normalization

Three analyses were performed to evaluate the performance of the angular normalization approaches: (i) for directional effects; (ii) solar illumination effects; (iii) for IVs time series. These analyses will be described in the next sections.

6.3.4.1 Directional effects

Due to the wide swath, the WFI sensor observes the same location on the earth surface from multiple CBERS-4 paths (total of 9 at equator). This allows the same location to be observed with different viewing geometry. Pairs of images from adjacent orbits that have an intersection area were selected, as described in Section 6.2.1, to evaluate the directional effects from existing in CBERS-4/WFI images, to estimate the parameters f'_{vol} and f'_{geo} described in Section 6.3.3, and to evaluate the angular normalization methods described in Sections 6.3.1, 6.3.2, 6.3.3. To analyze bidirectional effects and evaluate methods of normalizing these effects, we took pairs of images with overlap areas from different adjacent paths. This makes it possible to obtain observations from the same point on the Earth's surface with different angular configurations and without substantial changes in the surface characteristics. So, we selected images from the same row and difference in path ranging from 3 to 7, which forms an overlapping area of ~550 to 130 km. To avoid substantial changes in the land surface, pairs of images with a maximum difference of 16 days between them were selected. The maximum cloud cover threshold was set to 10%. A total of 459 CBERS-4/WFI images satisfied these criteria. The largest number of images used (Figure 6.1) were acquired during the dry season when there is less cloud cover. A total of 401 pairs were formed with these images.

Figure 6.1 – Distribution of the number of CBERS-4/WFI images throughout the year (2020) used in this study.
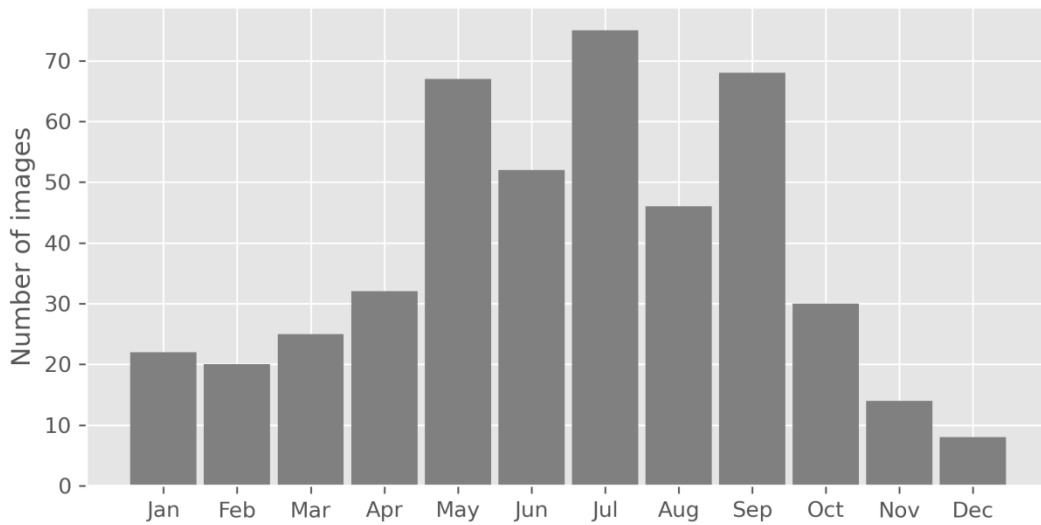
In the intersection area, points were systematically distributed in a grid of 100x100 pixels. For each of these points there is a pair of reflectance ρ_A and ρ_B, observed from two different set of angles A and B. Due to some targets that can show rapid changes in phenology (e.g., agriculture (ESQUERDO; ZULLO JÚNIOR; ANTUNES, 2011) and savanna (PETRI; GALVÃO; LYAPUSTIN, 2019)) the difference between the dates of observations A and B was limited to 16 days, to avoid difference in reflectance due to this type of change. The points were also filtered by land cover type, keeping only points belonging to vegetation classes, i.e., Forest Formation, Savanna Formation, Grassland, Pasture, Forest Plantation, Soybean, Other Temporary Crops, Sugar Cane, Perennial Crop, Mosaic of Agriculture and Pasture (Figure 6.2). Points with a relative azimuthal angle (RAA) greater than 90° when viewed from the east side or RAA less than 90° when viewed from the west side of the overlap have also been removed. This ensures that all points are seen in the backward scattering direction in the image

from the east of the overlap area and forward scattering direction in the image from the west.

Figure 6.2 – Distribution of points generated in areas of overlapping images of adjacent paths used to assess directional effects on CBERS-4/WFI images and methods to normalize these effects by land cover class.
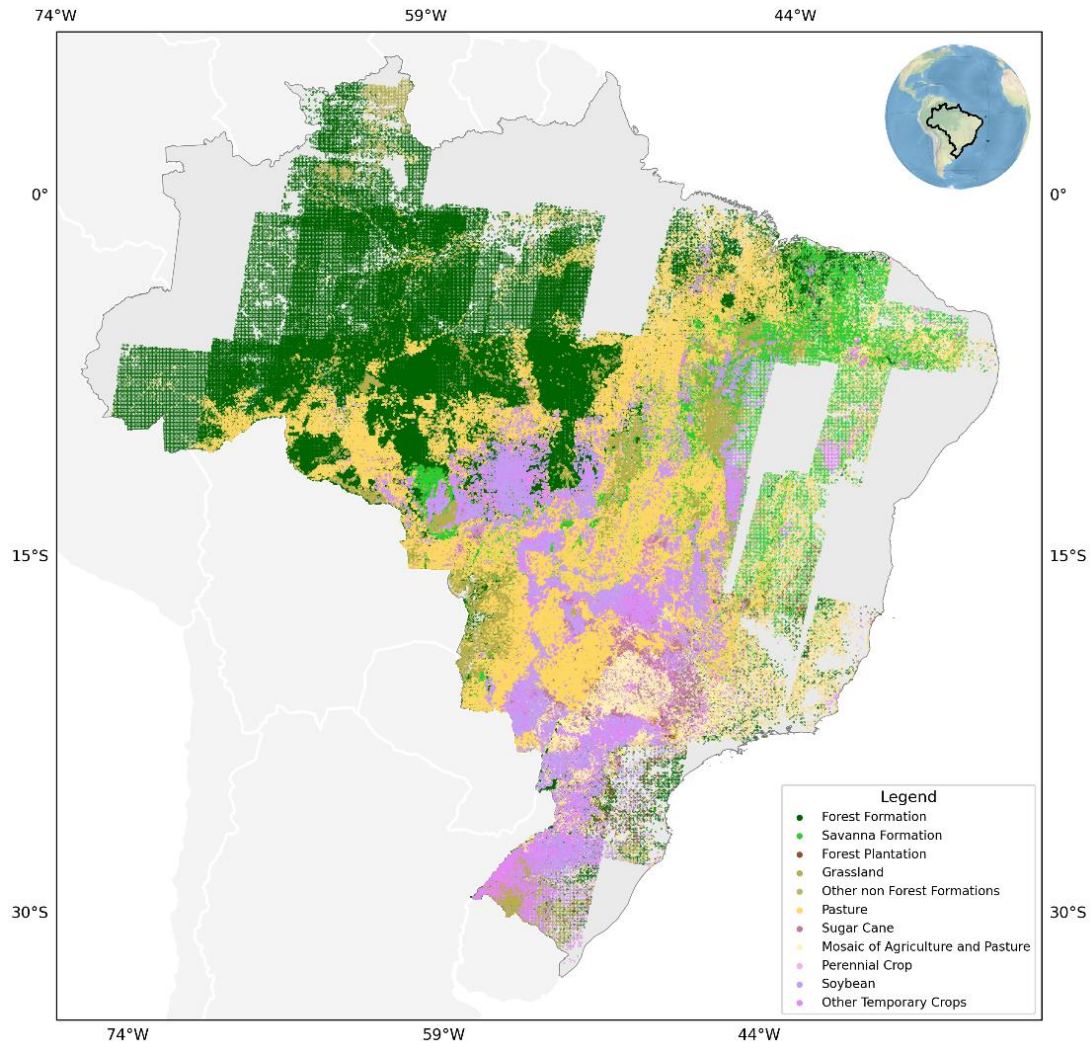
We present a scatter plot of reflectance data from each of the approaches for directional effects normalization presented in Sections 6.3.1, 6.3.2, 6.3.3 and summarized in Table 6.2. In approaches 2 to 6, a full bidirectional reflectance adjustment is performed using the RossThick-LiSparse-Reciprocal (RTLS)

model. The reflectance of the CBERS-4/WFI data was adjusted to the Nadir at a standard angular configuration ($\theta=35^{0}$, $\upsilon=0^{0}$, $\phi=0^{0}$) (VAN DONINCK; TUOMISTO, 2017). Scatter plots are also showed when no angular normalization is applied. This allows showing the magnitude of the BRDF effects and serves as a basis for comparing the approaches for normalization of the BRDF effects. A scatter plot is shown for each case and for each band. The *x*-axis shows the reflectance seen from the west, in the forward scattering direction, while the *y*-axis shows the reflectance seen from the east, in the backward scattering direction. The results were also assessed by three statistical metrics. The linear correlation coefficient (r) is an indicator of how strong a linear relationship is between the two sets of data. A linear regression was also fitted using orthogonal distance regression (ODR). The linear regression slope is a measure of the systematic bias existing between the reflectance observed in the two different angular configurations considered. The Root-Mean-Square Deviation (RMSD) was calculated as an indication of error, in reflectance units.

Table 6.2 – Summary of the six approaches of angular normalization compared in this work.

Approach	Summary	Reference
1	Based on the empirical gradient existing in each scene between the bias of reflectance in the CBERS-4/WFI data and the NBAR reflectance product (MCD43A4) in function of the VZA	(HANSEN et al., 2008; POTAPOV et al., 2012)
2	BRDF parameters of the model were obtained from MODIS of the coincident date, by taken from the MODIS pixels in which the CBERS-4/WFI pixels are contained	(Roy et al., 2008)
3	BRDF parameters of the model were obtained from MODIS of the coincident date averaged from pure MODIS pixels for different types of land cover	(Shuai et al., 2011)
4	BRDF parameters of the model were obtained from MODIS of the coincident date averaged over the CBERS-4/WFI scene	(Li et al., 2010)
5	Uses a single global set of BRDF parameters, obtained from a large number of MODIS pixels	(Roy et al., 2016)
6	Uses a single global set of BRDF parameters, inverted from CBERS-4/WFI image pairs	(Flood et al., 2013)

6.3.4.2 Solar illumination effects

To assess how the six angular normalization approaches perform with large changes in the solar vector we selected another set of pairs of images, because with the interval of 16 days the change in the solar vector is small. Only images with less than 15% of cloud cover over the Amazon Forest were selected because they have fewer phenological and land surfaces changes than other land covers such as savannas and agriculture. In each pair, an image with high SZA (between

January and March or between October and December) and another image with low SZA (between 15-May to 15-August) was selected. As in the case of view angle analyses, points were systematically distributed in a grid of 100x100 pixels in the intersection area. The average, maximum and minimum SZA of the high SZA points set were 39.73º, 47.35º, 28.88º, respectively. The set of points with low SZA had average, maximum and minimum SZA equal to 24.64º, 37.32º and 17.89º, respectively. The average, maximum, and minimum difference between the first and second sets were equal to 15.08º, 26.53º, and 4.68º, respectively. The Mean Absolute Difference (MAD) of each pair of pixels was calculated as a measure of accuracy for each angular normalization approach in each of the four spectral bands, in addition to the NDVI and EVI. The NDVI is a normalized index that is less influenced by angular effects, while the EVI is heavily influenced (PETRI; GALVÃO; LYAPUSTIN, 2019). Box plot of the MAD was generated. Even though over the Amazon Forest there is still spectral variation due to phenology or other surface changes difficult to separate from the angular effect, this analysis serves for a relative comparison between the six angular normalization methods.

6.3.4.3 IVs time series

We also accessed the effects of angular normalization methods on the IVs time series. To that, we selected the Aripuanã National Park which has a preserved area of Amazon rainforest. We follow the work of Petri et al. (2019) that analyzed the effects of BRDF normalization on MODIS data on this site. Between 20 and 50 pixels were visually selected in each image. The mean and standard deviation

of the EVI and NDVI were calculated for each image for the year 2020 that had cloud-free pixels.

6.4 Results

6.4.1 Directional effects

The relationship between reflectance from west and east view of the overlap areas of images for the four CBERS-4/WFI spectral bands can be observed in Figure 6.3. In Figure 6.3a, in which no angular normalization was applied, a systematic bias can be seen, indicated by the slope of the ODR regression line that reached 1.16 in the NIR band. The reflectance is higher when the view is from the east than the view from the west. The systematic bias was lower in the visible bands than in the NIR. The blue and green bands also showed greater data dispersion. This may be indicative of residual atmospheric contamination unaccounted in the atmospheric correction process or by unmasked clouds.

Figure 6.3 – Scatter plots of CBERS-4/WFI reflectance compared from opposite view directions. Horizontal and vertical axis shows reflectance from west view and east view, respectively. The columns of scatter plots represent the bands from blue to NIR. The rows of scatter plots represent the different sets of input data: (a) no angular normalization adjusts applied; (b) Approach 1; (c) Approach 2; (d) Approach 3; (e) Approach 4; (f) Approach 5; (g) Approach 6. Regression was calculated using orthogonal distance regression (ODR). Black dashed line represents 1-to-1 line, and red dashed line is the regression line. RMSD is Root Mean Square Deviation.
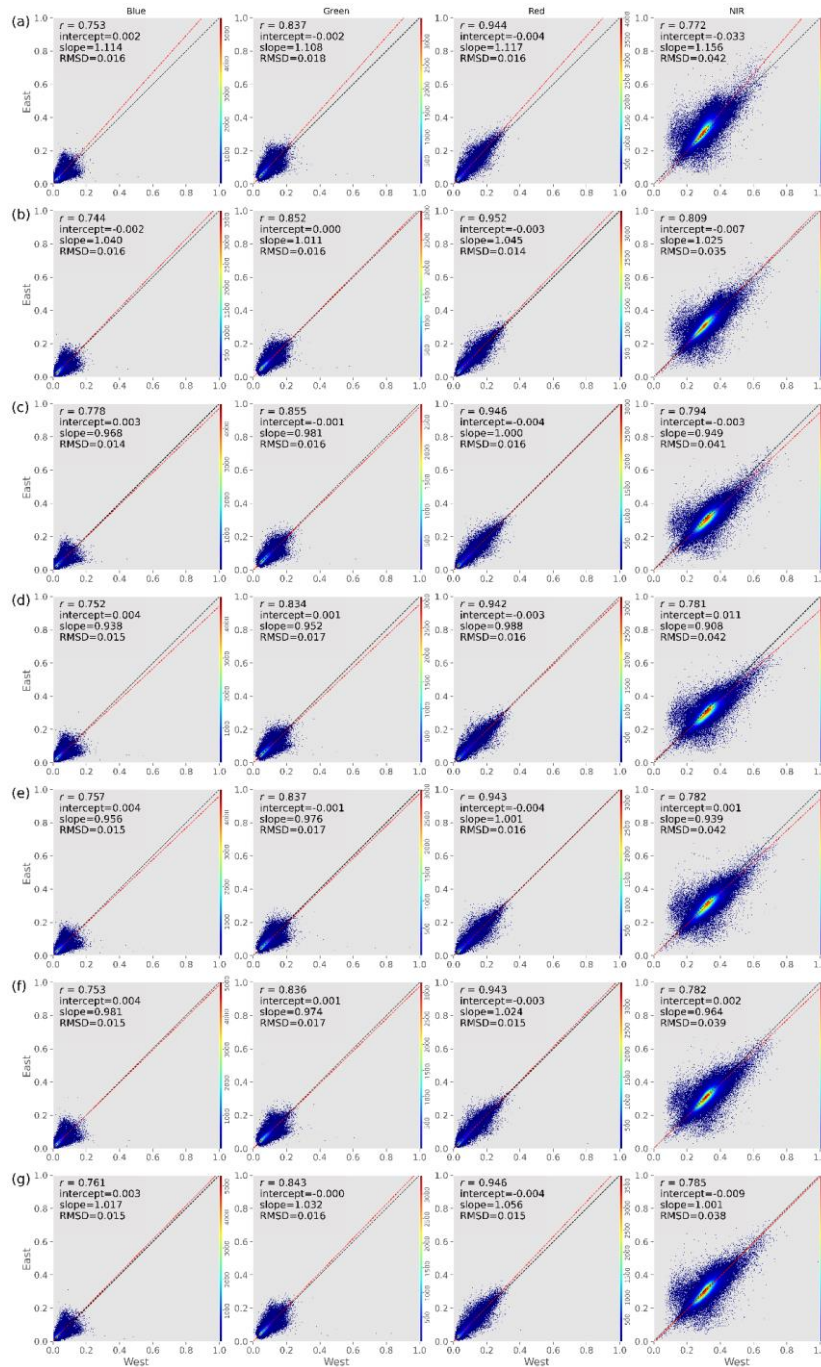
The six angular normalization approaches reduced the view angle effects (Figure 6.3b-g) for all bands. In all cases, the slope of the regression line was closer to 1.0 than when no angular normalization was applied, indicating a reduction in the systematic bias in the function of the view angle. In some cases, there was also a reduction in data dispersion. In most cases, there was an increase in the regression coefficient and a reduction in the RMSD. It is also possible to notice that for the blue, green and mainly NIR bands, the reflectance when viewed from the west presented higher values than that viewed from the east after applied the angular normalization using the BRDF parameters derived from MODIS (with lower intensity when using the set of parameters derived by Roy et al., 2016) (Figure 6.3c-f). This is an indication that there was overcorrection in the angular normalization in these approaches.

Three CBERS-4/WFI NIR images of the adjacent paths acquired every two days (maximum four days apart) are shown in Figure 6.4. With this short period of time, any change in the images due to the phenology of the vegetation is unlikely. Before the angular normalization (Figure 6.4a) directional effects are evident, with increasing brightness when increasing the VZA in the backscattering direction. While there is a reduction in brightness with increasing of VZA in the forward scattering direction. There is almost no difference between the edges of the images after angular normalization (Figure 6.4b, Approach 6 - angular normalization using BRDF parameters derived from the WFI image itself).

Figure 6.4 – CBERS-4/WFI images over amazon region from 27-Jul-2020, 29-Jul-2020 and 31-Jul-2020 (path 165, 173, 181, respectively, row 105) before (a) and after angular normalization using BRDF parameters derived from the WFI images itself (Approach 6) (b). These images are displayed with no contrast or histogram handle, reflectance values between 0.0 and 1.0.
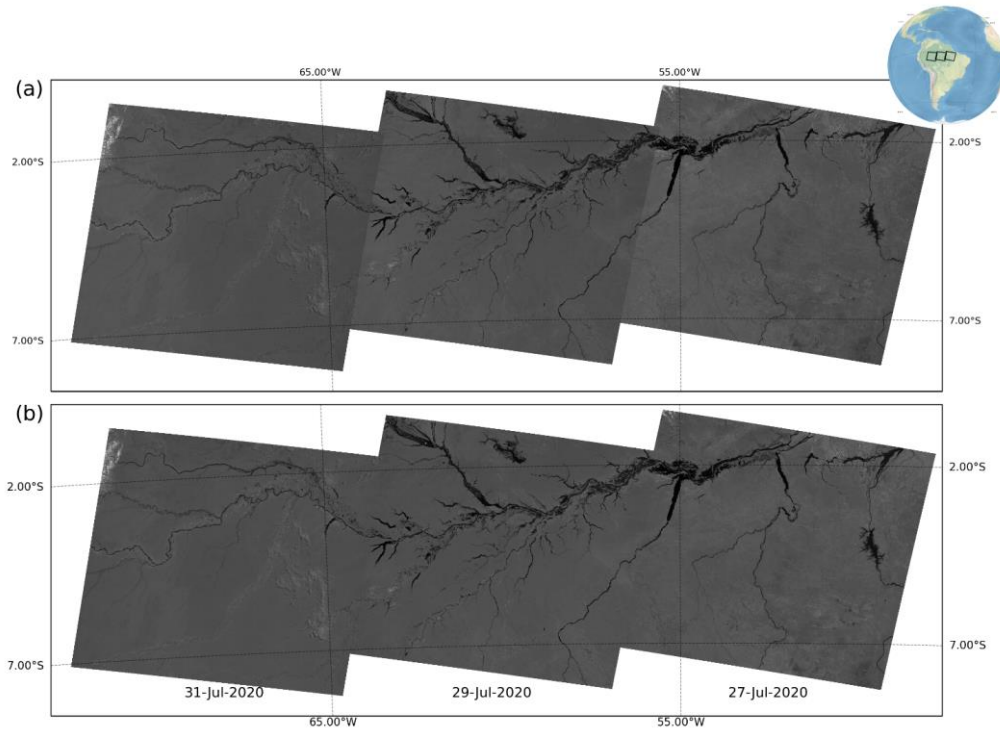
6.4.2 Solar illumination effects

The MAD between image pairs from adjacent paths acquired with high SZA (January-March and October-December) and low SZA (15-May to 15-August) for the CBERS-4/WFI reflective bands, NDVI and EVI in each of the six angular normalization method is presented in Figure 6.5. As in the analysis of directional effects, the angular effects in function of illumination angle were also stronger in the NIR compared to the visible spectral bands. In the case of vegetation indices, EVI was much more influenced by angular effects than NDVI.

After angular normalization, a reduction in MAD values occurred for the four spectral bands and for the EVI. While for the NDVI there was practically no

change. The reduction in MAD occurred for all normalization approaches, except

for Approach 1. The three angular normalization approaches that use BRDF

parameters of coincident MODIS images (Approach 2, 3, and 4) promoted greater

reduction of MAD values. While the two approaches that use fixed BRDF

parameters (Approach 5 - from MODIS, Approach 6 - from the CBERS-4/WFI

images themselves) caused less reduced of the MAD values.

Figure 6.5 – Mean absolute differences (MAD) between imagens from low and high SZA for each CBERS-4/WFI reflectance band, NDVI and EVI images. The high SZA images were from January-March and October-December, and low SZA images were from 15-May to 15-August.
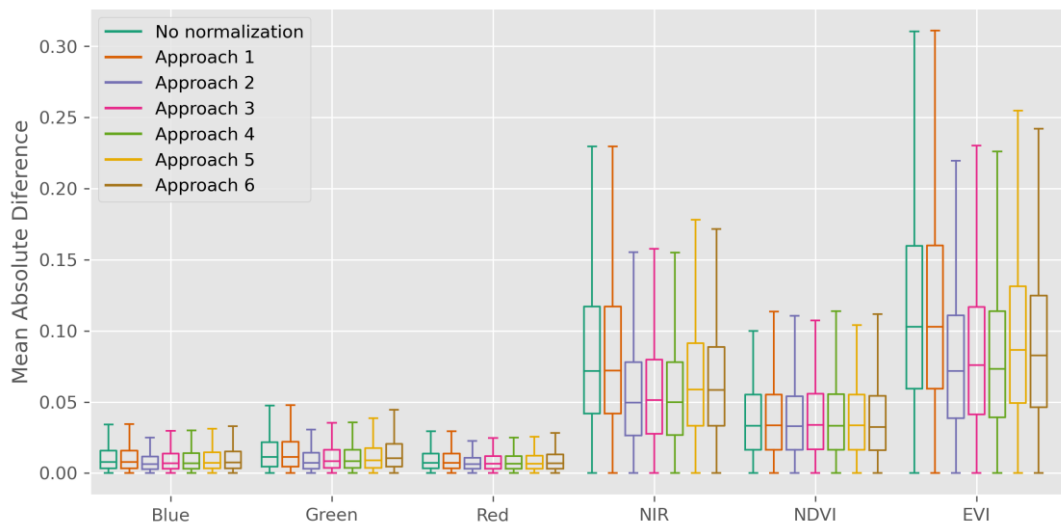
6.4.3 IVs time series

Figure 6.6 and Figure 6.7 shows the EVI and NDVI time series of a protected

area in the Amazon rainforest, before angular normalization (Figure 6.6d and

Figure 6.7d) and after normalization with the six different approaches (Figure

6.6e-j and Figure 6.7e-j), in addition to SZA (Figure 6.6a and Figure 6.7a), RAA

(Figure 6.6b and Figure 6.7) and VZA (Figure 6.6c and Figure 6.7c). Tropical

forest EVI and NDVI has less variation throughout the year than other vegetation

types, such as savannas, due to phenology. EVI from rainforests are also more affected by angular effects (PETRI; GALVÃO; LYAPUSTIN, 2019). At the beginning and at the end of the year, there is greater variation in the EVI for each date indicated by the largest error bar, probably due to cloud contamination and cloud shadows since this is the wettest period in the region. During the driest period, discontinuities in the EVI time series without angular normalization can be seen when there is a change from the observation from backscattering (RAA<90º) to the forward scattering direction (RAA >90º) (Figure 6.6d and Figure 6.6b). These discontinuities can also be seen in the NDVI time series, but with a smaller range (Figure 6.7d and Figure 6.7b). After angular normalization, for all the six approaches, there is an increase in EVI for observations in the forward scatter direction and a reduction in EVI for observations in the backscattering direction (Figure 6.6e-j). This reduces discontinuities in the EVI time series. However, there is practically no effect of angular normalization approaches on the NDVI time series (Figure 6.7e-j). During the year, higher EVI values can be seen near the beginning and end of the year and lower values in the middle of the year. After the angular normalization with the five approaches that use the RTLS and BRDF parameters (Approaches 2-6, Figure 6.6f-j) a reduction in the EVI values can be seen in these periods. This reduction is more pronounced when using the BRDF parameters derived from coincident images (Approaches 2-4, Figure 6.6f-h). In the case of the NDVI, there is a smaller variation during the year compared to the EVI (Figure 6.7d-j).

Figure 6.6 – CBERS-4/WFI EVI time series of points collected in Aripuanã National Park. (a) Solar zenith angle (SZA) (b) Relative azimuth angle (RAA); (c) View zenith angle (VZA) – VZA from RAA < 90⁰ were multiplied by -1 for better visualization; (d) no angular normalization adjusts applied; (e) Approach 1; (f) Approach 2; (g) Approach 3; (h) Approach 4; (i) Approach 5; (j) Approach 6.
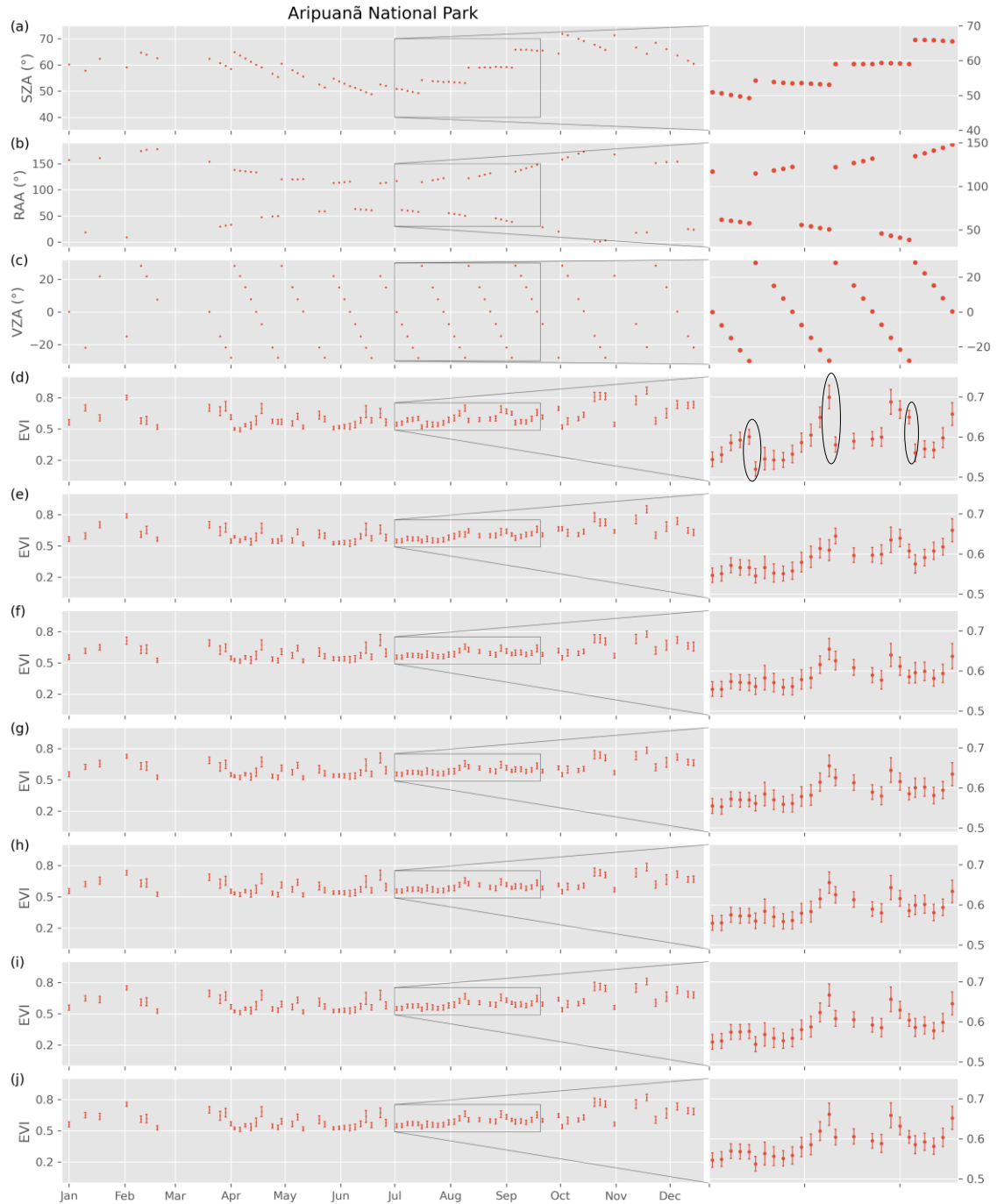
Figure 6.7 – CBERS-4/WFI NDVI time series of points collected in Aripuanã National Park. (a) Solar zenith angle (SZA) (b) Relative azimuth angle (RAA); (c) View zenith angle (VZA) – VZA from RAA < 90⁰ were multiplied by -1 for better visualization; (d) no angular normalization adjusts applied; (e) Approach 1; (f) Approach 2; (g) Approach 3; (h) Approach 4; (i) Approach 5; (j) Approach 6.
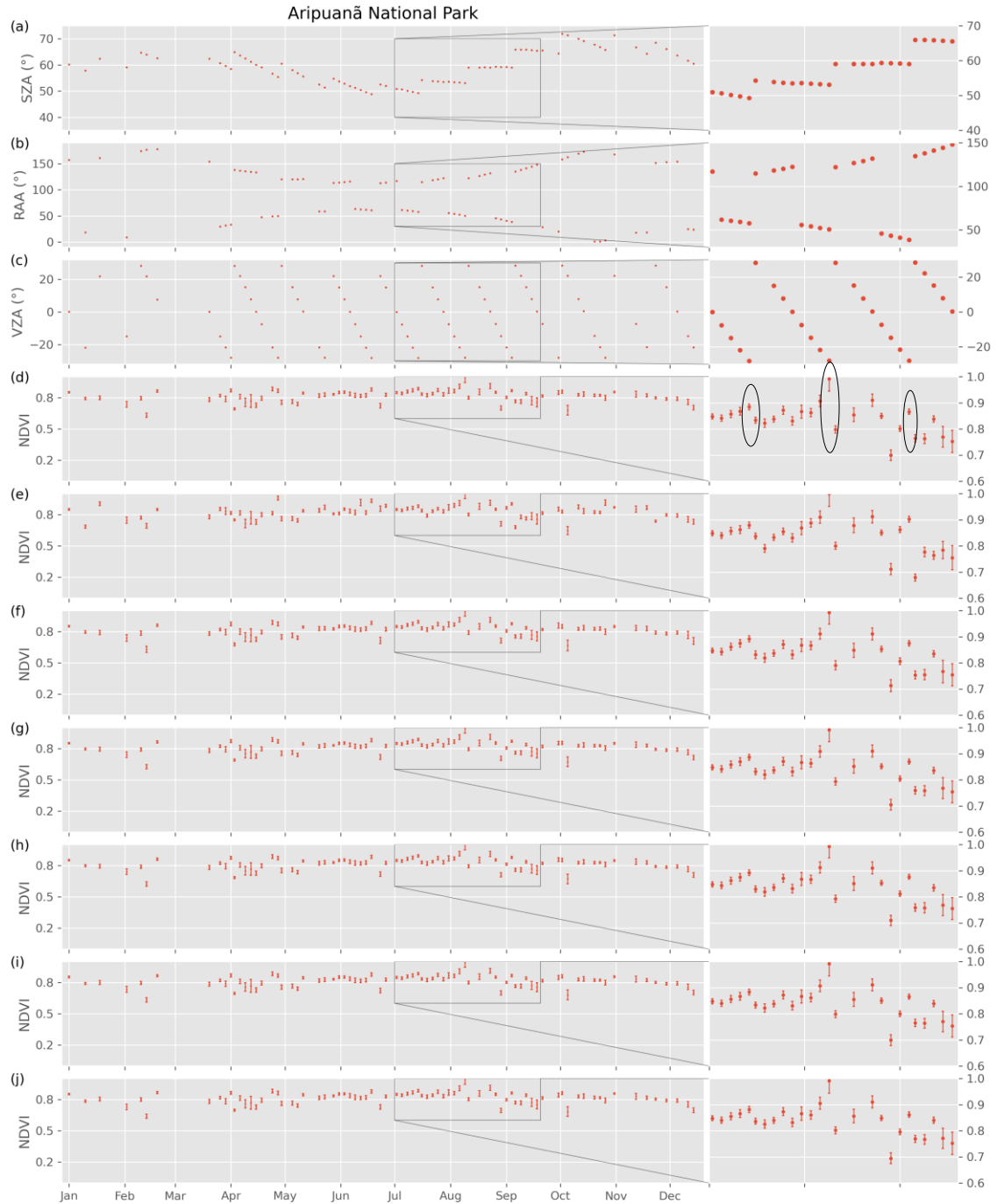
6.5 Discussions

The WFI sensor onboard of CBERS-4 has a wide FOV, that reach ±28.63°, so a directional effect from view angle is expected. To isolate these effects and allow their analysis, following previous work with Landsat images (FLOOD, 2013; FLOOD et al., 2013; VAN DONINCK; TUOMISTO, 2017), we analyzed pixels of intersection areas between adjacent paths of CBERS-4/WFI of close dates. A systematic bias was observed between the observations from east and from west (Figure 6.3). When the pixel is viewed from the east, the RAA is less than 90°, so the sensor is on the same side as the sun. In this case, the sensor is viewing the illuminated part of the sub-pixel structural elements than when viewed from the west (FLOOD et al., 2013). This explains the greater brightness when the pixels are observed from the east in relation to the observations from the west. The six angular normalization approaches considered reduced the systematic bias caused by the viewing angle. Some of them almost eliminated this bias.

The angular effects observed were stronger in the NIR than in the visible bands, both caused by the view angle (Figure 6.3) and the change in the solar vector (Figure 6.5). This effect was also observed in Landsat data for TM/ETM+ sensors by Van doninck and Tuomisto (2017). The effects of angular normalization in pairs of images obtained with high and low SZA over Amazon Forest were more pronounced in the NIR. The same happened with the EVI. With NDVI there was practically no difference between the data before and after angular normalization. This is in agreement with previous work in the same region using MODIS data that founded greater angular effects in EVI than in NDVI (PETRI; GALVÃO;

LYAPUSTIN, 2019). In NDVI the angular effects are smaller due to the cancellation of the BRDF effects from red and NIR bands (GAO et al., 2014). Directional effects are also present in the EVI time series of pixels from Aripuanã National Park. Discontinuities are seen when the observation moves from the backscattering to the forward scattering direction (Figure 6.6). There is also an increase in the EVI value from June to October coincident with shifts in RAA into the principal plane (0°-180° azimuth direction), similar to what was observed by Petri et al. (2019) with MODIS data. Despite this, it is difficult to separate spectral variations resulting from shifts in solar vector from those caused by changes in phenology or others change in the surface. So, our analyzes (Figure 6.5 and Figure 6.6) serve more as a relative comparison among the angular normalization approaches employed.

Approach 1 showed no difference between normalized and non-normalized data when analyzing the variation of the illumination vector (Figure 6.5 and Figure 6.6d). This is to be expected because this method does not take solar angular information into account. This non-existence of difference between the corrected and uncorrected data from low and high SZA of Approach 1 is also an indicator that there was no influence of the view angle in this analysis. All other approaches that perform a full BRDF correction using the RossThick–LiSparse–Reciprocal model reduced the differences as a function of SZA change. This is indicative of the existence of angular effects as a function of the solar vector in the CBERS-4/WFI images, although the magnitude of this difference was not quantified.

The empirical normalization to nadir view was the simplest normalization methods validated here (Approach 1). As we apply the analysis on various types of land cover, we use linear regression of the difference between the surface reflectance of the CBERS-4/WFI and the MODIS MCD43A4 product versus VZA. As the MCD43A4 product is normalized for nadir view we use them as a reference minimizing the influence of different land cover in the scene. This probably did not completely eliminate the influence of the land cover, as the magnitude of the angular effects are different for each target on the surface. But it allowed to remove much of the influence of the VZA (Figure 6.3b). Including increasing the agreement between the reflectance of pixels when viewed in the forward and backscattering direction with increasing correlation coefficient (except for the blue band). In the case there is only one type of landcover in the whole scene the linear regression could be done directly between the surface reflectance of the CBERS-4/WFI versus the VZA (HANSEN et al., 2008; VAN DONINCK; TUOMISTO, 2017). The RANSAC filter during the linear regression allowed to eliminate part of the noise caused by the influence of clouds in an edge of the image. However, under more cloudy conditions the available range in sensor view angles may be too small to reliably derive an empirical gradient (VAN DONINCK; TUOMISTO, 2017). Another limitation can be caused by the large difference in relief faces between the east and west edges of the scene.

The five approaches that perform the full BRDF normalization using the RossThick–LiSparse–Reciprocal model were able to reduce both the angular effects caused by the view angle and the change in the solar vector. The three approaches using BRDF parameters derived from concomitant MODIS images

showed the greatest reduction in reflectance differences or vegetation indices between images observed with high and low SZA. However, when analyzing the normalization for the view angle, there is an indication of overcorrection in all bands (except for red), with the reflectance in forward scattering direction becoming greater than in the backscattering direction. For Landsat images, Van doninck and Tuomisto (2017) found that using the BRDF coefficients of the concomitant MODIS pixel or the image average undercorrected surface reflectance of the NIR band. This difference may be related to the fact that the authors analyzed only forest pixels, and in our analysis, we considered different land uses and land cover. Van doninck and Tuomisto (2017) also raise the possibility that these methods performed worse in their study as a result of differences in the spectral response function, although they also consider that no other study has suggested that MODIS BRDF parameters should not be used because of this reason. This could be one of the causes of our result as well, as MODIS and CBERS-4/WFI also have differences in the spectral response function. Another cause may be associated with the model parameters in the MCD43 products were noisy (BRÉON; VERMOTE, 2012a), and we don't apply any filter on these parameters. Despite Flood (2013) and Van doninck and Tuomisto (2017) found no difference between per-pixel BRDF information compared to using a scene-averaged set of BRDF parameters, in our analysis the BRDF parameters of the MODIS pixel corresponding to each CBERS-4/WFI pixel showed slightly better results than using the average BRDF parameters for each class, which in turn was slightly better than using a single set of BRDF

parameters per Landsat scene. This can be seen by the higher correlation coefficient and slope closer to 1.0 (Figure 6.3) and lower MAD (Figure 6.5).

The two approaches that use fixed BRDF coefficients, either those derived from MODIS by Roy et al. (2016) or derived from the WFI images themselves following the methodology proposed by Flood et al. (2013), were also able to reduce the angular effects, both those caused by the view angle and by the change in the solar vector. Roy used the MODIS BRDF parameters initially to perform angular normalization on Landsat images. These parameters were also validated to perform angular normalization of Sentinel-2/MSI images. Both have much narrower FOVs than CBERS-4/WFI images. Our analysis showed that at least parts of the angular effect in WFI images can be reduced by employing these same parameters in the LTRS function.

Fixed BRDF parameters derived from the WFI images themselves also had similar results, with a small under correction in the visible bands compared to the other methods. Different set of random pixels used for parameterizing the model, or slightly different criteria for selecting image pairs may result in very different estimates of f'_{vol} and f'_{geo} (VAN DONINCK; TUOMISTO, 2017), which could also influence the result of the normalization. According to Flood et al. (2013), due to global nature of the BRDF correction using a single set of BRDF parameter, there will remain some variation due to BRDF effects which are specific to the land cover at each pixel.

The two approaches that use a single set of BRDF parameters are the easiest to apply, as they do not depend on MODIS data. The parameters set derived by

114

Roy et al. (2016) can be directly applied. While calculating model parameters in pairs from the WFI images themselves can be computationally demanding, once obtained, they can be easily applied to normalize the WFI images.

6.6 Conclusions

In this work, we investigated the angular effects existing in CBERS-4/WFI images, which have a wide FOV (±28.63°). Our results suggest that there are directional effects due to VZA and the change of the solar vector (SZA), in all spectral bands, being stronger in the NIR. Our analysis showed that there is also a strong angular influence on EVI compared with NDVI.

The six angular normalization approaches evaluated were able to reduce the angular effects resulting from the view angle. While the five methods that perform the full BRDF normalization using the RossThick–LiSparse–Reciprocal model were able to reduce the angular effects caused by the change in the solar vector (SZA). The empirical approach that uses linear regression of the difference between the surface reflectance of the CBERS-4/WFI and the MODIS NBAR product versus the VZA, was able to normalize the WFI images to the nadir view. The three approaches that use BRDF parameters derived from the concomitant MODIS product showed reduction in the angular effects resulting from the angle of view in the visible bands but overcorrected the NIR band. These approaches promoted the greatest reduction in MAD values between images obtained with high sun and low SZA. The two approaches that use a single set of BRDF parameters (either derived from MODIS data or derived from the WFI images themselves) show good ability to reduce the angular effects both in terms of the

view angle and the change in the solar angle. In addition, they are the easiest to apply because they do not depend on MODIS imagery. Then they can be easily used to perform angular normalization of other set of CBERS-4/WFI image. We believe that the results obtained in this work can be expanded to the images of the WFI sensors on board CBERS-4A and Amazonia-1, as they have similar geometric and spectral characteristics to the WFI sensor on board CBERS-4. Angular normalization should be important for the analysis of CBERS-4/WFI time series or image mosaics from spectral bands, mainly NIR, and also from non-normalized vegetation indices such as EVI. Angular normalization will produce a more consistent time series over time.

7 INTER-SATELLITE CROSS-COMPARISON OF WFI DATA FROM CBERS-4, CBERS-4A, AND AMAZONIA-1

This chapter presents the inter-satellite cross-comparison of WFI data from CBERS-4, CBERS-4A, and Amazonia-1, to identify possible differences between data from the different sensors and derive transformation functions between them.

7.1 Introduction

Inter-satellite cross-comparison among multiple sensors is indispensable when aiming to combine Earth observation data products obtained from different missions (ANDERSON et al., 2011; CHEN et al., 2013; LI; JIANG; FENG, 2013; FLOOD, 2014; ROY et al., 2016a; LI et al., 2017a; ZHANG et al., 2018). Cross-comparison among satellite sensor systems covers almost all the existing airborne and spaceborne sensors (LI; JIANG; FENG, 2013). The spectral reflectance of the same target in the same period can be different even when using similar sensors (ZHANG et al., 2018). Geometric calibration, radiometric calibration, the difference in spectral response function, atmospheric correction model, and BRDF effects are factors that can contribute to the difference between the spectral surface reflectance of different satellite sensors (FLOOD, 2017; CLAVERIE et al., 2018; HELDER et al., 2018; MARTINS et al., 2018; ZHANG et al., 2018).

From cross-comparison, it is possible to define quantitative transformations between sensors, i.e., it allows the reflectance of a sensor or the spectral indices to be converted into the equivalent of the other sensor (STEVEN et al., 2003; LI;

JIANG; FENG, 2013; FLOOD, 2014; ROY et al., 2016a; ZHANG et al., 2018). Transformations developed by statistical comparison of contemporary satellite sensor observations are a common approach (FLOOD, 2014; ROY et al., 2016a; ZHANG et al., 2018). Differences between reflectance values from different sensors depend on the surface being observed (FLOOD, 2014). The observed radiance sensor differs as a function of differences in spectral response in a way that is dependent on the observed surface component (ROY et al., 2016a).

Furthermore, comparison of data with different solar and view zenith geometry may introduce differences when surfaces are non-Lambertian, with target-dependent magnitudes (GAO et al., 2014). Reliable and representative determination of statistical functions to transform data between sensor bands require a comparison of data sensed over a wide range of surface conditions. The images capture time must be short, so there is no change in the surface state and condition (ROY et al., 2016a).

Given all these differences between different sensors, a question to be answered is whether the reflectance of WFI sensors from CBERS-4, CBERS-4A, and Amazonia-1 can be directly compared and combined in the same time series seamless. Despite the radiometric calibration showing that the quality of WFI onboard CBERS-4 is comparable to Landsat-8/OLI data for the common spectral bands (PINTO et al., 2016a), the radiometric calibration status of the other two WFI sensors is not documented in the literature yet. Furthermore, in the previous chapters, we showed that there is a larger geometric displacement of WFI imagery (Chapter 5) and that they are affected by BRDF effects (Chapter 6).

Thus, to test whether these factors are important it is necessary to evaluate real imagery. We conducted cross-comparative pairwise analyses of near-coincident data from WFI sensors from CBERS-4, CBERS-4A, and Amazonia-1. The objectives of the study are: (i) to compare the differences of spectral bands, and (ii) to derive statistical transformation functions between WFI data from the three different satellites. We believe that such an assessment will contribute to better monitoring and mapping of agriculture and natural vegetation in Brazil by combining images with the 2-3 day temporal resolution of three sensors.

7.2 Remote sensing data acquisition

7.2.1 Wide-Field Imager (WFI) data

The WFI sensors onboard CBERS-4, CBERS-4A, and Amazonia-1 have two optics (right and left). Although the WFI sensors onboard the three satellites have the same specifications, the spectral response functions are not the same. This difference exists even between the optics of the same sensor (Figure 7.1). This can cause differences in the images generated, even if they were acquired over the same location and under the same conditions.

Figure 7.1 – Relative spectral response functions for right and left optics from the WFI sensor onboard CBERS-4 (a), CBERS-4A (b), and Amazonia-1 (c).
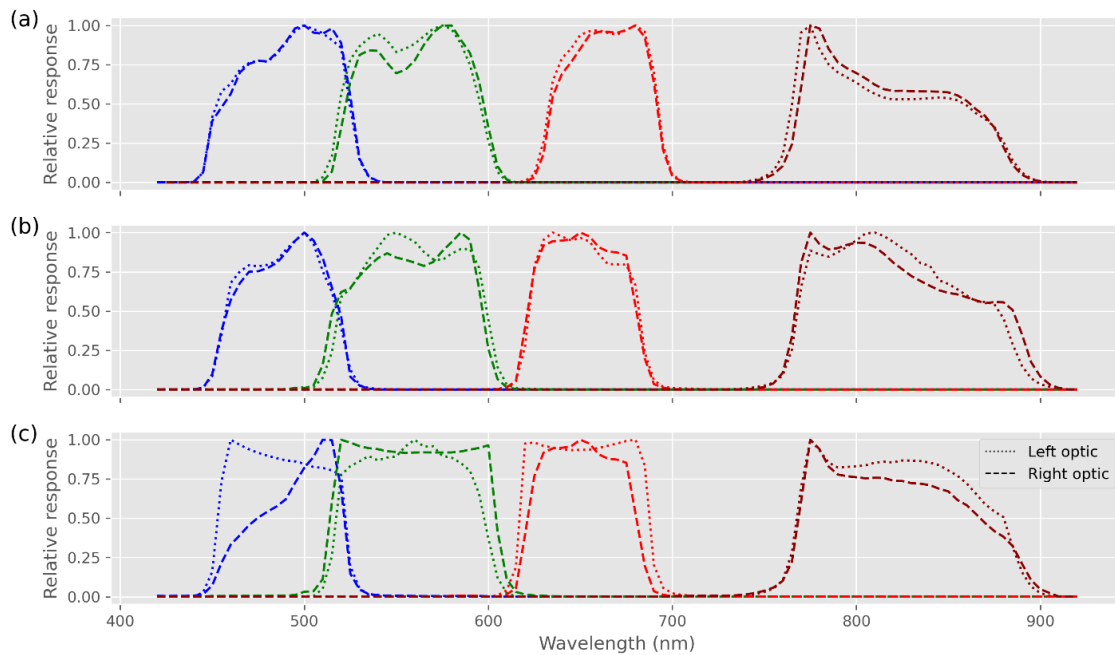
The temporal resolution for each sensor is five days at the Equator line. Because of the difference in the satellite altitude, the images generated by CBERS-4A have a spatial resolution of 55 m, while those generated by CBERS-4 and Amazonia-1 have 64 m. In addition, the three satellites also have different orbits, which combined with different scene sizes (Figure 7.2). This causes different scenes to cover the same point on the land surface. For CBERS-4 and CBERS-4A, up to nine passes can cover the same point on the earth's surface, while for Amazonia-1 only two.

Figure 7.2 – WFI grid from CBERS-4 (a), CBERS-4A (b), and Amazonia-1 (c). The black polygons indicate an example of all paths that may cover the same point on the land surface.
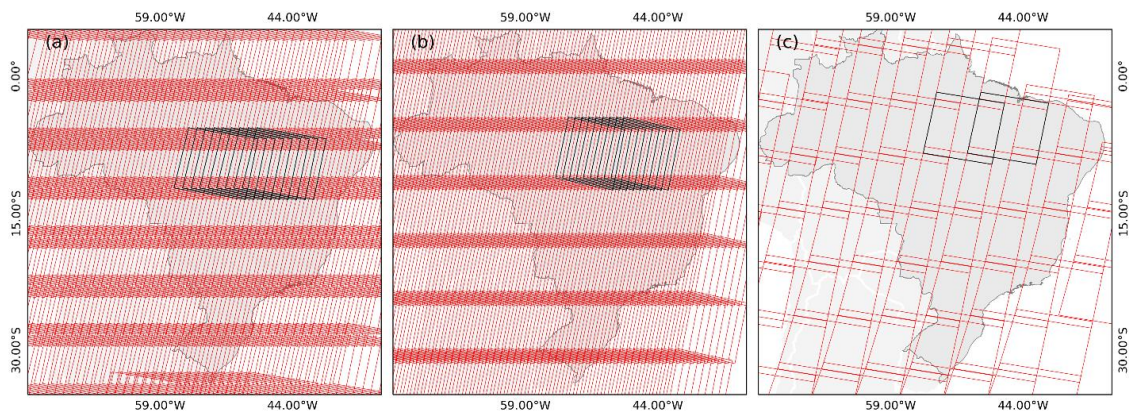
For the cross-comparison of the images of the WFI, we did a paired analysis of the images (images generated by the WFI of two satellites at a time). We selected all pairs of images between January 1, 2021, to December 31, 2021, acquired on the same date, with less than 10% of clouds that had at least 30% intersection area. A total of 120, 121, and 136 pairs were formed for CBERS-4/WFI-CBERS-4A/WFI, CBERS-4/WFI-Amazonia-1/WFI, and CBERS-4A/WFI-Amazonia-1/WFI, respectively. To compose these pairs, 171, 188, and 157 WFI images for CBERS-4, CBERS-4A, and Amazonia-1, respectively, were downloaded from the INPE website (http://www.dgi.inpe.br/catalogo/ and http://www2.dgi.inpe.br/catalogo/explore) at Level 4. The WFI Level 4 images provided by INPE are geometrically corrected with ground control points and ortho-rectified (INPE, 2021c). We used the surface reflectance product, which has been processed by the MS3 software (SILVA; ANDRADE, 2013). The product is delivered in the Universal Transverse Mercator (UTM) projection with the World Geodetic System 1984 (WGS84) datum.

121

7.2.2 Multispectral Instrument (MSI) data

We downloaded the NIR band at 10 m (B08) cloud-free image from Sentinel-2/MSI Level-2A (L2A) product for each MGRS tile in areas covered by the WFI images described in Section 7.2.1. The images are from the Processing Baseline v03.00 and v03.01, covering the period from April to December 2021. This product is radiometrically and geometrically corrected with ortho-rectification and atmospherically corrected to surface reflectance (ESA, 2015). The MSI L2A uses Global Reference Image (GRI) (DECHOZ et al., 2015) in its processing chain. GRI is a set of orthorectified Sentinel-2/MSI cloud-free images used as a ground control reference to improve geolocation accuracy to meet the requirements of multi-temporal registration of 0.3 pixels for 10 m bands (GAUDEL et al., 2017). The MSI L2A images are provided in UTM projection with WGS84 datum using the U.S. MGRS as a reference to the tiling grid.

7.2.3 Hyperion data

To simulate the reflectance of the WFI sensor's cameras reflectance spectra Earth Observing-1 (EO-1) Hyperion images were used. We downloaded 21 cloud-free Level 1R EO-1 Hyperion images from the Earth Explorer site (https://earthexplorer.usgs.gov/) across Brazil. The Hyperion L1R images were processed to surface reflectance using the Fast Line-of-sight Atmospheric Analysis of Spectral Hypercubes (FLAASH) atmospheric correction algorithm (FELDE et al., 2003). Hyperion sensor has 220 continuous bands, ranging from 357 to 2,576 nm with a 10-nm bandwidth. We only used 47 bands (447.17 nm to 915.23 nm) corresponding to the WFI response function range (Figure 7.1).

122

7.3 Methodology

7.3.1 WFI reflectance simulation

We simulated WFI sensor reflectance to identify possible differences between the left and right optic of each sensor and between sensors present in the CBERS-4, CBERS-4A, and Amazonia-1 due to the variability in the relative spectral response function. The WFI reflectance at each band was simulated by integrating the spectral response of the sensor with the hyperspectral reflectance spectra at each sampled wavelength weighted by the respective relative spectral response (Figure 7.1) (STEVEN et al., 2003; PINTO et al., 2016a; ZHANG et al., 2018). The simulated reflectance at each spectral band is computed according to the equation:

$$\bar{\rho}_{band} = \frac{\int_{\lambda_1}^{\lambda_2} RSR\,(\lambda_i)\,\rho'\,(\lambda_i)d\lambda}{\int_{\lambda_1}^{\lambda_2} RSR\,(\lambda_i)d\lambda} \tag{7.1}$$

where $\bar{\rho}_{band}$ is the simulated reflectance value of the specific-sensor and spectral band, ρ' is Hyperion reflectance centered at λ_i wavelength, RSR is the relative spectral response between the minimum (λ_1) and maximum (λ_2) interval where the RSR is greater than zero. A total of 14,610,062 spectra were used.

7.3.2 WFI data processing

7.3.2.1 Co-registration

As the WFI images of the three satellites have different grids, we defined a tiling system to be used for all images. They were defined using an AEA projection and SIRGAS 2000 datum. The grids were generated by taking -54 longitude and -12

latitude as the central reference and defining tiles of 3 × 2 degrees. Each image has 5807x4115 pixels and 4990x3536 at 55 m and 64 m, respectively. For each tile that contained a WFI image, a Sentinel-2/MSI mosaic with the NIR band at 10 m was generated. This mosaic was used as a reference for the co-registration of WFI images. The MSI mosaics were generated in the same spatial reference system as the respective WFI images, i.e., UTM projection, using the correct UTM zone.

We used the Python implementation of the Automatic and Robust Open-Source Image Co-Registration Software (AROSICS) (SCHEFFLER et al., 2017) to find control points (CP) that represent the correspondence between the reference image (MSI) and the target image (WFI). We used a grid resolution of 50 pixels in the AROSICS, i.e., looking for CPs every 50 pixels. To correct the misregistration a transformation function is necessary to find correspondence between points in the target image and points in the reference image. We selected the 2nd-degree polynomial as a transformation function because it proved to be sufficient to reduce displacement in the WFI images (Chapter 5). After the transform function was created, the target image was warped using a cubic resampling technique. The processing chain has also added a transformation from UTM to AEA projection. This allows all images to have the same spatial reference system without additional resampling, avoiding undesired geometric and spectral image quality degradation.

7.3.2.2 BRDF normalization

Most land surfaces are not Lambertian, so variations in viewing and illumination geometry can cause significant spatial and temporal variation in the retrieved directional reflectance independent of land surface characteristics (GAO et al., 2014). In Chapter 6, our experiments showed that the CBERS-4/WFI images suffered directional effects as a function of the observation angle. Thus, the surface reflectance is higher when observed in the backscattering direction and lower when observed in the forward scattering direction. As the WFI sensor on the CBERS-4A and Amazonia-1 have the same angular characteristics as the onboard WFI on the CBERS-4, we assume that your images suffered the same directional effect. This type of effect may constitute a significant source of noise for many applications (ZHANG et al., 2018). It may also be a source of difference between the reflectance of different sensors. We selected the c-factor technique and the global coefficients provided by Roy et al. (2016). This approach was initially used for Landsat application (ROY et al., 2016b), demonstrated for Sentinel-2/MSI data (ROY et al., 2017), and according to the results shown in Chapter 6 it is also able to reduce directional effects in WFI images. The c-factor technique uses fixed BRDF coefficients for each spectral band. Normalized reflectance is calculated by multiplying the original reflectance by the c-factor (CLAVERIE et al., 2018) as follow:

$$\rho(\lambda, \theta_n, v_n, \phi_n) = c\ (\lambda)\ \times \rho(\lambda, \theta_s, v_s, \phi_s)\ \ (2) \tag{7.2}$$

The c-factor is calculated from the semiempirical kernel-driven RossThick-LiSparse Reciprocal BRDF model (SCHAAF et al., 2002), using two kernels, K_{vol}

and K_{geo}, that describe volumetric and geometric scattering components, and three model parameters (Table 6.1) as follow:

$$c\,(\lambda) = \frac{f_{iso}(\lambda) + f_{vol}(\lambda)\,K_{vol}(\,\theta_n, v_n, \phi_n) + f_{geo}(\lambda)\,K_{geo}(\theta_n, v_n, \phi_n)}{f_{iso}(\lambda) + f_{vol}(\lambda)\,K_{vol}(\theta_s, v_s, \phi_s) + f_{geo}(\lambda)\,K_{geo}(\theta_s, v_s, \phi_s)} \qquad (7.3)$$

where θ_s, v_s, ϕ_s represents the view azimuth angle (VAA), VZA e RAA from input data, and θ_n, v_n, ϕ_n represents the VAA, VZA, and RAA of the normalized data. The VZA was set to nadir, the RAA was set to zero, and the SZA was set to the mean between the two images compared (Chapter 6).

7.3.3 WFI reflectance comparison

7.3.3.1 *Simulated reflectance comparison using Hyperion*

To analyze the effect of differences in the spectral response function between the right and left optics (Figure 7.1) on the surface reflectance, we compared the simulated surface reflectance for them in each WFI sensor. We present a scatter plot of the simulated surface reflectance from Hyperion hyperspectral spectra between the right and left optic of the WFI sensor for CBERS-4, CBERS-4A, and Amazonia-1. A scatter plot is shown for each band of each WFI sensor combination. The *x*-axis shows the simulated surface reflectance of the right optic, while the *y*-axis shows the simulated surface reflectance for the left optic. The results were assessed by three statistical metrics: linear correlation coefficient (r), orthogonal distance regression (ODR), and Root-Mean-Square Deviation (RMSD). The linear correlation coefficient is an indicator of how strong a linear relationship is between the two sets of data. Linear regression was also fitted using orthogonal distance regression. We chose the ODR regression

because there is equal uncertainty in both variables. The linear regression slope measures the systematic bias between the simulated surface reflectance from the right and left optic. The Root-Mean-Square Deviation (RMSD) was calculated as an indication of error, in reflectance units.

After that, we also compared the simulated surface reflectance between the WFI sensors in pairs, i.e., CBERS-4 versus CBERS-4A, CBERS-4 versus Amazonia-1, and CBERS-4A versus Amazonia-1. This analysis evaluates possible expected differences between the surface reflectance of the WFI sensor on the different satellites only as a function of the differences in the relative spectral response function. For this analysis, we also generated scatter plots and calculated the linear correlation coefficient, the RMSD and the ODR linear regression.

7.3.3.2 WFI spectral reflectance comparison

To assess any systematic differences between WFI sensor data on different satellites, we performed a pairwise comparison using the dataset described in Section 8.3.1. In all pairs of images acquired on the same day, pixels were sampled every 6400 m (or 100 pixels at 64 m) in the row and column directions across all overlap areas. The spatial distribution of points is shown in Figure 7.3. For the simulated reflectance, we also presented scatter plots of these points for each band and for each satellite combination. The linear correlation coefficient, the RMSD, and the ODR linear regression were also calculated to quantify the difference between data of WFI on the three different satellites combinations. The analyzes were performed for surface reflectance data before and after co-

127

registration, and for Nadir BRDF-adjusted reflectance (NBAR) data. In addition, we analyzed the surface reflectance data after co-registration filtering only pixels with less than 7° of VZA to evaluate systematic differences without the influence of directional effects.

Figure 7.3 – Distribution of points for cross-comparison between WFI data of CBERS-4 versus CBERS-4A (a), CBERS-4 versus Amazonia-1 (b), and CBERS-4A versus Amazonia-1 (c).
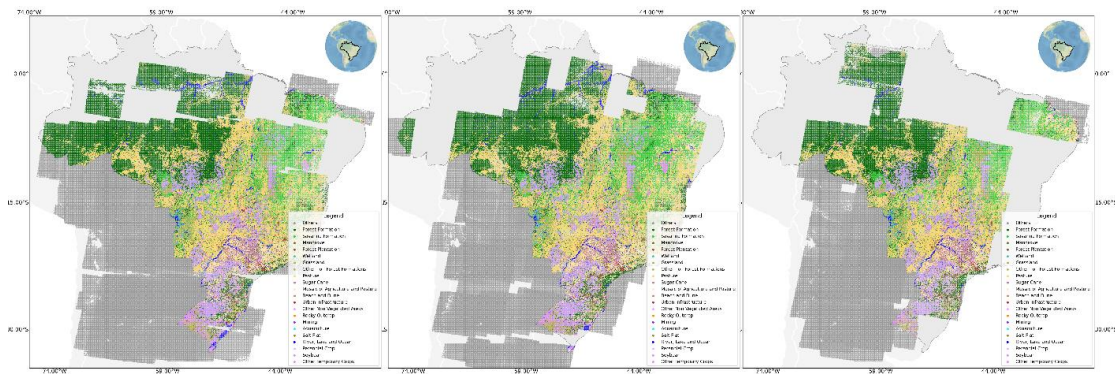
Statistical functions were built to transform the reflectance obtained by the WFI in one satellite into what it would look like if obtained by the WFI from the other satellite. Ordinary least-squares (OLS) linear regression was fitted as the statistical transformation function. The quality of the OLS regression adjustments was assessed by calculating the coefficients of determination (r^2) and the significance by examining the F-statistic *p*-value.

7.4   Results and discussion

7.4.1   Simulated spectral reflectance

Figure 7.4 shows scatter plots of the simulated reflectance for the right and left optics of the WFI sensor from CBERS-4 (Figure 7.4a), CBERS-4A (Figure 7.4b), and Amazonia-1 (Figure 7.4c). The data were highly correlated, with a correlation

coefficient equal to 1.000 for all cases, except for the blue band of Amazonia-1. The intercept of the ODR regression in all cases was equal to 0.00, indicating the absence of systematic biases. The ODR regression slope was equal to 1.00 for the NIR and the red band of the three satellites, except for the red band of Amazonia-1. In the blue and green bands, the slope difference concerning the unit line was 0.01. The exception was the green band of CBERS-4 (0.98) and the blue band of Amazonia-1 (0.95). The RMSD was equal to or less than 0.001 for all cases, excepted for the blue band of Amazonia-1 (0.007). The spectra from Hyperion data used in this study represent a variety of land use and land cover classes and provides simulated values that fall over a wide range of reflectance and still close to the 1:1 line in all cases. The only exception was for the blue band of Amazonia-1, in which there was greater data dispersion. This can be explained by the large difference between the relative response function of the right and left optics. The right optic has a maximum value close to 510 nm, while the left optic has a maximum value close to 460 nm. This difference combined with the spectra of each target can cause a larger difference between the simulated reflectance of optical right and left for this band. Despite this, as for all the other bands of the three satellites, there was practically no difference, thus, the following analysis will disregard the difference between left and right optic.

Figure 7.4 – Scatter plot of simulated spectral reflectance for WFI relative response function from CBERS-4 (a), CBERS-4A (b), and Amazonia-1 (c). The horizontal and vertical axis shows reflectance from the right and the left optic, respectively. Regression was calculated using orthogonal distance regression (ODR). The black dashed line represents the 1:1 line, and the red dashed one is the regression line. RMSD is Root Mean Square Deviation.
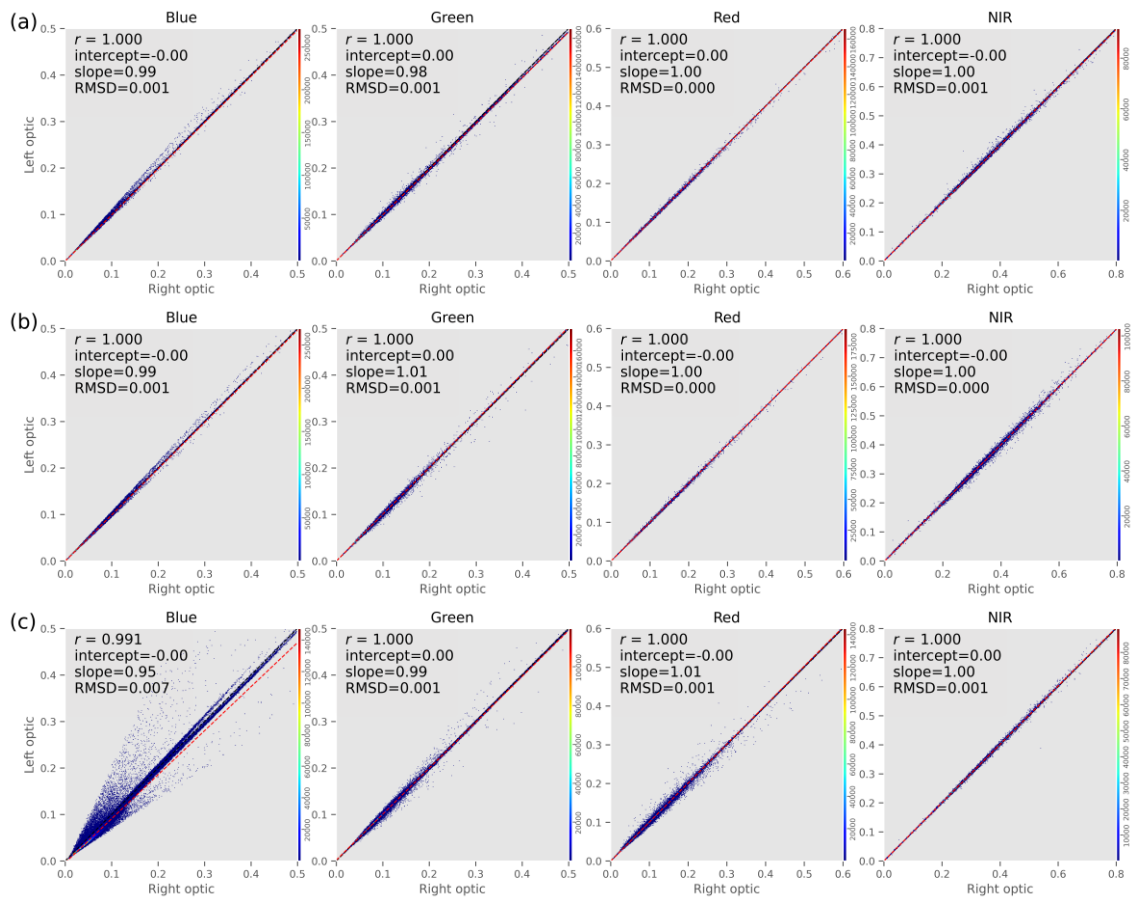
Figure 7.5 shows scatter plots of WFI inter-satellite simulated reflectance between CBERS-4 and CBERS-4A (Figure 7.5a), CBERS-4 and Amazonia-1 (Figure 7.5b), and CBERS-4A and Amazonia-1 (Figure 7.5c) considering the relative response function of the right optics. The slope is equal to the unit, the intercept equal to zero, and the coefficient of correlation equals to 1.000 for the three combinations of satellites in the NIR band. The same occurs for the red band between CBERS-4A and Amazonia-1. The greatest differences in terms of

130

bands occurred between the red band of CBERS-4 and CBERS-4A, and CBERS-4 and Amazonia-1. In both cases, the ODR slope was equal to 0.94, i.e., in general, the simulated WFI/CBERS-4 was lower than the simulated reflectance of WFI/CBERS-4A or WFI/Amazonia-1. The relative response function for this band extends in WFI/CBERS-4 to close to 700 nm, while for CBERS4A and Amazonia-1 it decreases earlier (Figure 7.1). This same pattern of simulated reflectance occurs between the right and left optics (not shown), showing that there is almost no difference between them for the NIR and red bands. In the green band, the ODR slope differs from the 1:1 line by at most 0.01, and the correlation coefficient is not equal to 1.000 only between CBERS-4A and Amazonia-1 (r=0.999). The greatest differences in simulated reflectance occur in the blue band. For this band, the slope between CBERS-4 and Amazonia-1, and between CBERS-4A and Amazonia-1 is greater than 1.00, indicating that in most cases, the simulated reflectance of Amazonia-1 is greater than the simulated reflectance of CBERS-4 and CBERS-4A. In the case between CBERS-4A and Amazonia-1, the ODR slope reaches 1.04, and the RMSD reaches 0.005. However, in cases where the scatter plots involve Amazonia-1 in the blue band, if we analyze the left optic (not shown), the slope is less than 1.00 for both CBERS-4 and CBERS-4A. This indicates that the differences observed in the inter-optic comparison also affect the inter-satellite comparison.

Simulation of reflectance implicitly assumed that the surface had no BRDF effect, and that there were no calibration or geolocation errors, no atmospheric scattering or absorption, no residual clouds or shadow, which is not the case for

131

real data (ZHANG et al., 2018). Thus, in the next sections we analyze the real data.

Figure 7.5 – Scatter plot of simulated spectral reflectance for WFI relative response function between CBERS-4 and CBERS-4A (a), CBERS-4 and Amazonia-1 (b), and CBERS-4A and Amazonia-1 (c) for the right optics. Regression was calculated using orthogonal distance regression (ODR). The black dashed line represents the 1:1 line, and the red dashed one is the regression line. RMSD is Root Mean Square Deviation.
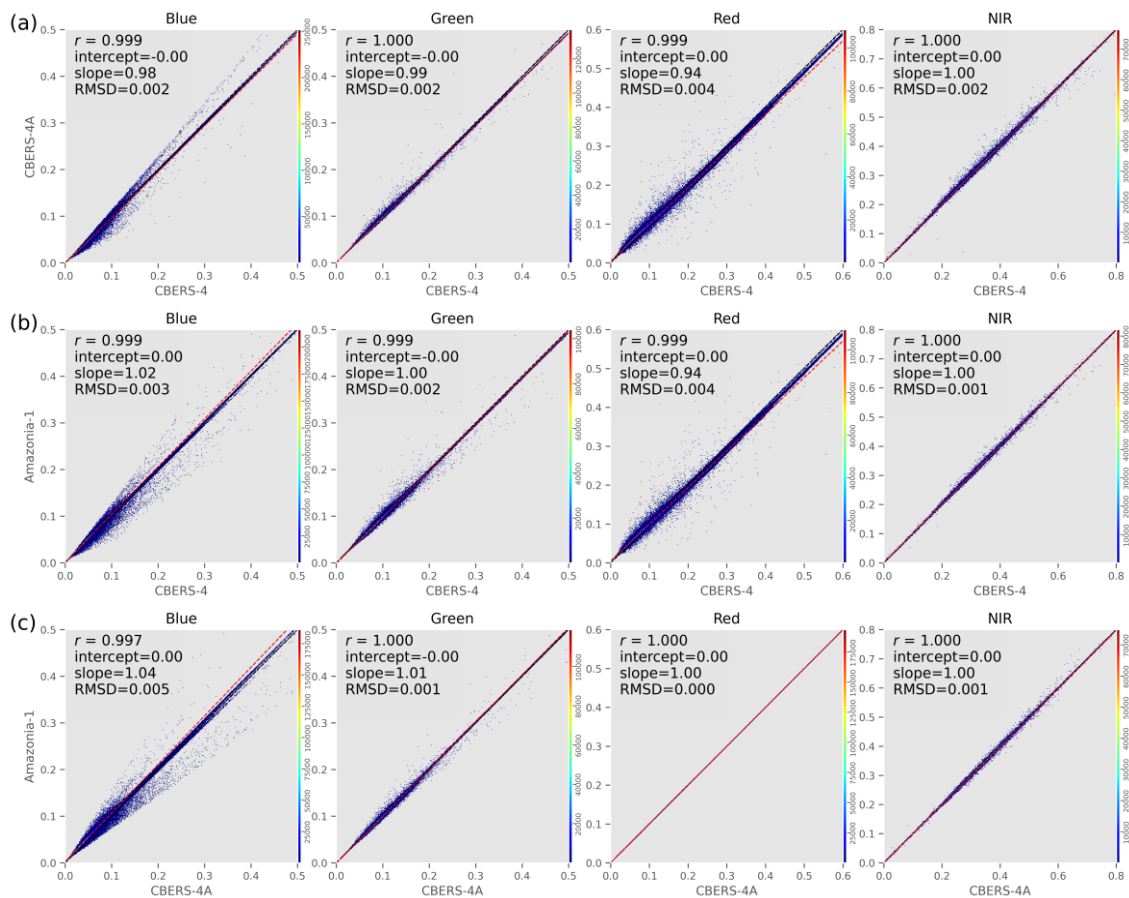
7.4.2 Spectral surface reflectance before co-registration

Figure 7.6 shows scatter plots of WFI inter-satellite spectral surface reflectance between CBERS-4 and CBERS-4A (Figure 7.6a), between CBERS-4 and Amazonia-1 (Figure 7.6b), and between CBERS-4A and Amazonia-1 (Figure 7.6c) before co-registration. The slope of the ODR regression between the CBERS-4 and CBERS-4A WFI data for all bands was less than 1.000 (Figure

7.6a). This indicates in all bands, the tendency of the surface reflectance of CBERS-4 to be greater than that of CBERS-4A. In the bands of shorter wavelength, the slope of the ODR regression was more distant from the line 1:1.

In all bands, there was the same pattern in the scatter plot between CBERS-4 and Amazonia-1 (Figure 7.6b), and between CBERS-4A and Amazonia-1 (Figure 7.6c), with similar slopes in the two cross-satellite comparisons. The ODR slope is less than 1.000 in the blue and NIR bands and greater in the green and red bands in both cases. Two clusters can be observed in the scatter plots in the blue and NIR bands. In the case of the blue band, it may be due to differences in the spectral response function between the right and left optics on the Amazonia-1's WFI sensor (Figure 7.1c), which caused a difference in the simulated reflectance between the two optics (Figure 7.4). But this difference does not occur in the NIR band. It could be a spectral calibration effect. This difference could be caused by differences in radiometric calibration in some of the detectors in the NIR band. However, in the literature there is no information about the radiometric calibration status of the WFI sensor onboard of Amazonia-1.

As the results of Chapter 5 showed the need to perform the co-registration for a consistent analysis of the WFI data, we did not build the transform functions previous to the co-registration. This analysis will be presented in the next section.

Figure 7.6 – Scatter plot of WFI spectral surface reflectance between CBERS-4 and CBERS-4A (a), CBERS-4 and Amazonia-1 (b), and CBERS-4A and Amazonia-1 (c) before co-registration. Regression was calculated using orthogonal distance regression (ODR). The black dashed line represents the 1:1 line, and the red dashed one is the regression line. RMSD is Root Mean Square Deviation. The color bar shows the frequency of occurrence of values.
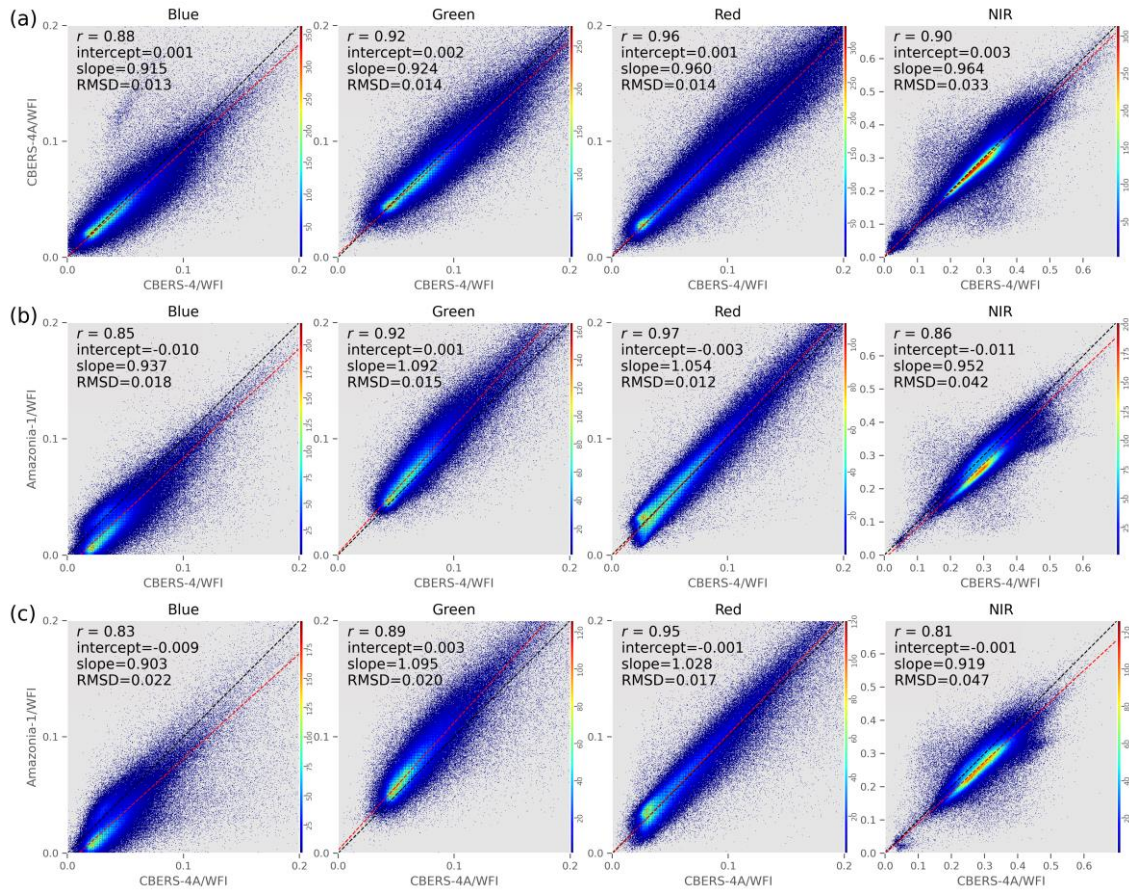
7.4.3 Spectral surface reflectance after co-registration

Figure 7.7 shows scatter plots of WFI inter-satellite spectral surface reflectance between CBERS-4 and CBERS-4A (Figure 7.7a), CBERS-4 and Amazonia-1 (Figure 7.7b), and CBERS-4A and Amazonia-1 (Figure 7.7c) after co-registration. There were no major changes in the scatter plot patterns comparing to the data before co-registration. But a reduction in the dispersion of reflectance data can be seen. The correlation coefficient and the RMSD confirm this. In almost all

combinations of satellites and bands, there was at least an increase in the correlation coefficient, a decrease in RMSD, or both. Differences in reflectance values due to misregistration are greater in heterogeneous landscapes, mainly near edges of different land use and land cover classes (Chapter 5). As the data were distributed across a wide variety of land use cover classes and regions in Brazil, the effects of misregistration are smaller as many of these landscapes are homogeneous. Otherwise, the observed data dispersion reduction could be even greater.

Figure 7.7 also shows the transformation lines fitted using the OLS regression, in addition to the ODR regression line. The green line is the fitted function of the WFI reflectance from the satellite on the x-axis versus the one on the y-axis. The magenta line is the fitted function the WFI reflectance from the satellite on the y-axis versus the one on the x-axis. Both are different from each other and the ODR regression line. The ODR regression systematically indicates differences between sensor inter-satellites because there is noise in either variable, so it does not bias towards one or the other (FLOOD, 2014). The OLS regression assumes that all unmodeled variation is in the dependent variable, considering that the independent variable has no noise. The transformation equations for WFI surface reflectance data between satellites after co-registration are presented in Table 7.1. All the OLS regressions are significant (p-value < 0.01) and the r^2 was greater than 0.67 in all cases.

Figure 7.7 – Scatter plot of WFI spectral surface reflectance between CBERS-4 and CBERS-4A (a), CBERS-4 and Amazonia-1 (b), and CBERS-4A and Amazonia-1 (c) after co-registration. The black dashed line represents the 1:1 line, and the red dashed one is the ODR regression line. Slope and intercept are from ODR regression. The green line is the ordinary least squares (OLS) regression of the WFI data on the x-axis versus the y-axis, the magenta line is the OLS regression of the WFI data on the y-axis versus the x-axis. RMSD is Root Mean Square Deviation. The color bar shows the frequency of occurrence of values.
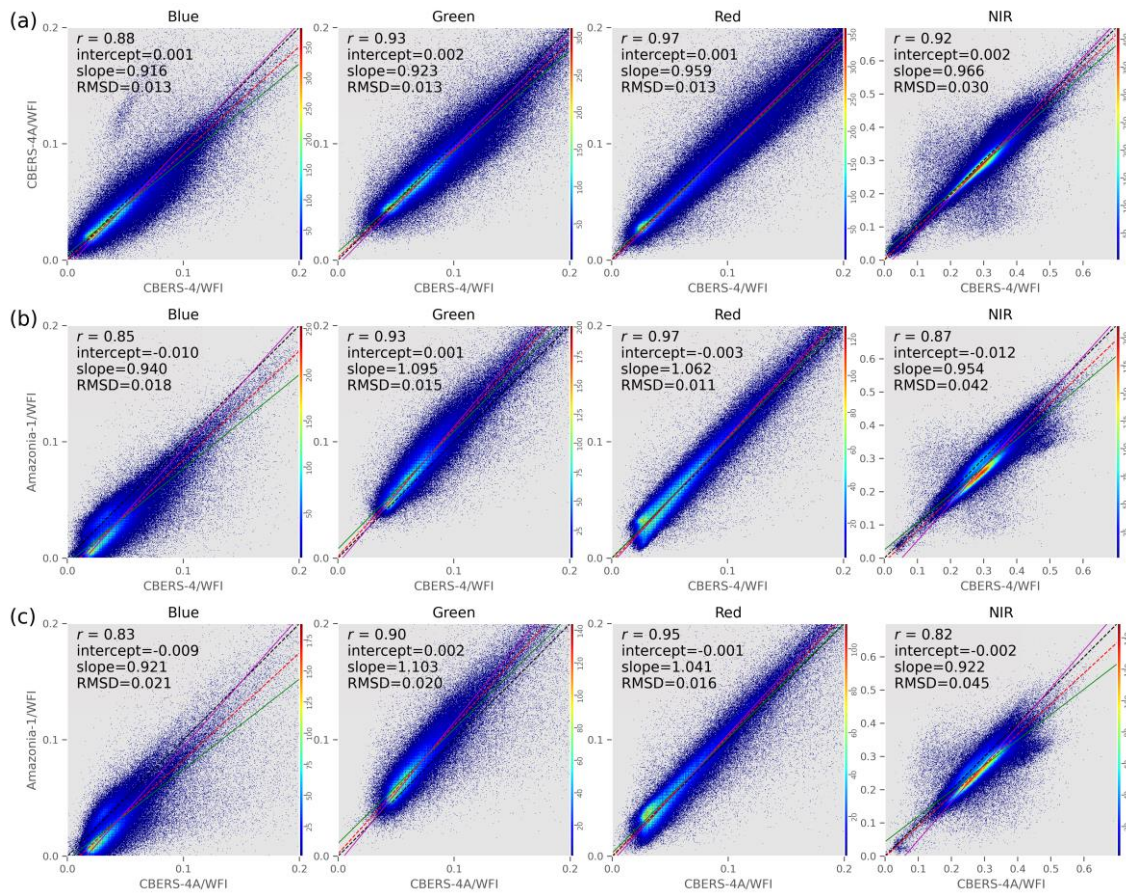
Table 7.1 – WFI surface reflectance transformation function inter-satellite fitted by ordinary least squares (OLS) regression for the co-registered data.

	Band	OLS transformation functions	r^2	p-value
CBERS-4 x CBERS-4A	Blue	C4A = 0.8184 C4 + 0.0051 C4 = 0.9561 C4A + 0.0054	0.78	0.0
	Green	C4A = 0.8638 C4 + 0.0070 C4 = 1.0021 C4A + 0.0038	0.87	0.0
	Red	C4A = 0.9291 C4 + 0.0034 C4 = 1.0073 C4A + 0.0018	0.94	0.0
	NIR	C4A = 0.8872 C4 + 0.0254 C4 = 0.9449 C4A + 0.0231	0.84	0.0
CBERS-4 x Amazonia-1	Blue	Am1 = 0.8105 C4 - 0.0044 C4 = 0.9005 Am1 + 0.0154	0.73	0.0
	Green	Am1 = 1.0089 C4 + 0.0079 C4 = 0.8522 Am1 + 0.0038	0.86	0.0
	Red	Am1 = 1.0290 C4 - 0.0005 C4 = 0.9164 Am1 + 0.0045	0.94	0.0
	Nir	Am1 = 0.8323 C4 + 0.0249 C4 = 0.9032 Am1 + 0.0524	0.75	0.0
CBERS-4A x Amazonia-1	Blue	Am1 = 0.7776 C4A - 0.0031 C4A = 0.8918 Am1 + 0.0162	0.69	0.0
	Green	Am1 = 0.9833 C4A + 0.0110 C4A = 0.8240 Am1 + 0.0050	0.81	0.0
	Red	Am1 = 0.9881 C4A + 0.0028 C4A = 0.9157 Am1 + 0.0041	0.90	0.0
	NIR	Am1 = 0.7646 C4A - 0.0436 C4A = 0.8738 Am1 + 0.0581	0.67	0.0

As can be observe in the scatter plots of Figure 7.7 the data dispersion was much greater and the ODR regression line much further from the 1:1 line than in the simulated reflectance case (Figure 7.5). In addition to the differences in the spectral response function, other factors such as atmospheric contamination, radiometric calibration, and bi-directional effects can cause these across satellite differences in surface reflectance (ZHANG et al., 2018). To try to isolate these

effects, in Figure 7.8 we presented the scatter plots only with WFI surface reflectance data after co-registration with VZA < 7⁰, thus minimizing BRDF effects. The cross-comparison between WFI surface reflectance from CBERS-4 and CBERS-4A shows similar patterns to the simulated reflectance data (Figure 7.5). The slope of the ODR regression was very close to line 1:1, and the coefficient of correlation was > 0.93 for all bands. This indicates that a large part of the bias between the WFI surface reflectance of the CBERS-4 and CBERS-4A in concerning the 1:1 line observed in Figure 7.7 is due to bidirectional effects.

The scatter plots between WFI data from CBERS-4 and Amazonia-1 (Figure 7.8b), and between CBERS-4A and Amazonia-1 (Figure 7.8c) show the same pattern, similar to each other in all bands. In both cases, they differed from the simulated reflectance data. The WFI surface reflectance data of Amazonia-1 are generally higher than that of CBERS-4 and CBERS-4A in the blue and NIR bands and higher in the green and the red band. These differences in surface reflectance from the WFI onboard Amazonia-1 to CBERS-4 and CBERS-4A may be due to differences in the radiometric calibration of Amazonia-1. As previously discussed, information on the radiometric calibration status of Amazonia-1 was not found in the literature. The two clusters found in the blue and NIR bands in the WFI data between CBERS-4 and Amazonia-1 (Figure 7.7b), and between CBERS-4A and Amazonia-1 (Figure 7.7c) can also be seen in Figure 7.8b-c. Note that the smaller cluster in both bands and for both CBERS-4 and CBERS-4A is located on the 1:1 line, while the larger clusters are displaced. The inter-satellite transformation function of the WFI surface reflectance with VZA < 7⁰ fitted by OLS regression was significant in all cases (p-value < 0.01) (Table 7.2).

Figure 7.8 – Scatter plot of WFI spectral surface reflectance between CBERS-4 and CBERS-4A (a), CBERS-4 and Amazonia-1 (b), and CBERS-4A and Amazonia-1 (c) after co-registration for view zenith angle less than 7º. The black dashed line represents the 1:1 line, and the red dashed one is the ODR regression line. Slope and intercept are from ODR regression. The green line is the ordinary least squares (OLS) regression of the WFI data on the x-axis versus the y-axis, and the magenta line is the OLS regression of the WFI data on the y-axis versus the x-axis. RMSD is Root Mean Square Deviation. The color bar shows the frequency of occurrence of values.
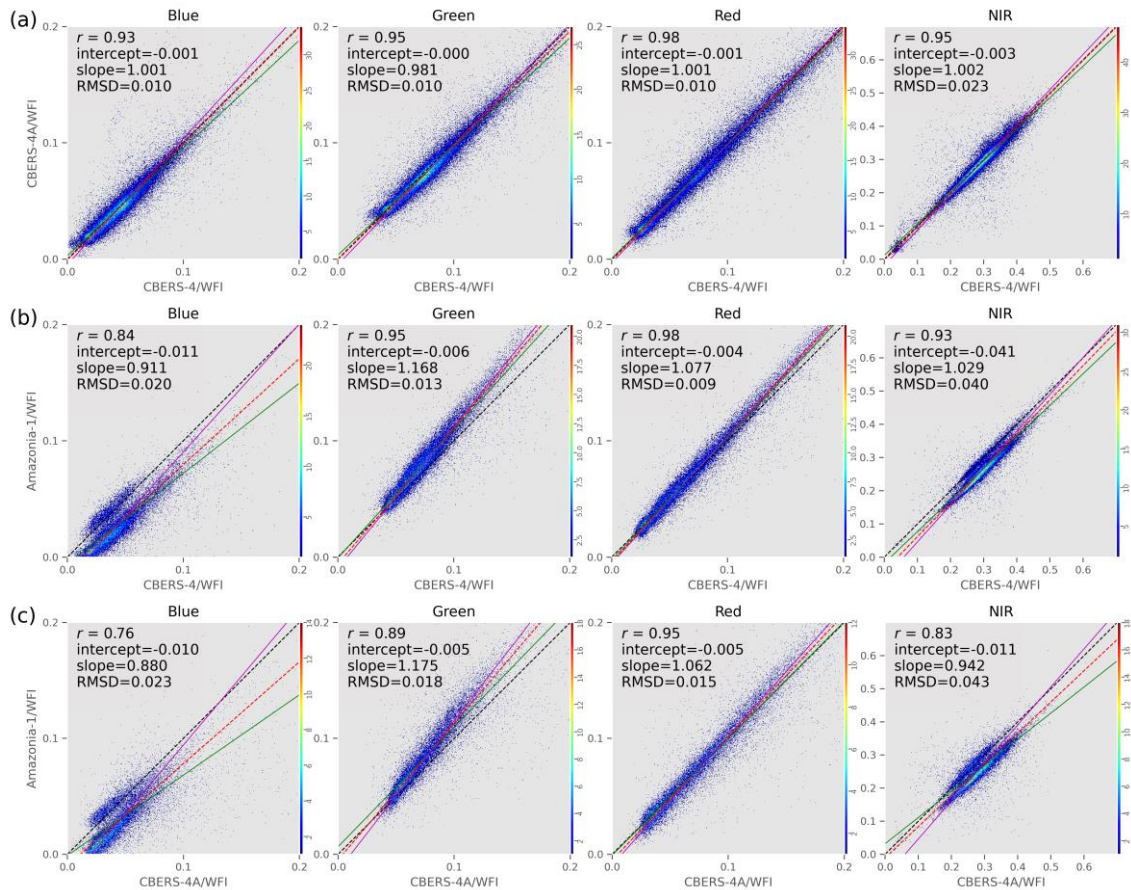
Table 7.2 – WFI surface reflectance transformation function inter-satellite fitted by ordinary least squares (OLS) regression for the co-registered data and view zenith angle < 7°.

	Band	OLS transformation functions	r^2	p-value
CBERS-4 x CBERS-4A	Blue	C4A = 0.9264 C4 + 0.0028 C4 = 0.9243 C4A + 0.0043	0.86	0.0
	Green	C4A = 0.9331 C4 + 0.0035 C4 = 0.9679 C4A + 0.0046	0.90	0.0
	Red	C4A = 0.9794 C4 + 0.0006 C4 = 0.9766 C4A + 0.0030	0.96	0.0
	NIR	C4A = 0.9488 C4 + 0.0115 C4 = 0.9449 C4A + 0.0177	0.90	0.0
CBERS-4 x Amazonia-1	Blue	Am1 = 0.7762 C4 - 0.0057 C4 = 0.9085 Am1 + 0.0179	0.71	0.0
	Green	Am1 = 1.1017 C4 - 0.0008 C4 = 0.8202 Am1 +0.0081	0.90	0.0
	Red	Am1 = 1.0543 C4 - 0.0023 C4 = 0.9117 Am1 + 0.0051	0.96	0.0
	Nir	Am1 = 0.9500 C4 - 0.0180 C4 = 0.9007 Am1 + 0.0587	0.86	0.0
CBERS-4A x Amazonia-1	Blue	Am1 = 0.6933 C4A - 0.0010 C4A = 0.8433 Am1 + 0.0205	0.58	0.0
	Green	Am1 = 1.0322 C4A + 0.0065 C4A = 0.7735 Am1 + 0.0109	0.80	0.0
	Red	Am1 = 1.0079 C4A - 0.0008 C4A = 0.8991 Am1 + 0.0082	0.91	0.0
	NIR	Am1 = 0.7886 C4A + 0.0321 C4A = 0.8708 Am1 + 0.0598	0.69	0.0

As the coverage of WFI data with VZA less than 7° is limited, we applied BRDF normalization to transform the surface reflectance as if observed from the nadir, also called Nadir BRDF-Adjusted Reflectance (NBAR). These results will be discussed in the next section.

7.4.4 Surface NBAR

Figure 7.9 shows scatter plots of WFI inter-satellite surface NBAR between CBERS-4 and CBERS-4A (Figure 7.9a), CBERS-4 and Amazonia-1 (Figure 7.9b), and CBERS-4A and Amazonia-1 (Figure 7.9c). In the cross-comparison between the WFI NBAR reflectance of the CBERS-4 and CBERS-4A (Figure 7.9a) in all bands, the slope of the ODR regression approached the line 1:1 compared to the surface reflectance data (Figure 7.7a). The slope of the ODR regression of the bands with shorter wavelengths were the ones that most distanced themselves from line 1:1. This differs from the previous chapter (Chapter 6) in which the results showed greater directional effects on the NIR band. Other factors might affect this in cross-comparison analysis such as uncertainties in atmospheric correction and residual cloud contamination because there is stronger atmospheric scattering at short wavelengths (MARTINS et al., 2018). The MS3 algorithm does not consider the information on viewing angles (SILVA; ANDRADE, 2013), which can lead to uncertainties in the characterization of the atmosphere. In addition, it uses atmospheric products from MODIS, and there may be changes in the condition of the atmosphere between the acquisition of images by MODIS and the WFI sensors.

Figure 7.9 – Scatter plot of WFI spectral surface NBAR between CBERS-4 and CBERS-4A (a), CBERS-4 and Amazonia-1 (b), and CBERS-4A and Amazonia-1 (c). The black dashed line represents the 1:1 line, and the red dashed one is the ODR regression line. Slope and intercept are from ODR regression. The green line is the ordinary least squares (OLS) regression of the WFI data on the x-axis the y-axis, and the magenta line is the OLS regression of the WFI data on the y-axis versus the x-axis. RMSD is Root Mean Square Deviation. The color bar shows the frequency of occurrence of values.
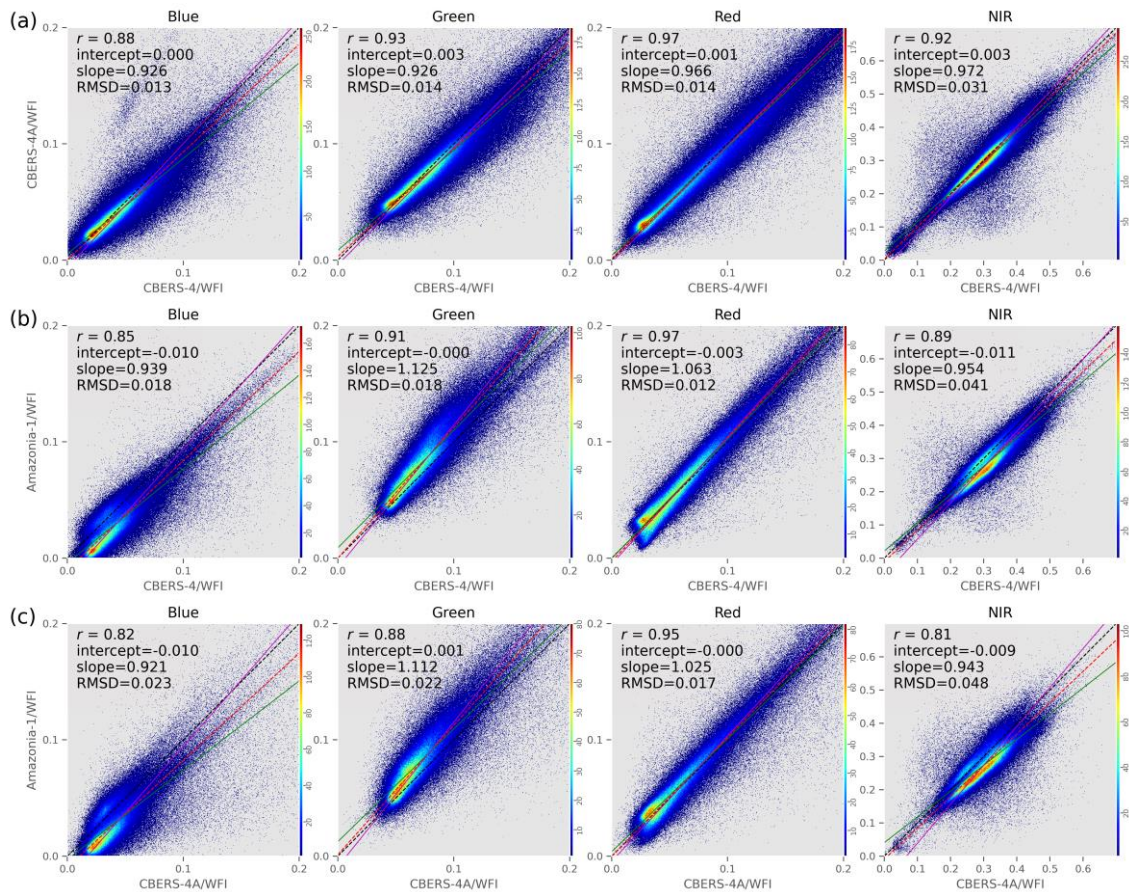
After the normalization of surface reflectance to the nadir viewing angle, there was a small reduction in the correlation coefficient and a small increase in the RMSD in some cases. This may be related to our approximate approach to calculate the view azimuth angle (VAA) and ZVA. Another factor that can contribute to this is the use of fixed BRDF coefficients, which probably just capture the BRDF effects from the component which could be said to be roughly

the same for all pixels (FLOOD, 2013), so, there could still be part of the BRDF effects that is heterogeneous between pixels. Zhang et al. (2018) also found a greater mean relative difference in surface NBAR than in surface reflectance for some bands in the cross-comparison between OLI and MSI.

The slope of the ODR regression in the cross-comparison between CBERS-4 and Amazonia-1 (Figure 7.9b), and CBERS-4A and Amazonia-1 (Figure 7.9c) WFI surface NBAR became closer to the slope in the ODR regression of the data from surface reflectance with VZA<7º (Figure 7.8b-c). Except for the blue band between CBERS-4A and Amazonia-1, NIR band between CBERS-4 and Amazonia-1, where there were no changes, and the red band between CBERS-4A and Amazonia-1, which became closer to the 1:1 line. This shows that surface reflectance normalization to the nadir approximates the surface reflectance as it would be without the directional effects. But in the case of data that involves the cross-comparison between CBERS-4 and CBERS-4A with Amazonia-1, it does not become closer to the 1:1 line. As previously discussed, one of the possible reasons is the differences in radiometric calibration, which is beyond the objectives of this work. Another issue that needs to be better investigated in the future is the formation of two clusters in the blue and NIR bands in the data involving Amazonia-1. This may also be related to the radiometric calibration of Amazonia-1.

In Table 7.3 we present the transformation functions of the NBAR WFI cross-satellite surface adjusted by the OLS regression. The OLS regressions were significant (p-value < 0.01) for all bands and the three-satellite cross-

143

comparisons. The coefficient of determination in the transformation functions between the surface NBAR WFI between CBERS-4 and CBERS-4A, CBERS-4 and Amazonia-1, CBERS-4A and Amazonia-1 were > 0.77, > 0.73, and >0.66 for all bands. The lowest coefficients of determination were in the blue and NIR bands. In the case of the transformation functions of the surface NBAR WFI between CBERS-4 and Amazonia-1, and between CBERS-4A and Amazonia-1, this is due to the formation of the two clusters in the blue and NIR bands.

Table 7.3 – WFI surface NBAR transformation function inter-satellite fitted by ordinary least squares (OLS) regression.

	Band	OLS transformation functions	r^2	p-value
CBERS-4	Blue	C4A = 0.8206 C4 + 0.0055	0.77	0.0
x		C4 = 0.9390 C4A + 0.0060		
CBERS-4A	Green	C4A = 0.8616 C4 + 0.0085	0.86	0.0
		C4 = 0.9935 C4A + 0.0039		
	Red	C4A = 0.9348 C4 + 0.0040	0.93	0.0
		C4 = 0.9991 C4A + 0.0017		
	NIR	C4A = 0.8925 C4 + 0.0271	0.84	0.0
		C4 = 0.9399 C4A + 0.0231		
CBERS-4	Blue	Am1 = 0.8080 C4 - 0.0042	0.73	0.0
x		C4 = 0.9003 Am1 + 0.0157		
Amazonia-1	Green	Am1 = 1.0112 C4 + 0.0088	0.83	0.0
		C4 = 0.8160 Am1 + 0.0066		
	Red	Am1 = 1.0286 C4 - 0.0003	0.94	0.0
		C4 = 0.9135 Am1 + 0.0047		
	Nir	Am1 = 0.8504 C4 + 0.0215	0.79	0.0
		C4 = 0.9251 Am1 + 0.0467		
CBERS-4A	Blue	Am1 = 0.7674 C4A - 0.0028	0.67	0.0
x		C4A = 0.8776 Am1 + 0.0173		
Amazonia-1	Green	Am1 = 0.9688 C4A + 0.0125	0.78	0.0
		C4A = 0.8036 Am1 + 0.0074		
	Red	Am1 = 0.9695 C4A + 0.0037	0.90	0.0
		C4A = 0.9260 Am1 + 0.0042		
	NIR	Am1 = 0.7758 C4A + 0.0408	0.66	0.0
		C4A = 0.8540 Am1 + 0.0665		

These transformation functions were generated considering a large amount of data from different land use and land cover over Brazil. They can be used to remove the differences in WFI reflectance between-satellite, which is systematic across the landscape. This will make possible to combine the WFI data from the three satellites into a more dense time series contributing to better monitoring and mapping of agriculture and natural vegetation in Brazil.

7.5 Conclusion

Inter-satellite WFI sensor cross-comparison between CBERS-4 and CBERS-4A, CBERS-4 and Amazonia-1, and CBERS-4A and Amazonia-1 was performed in this work. Reflectance simulated from the convolution of Hyperion reflectance spectra by the spectral response function between the right and left optics of the WFI sensors for each band and each satellite showed no major systematic differences between the optics (|slope of ODR regression| < 0.02 from line 1:1), except for Amazonia-1 blue band (slope of ODR regression equal to 0.95). When the simulated WFI reflectance was cross-satellite compared, there were systematically greater differences only in the red bands between CBERS-4 and CBERS-4A and between CBERS-4 and Amazonia-1 (slope of ODR regression equal to 0.94). Comparing WFI surface reflectance between Amazonia-1 with CBERS-4 and CBERS-4A, there were also differences between the slope of the ODR regression considering the left (<1.0) and right (>1.0) optics in the blue band.

In the WFI inter-satellite surface reflectance cross-comparison, in almost all combinations of satellites and bands there was at least an increase in the

correlation coefficient, a decrease in RMSD, or both, from before to after the co-registration. The slope of the ODR regression between the CBERS-4 and CBERS-4A WFI data for all bands was less than 1.0, indicating, in all bands, the tendency of the surface reflectance of CBERS-4 to be greater than that of CBERS-4A. In all bands, there was the same pattern in the scatter plot between CBERS-4 and Amazonia-1, and between CBERS-4A and Amazonia-1, with similar slopes in the two cross-satellite comparisons. When only data with VZA < 7⁰ were considered slope of the ODR regression was very close to the 1:1 line, and the coefficient of correlation was > 0.93 for all bands between WFI surface reflectance of CBERS-4 and CBERS-4A. The scatter plots between the WFI data from CBERS-4 and Amazonia-1, and between from CBERS-4A and Amazonia-1 show the same pattern similar to each other in all bands, and in both cases, they differed from the simulated reflectance data. In addition, in these two WFI inter-satellite cross-comparisons, two clusters were formed in the blue and NIR bands. This indicate of the need to evaluate the radiometric calibration of the Amazonia-1/WFI. The results showed that the slope of the ODR regression for the surface NBAR data approached the data with VZA < 7⁰.

The WFI surface reflectance and surface NBAR transformation functions between satellites were also calculated using OLS regression. The regressions were significant in all cases and bands. These transformation functions can be used to convert the WFI data from one satellite to the equivalent of the other satellite, enabling the generation of a denser time series.

8 MAPPING FROST-DAMAGED CORN COMBINING WFI TIME SERIES FROM CBERS-4, CBERS-4A, AND AMAZONIA-1

In this chapter we evaluate the combination of WFI data from the three satellites using what was investigated in the previous chapters in an agricultural monitoring application. The WFI NDVI time series was used to map frost-damaged corn areas in western Paraná.

8.1 Introduction

World food production needs to increase to meet the projected demands from population growth, dietary changes, and increasing bioenergy use, ensuring food security and access to sustainable energy (FAO, 2018; VAN DIJK et al., 2021). Corn is the most produced cereal in the world (FAOSTAT, 2022a), being processed for a variety of food and industrial products, consumed mainly for human and animal food, and biofuel production (RANUM; PEÑA-ROSAS; GARCIA-CASAL, 2014). Brazil is an important world food supplier (BRANCO et al., 2021), the country is the third largest corn producer (FAOSTAT, 2022b) and is expected to be the second largest exporter in 2022/2023 (USDA, 2021, 2022). In the last two decades, corn production in Brazil has grown by 324%, reaching 102.59 million tons in the 2019/2020 harvest season (CONAB, 2022a), to meet growing domestic and foreign demand. However, the 2020/2021 harvest season had a production 15.5% lower than the previous one due to reduced productivity caused by adverse weather conditions (CONAB, 2021a).

Agriculture is a high-risk activity with significant uncertainty, these risks arise from unstable weather conditions, sanitary events, and market fluctuations

(KOMAREK; DE PINTO; SMITH, 2020). Globally, ~32–39% of agricultural yield variability is due to the variability of weather conditions, and in Brazil, the percentages are between 15% and 75%, depending on the regions and crop analyzed (RAY et al., 2015). Among the weather conditions that incur agricultural losses are droughts, heat waves, windstorms, hail storm and frosts (MONTEIRO, 2009). Frost can lead to poor yields and even complete crop failure depending on the phenological stage of the crop when the event occurs and its severity (CHOUDHURY et al., 2019).

Radiation frosts occur on clear nights when energy loss by longwave radiation from both soil and vegetation to space is greater from the upper layers of the crop compared with that occurring at the soil surface, as a result, the air temperature becomes coldest in the upper canopy (STUTSEL et al., 2020a). Frost damage is mainly caused by ice formation rather than low temperatures, which can be either extra-cellular or intra-cellular (RODRIGO, 2000). In severe frost, ice crystals in the intercellular space break down chloroplast structures and cause a rapid change in leaf biochemical constituents. In less severe frost, the plants' cells might not be damaged, but it can still affect the biochemistry and hence the absorption of light and the color of the leaves (CHOUDHURY et al., 2019). Frost tends to be unpredictable (CHOUDHURY et al., 2019), and its severity is spatially variable across regions and positions in the landscape (FITZGERALD et al., 2019). It can be influenced by local factors such as topography and terrain orientation, soil types, soil moisture, etc. (CADENAS et al., 2020; STUTSEL et al., 2020b). These factors, translates to crop frost damage being highly variable at inter- and intra-field scales (FITZGERALD et al., 2019).

In Brazil, frosts are more common in the center-south region, being more severe in the south (WREGE et al., 2018b). Among Brazil's crops affected by frost there are wheat, coffee, sugarcane, and corn (CONAB, 2021b). The second corn season is highly vulnerable to frost damage, as this crop may still be in the reproductive phase during frost-susceptible periods of the year. The consequences can be disastrous as the second crop season represents most of Brazil's corn production (73% of production came from the second crop season in 2019/2020 - CONAB, 2022). In 2021, two frost events, one on 25-May and the other on 30-June, caused great economic losses, affecting Brazilian production of sugarcane, coffee and corn (CONAB, 2021c). Although farmers have few options for crop protection from frost, monitoring the occurrence, impact, and spatial distribution of frost damage are important for agricultural agencies and individual farmers to adopt the measures necessary to mitigate production losses for food security and the economy (FITZGERALD et al., 2019; WANG et al., 2020; ZHAO et al., 2020). In Brazil, the CONAB is responsible for providing statistical information on Brazilian production, accounting for losses due to weather conditions such as frost. However, this is challenging due to the country's continental dimensions, soil and climate diversity, and high agricultural dynamics. In addition, the frost damage information produced by CONAB is not spatialized.

Remote sensing can provide objective information over large areas periodically, being one of the most promising sources of data for agricultural monitoring (CHAVES; PICOLI; SANCHES, 2020; WEISS; JACOB; DUVEILLER, 2020). Remote sensing has been used for frost damage assessment in several crops, such as oat (MACEDO-CRUZ et al., 2011), wheat (FITZGERALD et al., 2019),

grape (LIU et al., 2021), canola (DUDDU et al., 2018), rapeseed (JEŁOWICKI et al., 2020), and corn (CHOUDHURY et al., 2019). In corn, frost damage increased the reflectance in the photosynthetically active regions. At the same time, it caused a sharp decline in the near-infrared (between 720 and 1350 nm) and a shift in the red edge, also causing a decrease in the Normalized Difference Vegetation Index (NDVI) (CHOUDHURY et al., 2019). These changes in spectral reflectance could be identified in NDVI time series, allowing the identification of areas affected by frost damage. However, a similar pattern can occur as a result of the natural senescence of corn (PONZONI; SHIMABUKURO; KUPLICH, 2012). While there is a slight reduction in the values of vegetation indexes due to senescence (OLDONI et al., 2021b), frost damage causes an abrupt reduction in the time series (CHOUDHURY et al., 2019). Thus, to avoid confusion between frost damage and natural senescence, a dense satellite image time series is necessary to allow the acquisition of images soon after the frost event and identification of rapid changes in the time series.

The WFI onboard the CBERS-4, CBERS-4A and Amazonia-1 can provide dense time series data with a medium spatial resolution (55-64m). Combining the WFI data from the three satellites allows for a 1–3-day revisit time. WFI/CBERS-4 time series have recently been successfully used to map land use and land cover (PICOLI et al., 2020b; CHAVES et al., 2021b). Despite this, there are no works in the literature that used the combination of WFI data from the three satellites for applications in agriculture. Given the context presented, this work aims to map the extent of the corn frost damaged areas that occurred in the second crop

season of 2020/2021 in the west of the state of Paraná, Brazil, using the WFI time series.

8.2 Study site

The Paraná state, located in southern Brazil, is currently the second largest corn producer in the country. The state produced 15 million tons in the 2019/2020 harvest season, corresponding to 15% of the national production (CONAB, 2022b). In Paraná, two crops season are normally grown in one year. The first crop season occurs between spring and summer, from September to March. The second crop season that occurs between autumn and winter, from January to August, is the one that has a major production. In 2019/2020, the second crop season accounted for 68% of the state's corn production (CONAB, 2022b).

About 25% of Paraná's corn production was cultivated in the west region in the 2019/2020 harvest. We selected this region as our study area (Figure 8.1). In addition to the large corn production, this region was affected by a severe frost in the second season of the 2020/2021 harvest. The major soils in the region are Dystrophic Red Ultisols, Dystroferric Red Latosols, Eutrophic Lithological Neosols, Eutrophic Red Nitosols (EMBRAPA, 2011). The climate is subtropical mesothermal (Cfa), according to the Köppen classification, with average annual precipitation of 1200 - 1800 mm and an average annual temperature of 18.5 - 22.9 °C (APARECIDO et al., 2016). The altitude in the region ranges from 87 to 919 m (JARVIS et al., 2008).

Figure 8.1 – (a) Study site, Paraná state, Brazil. (b) Digital elevation from Shuttle Radar Topography Mission (SRTM) (Jarvis et al., 2008).
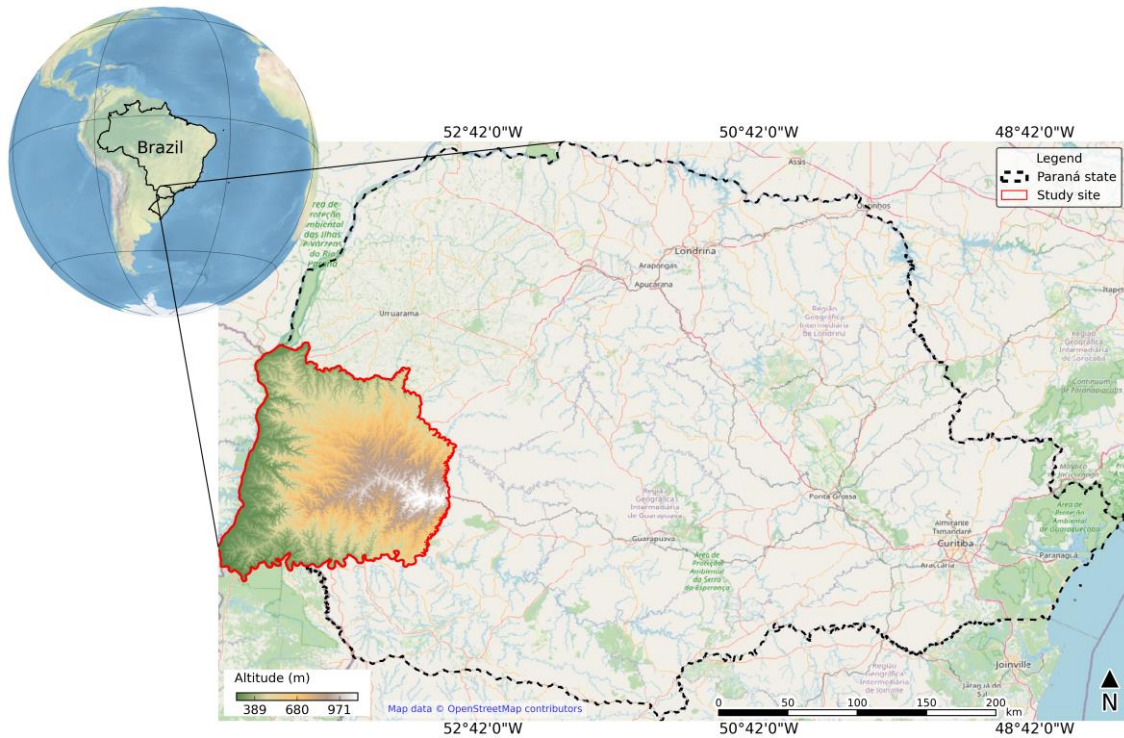
8.3 Remote sensing data acquisition

8.3.1 Wide-Field Imager (WFI) data

We selected all available WFI images from CBERS-4, CBERS-4A and Amazonia between February 1 to August 12, 2021, Level L4 that intersected the study area. A total of 57, 60, and 43 WFI images for CBERS-4, CBERS-4A, and Amazonia-1, respectively, were downloaded from the INPE website (http://www.dgi.inpe.br/catalogo/ and http://www2.dgi.inpe.br/catalogo/explore) at Level 4. The WFI Level 4 images provided by INPE are geometrically corrected with ground control points and ortho-rectified (INPE, 2021c). We use the surface reflectance product, which has been processed by the MS3 software (SILVA;

ANDRADE, 2013). The product is delivered in the Universal Transverse Mercator (UTM) projection with the World Geodetic System 1984 (WGS84) datum.

8.3.2 MultiSpectral Instrument (MSI) data

We used a cloud free mosaic of the Sentinel-2/MSI Level-2A (L2A) NIR band (B08) at 10 m from the study site as a reference for the co-registration of WFI images. The mosaic was composed using the median of the images with less than 5% of clouds between June 1st and 30th, 2021, in Google Earth Engine. The L2A product is radiometrically and geometrically corrected with ortho-rectification and atmospherically corrected to surface reflectance (ESA, 2015).

8.3.3 MODIS data

We downloaded MODIS MCD43A4 version 6 product for the study area on the same date as each WFI image from NASA's Land Processes Distributed Active Archive Center (LP DAAC) products located at the USGS Earth Resources Observation and Science (EROS) Center (https://lpdaac.usgs.gov/products). We only use the data from MODIS products referring to the spectral bands of blue (B3), green (B4), red (B1), and NIR (B2), which can be considered equivalent to the respective bands B13/B1 (blue), B14/B2 (green), B15/B3 (red) and B16/B4 (NIR) of the WFI data (CBERS-4 and -4A/Amazonia-1).

8.3.4 Corn map

The corn map used in this work was provided by Chaves et al. (In review). This map was generated using attributes derived from the surface reflectance of nine Sentinel-2/MSI spectral bands and three spectral indices calculated from them. The bands considered were band 3 (Green) to band 12 (SWIR) except the bands

9 (Water vapor) and 10 (Cirrus). And the indices used were the Normalized Difference Vegetation Index (NDVI) (ROUSE et al., 1974b), Normalized Water Difference Index (NDWI) (GAO, 1996), and Green Normalized Difference Vegetation Index (GNDVI) (GITELSON; KAUFMAN; MERZLYAK, 1996). The authors used matrix attributes (median, first and third quartiles, minimum and maximum values) monthly for the sowing and flowering periods and the total period for each variable in the Random Forest model. Their classification reached an overall accuracy (OA) equal to 0.96. For our analysis, we resampled the corn map from 20 m to 64 m, using the mode resampling algorithm, only for the areas identified as corn in the 2021 second crop season.

8.4 Methodology

Figure 8.2 shows the methodological flowchart of this chapter. Section 8.4.1 describes the pre-processing steps that include co-registration and cloud masking. Section 8.4.2 describes the two methods compared for normalizing the differences between inter-satellite WFI sensors. Sections 8.4.3, 8.4.4, and 8.4.5 describe the procedures for extracting phenological metrics, classification algorithm, and accuracy assessment of maps of corn frost damaged areas.

Figure 8.2 – Flowchart of Chapter 8. S2, C4, C4A and Am1 are Sentinel-2, CBERS-4, CBERS-4A and Amazonia-1, respectively.
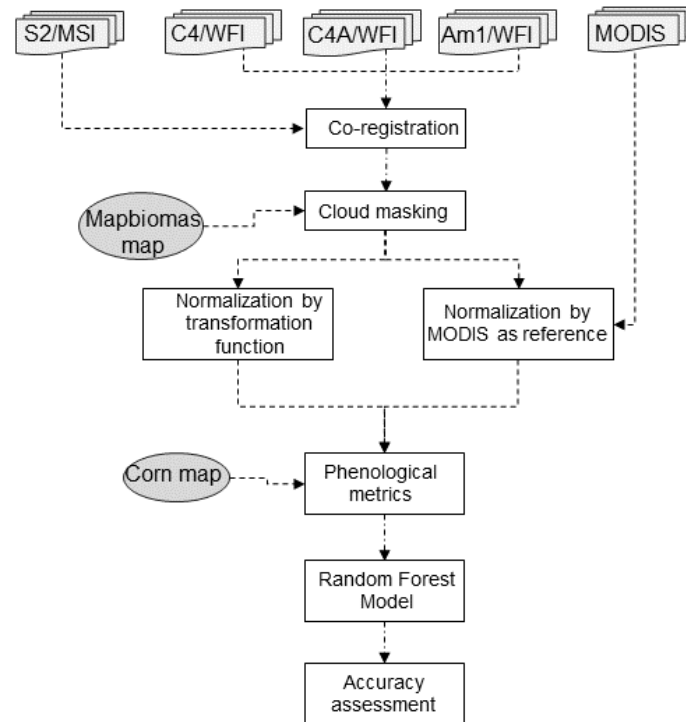
8.4.1 WFI data pre-processing

8.4.1.1 Co-registration

According to Chapter 5 the co-registration of WFI images is a fundamental step, as the images have displacement up to 1.45 pixels for CBERS-4/WFI and Amazonia-1/WFI and 2.5 pixels for CBERS-4A/WFI. We used the Sentinel-2/MSI mosaic with the NIR band at 10 m described in Section 8.3.2 as reference to co-register the WFI images. The MSI mosaics were generated in the same spatial reference system as the respective WFI images, i.e., UTM projection, using the correct UTM zone. We used the Python implementation of the Automatic and Robust Open-Source Image Co-Registration Software (AROSICS) (SCHEFFLER et al., 2017) to find control points (CP) that represent the

correspondence between the reference image (MSI) and the target image (WFI). We used a grid resolution and window size of 100 and 400 pixels in the AROSICS, i.e., looking for CPs every 100 pixels in an image subset of 400 x 400 pixels. We selected the 2nd-degree polynomial as a transformation function because it proved sufficient to reduce displacement in the WFI images (Chapter 5). After the transform function was created, the target image was warped using a cubic resampling technique. A transformation from UTM to AEA projection has also been added to the processing chain. This allows all images to have the same spatial reference system without additional resampling, avoiding undesired geometric and spectral image quality degradation.

8.4.1.2 Cloud mask

We applied the ATSA algorithm (Zhu and Helmer, 2018) to generate cloud masks and cloud shadows. ATSA uses image time series to mask clouds and cloud shadows. As there are differences between the WFI images of the three satellites (Chapter 7), we apply ATSA individually to the WFI time series of each of them. After co-registration, the WFI images of each satellite were stacked in a data cube. The elevation and azimuth solar angles information were extracted from the metadata. The ATSA requires a water mask. The water mask was extracted from the land use and land cover map produced by MapBiomas Collection 5 for 2019 (most recent data during data processing) (Souza et al., 2020). The MapBiomas map was reclassified to water and non-water and resampled to the spatial resolution of the WFI images using the mode resample algorithm. We set some parameters in the ATSA algorithm to generate the cloud and shadow cloud mask. First, the longest and shortest distance between the shadow and its

156

corresponding cloud was selected. These values were empirically set to 1 and 40 pixels (64 m and 2560 m, respectively) after the images' inspection, as Zhu and Helmer (2018) recommended. Two other parameters, A and B, are the thresholds used by ATSA to identify cloud and shadow, respectively. We set the parameters A and B equal to 0.5 and 3.0, respectively, because they successfully balanced omission and commission errors (Chapter 4).

8.4.2 WFI inter-satellite spectral normalization

Although the WFI sensors onboard CBERS-4, CBERS-4A and Amazonia-1 have similar characteristics, their surface reflectance may have differences, as shown in the previous Chapters. We tested two approaches to normalize the WFI data from the three satellites and generate a more consistent time series: (*i*) the first uses the MODIS MCD43A4 product as a reference; (*ii*) the second uses the transformation functions from WFI inter-satellite cross comparison derived in Chapter 7. These two approaches will be detailed in Sections 8.4.2.1 and 8.4.2.2.

8.4.2.1 WFI normalization using MODIS MCD43A4 as reference

The empirical normalization of the WFI using the MODIS product MCD43A4 as a reference was divided into two steps: (*i*) normalization as a function of the VZA, and (*ii*) spectral normalization.

8.4.2.1.1 WFI normalization as a function of the zenith view angle

Our results from Chapter 6 showed that the surface reflectance of WFI images is influenced by BRDF effects. Furthermore, there is a reflectance gradient introduced by the surface anisotropy and the variation of the VZA, which is approximately linear. This reflectance gradient can be removed using the linear

relationship between surface reflectance and the VZA (HANSEN et al., 2008; POTAPOV et al., 2012), as the results of Chapter 6 demonstrated.

BRDF effects depend on the land surface and the reflectance gradient can vary depending on the target. Therefore, we use the MODIS product MCD434A4 as a reference, as this product has already been normalized to nadir. The WFI images were resampled to 500 m using the pixels average to match the MCD43A4 resolution. All 500 m pixels within some CBERS-4/WFI pixels marked as cloud in the cloud mask were not considered. The mean difference between the MCD43A4 NBAR reflectance and the WFI surface reflectance was aggregated at every 1^0 of VZA. The reflectance gradient (α) was estimated for each band as the slope of the linear regression between the surface reflectance bias of MODIS and CBERS-4 (ρ) and the VZA (v) as follows:

$$\rho = \alpha\, v + \beta \tag{8.1}$$

A Random Sample Consensus (RANSAC) filter was used to detect outliers and eliminate them from the linear regression. The function (8.1 was fitted using Ordinary Least Squares (OLS) regression. After calculating the reflectance gradient, the α was used to remove the BRDF effects caused by the VZA variation. The WFI surface reflectance normalized to the nadir ($\rho_{WFI\,(v=0)}$) was calculated as follows (Equation 8.2):

$$\rho_{WFI\,(v=0)} = \rho_{WFI\,(v_{obs})} + \alpha\, v \tag{8.2}$$

8.4.2.1.2 Spectral normalization using MODIS as a reference

After normalizing the directional effects, spectral normalization was also performed using the MODIS MCD43A4 product as a reference. In this case, the

normalized surface reflectance for each band of each WFI image was cross compared with the NBAR MCD43A4 reflectance at 500 m. A transformation function was fitted to transform the WFI reflectance to the equivalent of the MODIS reflectance using OLS regression as follows:

$$\rho_{MODIS} = \rho_{WFI\,(v=0)} \times a + b \tag{8.3}$$

where a and b are the slope and intercept, respectively, of the OLS regression.

8.4.2.2 WFI normalization using inter-satellite cross-comparison transformation function

The WFI normalization using the inter-satellite cross-comparison transformation function is divided into two steps: (*i*) the BRDF effect is removed using the factor c; (*ii*) the application of the transformation functions derived in the previous chapter.

8.4.2.2.1 BRDF normalization

We selected the c-factor technique and the global coefficients provided by Roy et al. (2016) to remove the BRDF effects on the WFI imagens for this second approach. According to the results showed in the Chapter 6 it can also reduce directional effects in WFI images. The c-factor technique uses fixed BRDF coefficients for each spectral band. Normalized reflectance is calculated by multiplying the original reflectance by the c-factor (CLAVERIE et al., 2018) (Equation (8.4):

$$\rho(\lambda, \theta_n, v_n, \phi_n) = c\,(\lambda) \times \rho(\lambda, \theta_s, v_s, \phi_s) \tag{8.4}$$

The c-factor is calculated from the semiempirical kernel-driven RossThick-LiSparse Reciprocal BRDF model (SCHAAF et al., 2002), using two kernels, K_{vol} and K_{geo}, that describe volumetric and geometric scattering components, and three model parameters (Table 6.1) (8.5):

$$c(\lambda) = \frac{f_{iso}(\lambda) + f_{vol}(\lambda)\, K_{vol}(\theta_n, v_n, \phi_n) + f_{geo}(\lambda)\, K_{geo}(\theta_n, v_n, \phi_n)}{f_{iso}(\lambda) + f_{vol}(\lambda)\, K_{vol}(\theta_s, v_s, \phi_s) + f_{geo}(\lambda)\, K_{geo}(\theta_s, v_s, \phi_s)} \qquad (8.5)$$

where θ_s, v_s, ϕ_s represents the VAA, VZA e RAA from input data, and θ_n, v_n, ϕ_n represents the VAA, VZA e RAA of the normalized data. The VZA was set to nadir, the RAA was set to zero, and the SZA was set to 35° (Chapter 6).

8.4.2.2.2 Application of transformation functions

After the BRDF normalization, the transformation functions derived in Chapter 7 and presented in Table 7.3 were applied. In this case, the CBERS-4/WFI was used as a reference, i.e., the CBERS-4A/WFI and Amazonia-1/WFI images were converted to reflectance values equivalent to if they had been obtained by the CBERS-4/WFI.

8.4.3 Phenological metrics derivation

Severe frost causes changes in plants that are noticeable within one or two days. Among these changes is the increase in the reflectance of the blue and red regions of the electromagnetic spectrum and reduced reflectance in the NIR region, which causes a reduction in the NDVI value (CHOUDHURY et al., 2019). This abrupt change can be identified in a dense NDVI time series. To identify these changes, we derived phenological metrics. Phenological transition dates were derived by fitting a pre-defined curve from the NDVI values. An asymmetric

160

double sigmoid function was selected as the curve function (SOUDANI et al., 2008), and phenological variables were extracted either directly or indirectly (ZHONG et al., 2016a):

$$V(t) = V_b + \frac{1}{2}V_a\big[\tanh\big(p(t - D_i)\big) - \tanh\big(q(t - D_d)\big)\big] \qquad (8.6)$$

where $V(t)$ is the NDVI time series. Metrics extracted directly or indirectly from the curve fit are described in Table 8.1. The curve fitting was carried out using the Levenberg-Marquardt algorithm (MORÉ, 1978) available in *SciPy* library (VIRTANEN et al., 2020). Only phenological metrics related to the end or duration of the cycle were used. These were the sets of attributes used in the Random Forest classifier.

8.4.4 Classification algorithm

We consider four classes in the classification process: (*i*) *Frost damage 25-May*, the areas affected by frost on May 25, 2021; (*ii*) *Frost damage 30-June*, the areas affected by frost on June 30, 2021; (*iii*) *Harvested/senescent*, areas that were already senescent or were harvested during frost events; and (*iv*) *Not frost damage*, areas that were not affected by any of the frosts and that were not in senescence or have been harvested. The training samples were generated based on analysis of the WFI NDVI time series and the multi-temporal false-color composites (NIR-red-green) from before and after frost events, i.e., May 23; June 12 and 30; July 2, 7, and 22, 2021.

Table 8.1 Metrics extracted directly or indirectly from NDVI curve fitting.

Phenological metric	Description	Use in the classification
V_b	Base value corresponding to the non-growing period	Not used
V_a	Amplitude of variation (the difference between the maximum and minimum NDVI with the growing cycle)	Not used
p, q	rate of change of the increasing and decreasing segments in the cycle	Only q was used. In frost-damaged areas the rate of change of the decreasing segment is higher than in unaffected areas
D_i, D_d	The dates when the increasing or decreasing rates (first derivative) of the NDVI time series are maximum	Only D_d was used. In frost-damaged areas Dd is closer to the frost event date
D_1, D_2, D_3, D_4	Four dates when the second derivative of the curve reaches the local maximum or minimum	Only D_3 and D_4 were used. D3 indicates the date that the fitted NDVI curve starts to decrease. In frost damaged areas D3 is close to the frost event
Lgs	Difference between D_4 and D_1 representing the length of the growing season	The duration of the growing season has been reduced in frost-damaged areas
Lhvp	Difference between D_3 and D_2	D3 generally occurred earlier in frost-affected areas, which shortened the time between D_2 and D_3
D70, D90, D90, D95	Dates of the 70th, 80th, 90th, and 95th percentiles of the NDVI values between D_3 and D_4	Indicates the dates that the NDVI reached certain decreases. In frost-damaged areas, these dates are close to frost events.
Slope	Slope of the line between points D3 and D4	In frost-damaged areas the slope is lower than in unaffected areas.

Source: Adapted from Zhong, Gong and Biging (2012); Zhong et al., (2016a;b).

162

We used the Random Forest (RF) model (BREIMAN, 2001) from the implementation in the *Scikit-learn* library (PEDREGOSA et al., 2011). RF classifier is a machine learning ensemble classifier that produces multiple decision trees from a randomly selected subset of training samples and variables (BELGIU; DRĂGU; DRĂGUŢ, 2016). Each tree is independently created during the training process using bootstrap samples from the training dataset (Reis et al. 2020). The final classification decision corresponds to the averaged (using the arithmetic mean) class assignment probabilities calculated by all individual decision trees (BELGIU; DRĂGU; DRĂGUŢ, 2016). To classify new unlabeled data, it is evaluated against all decision trees created in the ensemble and each tree votes for the membership class, with the most voted membership class being the one selected in the final output (BELGIU; DRĂGU; DRĂGUŢ, 2016). RF has the ability to deal with small sample sizes, process high-dimensional feature spaces and not overfit (GERGELY DAROCZI, 2015; BELGIU; DRĂGU; DRĂGUŢ, 2016; BIAU; SCORNET, 2016a). The popularity of RF comes from the fact that it can be applied to solve a wide range of prediction problems (BIAU; SCORNET, 2016a). Furthermore, RF has shown good performance in remote sensing application (PELLETIER et al., 2016; SANTOS et al., 2019; NGUYEN et al., 2020; CHAVES et al., 2021b; OLDONI et al., 2021a). Each node of each decision tree in the RF is split using a user-defined number of features (*max_features*) selected at random, and the forest grows up to a number of tree (*n_estimators*), allowing to create trees with high variance and low bias (BELGIU; DRĂGU; DRĂGUŢ, 2016). The *n_estimators* was set to 100, the function to

measure the quality of a split (*criterion*) was set to gini, and the *max_features* was set to the default value, i.e., square root of the total number of features.

8.4.5 Accuracy assessment

To perform the classification accuracy assessment, we sampled stratified random points across the study site. The goal of stratified random points is to have a practical design that satisfies the accuracy measurement objectives and most of the desirable design criteria (PRUDENTE et al., 2022). The number of points was weighted by the areas of each class and the expected accuracies following the good practices of assessing accuracy proposed by Olofsson et al. (2014). The sample size was increased in the classes that occupy a small proportion of the area to reduce the standard errors of the class-specific accuracy for these classes. Thus, 632 random sample points were distributed stratified according to *Harvested/Senescent*: 102; *Frost damage May-25*: 75; *Frost damage June-30*: 365; and *Not frost affected*: 90. The points were labeled based on analysis of the WFI NDVI time series and the multi-temporal false-color composites (NIR-red-green) from before and after frost events, i.e., May 23; June 12 and 30; July 7, 2021. The interpreter did not access the sample class to avoid any influence and possible bias.

After, these points were used as validation points to create an error matrix. These validation points are independent of the training samples. The overall accuracy (OA) derived from the error matrix was computed to evaluate the classification accuracy. The producer's accuracy (PA), which indicates the likelihood that a pixel in a given class was classified correctly, and the user's accuracy (UA), which

indicates the likelihood that a pixel classified on the map represents that class on the ground (CONGALTON, 1991), were also calculated.

8.5 Results and discussion

8.5.1 Spectral normalization of the WFI time series

We used two approaches to normalize the WFI data and generate a consistent time series. In the first, the WFI surface reflectance values of the three sensors were normalized using the MODIS MCD43A4 product as a reference. The MCD43A4 product already has normalization of the VZA to nadir, which allows it to be used as a reference. Figure 8.3 shows the scatter plots between WFI surface reflectance from CBERS-4 (Figure 8.3a-b) and Amazonia-1 (Figure 8.3c-d) versus MODIS MCD43A4 reflectance for the red (Figure 8.3a-c) and NIR bands (Figure 8.3b-d) from June 30, 2021. The scatter plots in Figure 8.3 exemplify the differences between the WFI surface reflectance from the sensor onboard CBERS-4 and the Amazonia-1. As the images were acquired on the same day, no differences in surface reflectance were expected. However, in the NIR band, while the CBERS-4/WFI surface reflectance values are generally higher than the MCD43A4 product, the Amazonia-1/WFI is lower. In the red band, both WFI reflectance values are greater than the MCD43A4 product, but the Amazonia-1 is further from the 1:1 line.

Figure 8.3 – Scatter plots of WFI surface reflectance from CBERS-4 (a-b) and Amazonia-1 (c-d) versus MODIS MCD43A4 product for bands red (a-c) and NIR (b-d). WFI images and MODIS MCD43A4 product from June 30, 2021. Regression was fitted by ordinal least square (OLS) regression. The black dashed line represents 1:1 line, and the red dashed one is the regression line. RMSD is Root Mean Square Deviation.
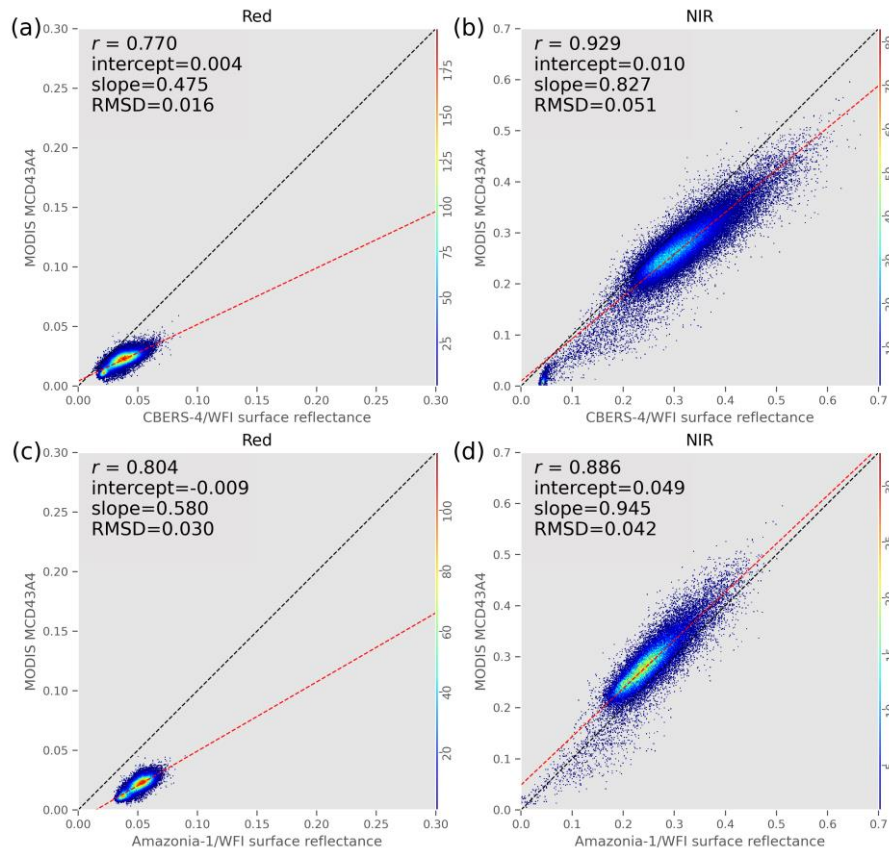
The differences in surface reflectance in the red and NIR bands between the WFI sensors of the three satellites cause discrepancies in the NDVI time series (Figure 8.4). On most dates, before normalization, the NDVI from Amazonia-1/WFI is smaller than the NDVI from CBERS-4 and CBERS-4A. After spectral normalization with the first approach, i.e., using coefficients fitted using OLS regression taking MODIS MCD43A4 as a reference, the difference among NDVI of the WFI from the three satellites was reduced (Figure 8.4a). The NDVI values became higher after spectral normalization, probably due to differences in the

166

spectral response function between WFI and MODIS. This approach also reduces the range between the highest and lowest values after normalization. The NDVI time series became more consistent after spectral normalization, with the variations being due to the target and not the difference between the sensors.

The second approach, which uses transformation functions fitted from OLS regression from WFI inter-satellite cross-comparison (Chapter 7), also reduced the differences in NDVI values between the WFI sensors (Figure 8.4b). However, the time series is noisier than the one derived from normalization using MODIS as a reference. The same coefficients are applied to all images using transformation functions derived from cross-comparison between WFI sensors. The incorrect characterization of the atmosphere condition on some dates may contribute to differences in some images in the time series. Whereas, when using MODIS as a reference, the WFI reflectance is converted to the equivalent reflectance of the MCD43A4 product. This is a consolidated product, with high quality and consistency over time. Even so, the second approach which uses transformation functions fitted from WFI data itself does not change neither the maximum values nor the amplitude of the NDVI values of the time series.

The time series of a corn pixel affected by the frost on June 30, 2021, is plotted in Figure 8.4. After this date, an abrupt drop in NDVI values can be observed, due to the damage to the corn leaves caused by frost. These markers in the NDVI time series can be quantified by extracting phenological metrics through curve fitting and inflection points, as will be discussed in the next section.

Figure 8.4 – Frost damage NDVI time series from WFI of CBERS-4, CBERS-4A e Amazonia-1 before and after spectral normalization using MODIS as reference (a) or using transformation function from inter-satellite cross-comparison (b). The dotted black line indicates the post-frost period. No filtering process was applied to the NDVI time series.
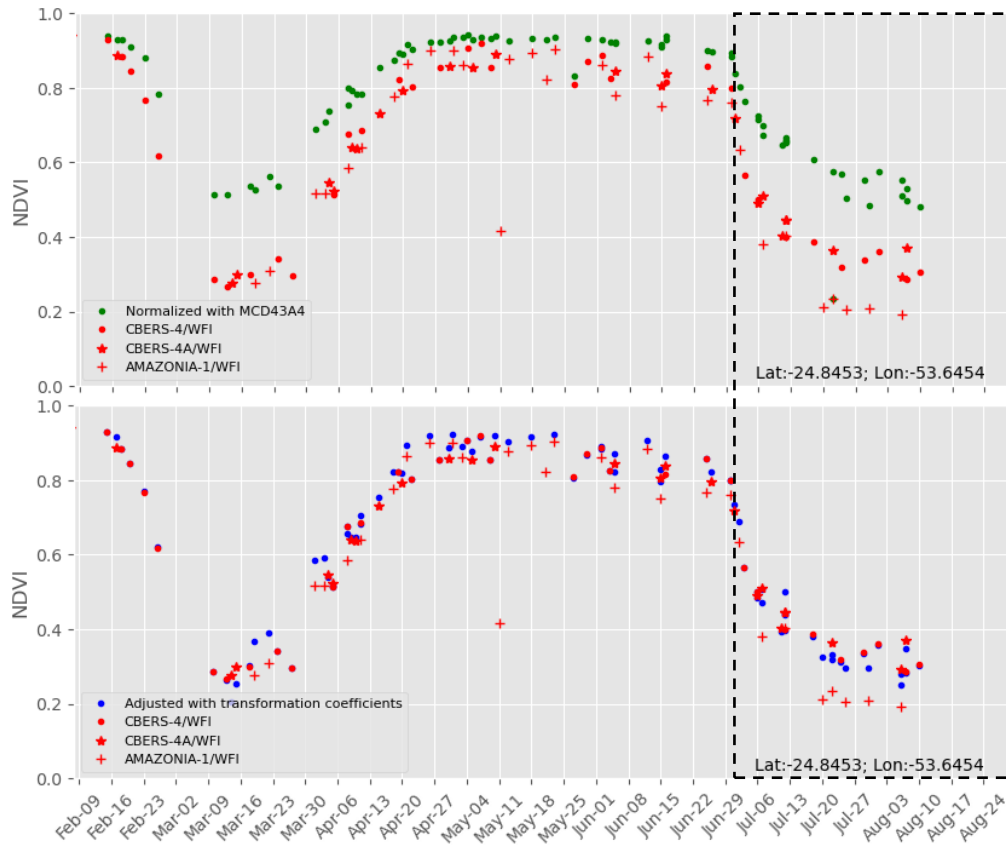
8.5.2 Curve fitting and phenological metrics

Fitting the asymmetric double sigmoid function to NDVI time series of WFI normalized data (Figure 8.5a-d, Figure 8.6a-d) allowed to extract of six phenological metrics directly and ten indirectly (but only the metrics related to the middle to the end of the growing season were used) (Figure 8.5e, Figure 8.6e). *Harvested/Senescent* (Figure 8.5a and Figure 8.6a) and *Frost damage 25-May* (Figure 8.5c and Figure 8.6c) classes had differences between the time series fitted with normalized data using MODIS as a reference and using transformation

168

functions from WFI inter-satellite cross-comparison. In both classes the fall of the fitted NDVI values is smoother in the normalized data using MODIS as a reference, and this happened due to the reduced amplitude of the time series fitted to these data. This can also be seen in the q and slope metrics (Figure 8.5e and Figure 8.6e). The q is larger, and the slope is smaller in the data normalized using the transformation functions compared to the normalized data using MODIS as a reference, indicating a more abrupt drop in the NDVI fitted for these two classes.

Despite these differences, in the fitted NDVI time series from both approaches of normalization, frost damaged pixels have an abrupt drop right after the respective frost events (Figure 8.5c-d, Figure 8.6c-d). The fitted time series of pixel that were already going into senescence when the 25-May frost occurs has a smooth drop in NDVI values (Figure 8.5a, Figure 8.6a). The same occurs with the pixel that is not affected by any frost, but in this case the reduction of NDVI values only starts a few weeks after the 30-Jun frost (Figure 8.5b, Figure 8.6b). The areas that were damaged by the 25-May frost (in dark green tones in the false color composition of 02-Jun-2021 - Figure 8.5e, Figure 8.6e) are in micro relief with lower altitude (Figure 8.5, Figure 8.6 – SRTM). The areas that were not affected by any frost (in shades of red in the false color composition of 07-Jul-2021 - Figure 8.5e, Figure 8.6e) are mostly located in the highest portion of the micro relief.

Figure 8.5 – Four examples of fitted curve from the NDVI time series of WFI normalized using the MODIS data as reference for: (a) a pixel of *Harvested/senescent*, (b) *Not frost damaged*, (c) *Frost damage 25-May*, and (d) *Frost damage 30-June*. (e) Zoomed raster: WFI false-color composite (R: NIR, G: red, and B: green) for 23-May-2021, 02-June-2021, 30-June-2021, and 07-July-2021; the SRTM digital elevation model; and ten phenological metrics. The figure highlighted four points representing the four analyzed classes (*Frost damage 25-May*, *Frost damage 30-June*, *Harvested/senescent*, and *Not frost damage*).
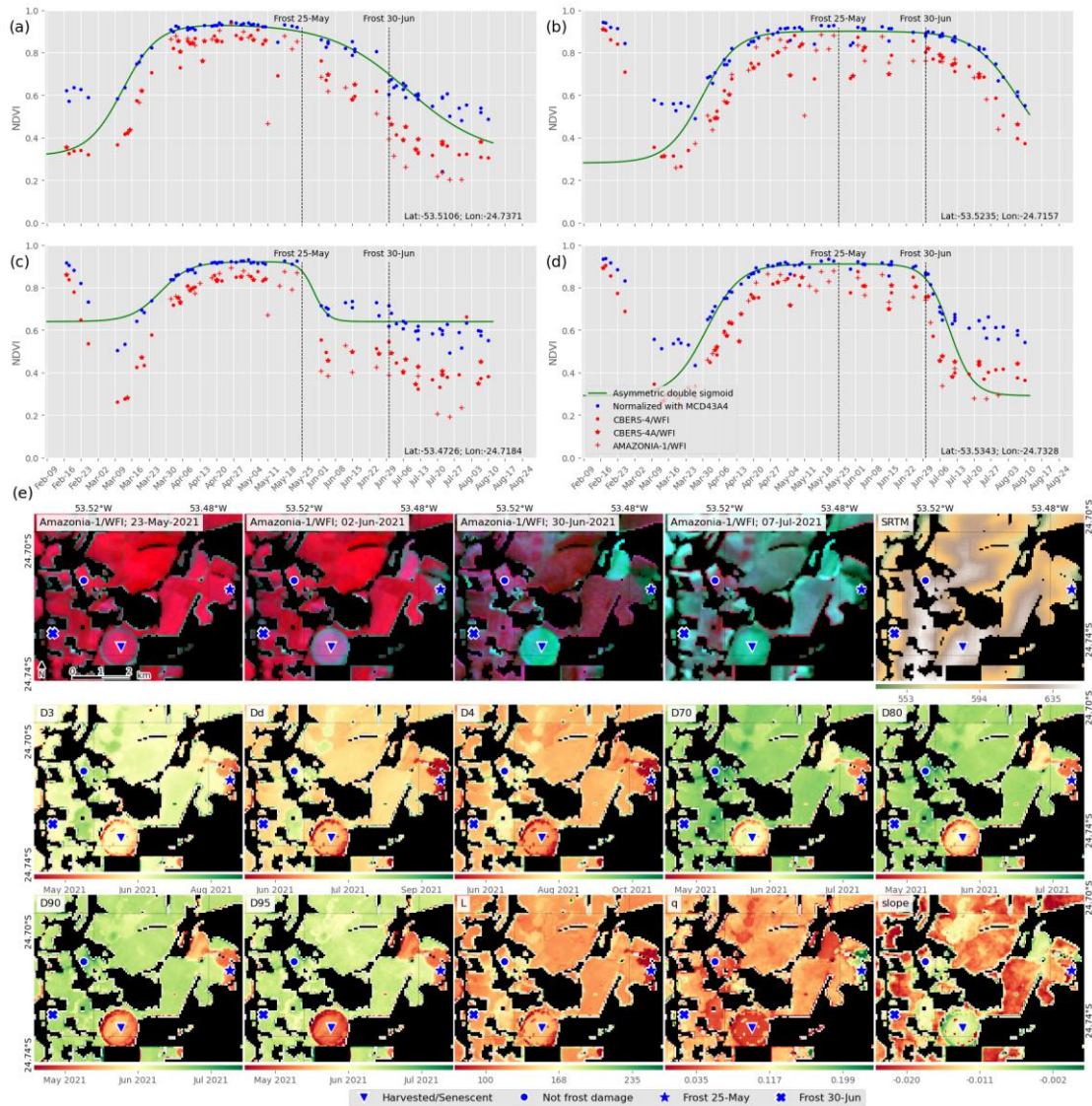
Figure 8.6 – Four examples of the fitted curve from the NDVI time series of WFI normalized transformation function fitted from WFI images itself for: (a) a pixel of *Harvested/senescent*, (b) *Not frost damaged*, (c) Frost *damage 25-May*, and (d) *Frost damage 30-Jun*. (e) Zoomed raster: WFI false-color composite (R: NIR, G: red, and B: green) for 23-May-2021, 02-June-2021, 30-June-2021, and 07-July-2021; the SRTM digital elevation model; and ten phenological metrics. The figure highlighted four points representing the four analyzed classes (*Frost damage 25-May*, *Frost damage 30-June*, *Harvested/senescent*, and *Not frost damage*).
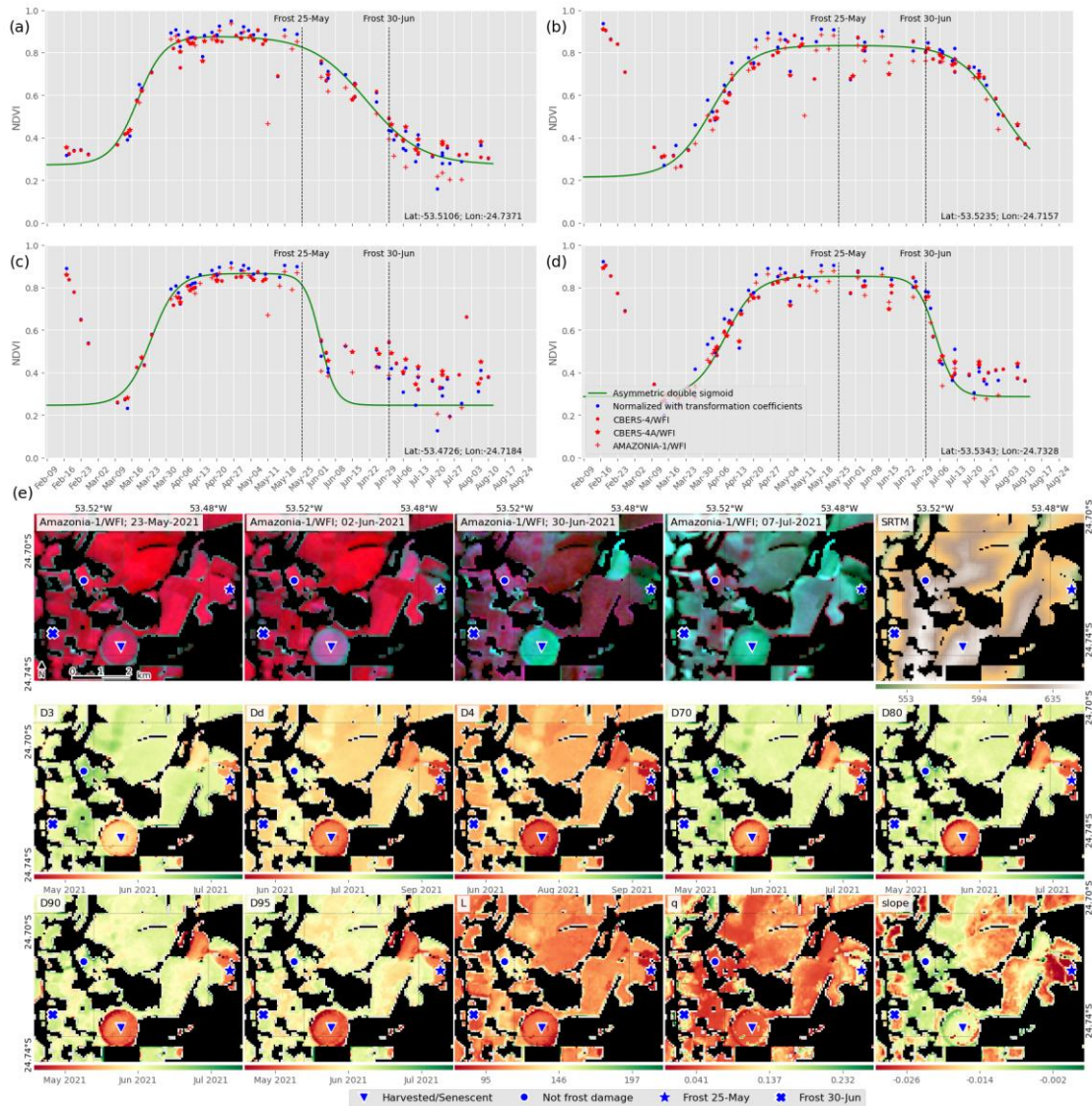
D3, which represents the date when the NDVI starts to decrease, still occurs in May for the areas affected by the frost on May 25th. While in the areas that have not been affected by any frost, it only occurs in July. A similar pattern occurred

with Dd and D4, but with a delay relative to D3. It is noticed that the cycle duration (Lgs) of the areas affected by the frost on May 25th is reduced concerning the other areas. This is expected, as the frost occurred prematurely, interrupting the corn phenological cycle. The area that was in senescence when the frost occurred on May 25th (pivot field area) has similar Dd and D4 values to the areas affected by the frost on June 30th. The same occurred for the metrics D80, D90, and D95, they had similar values to the areas damaged by the frost on May 25th. This could cause confusion during the classification. However, the q values are lower and the NDVI slope is higher, which indicates a smoother reduction of the NDVI value, similarly to what occurred with the areas that were not affected by any frost event. The combination of these metrics allows the separation of the four classes using the Random Forest model, as will be discussed in the next section.

8.5.3 Frost damage map

The spatial distribution of the frost-affected areas is similar in the maps generated from the fitted NDVI WFI time series normalized using MODIS as a reference (Figure 8.7a) and normalized using the transformation functions derived from the WFI inter-satellite cross comparison (Figure 8.7b). The classification that uses the normalized WFI time series as input using MODIS as a reference identified more areas as harvested/senescent, mainly in the southwest and northwest portions of the study region. These two regions have in common the recurrence of clouds during the analyzed period. Thin clouds cause NDVI reduction, and the omission of these clouds in the cloud mask on the dates before the frost caused

a smoother drop in the fitted NDVI value. The omission of thin clouds combined with the amplitude reduction in the NDVI time series normalized using MODIS as a reference caused this misclassification of frost affected areas as harvested/senescent.

In the two WFI time series normalization approaches, the areas not affected by frost are located mainly in the north and west (Figure 8.6a-b) of the study region and in the places with the highest topography (Figure 8.6c-e). The latitude to the north is higher, which makes this region warmer than regions in further south (APARECIDO et al., 2016). The west region is on the shores of Lake Itaipu. These two regions (north and west) have the lowest altitudes in the study site (Figure 8.1) and are less prone to frost (WREGE et al., 2018a). This is probably linked to macroclimatic factors, in which regions with lower altitudes are generally less cold and less susceptible to frost (PEREIRA et al., 2002).

From the total corn area, 69.7% was mapped as frost damaged in the approach that uses the normalized NDVI WFI time series as input using MODIS as a reference. In comparison, 72.4% was mapped as frost damaged in the approach with the WFI data normalized using the transformation functions. Only ~2.4% of the corn areas were damaged by the frost on May 25th in both approaches, while the rest of the damaged corn was affected by the June 30th frost. The May 25th frost mainly damaged the corn in the lower regions of the microrelief. This can be seen in the changes in the lower areas (Figure 8.7c - SRTM) between the May 23th image and June 2nd image (Figure 8.7c). Topo climatic factors can explain this effect, because the denser and colder air is deposited in the lower regions,

mainly in river valleys (PEREIRA et al., 2002). Areas damaged by the June 30th frost changed from shades of red to cyan between June 30 to July 7 images. In the June 30, 2021 image it is not possible to see the effects of the frost that occurred on that day (Figure 8.7c-e). Areas that have not been affected by any frost are still shaded red in all four images. The areas in senescence or harvested did not show changes in the images before and after the frost events.

Figure 8.7 – Frost damage map with WFI time series (a) normalized using MODIS as reference and (b) normalized using transformation function derived from WFI inter-satellite cross-comparison, and three zooming locations. All WFI images are false-colour composites (R: NIR, G: red, and B: green). Scale bar from SRTM in meters.
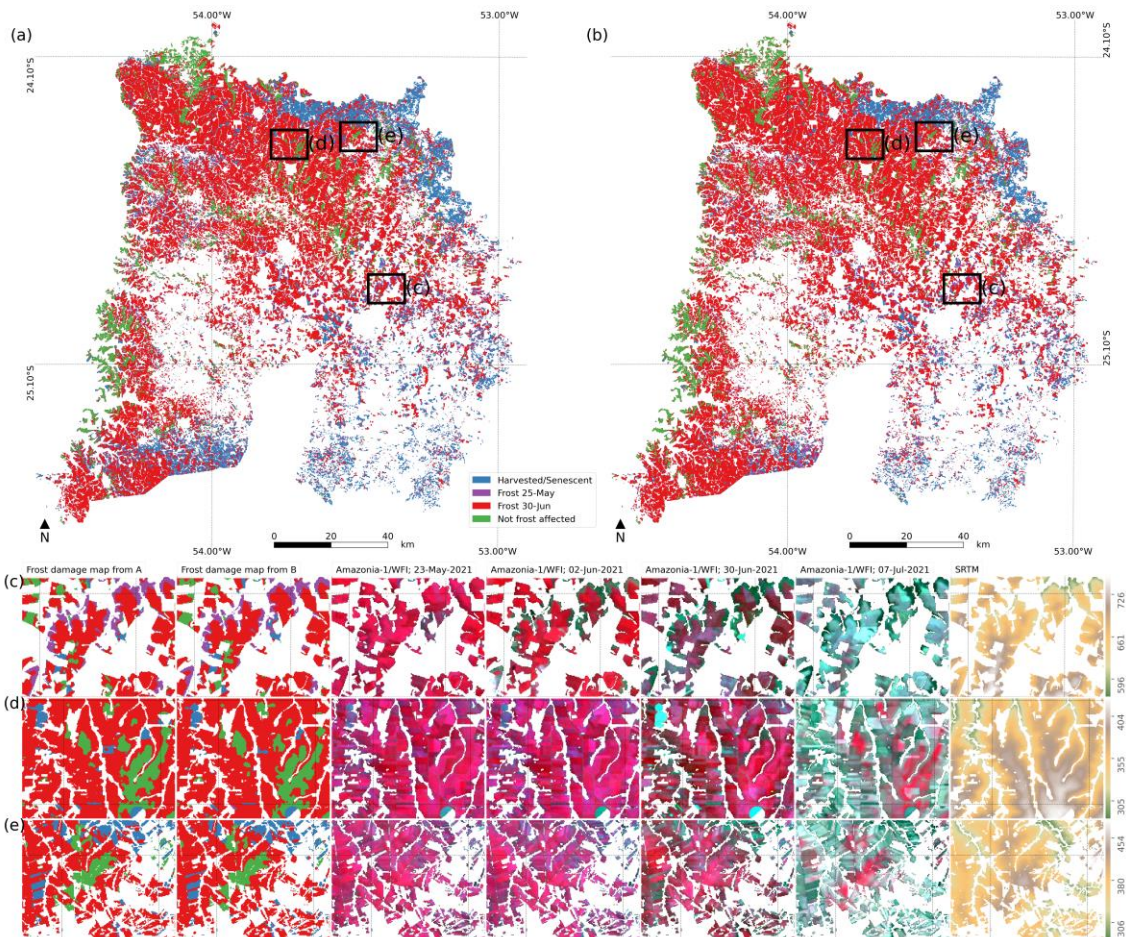
The rate of change of the NDVI decrease (*q)* was the most important variable used by Random Forest model when the WFI NDVI time series was normalized

using MODIS as a reference, and the second more important when the input data was normalized using the transformation function derived from WFI inter-satellite cross-comparison (Figure 8.8). Frost breaks down chloroplast structures and causes a rapid change in leaf biochemical constituents causing an increase in reflectance in the photosynthetically active regions. In contrast, it caused a decline in the near-infrared region (Choudhury et al., 2019). The increase in red reflectance and the decrease in infrared reflectance cause an abrupt drop in NDVI shortly after frost. This causes a high rate of change in the decrease of the NDVI, i.e., high value of q. In areas where corn senescence occurred naturally (areas that did not have frost damaged or were already harvested), the decrease in NDVI is smoother, with lower values of q. Dd was the most important variable for Random Forest model when the WFI input data were normalized using the transformation function from WFI inter-satellite cross-comparison. Dd is related to q, as it is the date when the maximum rate of the adjusted NDVI decline occurred. Another important variable in both approaches was the D70. While D80 was the second most important variable for the approach in which the data was normalized with MODIS, D3 was the third most important variable in the approach where the data was normalized with the transformation functions. D70, D80, and D3 are metrics related to the dates when there was a percentage of NDVI decline, or the start of the inflection point for NDVI decline, in frost damaged areas this occurs shortly after the frost event. Combining these metrics allowed the separation of frost-damaged areas from unaffected areas.
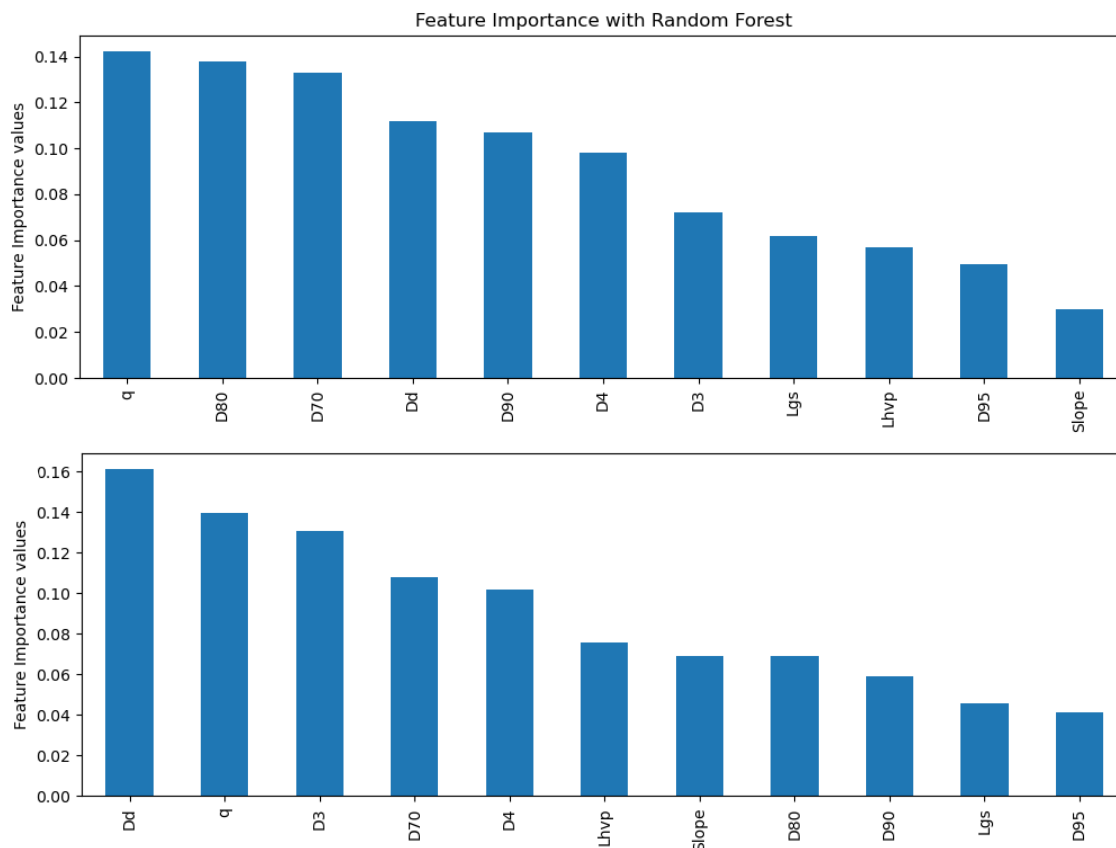
According to the classification accuracy analysis using phenological metrics derived from WFI NDVI time series normalized with MODIS as a reference as input for the Random Forest model, the result had an overall accuracy of 0.93 (Table 8.2). Producer (PA) and User (UA) accuracy were greater than 0.88 for all classes, except the AU for *Harvested/Senescent,* which was equal to 0.78. This class's biggest confusion was for areas misclassified as damaged by the June 30 frost. There was also confusion between areas of the *Not affected* class being classified as *Frost damage 30-June* class.

Table 8.2 – Error matrix for corn frost damages classification by frost, in 2021, in western Paraná, using WFI normalization with MODIS as reference.

| | | Reference | | | | | |
		Harvested/ Senescent	Frost 25-May	Frost 30-Jun	Not affected	Total	UA
Classification	Harvested/ Senescent	80	5	12	5	102	0.78
	Frost 25-May	2	70	2	0	75	0.95
	Frost 30-Jun	0	0	360	5	365	0.99
	Not affected	2	0	9	79	90	0.88
	Total	84	75	383	89	OA	
	PA	0.95	0.93	0.94	0.89	0.9334	

The classification that used as input the phenological metrics derived from the WFI NDVI time series normalized applying the transformation functions from WFI inter-satellite cross-comparison reached overall accuracy of 0.96 (Table 8.3). UA and PA were greater than 0.90 for all classes. In this approach, the biggest confusions were also from frost damaged areas classified as the *Harvest/Senescent* class. However, in this approach there was more confusion of areas damaged by the May 25 frost than by the June 30 frost misclassified as *Harvest/Senescent*.

Table 8.3 – Error matrix for corn frost damages classification by frost, in 2021, in western Paraná, using WFI normalization with transformation function.

| | | Reference | | | | | |
		Harvested/ Senescent	Frost 25-May	Frost 30-Jun	Not affected	Total	UA
Classification	Harvested/ Senescent	92	5	4	1	102	0.90
	Frost 25-May	2	71	2	0	75	0.95
	Frost 30-Jun	5	0	357	4	366	0.98
	Not affected	0	0	2	88	90	0.98
	Total	99	76	365	93	OA	
	PA	0.93	0.93	0.98	0.95	0.9605	

Classification errors may be related to poor curve fitting of the NDVI time series that leads to the extraction of phenological metrics that do not adequately represent the events that occurred in the field. They may also be related to errors in the corn mask used. These two factors may explain the difference in accuracy between the maps generated by the two data normalization approaches. The normalized time series using MODIS as a reference has a smaller amplitude between the maximum and minimum values of NDVI. Combining this with the incorrect identification of clouds in the cloud mask led to a more similar curve fit between some classes in some cases, which caused misclassification. The difference in resolution between the used corn mask, which was generated based on Sentinel-2/MSI at 10 m, and the WFI images (64 m) can also be a source of error because the fields edges there may be spectral mixing with other classes, generated by resampling.

Our approach allowed us to spatially identify crop areas damaged by each of the two-frost events that occurred in western Paraná. The frost on May 25, 2021, affected the corn in earlier stages of the reproductive stage, grain filling, and

maturation. The frost on June 30, 2021, affected the corn in the final stages of grain filling, maturation, and other fields already in the harvest phase. The damage caused by frost is greater at earlier stages than closer to harvest. Corn productivity in the second crop in Paraná felt from 5684.00 kg ha^{-1} in the 2019/2020 crop to 3340.57 kg ha^{-1} in the 2020/2021 crop (CONAB, 2022b), due to two frost events and a drought that occurred in the region.

Frost, as well as other disasters, can negatively affect agriculture's growing cycle and production. In this way, data related to frost monitoring in crops can support decision-making and inform policy interventions and market transparency, especially for major commodity crops such as corn. Furthermore, corn is the basis of many people's diets, and a large part of the corn produced in Brazil is exported. Therefore, the negative effects of a lack of monitoring and poor management of agricultural land in Brazil can have a dangerous impact on food security in many other countries. Therefore, the results generated with the methodology proposed in this work can help the corn crop condition monitoring. Our approach can be extended to other regions in the future to identify the corn phenological phase during the frost event and the areas that are susceptible to frost damage.

8.6 Conclusion

In this work, we mapped the corn areas damaged by the frosts that occurred in May and June 2021, in western Paraná, using the Random Forest model and as input phenological metrics extracted from the NDVI time series from the WFI sensor onboard CBERS-4, CBERS-4A and Amazonia-1. Two approaches were used to normalize the WFI data from the three sensors into a more consistent

179

time series. The first uses the MODIS sensor as a reference. The second uses transformation functions derived from WFI inter-satellite cross-comparison. The two approaches managed to reduce the difference between the WFI sensors of the three satellites. However, the first approach, despite being able to reduce the difference between sensors better, also reduced the amplitude of NDVI values.

The phenological metrics extracted from the NDVI time series of the two WFI data normalization approaches allowed the Random Forest model to identify areas affected by frost. The overall accuracy of the classifications was 0.93 and 0.96 for the normalization approach using MODIS as a reference and the transform functions, respectively. The biggest confusions were in areas damaged by frost misclassified as harvested/senescent, mainly in the normalization approach that uses MODIS as a reference.

Our approach allowed us to identify the corn areas damaged by the two frost events in 2021 in western Paraná using WFI data from CBERS-4, CBERS-4A, and Amazonia-1. The approach can be expanded in the future to identify the corn phenological stage when it is affected by frost, thus allowing improvement in frost damage monitoring and production estimates.

Corn monitoring in Brazil is essential for government services dealing with the import and export of this commodity, corn producers, agencies with a role in food relief, international organizations that monitor the world food production, and commodity traders. An adequate monitoring system that provides information regarding productivity losses can help combat food security with strategic

planning in the country and other countries since Brazil is the second largest corn

exporter.

9   OVERALL DISCUSSION

Agricultural monitoring requests RS data with a high revisit frequency to generate dense SITS. The combination of WFI data from sensors onboard the CBERS-4, CBERS-4A and Amazonia-1 satellites can generate dense SITS, reaching a revisits frequency of 1-3 days over Brazil. However, several factors can cause differences in surface reflectance between sensors. These factors need to be evaluated and minimized so that variations in reflectance or derived spectral indices are due only to changes in the target or agricultural crop. Therefore, allowing the generation of consistent SITS and the development of studies whose objective is to analyze and compare targets over time.

An accurate and reliable cloud mask is mandatory for effective EO optical imagery exploitation and time series analysis (REWEHEL; LI; KESHK, 2022a). However, WFI sensors only have four spectral bands making accurate cloud and cloud shadow detection quite difficult. Furthermore, few cloud and cloud shadow detection algorithms are compatible with sensor data that have a limited number of spectral bands. Nonetheless, it is important to understand the strength and limitations of each of these algorithms. When comparing the CMASK and ATSA algorithms, our results showed that CMASK has high reliability in detecting clouds, i.e., almost all pixels identified as clouds are actually clouds (UA close to 100%). However, the algorithm also has a high omission rate of cloud pixels (PA ~70%) misclassifying them as clear pixels. In comparison, the ATSA brings more balanced results between omission and commission errors. In regions or areas with low availability of clear pixels, CMASK may be better, as it practically does

not mislabel clear pixels as clouds. However, unidentified cloud pixels in the cloud mask generally bring noise to the time series, which can generate worse results in its applications (OLDONI et al., 2021a). In this case, ATSA may be more suitable as it can better identify shadows and cloud shadows. Algorithms based on deep learning have brought advances in cloud identification (LI et al., 2019a; REWEHEL; LI; KESHK, 2022b) and may be an option to obtain more accurate cloud masking and cloud shadows for the WFI images in the future.

Second, precisely co-registered images are extremely important for combining data from different sensors and for time series analysis (GAO; MASEK; WOLFE, 2009). In this sense, it is necessary to know the geometric accuracy of the images. When co-registration between bands was evaluated, the results showed average RMSE of spatial shifts close to specifications (0.3 pixel; EPIPHANIO, 2009). Thus, it was decided not to perform the correction of the band-to-band detected displacement, considering that additional resampling induces an alteration in the pixel value (SCHEFFLER et al., 2017). However, when assessing the geometric accuracy between multitemporal WFI data and using Sentinel-2/MSI data as a reference, large displacements were observed, reaching 1.45 pixels (93m) for CBERS-4/WFI and Amazonia-1/WFI, and 2.5 pixels (138 m) for CBERS-4A/WFI. These large displacements can lead to degradation of results when combining data from three WFI sensors and also for time series analysis. Thus, a framework for automatically correcting these displacements was introduced. After the co-registration procedures, the geometric accuracy of the images was improved, reaching an average RMSE of spatial shifts on a tile basis of 0.29±0.05. In addition, our approach of the co-registration avoid additional

resampling of the images, that reduce the pixel values degradation, and allowing to align the images in regular grids, as required for the data cubes generation (FERREIRA et al., 2020). The image registration is required for further time series analysis of WFI images in several applications that require precise sub-pixel registration, but mainly for targets spatially heterogeneous such as agriculture.

Angular effects can occur as a function of the view angle and changes in the solar illumination vector as most surfaces are not Lambertian. These effects can bring differences in surface reflectance even in images of the same date and location when observed by different sensors or over time in the time series. The WFI images presented angular effects both as a function of the VZA and as a function of the change in the vector of solar illumination (SZA). All approaches tested were able to reduce the effects from directional effects, while only those using full BRDF normalization were able to reduce the SZA effects. The two approaches, that use RossThick–LiSparse–Reciprocal model fixed parameters derived from MODIS (ROY et al., 2016b) or inverted from the medium resolution images themselves (FLOOD et al., 2013), showed good ability to reduce the angular effects and were easier to apply because they do not depend on MODIS data. Still, none of the approaches completely eliminate the angular effects. Our approach to calculate the VZA and VAA is only approximate, which may have brought some uncertainty in the angular normalizations. The exact modeling mainly of the vector of VAA of each pixel can bring improvement in the results. Different land use and land cover classes may have different magnitudes of angular effects (PETRI; GALVÃO; LYAPUSTIN, 2019), so, the analysis of these effects by class can provide insights to improve the results of BRDF

normalization. In addition, approaches that disaggregate the BRDF parameters to the resolution of the image to be normalized can also bring improvements in reducing angular effects (FRANCH et al., 2019).

The WFI inter-satellite cross-comparison results showed that co-registration and BRDF normalization contribute to reduce differences between sensors. When only data with a VZA smaller than 7º were considered, the ODR regression line between the surface reflectance WFI from CBERS-4 and CBERS-4A approached the identity line, indicating greater similarity between these data. Even after the BRDF normalization, there was still a greater distance from the identity line concerning the data close to the nadir, indicating that there is still a residual angular effect. Another factor that can influence this aspect is the atmospheric correction uncertainties that do not consider the view angles or the misidentification of clouds and cloud shadows. The cross-comparison between the WFI data from Amazonia-1, CBERS-4, and CBERS-4A showed the formation of two distinct clusters in the blue and NIR bands. This could be an effect of some radiometric calibration problem. During radiometric calibration, CBERS-4/WFI data showed comparable quality to Landsat-8/OLI data. However, periodic calibration activities are highly recommended to maintain the standard quality of data because the radiometric coefficients might change over time (MARTINS et al., 2018). Furthermore, there is no information in the literature about the radiometric calibration status of the WFI sensors onboard the CBERS-4A and Amazonia-1. Nevertheless, assessing the uncertainties of atmospheric correction and performing radiometric calibration of the WFI data are beyond the scope of this work, but should be considered in future research. Despite this, we derived

transformation functions to convert the WFI sensor reflectance data from one satellite to the equivalent of the other satellite, allowing us to combine them into a single time series.

As a case study, we evaluated the combination of the WFI data from the three satellites in a single time series by mapping second crop season corn damaged by the frosts that occurred in western Paraná in 2021. Two data normalization approaches were compared: using the previously derived transformation functions; and the MODIS product MCD43A4 as a reference. Although the normalization with MODIS further reduced the differences in the NDVI time series among WFI from the three satellites, it also reduced the amplitude of the values during the corn growth cycle. The approach with the transformation functions preserved the amplitude of the data, which was important in the extraction of the phenological metrics, which allowed the mapping of frost-damaged corn areas with greater accuracy. The Random Forest classifier using as input the phenological metrics derived from the normalized NDVI time series of the WFI data from the three satellites allowed mapping the areas affected by two frost events, separating them from areas in senescence/harvest and from unaffected areas. This proves the potential of the combined time series of the WFI data in a single consistent and seamless time series from the three satellites for agricultural monitoring. Other applications such as mapping crop types and estimating phenological phases also have great potential to be carried out using these time series. Future improvements in cloud masking, radiometric calibration, atmospheric correction and BRDF normalization may bring improvements in the

integration of WFI data from the three satellites into a single time series, bringing

improvements to agricultural monitoring applications.

10 OVERALL CONTRIBUTIONS

This research investigated various aspects of WFI data quality, and ways to improve the data, aiming to combine them into a more consistent time series, thus allowing agricultural monitoring. The main contributions produced by this research were:

- In Chapter 4, we investigated the quality of two cloud mask algorithms for WFI data, an essential product for automatic time series analysis. The results showed the strengths and limitations of each algorithm, serving as a guide for WFI data users. In addition to bringing insights to improve algorithms.

- In Chapter 5, we evaluated the geometric accuracy of the WFI data. The geometric accuracy quantification provides important guidance to improving geolocation accuracy and data application. As the results showed displacements, we introduced a framework for automatic sub-pixel co-registration. Thus, allowing to improve the geometric quality of the WFI data.

- In Chapter 6, we assessed the angular effects in WFI images and evaluated six approaches for normalizing BRDF effects in WFI imagery. The results showed the occurrence of bidirectional effects in the WFI images, both in the spectral bands and in the EVI. This chapter can also serve as a guide for choosing the most suitable normalization method, allowing WFI data users to reduce angular effects.

- In Chapter 7, we performed inter-satellite cross-comparison of WFI data from CBERS-4, CBERS-4A, and Amazonia-1, which allowed us to identify differences between the data and to derive transformation functions between the satellites. This, together with the processing developed in the previous chapters, makes it possible to combine the WFI data from the three satellites in a more consistent time series.

- In Chapter 8, we mapped frost-damaged corn areas in western Paraná state using time series of WFI data from the three satellites combined. The proposed methodology allowed to distinguish areas damaged by two frost events, allowing to distinguish them from corn areas already in senescence or harvested, and from unaffected areas. This chapter also demonstrated the enormous potential of WFI data for agricultural monitoring. An adequate monitoring system that provides information regarding crop production can help combat food security with strategic planning in the country and other countries since Brazil is a large food producer.

11 OVERALL CONCLUSION

In this research, we investigated the quality of WFI data onboard the CBERS-4, CBERS-4A, and Amazonia-1 satellites and data interoperability procedures to integrate them into a single, more consistent time series for agricultural monitoring. The main conclusions of the research were:

- Our results showed that despite CMASK having high reliability in pixels identified as a cloud (user accuracy close to 100%), it had omission errors in identifying clouds greater than 30 %. In comparison, ATSA showed a better balance between omission and commission errors.

- Spatial shifts were found in relation to the Sentinel-2/MSI images of up to 2.5 pixels (138 m) for CBERS-4A/WFI and up to 1.45 pixels (93 m) for CBERS-4/WFI and Amazonia-1/WFI, showing the need to co-register these images for WFI multi-temporal analysis or when they are combined with other data sources.

- Our approach to automatic co-registration improved the geometric quality of the WFI data, reducing the RMSE on a tile basis from 1.42±0.21 to 0.29±0.05, thus substantially reducing misregistration and providing more consistent and robust data.

- Our results suggest that there are directional effects as a function of the view angle and the change of the solar vector, in all spectral bands, being greater in the NIR and the EVI.

- The six angular normalization approaches evaluated reduced the angular effects resulting from the view angle. The five methods that perform the full BRDF correction using the RossThick–LiSparse–Reciprocal model reduced the angular effects caused by the change in the solar vector. Angular normalization should be conducted for the analysis of CBERS-4/WFI time series or image mosaics from spectral bands, mainly NIR, and non-normalized vegetation indices such as EVI.

- In the inter-satellite WFI cross-comparison, in most cases there was a reduction in the differences between sensors after co-registration and BRDF normalization, with the data approaching the 1:1 straight line and reduction of the RMSD. The surface reflectance and NBAR of the WFI sensors onboard the CBERS-4 and CBERS-4A were more similar than the WFI onboard the Amazonia-1.

- Statistical transformation functions were derived that allow the conversion of the surface reflectance and NBAR of one sensor to the equivalent if it had been obtained by the other.

- Combining all the previous findings in a case study to map corn frost-damaged areas in western Paraná state allowed extracting phenological metrics from the NDVI time series of the WFI sensor of the three satellites and separate areas affected by two frost events from areas that had already been harvested or in senescence and were not affected. The approach can be expanded

in the future to identify and map the crop's phenological phases, crop type, among others.

REFERENCES

ADAMI, M.; RUDORFF, B. F. T.; FREITAS, R. M.; AGUIAR, D. A.; SUGAWARA, L. M.; MELLO, M. P. Remote sensing time series to evaluate direct land use change of recent expanded sugarcane crop in Brazil. **Sustainability**, v. 4, n. 4, p. 574–585, 2012.

ANDERSON, J. H.; WEBER, K. T.; GOKHALE, B.; CHEN, F. Intercalibration and evaluation of ResourceSat-1 and Landsat-5 NDVI. **Canadian Journal of Remote Sensing**, v. 37, n. 2, p. 213–219, 2011.

APARECIDO, L. E. O.; ROLIM, G. D. S.; RICHETTI, J.; SOUZA, P. S.; JOHANN, J. A. Köppen, Thornthwaite and Camargo climate classifications for climatic zoning in the State of Paraná, Brazil. **Ciência e Agrotecnologia**, v. 40, n. 4, p. 405–417, 2016.

ATZBERGER, C. Advances in remote sensing of agriculture: context description, existing operational monitoring systems and major information needs. **Remote Sensing**, v. 5, n. 2, p. 949–981, 2013.

AZZARI, G.; JAIN, M.; LOBELL, D. B. Towards fine resolution global maps of crop yields: testing multiple methods and satellites in three countries. **Remote Sensing of Environment**, v. 202, p. 129–141, 2017.

BAETENS, L.; DESJARDINS, C.; HAGOLLE, O. Validation of copernicus Sentinel-2 cloud masks obtained from MAJA, Sen2Cor, and FMask processors using reference cloud masks generated with a supervised active learning procedure. **Remote Sensing**, v. 11, n. 4, p. 1–25, 2019.

BARAZZETTI, L.; CUCA, B.; PREVITALI, M. Evaluation of registration accuracy between Sentinel-2 and Landsat 8. In: INTERNATIONAL CONFERENCE ON REMOTE SENSING AND GEOINFORMATION OF THE ENVIRONMENT (RSCy2016), 4., 2016. **Proceedings…** 2016. p. 968809.

BÉGUÉ, A.; ARVOR, D.; BELLON, B.; BETBEDER, J.; DE ABELLEYRA, D.; FERRAZ, R. P. D.; LEBOURGEOIS, V.; LELONG, C.; SIMÕES, M.; VERÓN, S. R. Remote sensing and cropping practices: a review. **Remote Sensing**, v. 10, n. 1, 2018.

BELGIU, M.; DRĂGU, L.; DRĂGUŢ, L. Random forest in remote sensing: a review of applications and future directions. **ISPRS Journal of Photogrammetry and Remote Sensing**, v. 114, p. 24–31, 2016.

BENDINI, H. N.; GARCIA FONSECA, L. M.; SCHWIEDER, M.; SEHN KÖRTING, T.; RUFIN, P.; DEL ARCO SANCHES, I.; LEITÃO, P. J.; HOSTERT, P. Detailed agricultural land classification in the Brazilian cerrado based on phenological information from dense satellite image time series. **International**

Journal of Applied Earth Observation and Geoinformation, v. 82, e101872, 2019.

BIAN, J.; LI, A.; LIU, Q.; HUANG, C. Cloud and snow discrimination for CCD images of HJ-1A/B constellation based on spectral signature and spatio-temporal context. **Remote Sensing**, v. 8, n. 1, p. 31, 2016.

BIAU, G.; SCORNET, E. A random forest guided tour. **Test**, v. 25, n. 2, p. 197–227, 2016a.

BIAU, G.; SCORNET, E. A random forest guided tour. **TEST**, v. 25, n. 2, p. 197–227, 2016b.

BRAATEN, J. D.; COHEN, W. B.; YANG, Z. Automated cloud and cloud shadow identification in Landsat MSS imagery for temperate ecosystems. **Remote Sensing of Environment**, v. 169, p. 128–138, 2015.

BRANCO, J. E. H.; BARTHOLOMEU, D. B.; ALVES JUNIOR, P. N.; CAIXETA FILHO, J. V. Mutual analyses of agriculture land use and transportation networks: the future location of soybean and corn production in Brazil. **Agricultural Systems**, v. 194, 2021.

BREIMAN, L. Bagging predictors. **Machine Learning**, v. 24, n. 2, p. 123–140, 1996.

BREIMAN, L. Random forests. **Machine Learning**, v. 45, n. 1, p. 5–32, 2001.

BREIMAN, L.; FRIEDMAN, J. H.; OLSHEN, R. A.; STONE, C. J. **Classification and regression trees**. Belmont: Wadsworth, 1984. 368 p.

BRÉON, F. M.; VERMOTE, E. Correction of MODIS surface reflectance time series for BRDF effects. **Remote Sensing of Environment**, v. 125, p. 1–9, 2012a.

BRÉON, F.; VERMOTE, E. Correction of MODIS surface reflectance time series for BRDF effects. **Remote Sensing of Environment**, v. 125, p. 1–9, 2012b.

BROWN, K. M.; FOODY, G. M.; ATKINSON, P. M. Modelling geometric and misregistration error in airborne sensor data to enhance change detection. **International Journal of Remote Sensing**, v. 28, n. 12, p. 2857–2879, 2007.

BROWN, L. G. A survey of image registration techniques. **ACM Computing Surveys**, v. 24, n. 4, p. 325–376, 1992.

CADENAS, J. M.; GARRIDO, M. C.; MARTÍNEZ-ESPAÑA, R.; GUILLÉN-NAVARRO, M. A. Making decisions for frost prediction in agricultural crops in a soft computing framework. **Computers and Electronics in Agriculture**, v. 175,

e 105587, 2020.

CHANDER, G.; MISHRA, N.; HELDER, D. L.; AARON, D.; CHOI, T.; ANGAL, A.; XIONG, X. Use of EO-1 hyperion data to calculate spectral band adjustment factors (SBAF) between the L7 ETM+ and Terra MODIS sensors. In: IEEE INTERNATIONAL GEOSCIENCE AND REMOTE SENSING SYMPOSIUM, 2010. **Proceedings…** IEEE, 2010. Available from: <http://ieeexplore.ieee.org/document/5652746/>.

CHAVES, M. E. D.; ALVES, M. C.; SÁFADI, T.; OLIVEIRA, M. S.; PICOLI, M. C. A.; SIMOES, R. E. O.; MATAVELI, G. A. V. Time-weighted dynamic time warping analysis for mapping interannual cropping practices changes in large-scale agro-industrial farms in Brazilian Cerrado. **Science of Remote Sensing**, v. 3, e100021, 2021a.

CHAVES, M. E. D.; PICOLI, M. C. A.; SANCHES, I. D. Recent applications of Landsat 8/OLI and Sentinel-2/MSI for land use and land cover mapping: a systematic review. **Remote Sensing**, v. 12, n. 18, 2020.

CHAVES, M. E. D.; SOARES, A. R.; SANCHES, I. D.; FRONZA, J. G. CBERS data cubes for land use and land cover mapping in the Brazilian Cerrado agricultural belt. **International Journal of Remote Sensing**, v. 42, n. 21, p. 8398–8432, 2021b.

CHEN, X.; VOGELMANN, J. E.; CHANDER, G.; JI, L.; TOLK, B.; HUANG, C.; ROLLINS, M. Cross-sensor comparisons between Landsat 5 TM and IRS-P6 AWiFS and disturbance detection using integrated Landsat and AWiFS time-series images. **International Journal of Remote Sensing**, v. 34, n. 7, p. 2432–2453, 2013.

CHEN, Y.; LU, D.; MORAN, E.; BATISTELLA, M.; DUTRA, L. V.; SANCHES, I. D.; DA SILVA, R. F. B.; HUANG, J.; LUIZ, A. J. B.; DE OLIVEIRA, M. A. F. Mapping croplands, cropping patterns, and crop types using MODIS time-series data. **International Journal of Applied Earth Observation and Geoinformation**, v. 69, p. 133–147, 2018.

CHOUDHURY, B. U.; WEBSTER, R.; SHARMA, V.; GOSWAMI, J.; MEETEI, T. T.; KRISHNAPPA, R.; RAJU, P. L. N. Frost damage to maize in northeast India: assessment and estimated loss of yield by hyperspectral proximal remote sensing. **Journal of Applied Remote Sensing**, v. 13, n. 4, p. 1, 2019.

CLAVERIE, M.; JU, J.; MASEK, J. G.; DUNGAN, J. L.; VERMOTE, E. F.; ROGER, J.-C.; SKAKUN, S. V.; JUSTICE, C. The harmonized Landsat and Sentinel-2 surface reflectance data set. **Remote Sensing of Environment**, v. 219, p. 145–161, 2018.

CLAVERIE, M.; VERMOTE, E.; FRANCH, B.; HE, T.; HAGOLLE, O.; KADIRI,

M.; MASEK, J. Evaluation of medium spatial resolution BRDF-adjustment techniques using multi-angular SPOT4 (Take5) acquisitions. **Remote Sensing**, v. 7, n. 9, p. 12057–12075, 2015.

COGLIATI, S.; SARTI, F.; CHIARANTINI, L.; COSI, M.; LORUSSO, R.; LOPINTO, E.; MIGLIETTA, F.; GENESIO, L.; GUANTER, L.; DAMM, A.; PÉREZ-LÓPEZ, S.; SCHEFFLER, D.; TAGLIABUE, G.; PANIGADA, C.; RASCHER, U.; DOWLING, T. P. F.; GIARDINO, C.; COLOMBO, R. The PRISMA imaging spectroscopy mission: overview and first performance analysis. **Remote Sensing of Environment**, v. 262, 2021.

COHEN, W. B.; GOWARD, S. N. Landsat's role in ecological applications of remote sensing. **BioScience**, v. 54, n. 6, p. 535–545, 2004.

COMPANHIA NACIONAL DE ABASTECIMENTO (CONAB). Acompanhamento da safra brasileira. **Boletim da Safra 2021**, v. 8, p. 59, 2021a.

COMPANHIA NACIONAL DE ABASTECIMENTO (CONAB). **Monitoramento de geada - Safra 2020/21 - 27-Jul-2021**. 2021b. Available from: <https://www.conab.gov.br/info-agro/safras/progresso-de-safra/item/download/38512_0155549eee65cafe1fcf650317770843>.

COMPANHIA NACIONAL DE ABASTECIMENTO (CONAB). Acompanhamento da safra brasileira. **Boletim da Safra 2021**, v. 8, p. 59, 2021c.

COMPANHIA NACIONAL DE ABASTECIMENTO (CONAB). **Levantamento de safras - séries históricas (1976-2021)**. Available from: <https://www.conab.gov.br/info-agro/safras/serie-historica-das-safras?start=20>. Access on: 20 May 2022a.

CONGALTON, R. G. A review of assessing the accuracy of classifications of remotely sensed data. **Remote Sensing of Environment**, v. 37, n. 1, p. 35–46, 1991.

DAI, X. The effects of image misregistration on the accuracy of remotely sensed change detection. **IEEE Transactions on Geoscience and Remote Sensing**, v. 36, n. 5, pt. 1, p. 1566–1577, 1998.

DE SOUZA, C. H. W.; MERCANTE, E.; PRUDENTE, V. H. R.; JUSTINA, D. D. D. Methods of performance evaluation for the supervised classification of satellite imagery in determining land cover classes. **Ciencia E Investigacion Agraria**, v. 40, n. 2, p. 419–428, 2013.

DECHOZ, C.; POULAIN, V.; MASSERA, S.; LANGUILLE, F.; GRESLOU, D.; DE LUSSY, F.; GAUDEL, A.; L'HELGUEN, C.; PICARD, C.; TRÉMAS, T. Sentinel 2 global reference image. **Image and Signal Processing for Remote Sensing XXI**, v. 9643, p. 96430A, 2015.

DIAS, L. C. P.; PIMENTA, F. M.; SANTOS, A. B.; COSTA, M. H.; LADLE, R. J. Patterns of land use, extensification, and intensification of Brazilian agriculture. **Global Change Biology**, v. 22, n. 8, p. 2887–2903, 2016.

DINIZ, C. G.; SOUZA, A. A. D. A.; SANTOS, D. C.; DIAS, M. C.; LUZ, N. C.; MORAES, D. R. V.; MAIA, J. S. A.; GOMES, A. R.; NARVAES, I. D. S.; VALERIANO, D. M.; MAURANO, L. E. P.; ADAMI, M. DETER-B: The new Amazon near real-time deforestation detection system. **IEEE Journal of Selected Topics in Applied Earth Observations and Remote Sensing**, v. 8, n. 7, p. 3619–3628, 2015.

DONG, J.; METTERNICHT, G.; HOSTERT, P.; FENSHOLT, R.; CHOWDHURY, R. R. Remote sensing and geospatial technologies in support of a normative land system science: status and prospects. **Current Opinion in Environmental Sustainability**, v. 38, p. 44–52, 2019.

DOS REIS, A. A.; WERNER, J. P. S.; SILVA, B. C.; FIGUEIREDO, G. K. D. A.; ANTUNES, J. F. G.; ESQUERDO, J. C. D. M.; COUTINHO, A. C.; LAMPARELLI, R. A. C.; ROCHA, J. V.; MAGALHÃES, P. S. G. Monitoring pasture aboveground biomass and canopy height in an integrated crop–livestock system using textural information from PlanetScope imagery. **Remote Sensing**, v. 12, n. 16, p. 2534, 2020.

DRUSCH, M.; DEL BELLO, U.; CARLIER, S.; COLIN, O.; FERNANDEZ, V.; GASCON, F.; HOERSCH, B.; ISOLA, C.; LABERINTI, P.; MARTIMORT, P.; MEYGRET, A.; SPOTO, F.; SY, O.; MARCHESE, F.; BARGELLINI, P. Sentinel-2: ESA's optical high-resolution mission for GMES operational services. **Remote Sensing of Environment**, v. 120, p. 25–36, 2012.

DUDDU, H. S. N.; PAJIC, V.; NOBLE, S. D.; TANINO, K. K.; SHIRTLIFFE, S. J. Image-based rapid estimation of frost damage in Canola (Brassica napus L.). **Canadian Journal of Remote Sensing**, v. 44, n. 2, p. 169–175, 2018.

DUVEILLER, G.; LÓPEZ-LOZANO, R.; SEGUINI, L.; BOJANOWSKI, J. S.; BARUTH, B. Optical remote sensing requirements for operational crop monitoring and yield forecasting in Europe. In: SENTINEL-3 OLCI/SLSTR AND MERIS/(A)ATSR WORKSHOP, 2013. **Proceedings...** 2013.

EASTMAN, R. D.; LE MOIGNE, J.; NETANYAHU, N. S. Research issues in image registration for remote sensing. In: THE IEEE COMPUTER SOCIETY CONFERENCE ON COMPUTER VISION AND PATTERN RECOGNITION, 2007. **Proceedings…** IEEE, 2007.

EBERHARDT, I. D. R.; SCHULTZ, B.; RIZZI, R.; SANCHES, I. D. A.; FORMAGGIO, A. R.; ATZBERGER, C.; MELLO, M. P.; IMMITZER, M.; TRABAQUINI, K.; FOSCHIERA, W.; LUIZ, A. J. B. Cloud cover assessment for operational crop monitoring systems in tropical areas. **Remote Sensing**, v. 8, n.

3, p. 1–14, 2016.

EMPRESA BRASILEIRA DE PESQUISA AGROPECUÁRIA (EMBRAPA). **O novo mapa de solos do Brasil: legenda atualizada**. Rio de Janeiro: Embrapa, 2011. 130 p. ISBN(1517-2627).

ENNOURI, K.; KALLEL, A.; ALBANO, R. Remote sensing: an advanced technique for crop condition assessment. **Mathematical Problems in Engineering**, v. 2019, 2019.

EPIPHANIO, J. C. N. CBERS: estado atual e futuro. In: SIMPÓSIO BRASILEIRO DE SENSORIAMENTO REMOTO,14., 2009. **Anais...** São José dos Campos: INPE, 2009. Available from: <http://marte.sid.inpe.br/col/dpi.inpe.br/sbsr@80/2008/11.18.12.46/doc/2001-2008.pdf>.

EPIPHANIO, J. C. N. CBERS-3/4: características e potencialidades. In: SIMPÓSIO BRASILEIRO DE SENSORIAMENTO REMOTO, 15., 2011a, Curitiba, PR. **Anais...** São José dos Campos: INPE, 2011. Available from: <http://www.ncbi.nlm.nih.gov/entrez/query.fcgi?cmd=Retrieve&db=PubMed&dopt=Citation&list_uids=37237>.

EPIPHANIO, J. C. N. CBERS-3/4: características e potencialidades. In: SIMPÓSIO BRASILEIRO DE SENSORIAMENTO REMOTO, 15., 2011b, Curitiba, PR. **Anais...** São José dos Campos: INPE, 2011

EUROPEAN SPACE AGENCY (ESA). **SENTINEL-2 user handbook**. [S.l.]: ESA, 2015.

EUROPEAN SPACE AGENCY (ESA). **L1C data quality report. Ref. S2-PDGS-MPC-DQR**. 2021. Available from: <https://sentinel.esa.int/documents/247904/685211/Sentinel-2_L1C_Data_Quality_Report>.

ESQUERDO, J. C. D. M.; ANTUNES, J. F. G.; COUTINHO, A. C.; SPERANZA, E. A.; KONDO, A. A.; SANTOS, J. L. DOS. SATVeg: a web-based tool for visualization of MODIS vegetation indices in South America. **Computers and Electronics in Agriculture**, v. 175, e105516, 2020.

ESQUERDO, J. C. D. M.; ZULLO JÚNIOR, J.; ANTUNES, J. F. G. Use of NDVI/AVHRR time-series profiles for soybean crop monitoring in Brazil. **International Journal of Remote Sensing**, v. 32, n. 13, p. 3711–3727, 2011.

FOOD AND AGRICULTURE ORGANIZATION (FAO). **The future of food and agriculture – alternative pathways to 2050**. Rome: FAO, 2020. 224 p. ISBN(9789251301586).

FOOD AND AGRICULTURE ORGANIZATION (FAO). **Crops and livestock products - 1961-2020**. Available from: <https://www.fao.org/faostat/en/#data/QCL>. Access on: 18 Apr. 2022a.

FELDE, G. W.; ANDERSON, G. P.; COOLEY, T. W.; MATTHEW, M. W.; ADLER-GOLDEN, S. M.; BERK, A.; LEE, J. Analysis of hyperion data with the FLAASH atmospheric correction algorithm. **International Geoscience and Remote Sensing Symposium (IGARSS)**, v. 1, n. C, p. 90–92, 2003.

FERREIRA, K. R.; QUEIROZ, G. R.; VINHAS, L.; MARUJO, R. F. B.; SIMOES, R. E. O.; PICOLI, M. C. A.; CAMARA, G.; CARTAXO, R.; GOMES, V. C. F.; SANTOS, L. A.; SANCHEZ, A. H.; ARCANJO, J. S.; FRONZA, J. G.; NORONHA, C. A.; COSTA, R. W.; ZAGLIA, M. C.; ZIOTI, F.; KORTING, T. S.; SOARES, A. R.; CHAVES, M. E. D.; FONSECA, L. M. G. Earth observation data cubes for Brazil: requirements, methodology and products. **Remote Sensing**, v. 12, n. 24, p. 1–19, 2020.

FISCHLER, M. A.; BOLLES, R. C. Random sample paradigm for model consensus: a apphcatlons to image fitting with analysis and automated cartography. **Graphics and Image Processing**, v. 24, n. 6, p. 381–395, 1981.

FITZGERALD, G. J.; PERRY, E. M.; FLOWER, K. C.; NIKOLAUS CALLOW, J.; BORUFF, B.; DELAHUNTY, A.; WALLACE, A.; NUTTALL, J. Frost damage assessment in wheat using spectral mixture analysis. **Remote Sensing**, v. 11, n. 21, p. 1–17, 2019.

FLOOD, N. Testing the local applicability of MODIS BRDF parameters for correcting Landsat TM imagery. **Remote Sensing Letters**, v. 4, n. 8, p. 793–802, 2013.

FLOOD, N. Continuity of reflectance data between Landsat-7 ETM+ and Landsat-8 OLI, for both top-of-atmosphere and surface reflectance: a study in the Australian landscape. **Remote Sensing**, v. 6, n. 9, p. 7952–7970, 2014.

FLOOD, N. Comparing Sentinel-2A and Landsat 7 and 8 using surface reflectance over Australia. **Remote Sensing**, v. 9, n. 7, p. 659, 2017.

FLOOD, N.; DANAHER, T.; GILL, T.; GILLINGHAM, S. An operational scheme for deriving standardised surface reflectance from Landsat TM/ETM+ and SPOT HRG imagery for eastern Australia. **Remote Sensing**, v. 5, n. 1, p. 83–109, 2013.

FOGA, S.; SCARAMUZZA, P. L.; GUO, S.; ZHU, Z.; DILLEY, R. D.; BECKMANN, T.; SCHMIDT, G. L.; DWYER, J. L.; JOSEPH HUGHES, M.; LAUE, B. Cloud detection algorithm comparison and validation for operational Landsat data products. **Remote Sensing of Environment**, v. 194, p. 379–390, 2017.

FONSECA, L. M. G.; EPIPHANIO, J. C. N.; VALERIANO, D. M.; SOARES, J. V.; DALGE, J. C. L.; ALVARENGA, M. A. Earth observation applications in Brazil with focus on the CBERS program. **IEEE Geoscience and Remote Sensing Magazine**, v. 2, n. 2, p. 53–55, 2014.

FONSECA, L. M. G.; MANJUNATH, B. S. Registration techniques for multisensor remotely sensed imagery. **Photogrammetric Engineering and Remote Sensing**, v. 62, n. 9, p. 1049–1056, 1996.

FOODY, G. M. Status of land cover classification accuracy assessment. **Remote Sensing of Environment**, v. 80, n. 1, p. 185–201, 2002.

FORMAGGIO, A. R.; MOURA, V.; EPIPHANIO, J. C. N.; SILVA, H. R.; FIORIO, P. R.; CAMPOS, R. C. Dados TM/Landsat na estimativa de áreas destinadas a culturas de verão, no estado de São Paulo. In: SIMPÓSIO BRASILEIRO DE SENSORIAMENTO REMOTO, 11., 2003, Belo Horizonte. **Anais...** São José dos Campos: Instituto Nacional de Pesquisas Espaciais (INPE), 2003

FORMAGGIO, A. R.; SANCHES, I. D. A. **Sensoriamento remoto em agricultura**. São Paulo: Oficina de Textos, 2017. 284 p. ISBN(9788579752773).

FOROOSH, H.; ZERUBIA, J. B.; BERTHOD, M. Extension of phase correlation to subpixel registration. **IEEE Transactions on Image Processing**, v. 11, n. 3, p. 188–199, 2002.

FRANCH, B.; VERMOTE, E.; SKAKUN, S.; ROGER, J.; MASEK, J.; JU, J.; VILLAESCUSA-NADAL, J.; SANTAMARIA-ARTIGAS, A. A method for Landsat and Sentinel 2 (HLS) BRDF normalization. **Remote Sensing**, v. 11, n. 6, p. 632, 2019.

FRITZ, S.; SEE, L.; BAYAS, J. C. L.; WALDNER, F.; JACQUES, D.; BECKER-RESHEF, I.; WHITCRAFT, A.; BARUTH, B.; BONIFACIO, R.; CRUTCHFIELD, J.; REMBOLD, F.; ROJAS, O.; SCHUCKNECHT, A.; VAN DER VELDE, M.; VERDIN, J.; WU, B.; YAN, N.; YOU, L.; GILLIAMS, S.; MÜCHER, S.; TETRAULT, R.; MOORTHY, I.; MCCALLUM, I. A comparison of global agricultural monitoring systems and current gaps. **Agricultural Systems**, v. 168, p. 258–272, 2019.

FRITZ, S.; SEE, L.; MCCALLUM, I.; YOU, L.; BUN, A.; MOLTCHANOVA, E.; DUERAUER, M.; ALBRECHT, F.; SCHILL, C.; PERGER, C.; HAVLIK, P.; MOSNIER, A.; THORNTON, P.; WOOD-SICHRA, U.; HERRERO, M.; BECKER-RESHEF, I.; JUSTICE, C.; HANSEN, M.; GONG, P.; ABDEL AZIZ, S.; CIPRIANI, A.; CUMANI, R.; CECCHI, G.; CONCHEDDA, G.; FERREIRA, S.; GOMEZ, A.; HAFFANI, M.; KAYITAKIRE, F.; MALANDING, J.; MUELLER, R.; NEWBY, T.; NONGUIERMA, A.; OLUSEGUN, A.; ORTNER, S.; RAJAK, D. R.; ROCHA, J.; SCHEPASCHENKO, D.; SCHEPASCHENKO, M.; TEREKHOV, A.;

TIANGWA, A.; VANCUTSEM, C.; VINTROU, E.; WENBIN, W.; VAN DER VELDE, M.; DUNWOODY, A.; KRAXNER, F.; OBERSTEINER, M. Mapping global cropland and field size. **Global Change Biology**, v. 21, n. 5, p. 1980–1992, 2015.

GAO, B. NDWI: a normalized difference water index for remote sensing of vegetation liquid water from space. **Remote Sensing of Environment**, v. 58, n. 3, p. 257–266, 1996.

GAO, F.; ANDERSON, M. C.; ZHANG, X.; YANG, Z.; ALFIERI, J. G.; KUSTAS, W. P.; MUELLER, R.; JOHNSON, D. M.; PRUEGER, J. H. Toward mapping crop progress at field scales through fusion of Landsat and MODIS imagery. **Remote Sensing of Environment**, v. 188, p. 9–25, 2017.

GAO, F.; ANDERSON, M.; DAUGHTRY, C.; JOHNSON, D. Assessing the variability of corn and soybean yields in central Iowa using high spatiotemporal resolution multi-satellite imagery. **Remote Sensing**, v. 10, n. 9, p. 1489, 2018.

GAO, F.; HE, T.; MASEK, J. G.; SHUAI, Y.; SCHAAF, C. B.; WANG, Z. Angular effects and correction for medium resolution sensors to support crop monitoring. **IEEE Journal of Selected Topics in Applied Earth Observations and Remote Sensing**, v. 7, n. 11, p. 4480–4489, 2014.

GAO, F.; MASEK, J. G.; WOLFE, R. E. Automated registration and orthorectification package for Landsat and Landsat-like data processing. **Journal of Applied Remote Sensing**, v. 3, n. 1, e 033515, 2009.

GASCON, F.; CADAU, E.; COLIN, O.; HOERSCH, B.; ISOLA, C.; LÓPEZ FERNÁNDEZ, B.; MARTIMORT, P. Copernicus Sentinel-2 mission: products, algorithms and Cal/Val. **Earth Observing Systems XIX**, v. 9218, p. 92181E, 2014.

GAUDEL, A.; LANGUILLE, F.; DELVIT, J. M.; MICHEL, J.; COURNET, M.; POULAIN, V.; YOUSSEFI, D. Global reference image validation and application to multitemporal performances and high latitude digital surface model. **International Archives of the Photogrammetry, Remote Sensing and Spatial Information Sciences - ISPRS Archives**, v. 42, n. 1, p. 447–454, 2017.

GERGELY, D. **Mastering data analysis with R**. [S.l]: Packt, 2015. 398 p.

GITELSON, A. A.; KAUFMAN, Y. J.; MERZLYAK, M. N. Use of a green channel in remote sensing of global vegetation from EOS-MODIS. **Remote Sensing of Environment**, v. 58, n. 3, p. 289–298, 1996.

GÓMEZ, C.; WHITE, J. C.; WULDER, M. A. Optical remotely sensed time series data for land cover classification: a review. **ISPRS Journal of**

Photogrammetry and Remote Sensing, v. 116, p. 55–72, 2016.

GOWARD, S. N.; CHANDER, G.; PAGNUTTI, M.; MARX, A.; RYAN, R.; THOMAS, N.; TETRAULT, R. Complementarity of ResourceSat-1 AWiFS and Landsat TM/ETM+ sensors. **Remote Sensing of Environment**, v. 123, n. 2012, p. 41–56, 2012.

GRIFFITHS, P.; NENDEL, C.; HOSTERT, P. Intra-annual reflectance composites from Sentinel-2 and Landsat for national-scale crop and land cover mapping. **Remote Sensing of Environment**, v. 220, p. 135–151, 2019.

GU, J.; CONGALTON, R. G. Analysis of the impact of positional accuracy when using a single pixel for thematic accuracy assessment. **Remote Sensing**, v. 12, n. 24, p. 1–21, 2020.

GU, J.; CONGALTON, R. G.; PAN, Y. The impact of positional errors on soft classification accuracy assessment: a simulation analysis. **Remote Sensing**, v. 7, n. 1, p. 579–599, 2015.

HANSEN, M. C.; LOVELAND, T. R. A review of large area monitoring of land cover change using Landsat data. **Remote Sensing of Environment**, v. 122, p. 66–74, 2012.

HANSEN, M. C.; ROY, D. P.; LINDQUIST, E.; ADUSEI, B.; JUSTICE, C. O.; ALTSTATT, A. A method for integrating MODIS and Landsat data for systematic monitoring of forest cover and change in the Congo Basin. **Remote Sensing of Environment**, v. 112, n. 5, p. 2495–2513, 2008.

HELDER, D.; MARKHAM, B.; MORFITT, R.; STOREY, J.; BARSI, J.; GASCON, F.; CLERC, S.; LAFRANCE, B.; MASEK, J.; ROY, D. P.; LEWIS, A.; PAHLEVAN, N. Observations and recommendations for the calibration of Landsat 8 OLI and Sentinel 2 MSI for improved data interoperability. **Remote Sensing**, v. 10, n. 9, p. 1–29, 2018.

HUANG, C.; GOWARD, S. N.; MASEK, J. G.; GAO, F.; VERMOTE, E. F.; THOMAS, N.; SCHLEEWEIS, K.; KENNEDY, R. E.; ZHU, Z.; EIDENSHINK, J. C.; TOWNSHEND, J. R. G. Development of time series stacks of Landsat images for reconstructing forest disturbance history. **International Journal of Digital Earth**, v. 2, n. 3, p. 195–218, 2009.

HUETE, A.; DIDAN, K.; MIURA, T.; RODRIGUEZ, E. .; GAO, X.; FERREIRA, L. Overview of the radiometric and biophysical performance of the MODIS vegetation indices. **Remote Sensing of Environment**, v. 83, n. 1–2, p. 195–213, 2002.

INSTITUTO BRASILEIRO DE GEOGRAFIA E ESTATÍSTICA (IBGE). **Censo agropecuário, florestal e aquícola 2017**. 2017. Available from:

<https://censos.ibge.gov.br/agro/2017/templates/censo_agro/resultadosagro/index.html>.

INSTITUTO NACIONAL DE PESQUISAS ESPACIAIS (INPE). **Metodologia utilizada nos projetos PRODES e DETER**. 2019. Available from: <http://www.obt.inpe.br/OBT/assuntos/programas/amazonia/prodes/pdfs/Metodologia_Prodes_Deter_revisada.pdf>.

INSTITUTO NACIONAL DE PESQUISAS ESPACIAIS (INPE). **Missão Amazonia-1**. Available from: <http://www3.inpe.br/amazonia-1/amazonia.php>. Access on: 9 Aug. 2021a.

INSTITUTO NACIONAL DE PESQUISAS ESPACIAIS (INPE). **Satélite Sino-Brasileiro de Recursos Terrestres CBERS**. Available from: <http://www.cbers.inpe.br/>. Access on: 8 Sept. 2021b.

INSTITUTO NACIONAL DE PESQUISAS ESPACIAIS (INPE). **Níveis de processamento das imagens dos satélites CBERS e Amazonia**. 2021c. Available from: <http://www.dgi.inpe.br/documentacao/arquivos/NiveisdeProcessamentoCBERSAMZ.pdf>.

JARVIS, A.; REUTER, H. I.; NELSON, A.; GUEVARA, E. **Hole-filled SRTM for the globe Version 4, available from the CGIAR-CSI SRTM 90m Database**. Available from: <http://srtm.csi.cgiar.org>. Access on: 9 May 2022.

JEŁOWICKI, Ł.; SOSNOWICZ, K.; OSTROWSKI, W.; OSIŃSKA-SKOTAK, K.; BAKUŁA, K. Evaluation of rapeseed winter crop damage using UAV-based multispectral imagery. **Remote Sensing**, v. 12, n. 16, p. 2618, 2020.

JEONG, J.; HAN, H.; PARK, Y. Geometric accuracy analysis of the Geostationary Ocean Color Imager (GOCI) Level 1B (L1B) product. **Optics Express**, v. 28, n. 5, p. 7634, 2020.

JING, Z.; LI, S.; HU, X.; TANG, F. Sub-pixel accuracy evaluation of FY-3D MERSI-2 geolocation based on OLI reference imagery. **International Journal of Remote Sensing**, v. 42, n. 19, p. 7215–7238, 2021.

KEARNEY, J. Food consumption trends and drivers. **Philosophical Transactions of the Royal Society B: Biological Sciences**, v. 365, n. 1554, p. 2793–2807, 2010.

KING, M. D.; PLATNICK, S.; MENZEL, W. P.; ACKERMAN, S. A.; HUBANKS, P. A. Spatial and temporal distribution of clouds observed by MODIS onboard the terra and aqua satellites. **IEEE Transactions on Geoscience and Remote Sensing**, v. 51, n. 7, p. 3826–3852, 2013.

KOMAREK, A. M.; DE PINTO, A.; SMITH, V. H. A review of types of risks in agriculture: what we know and what we need to know. **Agricultural Systems**, v. 178, e102738, 2020.

KRAVCHENKO, O.; LAVRENYUK, M.; KUSSUL, N. Orthorectification of Sich-2 satellite images using elastic models. **International Geoscience and Remote Sensing Symposium (IGARSS)**, p. 2281–2284, 2014.

LEE, W.; SIM, D.; OH, S. J. A cnn-based high-accuracy registration for remote sensing images. **Remote Sensing**, v. 13, n. 8, 2021.

LI, F.; LYMBURNER, L.; MUELLER, N.; TAN, P.; ISLAM, A.; JUPP, D. L. B.; REDDY, S. An evaluation of the use of atmospheric and BRDF correction to standardize Landsat data. **IEEE Journal of Selected Topics in Applied Earth Observations and Remote Sensing**, v. 3, n. 3, p. 257–270, 2010.

LI, P.; JIANG, L.; FENG, Z. Cross-comparison of vegetation indices derived from Landsat-7 Enhanced Thematic Mapper Plus (ETM+) and Landsat-8 Operational Land Imager (OLI) sensors. **Remote Sensing**, v. 6, n. 1, p. 310–329, 2013.

LI, S.; GANGULY, S.; DUNGAN, J. L.; WANG, W.; NEMANI, R. R. Sentinel-2 MSI radiometric characterization and cross-calibration with Landsat-8 OLI. **Advances in Remote Sensing**, v. 6, n. 2, p. 147–159, 2017a.

LI, Z.; SHEN, H.; CHENG, Q.; LIU, Y.; YOU, S.; HE, Z. Deep learning based cloud detection for medium and high resolution remote sensing images of different sensors. **ISPRS Journal of Photogrammetry and Remote Sensing**, v. 150, p. 197–212, 2019a.

LI, Z.; SHEN, H.; CHENG, Q.; LIU, Y.; YOU, S.; HE, Z. Deep learning based cloud detection for medium and high resolution remote sensing images of different sensors. **ISPRS Journal of Photogrammetry and Remote Sensing**, v. 150, p. 197–212, 2019b.

LI, Z.; SHEN, H.; LI, H.; XIA, G.; GAMBA, P.; ZHANG, L. Multi-feature combined cloud and cloud shadow detection in GaoFen-1 wide field of view imagery. **Remote Sensing of Environment**, v. 191, p. 342–358, 2017b.

LIU, W.; ZHANG, X.; HE, F.; XIONG, Q.; ZAN, X.; LIU, Z.; SHA, D.; YANG, C.; LI, S.; ZHAO, Y. Open-air grape classification and its application in parcel-level risk assessment of late frost in the eastern Helan Mountains. **ISPRS Journal of Photogrammetry and Remote Sensing**, v. 174, p. 132–150, 2021.

LOUIS, J.; DEBAECKER, V.; PFLUG, B.; MAIN-KNORN, M.; BIENIARZ, J.; MUELLER-WILM, U.; CADAU, E.; GASCON, F. Sentinel-2 SEN2COR: L2A processor for users. In: LIVING PLANET SYMPOSIUM, 2016, Prague.

Proceedings... Prague: 2016

LUCHT, W.; ROUJEAN, J. L. Considerations in the parametric modeling of BRDF and albedo from multiangular satellite sensor observations. **Remote Sensing Reviews**, v. 18, n. 2, p. 343–379, 2000.

LUCHT, W.; SCHAAF, C. B.; STRAHLER, A. H. An algorithm for the retrieval of albedo from space using semiempirical BRDF models. **IEEE Transactions on Geoscience and Remote Sensing**, v. 38, n. 2 II, p. 977–998, 2000.

MACEDO-CRUZ, A.; PAJARES, G.; SANTOS, M.; VILLEGAS-ROMERO, I. Digital image sensor-based assessment of the status of oat (Avena sativa L.) crops after frost damage. **Sensors**, v. 11, n. 6, p. 6015–6036, 2011.

MANDANICI, E.; BITELLI, G. Preliminary comparison of Sentinel-2 and Landsat 8 imagery for a combined use. **Remote Sensing**, v. 8, n. 12, p. 1014, 2016.

MANSARAY, L. R.; YANG, L.; KABBA, V. T. S.; KANU, A. S.; HUANG, J.; WANG, F. Optimising rice mapping in cloud-prone environments by combining quad-source optical with Sentinel-1A microwave satellite imagery. **GIScience & Remote Sensing**, p. 1–22, 2019.

MARTINS, V. S.; BARBOSA, C. C. F.; DE CARVALHO, L. A. S.; JORGE, D. S. F.; LOBO, F. DE L.; DE MORAES NOVO, E. M. L. Assessment of atmospheric correction methods for sentinel-2 MSI images applied to Amazon floodplain lakes. **Remote Sensing**, v. 9, n. 4, 2017.

MARTINS, V. S.; SOARES, J. V.; NOVO, E. M. L. M.; BARBOSA, C. C. F.; PINTO, C. T.; ARCANJO, J. S.; KALEITA, A. Continental-scale surface reflectance product from CBERS-4 MUX data: Assessment of atmospheric correction method using coincident Landsat observations. **Remote Sensing of Environment**, v. 218, p. 55–68, 2018.

MONTEIRO, J. E. B. A. **Agrometeorologia dos cultivos: o fator meteorológico na produção agrícola**. Brasília: INMET, 2009. 530 p. ISBN(9788562817007).

MORÉ, J. J. The Levenberg-Marquardt algorithm: implementation and theory. In: WATSON, G. A. (Ed.). **Numerical analysis.** Berlin: Springer, 1978. p. 105–116.

MOUTINHO, S. Brazil's first homemade satellite will put an extra eye on dwindling Amazon forests. **Science**, 2021.

NGUYEN, L. H.; JOSHI, D. R.; CLAY, D. E.; HENEBRY, G. M. Characterizing land cover/land use from multiple years of Landsat and MODIS time series: a novel approach using land surface phenology modeling and random forest

classifier. **Remote Sensing of Environment**, v. 238, e111017, 2020.

OLDONI, L. V.; MERCANTE, E.; ANTUNES, J. F. G.; CATTANI, C. E. V.; SILVA JUNIOR, C. A. DA; CAON, I. L.; PRUDENTE, V. H. R. Extraction of crop information through the spatiotemporal fusion of OLI and MODIS images. **Geocarto International**, p. 1–25, 2021a.

OLOFSSON, P.; FOODY, G. M.; HEROLD, M.; STEHMAN, S. V.; WOODCOCK, C. E.; WULDER, M. A. Good practices for estimating area and assessing accuracy of land change. **Remote Sensing of Environment**, v. 148, p. 42–57, 2014.

PAN, Z.; ZHANG, H.; MIN, X.; XU, Z. Vicarious calibration correction of large FOV sensor using BRDF model based on UAV angular spectrum measurements. **Journal of Applied Remote Sensing**, v. 14, n. 02, p. 1, 2020.

PAUL, S.; PATI, U. C. A comprehensive review on remote sensing image registration. **International Journal of Remote Sensing**, v. 42, n. 14, p. 5400–5436, 2021a.

PAUL, S.; PATI, U. C. A comprehensive review on remote sensing image registration. **International Journal of Remote Sensing**, v. 42, n. 14, p. 5400–5436, 2021b.

PEDREGOSA, F.; VAROQUAUX, G.; GRAMFORT, A.; MICHEL, V.; THIRION, B.; GRISEL, O.; BLONDEL, M.; PRETTENHOFER, P.; WEISS, R.; DUBOURG, V.; VANDERPLAS, J.; PASSOS, A.; COURNAPEAU, D.; BRUCHER, M.; PERROT, M.; DUCHESNAY, É. Scikit-learn: machine learning in Python. **Journal of Machine Learning Research**, v. 12, p. 2825–2830, 2011.

PELLETIER, C.; VALERO, S.; INGLADA, J.; CHAMPION, N.; DEDIEU, G. Assessing the robustness of Random Forests to map land cover with high resolution satellite image time series over large areas. **Remote Sensing of Environment**, v. 187, p. 156–168, 2016.

PELLETIER, N.; TYEDMERS, P. Forecasting potential global environmental costs of livestock production 2000-2050. **Proceedings of the National Academy of Sciences of the United States of America**, v. 107, n. 43, p. 18371–18374, 2010.

PEREIRA, A. R.; ANGELOCCI, L. R.; SENTELHAS, P. C.; ANTONIO. **Agrometeorologia - fundamentos e aplicações práticas**. [S.l.]: Agropecuária, 2002. 478 p.

PETRI, C. A.; GALVÃO, L. S.; LYAPUSTIN, A. I. MODIS BRDF effects over Brazilian tropical forests and savannahs: a comparative analysis. **Remote Sensing Letters**, v. 10, n. 2, p. 95–102, 2019.

PICOLI, M. C. A.; CAMARA, G.; SANCHES, I.; SIMÕES, R.; CARVALHO, A.; MACIEL, A.; COUTINHO, A.; ESQUERDO, J.; ANTUNES, J.; BEGOTTI, R. A.; ARVOR, D.; ALMEIDA, C. Big earth observation time series analysis for monitoring Brazilian agriculture. **ISPRS Journal of Photogrammetry and Remote Sensing**, v. 145,p. 328–339, 2018.

PICOLI, M. C. A.; RORATO, A.; LEITÃO, P.; CAMARA, G.; MACIEL, A.; HOSTERT, P.; SANCHES, I. D. Impacts of public and private sector policies on soybean and pasture expansion in Mato Grosso—Brazil from 2001 to 2017. **Land**, v. 9, n. 1, p. 20, 2020a.

PICOLI, M. C. A.; SIMOES, R.; CHAVES, M.; SANTOS, L. A.; SANCHEZ, A.; SOARES, A.; SANCHES, I. D.; FERREIRA, K. R.; QUEIROZ, G. R. CBERS data cube: a powerful technology for mapping and monitoring brazilian biomes. **ISPRS Annals of the Photogrammetry, Remote Sensing and Spatial Information Sciences**, v.3, n. 3, p. 533–539, 2020b.

PINTO, C.; PONZONI, F.; CASTRO, R.; LEIGH, L.; MISHRA, N.; AARON, D.; HELDER, D. First in-flight radiometric calibration of MUX and WFI on-board CBERS-4. **Remote Sensing**, v. 8, n. 5, p. 1–22, 2016a.

PINTO, C. T.; PONZONI, F. J.; CASTRO, R. M.; LEIGH, L.; KAEWMANEE, M.; AARON, D.; HELDER, D. Evaluation of the uncertainty in the spectral band adjustment factor (SBAF) for cross-calibration using Monte Carlo simulation. **Remote Sensing Letters**, v. 7, n. 9, p. 837–846, 2016b.

PONZONI, F. J.; SHIMABUKURO, Y. E.; KUPLICH, T. M. **Sensoriamento remoto da vegetação**. 2. ed. São Paulo: Oficina de Textos, 2012. 165 p. ISBN(9788579750533).

PONZONI, F. J.; ZULLO, J.; LAMPARELLI, R. A. C. In-flight absolute calibration of the CBERS-2 CCD sensor data. **Anais da Academia Brasileira de Ciencias**, v. 80, n. 2, p. 373–380, 2008.

POTAPOV, P.; TURUBANOVA, S.; HANSEN, M. C.; TYUKAVINA, A.; ZALLES, V.; KHAN, A.; SONG, X.-P.; PICKENS, A.; SHEN, Q.; CORTEZ, J. Global maps of cropland extent and change show accelerated cropland expansion in the twenty-first century. **Nature Food**, 2021.

POTAPOV, P. V.; TURUBANOVA, S. A.; HANSEN, M. C.; ADUSEI, B.; BROICH, M.; ALTSTATT, A.; MANE, L.; JUSTICE, C. O. Quantifying forest cover loss in Democratic Republic of the Congo, 2000-2010, with Landsat ETM+ data. **Remote Sensing of Environment**, v. 122, p. 106–116, 2012.

PRUDENTE, V. H. R.; MARTINS, V. S.; VIEIRA, D. C.; SILVA, N. R. DE F. E.; ADAMI, M.; SANCHES, I. D. Limitations of cloud cover for optical remote sensing of agricultural areas across South America. **Remote Sensing**

Applications: Society and Environment, v. 20, e 100414, 2020.

PRUDENTE, V. H. R.; SKAKUN, S.; OLDONI, L. V.; A. M. XAUD, H.; XAUD, M. R.; ADAMI, M.; SANCHES, I. D. A. Multisensor approach to land use and land cover mapping in Brazilian Amazon. **ISPRS Journal of Photogrammetry and Remote Sensing**, v. 189, p. 95–109, 2022.

QIU, S.; ZHU, Z.; HE, B. Fmask 4.0: Improved cloud and cloud shadow detection in Landsats 4–8 and Sentinel-2 imagery. **Remote Sensing of Environment**, v. 231, e111205, 2019.

RANUM, P.; PEÑA-ROSAS, J. P.; GARCIA-CASAL, M. N. Global maize production, utilization, and consumption. **Annals of the New York Academy of Sciences**, v. 1312, n. 1, p. 105–112, 2014.

RAY, D. K.; GERBER, J. S.; MACDONALD, G. K.; WEST, P. C. Climate variation explains a third of global crop yield variability. **Nature Communications**, v. 6, p. 1–9, 2015.

REWEHEL, E. M.; LI, J.; KESHK, H. M. Sentinel-2 cloud mask classification using deep learning method. **International Journal of Aeronautical and Space Sciences**, v. 23, n. 3, p. 622–635, 2022a.

RODRIGO, J. Spring frosts in deciduous fruit trees: morphological damage and flower hardiness. **Scientia Horticulturae**, v. 85, n. 3, p. 155–173, 2000.

ROGASS, C.; SEGL, K.; KUESTER, T.; KAUFMANN, H. Performance of correlation approaches for the evaluation of spatial distortion reductions. **Remote Sensing Letters**, v. 4, n. 12, p. 1214–1223, 2013.

ROSSOW, W. B.; SCHIFFER, R. A. Advances in understanding clouds from ISCCP. **Bulletin of the American Meteorological Society**, v. 80, n. 11, p. 2261–2287, 1999.

ROUJEAN, J.-L.; LEROY, M.; DESCHAMPS, P.-Y. A bidirectional reflectance model of the Earth's surface for the correction of remote sensing data. **Journal of Geophysical Research**, v. 97, n. D18, p. 20455, 1992.

ROUSE, J. W.; HAAS, R. H.; SCHELL, J. A.; DEERING, D. W.; HARLAN, J. C. **Monitoring the vernal advancements and retrogradation (Green Wave Effect) of natural vegetation**. Washington: NASA, 1974a.

ROUSE, J. W.; HAAS, R. H.; SCHELL, J. A.; DEERING, D. W.; HARLAN, J. C. **Monitoring the vernal advancement and retrogradation (greenwave effect) of natural vegetation**. NASA, 1974b. Available from: <http://scholar.google.com/scholar?q=related:kfZY0xukQScJ:scholar.google.com/&hl=en&num=20&as_sdt=0,5%5Cnpapers2://publication/uuid/FB22B85B-

B2F9-442E-AF63-58F3517012FC>.

ROY, D. P.; JU, J.; LEWIS, P.; SCHAAF, C.; GAO, F.; HANSEN, M.; LINDQUIST, E. Multi-temporal MODIS-Landsat data fusion for relative radiometric normalization, gap filling, and prediction of Landsat data. **Remote Sensing of Environment**, v. 112, n. 6, p. 3112–3130, 2008.

ROY, D. P.; KOVALSKYY, V.; ZHANG, H. K.; VERMOTE, E. F.; YAN, L.; KUMAR, S. S.; EGOROV, A. Characterization of Landsat-7 to Landsat-8 reflective wavelength and normalized difference vegetation index continuity. **Remote Sensing of Environment**, v. 185, p. 57–70, 2016a.

ROY, D. P.; LI, J.; ZHANG, H. K.; YAN, L.; HUANG, H.; LI, Z. Examination of Sentinel-2A multi-spectral instrument (MSI) reflectance anisotropy and the suitability of a general method to normalize MSI reflectance to nadir BRDF adjusted reflectance. **Remote Sensing of Environment**, v. 199, p. 25–38, 2017.

ROY, D. P.; ZHANG, H. K.; JU, J.; GOMEZ-DANS, J. L.; LEWIS, P. E.; SCHAAF, C. B.; SUN, Q.; LI, J.; HUANG, H.; KOVALSKYY, V. A general method to normalize Landsat reflectance data to nadir BRDF adjusted reflectance. **Remote Sensing of Environment**, v. 176, p. 255–271, 2016b.

SALES, V. G.; STROBL, E.; ELLIOTT, R. J. R. Cloud cover and its impact on Brazil's deforestation satellite monitoring program: evidence from the cerrado biome of the Brazilian Legal Amazon. **Applied Geography**, v. 140, e102651, 2022.

SANCHEZ, A. H.; PICOLI, M. C. A.; CAMARA, G.; ANDRADE, P. R.; CHAVES, M. E. D.; LECHLER, S.; SOARES, A. R.; MARUJO, R. F. B.; SIMÕES, R. E. O.; FERREIRA, K. R.; QUEIROZ, G. R. Comparison of cloud cover detection algorithms on sentinel-2 images of the Amazon tropical forest. **Remote Sensing**, v. 12, n. 8, p. 1–16, 2020.

SANO, E. E.; FERREIRA, L. G.; ASNER, G. P.; STEINKE, E. T. Spatial and temporal probabilities of obtaining cloud-free Landsat images over the Brazilian tropical savanna. **International Journal of Remote Sensing**, v. 28, n. 12, p. 2739–2752, 2007.

SANTOS, C. L. M. O.; LAMPARELLI, R. A. C.; DANTAS ARAÚJO FIGUEIREDO, G. K.; DUPUY, S.; BOURY, J.; LUCIANO, A. C. S.; TORRES, R. DA S.; LE MAIRE, G. Classification of crops, pastures, and tree plantations along the season with multi-sensor image time series in a subtropical agricultural region. **Remote Sensing**, v. 11, n. 3, p. 334, 2019.

SANTOS, J. S.; FONTANA, D. C.; SILVA, T. S. F.; RUDORFF, B. F. T. Identificação da dinâmica espaço-temporal para estimar área cultivada de soja

a partir de imagens MODIS no Rio Grande do Sul. **Revista Brasileira de Engenharia Agrícola e Ambiental**, v. 18, n. 1, p. 54–63, 2014.

SCHAAF, C. B.; GAO, F.; STRAHLER, A. H.; LUCHT, W.; LI, X.; TSANG, T.; STRUGNELL, N. C.; ZHANG, X.; JIN, Y.; MULLER, J.-P.; LEWIS, P.; BARNSLEY, M.; HOBSON, P.; DISNEY, M.; ROBERTS, G.; DUNDERDALE, M.; DOLL, C.; D'ENTREMONT, R. P.; HU, B.; LIANG, S.; PRIVETTE, J. L.; ROY, D. First operational BRDF, albedo nadir reflectance products from MODIS. **Remote Sensing of Environment**, v. 83, n. 1–2, p. 135–148, 2002.

SCHAEPMAN-STRUB, G.; SCHAEPMAN, M. E.; PAINTER, T. H.; DANGEL, S.; MARTONCHIK, J. V. Reflectance quantities in optical remote sensing-definitions and case studies. **Remote Sensing of Environment**, v. 103, n. 1, p. 27–42, 2006.

SCHEFFLER, D.; HOLLSTEIN, A.; DIEDRICH, H.; SEGL, K.; HOSTERT, P. AROSICS: an automated and robust open-source image co-registration software for multi-sensor satellite data. **Remote Sensing**, v. 9, n. 7, p. 676, 2017.

SCHMIDT, M.; KING, E. A.; MCVICAR, T. R. Assessing the geometric accuracy of AVHRR data processed with a state vector based navigation system. **Canadian Journal of Remote Sensing**, v. 34, n. 5, p. 496–508, 2008.

SCHULTZ, B. **Análise de imagens orientada a objetos e amostragem estatística no monitoramento de cana-de-açúcar, milho e soja no estado de São Paulo**. 2016. 210 p. Tese (Doutorado em Sensoriamento Remoto) - Insitituto Nacional de PEsquisase Espaciais, São José dos Campos, 2016.

SHUAI, Y.; MASEK, J. G.; GAO, F.; SCHAAF, C. B. An algorithm for the retrieval of 30-m snow-free albedo from Landsat surface reflectance and MODIS BRDF. **Remote Sensing of Environment**, v. 115, n. 9, p. 2204–2216, 2011.

SILVA, M. A. O.; ANDRADE, A. C. Geração de imagens de reflectância de um ponto de vista geométrico. **Revista Brasileira de Geomorfologia**, v. 1, n. 1, p. 29–36, 2013.

SILVA, M. A. O.; LIPORACE, F. D. S.; DA SILVA, M. A. O.; LIPORACE, F. D. S.; SILVA, M. A. O.; LIPORACE, F. D. S. Detecção automática de nuvem e sombra de nuvem em imagens de sensoriamento remoto. **Boletim de Ciências Geodésicas**, v. 22, n. 2, p. 369–388, 2016.

SKAKUN, S.; ROGER, J. C.; VERMOTE, E. F.; MASEK, J. G.; JUSTICE, C. O. Automatic sub-pixel co-registration of Landsat-8 operational land imager and Sentinel-2A multi-spectral instrument images using phase correlation and machine learning based mapping. **International Journal of Digital Earth**, v.

10, n. 12, p. 1253–1269, 2017a.

SKAKUN, S.; VERMOTE, E.; ROGER, J. C.; JUSTICE, C. Multispectral misregistration of Sentinel-2A images: analysis and implications for potential applications. **IEEE Geoscience and Remote Sensing Letters**, v. 14, n. 12, p. 2408–2412, 2017b.

SKAKUN, S.; WEVERS, J.; BROCKMANN, C.; DOXANI, G.; ALEKSANDROV, M.; HAGOLLE, O.; DAN, L.; ZUST, L. Remote sensing of environment Cloud Mask Intercomparison eXercise (CMIX): an evaluation of cloud masking algorithms for Landsat 8 and Sentinel-2. **Remote Sensing of Environment**, v. 274, 2022.

SNOW, A. D.; WHITAKER, J.; COCHRAN, M.; BOSSCHE, J. VAN DEN; MAYO, C.; MIARA, I.; KLOE, J. DE; KARNEY, C.; COUWENBERG, B.; LOSTIS, G.; DEARING, J.; OUZOUNOUDIS, G.; FILIPE; JURD, B.; GOHLKE, C.; HOESE, D.; ITKIN, M.; MAY, R.; HEITOR; WIEDEMANN, B. M.; BARKER, C.; WILLOUGHBY, C.; HABERTHÜR, D.; POPOV, E.; MAEYER, J. DE; RANALLI, J.; EVERS, K.; COSTA, M. A. DA; MMODENESI; RASPAUD, M. **pyproj4/pyproj: 3,2,1 Release**. 18 set. 2021.

SOTERRONI, A. C.; RAMOS, F. M.; MOSNIER, A.; FARGIONE, J.; ANDRADE, P. R.; BAUMGARTEN, L.; PIRKER, J.; OBERSTEINER, M.; KRAXNER, F.; CÂMARA, G.; CARVALHO, A. X. Y.; POLASKY, S. Expanding the soy moratorium to Brazil's Cerrado. **Science Advances**, v. 5, n. 7, eaav7336, 2019.

SOUDANI, K.; LE MAIRE, G.; DUFRÊNE, E.; FRANÇOIS, C.; DELPIERRE, N.; ULRICH, E.; CECCHINI, S. Evaluation of the onset of green-up in temperate deciduous broadleaf forests derived from Moderate Resolution Imaging Spectroradiometer (MODIS) data. **Remote Sensing of Environment**, v. 112, n. 5, p. 2643–2655, 2008.

SOUZA, C. M.; SHIMBO, J. Z.; ROSA, M. R.; PARENTE, L. L.; ALENCAR, A. A.; RUDORFF, B. F. T.; HASENACK, H.; MATSUMOTO, M.; FERREIRA, L. G.; SOUZA-FILHO, P. W. M.; DE OLIVEIRA, S. W.; ROCHA, W. F.; FONSECA, A. V.; MARQUES, C. B.; DINIZ, C. G.; COSTA, D.; MONTEIRO, D.; ROSA, E. R.; VÉLEZ-MARTIN, E.; WEBER, E. J.; LENTI, F. E. B.; PATERNOST, F. F.; PAREYN, F. G. C.; SIQUEIRA, J. V.; VIERA, J. L.; FERREIRA NETO, L. C.; SARAIVA, M. M.; SALES, M. H.; SALGADO, M. P. G.; VASCONCELOS, R.; GALANO, S.; MESQUITA, V. V.; AZEVEDO, T. Reconstructing three decades of land use and land cover changes in brazilian biomes with landsat archive and earth engine. **Remote Sensing**, v. 12, n. 17, 2020.

STEVEN, M. D.; MALTHUS, T. J.; BARET, F.; XU, H.; CHOPPING, M. J. Intercalibration of vegetation indices from different sensor systems. **Remote Sensing of Environment**, v. 88, n. 4, p. 412–422, 2003.

STOREY, J.; CHOATE, M.; LEE, K. Landsat 8 operational land imager on-orbit geometric calibration and performance. **Remote Sensing**, v. 6, n. 11, p. 11127–11152, 2014.

STUMPF, A.; MICHÉA, D.; MALET, J. P. Improved co-registration of Sentinel-2 and Landsat-8 imagery for Earth surface motion measurements. **Remote Sensing**, v. 10, n. 2, p. 1–20, 2018.

STUTSEL, B. M.; CALLOW, J. N.; FLOWER, K. C.; BIDDULPH, T. BEN; ISSA, N. A. Application of distributed temperature sensing using optical fibre to understand temperature dynamics in wheat (triticum aestivum) during frost. **European Journal of Agronomy**, v. 115, e126038, 2020a.

SUGAWARA, L. M.; RUDORFF, B. F. T.; ADAMI, M. Viabilidade de uso de imagens do Landsat em mapeamento de área cultivada com soja no Estado do Paraná. **Pesquisa Agropecuaria Brasileira**, v. 43, n. 12, p. 1763–1768, 2008.

SUN, L.; MI, X.; WEI, J.; WANG, J.; TIAN, X.; YU, H.; GAN, P. A cloud detection algorithm-generating method for remote sensing data at visible to short-wave infrared wavelengths. **ISPRS Journal of Photogrammetry and Remote Sensing**, v. 124, p. 70–88, 2017.

TANG, F.; ZOU, X.; YANG, H.; WENG, F. Estimation and correction of geolocation errors in FengYun-3C microwave radiation imager data. **IEEE Transactions on Geoscience and Remote Sensing**, v. 54, n. 1, p. 407–420, 2016.

TANG, Y.; WANG, Q. On the effect of misregistration on spatio-temporal fusion. In: INTERNATIONAL WORKSHOP ON THE ANALYSIS OF MULTITEMPORAL REMOTE SENSING IMAGES, 10., 2019. **Proceedings…** 2019. p.2019–2022.

TILMAN, D.; BALZER, C.; HILL, J.; BEFORT, B. L. Global food demand and the sustainable intensification of agriculture. **Proceedings of the National Academy of Sciences**, v. 108, n. 50, p. 20260–20264, 2011.

UNITED STATES DEPARTMENT OF AGRICULTURE (USDA). **USDA agricultural projections to 2030**. [S.l.]: USDA, 2021.

UNITED STATES DEPARTMENT OF AGRICULTURE (USDA). **Grain: world markets and trade**. [S.l.]: USDA, 2022.

VAKALOPOULOU, M.; CHRISTODOULIDIS, S.; SAHASRABUDHE, M.; MOUGIAKAKOU, S.; PARAGIOS, N. Image registration of satellite imagery with deep convolutional neural networks. In: INTERNATIONAL GEOSCIENCE AND REMOTE SENSING SYMPOSIUM (IGARSS), 2019. **Proceedings…** 2019. p. 4939–4942.

VAN DER WERFF, H.; VAN DER MEER, F. Sentinel-2A MSI and Landsat 8 OLI provide data continuity for geological remote sensing. **Remote Sensing**, v. 8, n. 11, p. 883, 2016.

VAN DIJK, M.; MORLEY, T.; RAU, M. L.; SAGHAI, Y. A meta-analysis of projected global food demand and population at risk of hunger for the period 2010–2050. **Nature Food**, v. 2, n. 7, p. 494–501, 2021.

VAN DONINCK, J.; TUOMISTO, H. Evaluation of directional normalization methods for Landsat TM/ETM+ over primary Amazonian lowland forests. **International Journal of Applied Earth Observation and Geoinformation**, v. 58, p. 249–263, 2017.

VIRTANEN, P.; GOMMERS, R.; OLIPHANT, T. E.; HABERLAND, M.; REDDY, T.; COURNAPEAU, D.; BUROVSKI, E.; PETERSON, P.; WECKESSER, W.; BRIGHT, J.; VAN DER WALT, S. J.; BRETT, M.; WILSON, J.; MILLMAN, K. J.; MAYOROV, N.; NELSON, A. R. J.; JONES, E.; KERN, R.; LARSON, E.; CAREY, C. J.; POLAT, İ.; FENG, Y.; MOORE, E. W.; VANDERPLAS, J.; LAXALDE, D.; PERKTOLD, J.; CIMRMAN, R.; HENRIKSEN, I.; QUINTERO, E. A.; HARRIS, C. R.; ARCHIBALD, A. M.; RIBEIRO, A. H.; PEDREGOSA, F.; VAN MULBREGT, P.; VIJAYKUMAR, A.; BARDELLI, A. PIETRO; ROTHBERG, A.; HILBOLL, A.; KLOECKNER, A.; SCOPATZ, A.; LEE, A.; ROKEM, A.; WOODS, C. N.; FULTON, C.; MASSON, C.; HÄGGSTRÖM, C.; FITZGERALD, C.; NICHOLSON, D. A.; HAGEN, D. R.; PASECHNIK, D. V.; et al. SciPy 1.0: fundamental algorithms for scientific computing in Python. **Nature Methods**, v. 17, n. 3, p. 261–272, 2020.

WALDNER, F.; CANTO, G. S.; DEFOURNY, P. Automated annual cropland mapping using knowledge-based temporal features. **ISPRS Journal of Photogrammetry and Remote Sensing**, v. 110, p. 1–13, 2015.

WANG, S.; CHEN, J.; RAO, Y.; LIU, L.; WANG, W.; DONG, Q. Response of winter wheat to spring frost from a remote sensing perspective: Damage estimation and influential factors. **ISPRS Journal of Photogrammetry and Remote Sensing**, v. 168, p. 221–235, 2020.

WANG, Z.; BOVIK, A. C.; SHEIKH, H. R.; SIMONCELLI, E. P. Image quality assessment: From error visibility to structural similarity. **IEEE Transactions on Image Processing**, v. 13, n. 4, p. 600–612, 2004.

WANNER, W.; LI, X.; STRAHLER, A H. On the derivation of kernels for kernel-driven models of bidirectional reflectance. **Journal of Geophysical Research**, v. 100, n. D10, p. 21077, 1995.

WEISS, M.; JACOB, F.; DUVEILLER, G. Remote sensing for agricultural applications: a meta-review. **Remote Sensing of Environment**, v. 236, e 111402, 2020.

WHITCRAFT, A. K.; BECKER-RESHEF, I.; JUSTICE, C. O. A framework for defining spatially explicit Earth observation requirements for a Global Agricultural Monitoring Initiative (GEOGLAM). **Remote Sensing**, v. 7, n. 2, p. 1461–1481, 2015a.

WHITCRAFT, A. K.; BECKER-RESHEF, I.; JUSTICE, C. O. Agricultural growing season calendars derived from MODIS surface reflectance. **International Journal of Digital Earth**, v. 8, n. 3, p. 173–197, 2015b.

WHITCRAFT, A. K.; BECKER-RESHEF, I.; JUSTICE, C. O.; GIFFORD, L.; KAVVADA, A.; JARVIS, I. No pixel left behind: toward integrating Earth Observations for agriculture into the United Nations Sustainable Development Goals framework. **Remote Sensing of Environment**, v. 235, e111470, 2019.

WHITCRAFT, A. K.; BECKER-RESHEF, I.; KILLOUGH, B.; JUSTICE, C. Meeting Earth observation requirements for global agricultural monitoring: an evaluation of the revisit capabilities of current and planned moderate resolution optical Earth observing missions. **Remote Sensing**, v. 7, n. 2, p. 1482–1503, 2015a.

WHITCRAFT, A. K.; VERMOTE, E. F.; BECKER-RESHEF, I.; JUSTICE, C. O. Cloud cover throughout the agricultural growing season: Impacts on passive optical earth observations. **Remote Sensing of Environment**, v. 156, p. 438–447, 2015b.

WOLFE, R. E.; NISHIHAMA, M. Trends in MODIS geolocation error analysis. **Earth Observing Systems XIV**, v. 7452, p. 74520L, 2009.

WOLFE, R. E.; NISHIHAMA, M.; FLEIG, A. J.; KUYPER, J. A.; ROY, D. P.; STOREY, J. C.; PATT, F. S. Achieving sub-pixel geolocation accuracy in support of MODIS land science. **Remote Sensing of Environment**, v. 83, n. 1–2, p. 31–49, 2002.

WREGE, M. S.; FRITZSONS, E.; SOARES, M. T. S.; PRELA-PÂNTANO, A.; STEINMETZ, S.; CARAMORI, P. H.; RADIN, B.; PANDOLFO, C. risco de ocorrência de geadas na região centro-sul do Brasil. **Revista Brasileira de Climatologia**, v. 22, p. 149–164, 2018a.

WU, X.; NAEGELI, K.; WUNDERLE, S. Geometric accuracy assessment of global coarse resolution satellite data sets: a study based on AVHRR GAC data at the subpixel level. **Earth System Science Data Discussions**, n. 1, p. 1–22, 2019.

WULDER, M. A.; COOPS, N. C.; ROY, D. P.; WHITE, J. C.; HERMOSILLA, T. Land cover 2.0. **International Journal of Remote Sensing**, v. 39, n. 12, p. 4254–4284, 2018.

WULDER, M. A.; HILKER, T.; WHITE, J. C.; COOPS, N. C.; MASEK, J. G.; PFLUGMACHER, D.; CREVIER, Y. Virtual constellations for global terrestrial monitoring. **Remote Sensing of Environment**, v. 170, p. 62–76, 2015.

WULDER, M. A.; WHITE, J. C.; GOWARD, S. N.; MASEK, J. G.; IRONS, J. R.; HEROLD, M.; COHEN, W. B.; LOVELAND, T. R.; WOODCOCK, C. E. Landsat continuity: Issues and opportunities for land cover monitoring. **Remote Sensing of Environment**, v. 112, n. 3, p. 955–969, 2008.

YAMAMOTO, Y.; ICHII, K.; HIGUCHI, A.; TAKENAKA, H. Geolocation accuracy assessment of himawari-8/AHI imagery for application to terrestrial monitoring. **Remote Sensing**, v. 12, n. 9, 2020.

YAN, L.; ROY, D. P. Automated crop field extraction from multi-temporal Web Enabled Landsat data. **Remote Sensing of Environment**, v. 144, p. 42–64, 2014.

YAN, L.; ROY, D. P.; LI, Z.; ZHANG, H. K.; HUANG, H. Sentinel-2A multi-temporal misregistration characterization and an orbit-based sub-pixel registration methodology. **Remote Sensing of Environment**, v. 215, p. 495–506, 2018.

YAN, L.; ROY, D.; ZHANG, H.; LI, J.; HUANG, H. An automated approach for sub-pixel registration of Landsat-8 Operational Land Imager (OLI) and Sentinel-2 Multi Spectral Instrument (MSI) imagery. **Remote Sensing**, v. 8, n. 6, p. 520, 2016.

ZALLES, V.; HANSEN, M. C.; POTAPOV, P. V; STEHMAN, S. V; TYUKAVINA, A.; PICKENS, A.; SONG, X.; ADUSEI, B.; OKPA, C.; AGUILAR, R.; JOHN, N.; CHAVEZ, S. Near doubling of Brazil ' s intensive row crop area since 2000. **PNAS,** v. 116, n. 2, 2019.

ZHANG, H. K.; ROY, D. P.; YAN, L.; LI, Z.; HUANG, H.; VERMOTE, E.; SKAKUN, S.; ROGER, J.-C. C. Characterization of Sentinel-2A and Landsat-8 top of atmosphere, surface, and nadir BRDF adjusted reflectance and NDVI differences. **Remote Sensing of Environment**, v. 215, p. 482–494, 2018.

ZHAO, L.; LI, Q.; ZHANG, Y.; WANG, H.; DU, X. Normalized NDVI valley area index (NNVAI)-based framework for quantitative and timely monitoring of winter wheat frost damage on the Huang-Huai-Hai Plain, China. **Agriculture, Ecosystems and Environment**, v. 292, e106793, 2020.

ZHONG, L.; GONG, P.; BIGING, G. S. Phenology-based crop classification algorithm and its implications on agricultural water use assessments in California's Central Valley. **Photogrammetric Engineering & Remote Sensing**, v. 78, n. 8, p. 799–813, 2012.

ZHONG, L.; HU, L.; YU, L.; GONG, P.; BIGING, G. S. Automated mapping of soybean and corn using phenology. **ISPRS Journal of Photogrammetry and Remote Sensing**, v. 119, p. 151–164, 2016a.

ZHONG, L.; YU, L.; LI, X.; HU, L.; GONG, P. Rapid corn and soybean mapping in US corn belt and neighboring areas. **Scientific Reports**, v. 6, p. 36240, 2016b.

ZHOU, J.; YANG, H.; ANDERSON, K. SNPP ATMS on-orbit geolocation error evaluation and correction algorithm. **IEEE Transactions on Geoscience and Remote Sensing**, v. 57, n. 6, p. 3802–3812, 2019.

ZHU, X.; HELMER, E. H. An automatic method for screening clouds and cloud shadows in optical satellite image time series in cloudy regions. **Remote Sensing of Environment**, v. 214, p. 135–153, 2018.

ZHU, Z.; WANG, S.; WOODCOCK, C. E. Improvement and expansion of the Fmask algorithm: cloud, cloud shadow, and snow detection for Landsats 4-7, 8, and Sentinel 2 images. **Remote Sensing of Environment**, v. 159, p. 269–277, 2015.

ZHU, Z.; WOODCOCK, C. E. Object-based cloud and cloud shadow detection in Landsat imagery. **Remote Sensing of Environment**, v. 118, p. 83–94, 2012.

ZHU, Z.; WOODCOCK, C. E. Automated cloud, cloud shadow, and snow detection in multitemporal Landsat data: an algorithm designed specifically for monitoring land cover change. **Remote Sensing of Environment**, v. 152, p. 217–234, 2014.

ZITOVÁ, B.; FLUSSER, J. Image registration methods: a survey. **Image and Vision Computing**, v. 21, n. 11, p. 977–1000, 2003.

ZU ERMGASSEN, E. K. H. J.; AYRE, B.; GODAR, J.; BASTOS LIMA, M. G.; BAUCH, S.; GARRETT, R.; GREEN, J.; LATHUILLIÈRE, M. J.; LÖFGREN, P.; MACFARQUHAR, C.; MEYFROIDT, P.; SUAVET, C.; WEST, C.; GARDNER, T. Using supply chain data to monitor zero deforestation commitments: an assessment of progress in the Brazilian soy sector. **Environmental Research Letters**, v. 15, n. 3, e 035003, 2020.